Intensified Electrochemical Processes

by

HUA CHENG, M. Sc.

A thesis submitted to the Faculty of Engineering of the University of Newcastle upon Tyne for the degree of Doctor of Philosophy

Department of Chemical & Process Engineering

University of Newcastle upon Tyne

September 1999

TO

MY WIFE, QINGQING

AND

MY SON, FANFAN

ACKNOWLEDGEMENTS

The work described in this thesis has been carried out in the Department of Chemical & Process Engineering at the University of Newcastle upon Tyne.

I am indebted to my family over many years and therefore would like to express my sincere gratitude to them first, especially my wife Qingqing, my son Fanfan, and my parents for their patience, understanding and encouragement. Indeed, without their genuine and heart-whole support, there were no this thesis.

Many thanks to my supervisor, professor Keith Scott and the joint-supervisor, professor Colin Ramshaw, from whom I learnt so much and to whom I owe even more. I will never forget their continuous support, invaluable supervision, and personal integrity that made my stay very beneficial. Particularly for them always putting up new ideas when the project for some reasons did not go to well and always finding time to discuss problems and new ideas. Also, I would like to thank other members of the electrochemical technology group for their help.

Thanks would pass to technical staff of the Department for their co-operation. In particular, Mr. B. Dourish, who gave me tremendous help when my experiments had to stop due to the centrifuge's trouble and when I had to interrupt writing my thesis by the computer's problem. Thanks also extend to Mr. E. T. Horsley, Mr. S. Latimer, Mr. V. Scott, Mrs. G. Reed and Dr. J. Backhurst for their help.

Financial support from the University as Scholarship and from British Universities as Overseas Student Research Award is cheerfully acknowledged.

ABSTRACT

Process intensification is in principle a strategy of making dramatic reductions in the capital cost of a production system, improving intrinsic safety, reducing environmental impact and energy consumption. An electrochemical cell is a specific example of a multiphase system that should be capable of being operated very intensively within a centrifugal acceleration field. This thesis presents the first systematical research work in this field. It demonstrates that many electrochemical processes can be enhanced considerably by using a high-acceleration field, which takes full advantage of the improvement in catalytic activity and optimal electrode structure.

Six electrochemical processes have been investigated. Namely, the electro-reduction of oxygen, electro-oxidations of hydrogen and methanol, chlorine evolution, water electrolysis, and methanol fuel cell reaction. Several catalysed electrodes including Ti mesh or carbon cloth were prepared and used for the above processes. A number of catalyst deposition routes were explored for the preparation of the technical electrodes, including Pt, Ag, Pt-Ru and RuO_2 electrodes.

The action of a centrifugal field is two fold: first, it acts as an mass transfer promotor; second, it accelerates gas bubble disengagement. For chlorine evolution, water electrolysis, and methanol oxidation, centrifugal fields play a very significant role in and lead to significant reductions in polarisation and mass transport resistance. The high acceleration fields reduce the cell resistance drastically through effectively disengaging gas bubbles from the electrode surface. It also overcomes mass transport limitations in these systems through generation of powerful interphase buoyancy force. The processes were therefore greatly intensified in centrifugal fields and

approached a maximum efficiency. Increase in the operating temperature and the concentration also benefit the processes. Interestingly, both effects were intensitfied in centrifugal fields, i.e., the current density increases more rapidly in centrifugal fields than in stationary cell at a constant potential corresponding to the same increment in temperature and concentration.

For the gas consuming systems, e.g., oxygen reduction and hydrogen oxidation, centrifugal fields also produce positive results. The degree of intensification for these systems was limited to a relatively low level.

Centrifugal fields have little benefit for methanol fuel cell operation. The results were disappointing and unexpected. It was realised that the cathode process, an oxygen gas consuming reaction, is difficult to be intensified by using centrifugal means due to the type of electrode used at the cathode, although the anode process was intensified in centrifugal fields.

A model for a centrifugal cell with gas evolving electrodes was proposed and tested. In the model the cell voltage and cell voltage reduction are obtained from the hydrodynamic electrochemical, and electrochemical engineering theories.

CONTENTS

Chapter 1. Introduction

This chapter discusses the basic principles in electrochemical technology and process intensification. A literature review of rotary electrochemical cells is also presented.

1.1. Electrochemical Technology

Electrochemical technology provides an efficient and competitive route in many industry sectors, particularly chemical synthesis, energy conversion, pollution control, metal extraction and formation of protective coatings [1-4]. The electrochemical process is a major part of electrochemical technology. In an electrochemical process, materials undergo required changes in chemical composition, energy distribution or physical state. The key means of processing is the electrochemical cell.

The industrial application of electrochemistry depends largely on the engineering design and implementation of an effective cell unit. There are several important considerations in electrochemical cell design which include productivity, energy requirement and cell voltage, mass and heat transfer, materials selection and geometry. However, the performance of an electrochemical cell is in particular judged on its production capacity and its energy consumption.

The production capacity of an electrochemical cell is proportional to the applied current density and current efficiency, i.e. the effective current density for the process, and the electrode area per unit volume. In practice, the production capacity of an electrochemical cell is often limited by several factors, such as materials of fabrication, current density and its distribution over the electrode, and hydrodynamics.

Energy consumption plays a significant role in an electrochemical process because the operation of the electrochemical cell can constitute a large part of the overall energy consumption of an electrolytic plant. The energy consumption of an electrochemical cell is determined by the thermodynamics of the reactions, the electrochemical kinetics and the cell design. It can be minimised by operating with a current efficiency as close to 100% as possible and with a low cell voltage.

Electrodes are at the heart of electrochemical cell. Intensified electrodes, e.g., electrodes with high conductivity, high catalytic activity, and high surface area are needed to intensify electrochemical processes. Gas diffusion electrodes are a good example of intensified electrodes, which are applied in several electrochemical devices such as fuel cells and electrolysers. Their high efficiency is due to the many catalytic centres in a unit geometric surface area. Electrodes adopted in this project will take advantage of the gas diffusion electrode concept.

As many electrochemical processes involve gas evolution, gas removal from electrodes is a major problem for practical operation in order to prevent "gas blinding", i.e., obscuring the electrode surface by gas bubbles. This will reduce electrolyte conductivity, which in turn, increases the potential drop and, with constant voltage operation, reduces cell current density leading to the unacceptable decline in performance. So the electrode design and material should facilitate efficient gas release from its surface to ensure that the IR drop in the electrolyte and the "bubble polarisation" is low.

It is worthwhile to note that the depth of penetration of the reaction into the porous matrix of the gas diffusion electrode is relatively small. Thus, the electrodes are thin and support only modest current densities. It would be of great benefit to the cost of

operating these electrodes if the level of current density could be significantly increased without causing a concurrent loss in the operating electrode potential. It is believed that this objective could be achieved by both increasing the active surface area and increasing the rate of mass transfer between the gas and the liquid [5].

1.2. Mass Transfer and Process Intensification

1.2.1. Mass Transfer

All processes in the electrochemical industry are concerned with the transfer of mass and energy. Thus, the theory and practice of mass transfer are constantly subject to intense study since any improvement in their efficiency, or the equipment within which such processes occur, could lead to considerable economic benefits.

Mass transfer of material is important in the field of electrochemical cell design, especially when the cell is operated on a large scale. The mass transfer of reacting species, together with the kinetics of electron transfer, determines the electrochemical reaction rate. The rate of mass transfer becomes particularly important when the reactant concentration is low and a reasonable conversion or rate of reaction is required. This is because with increasing polarisation of the electrode, as current density is increased, the electrode can become starved of reactant and the rate of mass transfer governs, and limits, the overall reaction rate.

Most industrial electrochemical processes unavoidably involve the generation of gases at one or both of the cell electrodes, for example, oxygen evolution at the anode and hydrogen evolution at the cathode. Therefore, the need to ensure efficient gas disengagement from the electrolyte, the electrodes and any intervening diaphragm/membrane, is a very important consideration in the design of electrolytic cells [5]. In conventional cells an acceptable mass transfer environment is

established by pumping the electrolyte across the electrode surface. However, significant power may be involved and this may limit the circulation velocity to about 2 m/s. Relatively poor mass transfer conditions exist even in a well-designed commercial cell such as the FM21 unit used in the chlor-alkali industry, and incur significant overvoltage, e.g. about 0.4 V at a current density of 3 kAm^{-2} [5]. This is due to the high resistance between the electrodes as a result of presence of gas bubbles.

The promotion of mass transfer can be achieved by various ways, such as pumping electrolyte through the electrochemical cell or using moving electrode, etc. However, such procedures can enhance mass transfer to a limited extent, especially during scale-up. For example, the rotating cylinder electrode, which only rotates the electrode, may be used in laminar, transitional or turbulent flow and has been routinely used in electrochemical industry for metal ion removal process [6.7]. Enhancement in mass transfer to a rotating cylinder electrode depends upon an increased surface area and enhanced microturbulence at the electrode surface. Therefore, its further improvement is severely limited. In order to develop compact equipment to meet the cost reduction and efficiency requirements of industrial production, the electrochemical processes must be subject to a degree of intensification.

1.2.2. Process Intensification

Process intensification is an attractive strategy in chemical industry. It was pioneered in ICI during the late 1970s, when the primary goal was to reduce the capital cost of a production system. While cost reduction was the original target for process intensification, it quickly became apparent that there were other important benefits,

particularly in respect of improved intrinsic safety, reduced environmental impact and energy consumption. The latter aspect is the subject of this project.

Process intensification is in principle particularly attractive for electrochemical processes. An electrochemical cell is a typical multiphase system. According to theory, when a centrifugal field is applied to a multiphase system, the light phase, e.g. gas, will flow inward, whereas the centrifugal effect will tend to sweep the denser fluid outward. This gives a rapid and efficient removal of the electrolytic gas product from the interelectrode gap, with possible improvement in the current efficiency, the space-time yield, and the overall energy consumption. As well known, the interphase buoyancy force determines the fluid dynamic behaviour of multiphase systems. Because this force is large in a centrifugal field, droplets and/or bubbles will be small and the interphase slip velocity will be high. This means that a high-acceleration environment should intensify the process operation by promoting high flooding velocities, large specific interfacial area and high heat/mass transfer coefficients [5]. Moreover, bubbles disengagement from the electrodes, electrolytes, membranes, and the inter-electrode area is greatly facilitated in centrifugal fields. This greatly reduces gas blanketing and enables the cell gap to be reduced, resulting in considerable reduction in the resistance of the cell , thereby making further significant savings in the overall cell voltage.

Since this energy is deployed within the liquid boundary layer, its impact on the transfer process should be more effective than an equal amount discharged throughout the electrolyte, as with a pumped cell, for example.

The above considerations suggest strongly that electrochemical processes that evolve a gas at one or both electrodes, should be capable of being performed very

intensively within a centrifugal acceleration field. The electrode surfaces, at short modest speeds of rotation, are subjected to centrifugal forces considerably in excess of that due to gravitational acceleration (9.81 ms^{-2}). For a packed device this means the minimum size of packing required to prevent flooding can be reduced thus allowing micro-packing to be used in conditions of high gas and liquid loadings. Therefore, the size of equipment needed for a given performance can be smaller than if a stationary contact surface is used.

It should be noted that the energy needed to rotate the cell and overcome windage, friction etc., will be quite trivial compared to that which is capable of being saved. For example, a 100 kA cell operating with a bubble overvoltage of 0.3 V has a potential energy saving of 30 kW whereas the cell rotor (1 m long x 0.5 m diameter) will require perhaps 2 kW to rotate at around 700 rpm.

1.3. Rotary Electrochemical Cells

This section reviews the area of rotary electrochemical cells.

1.3.1. The Rotary Water Electrolyser

A rotary water electrolyser, which was related to the electrolytic production of oxygen and hydrogen from water, was described in 1920s [8]. The invention aimed at assisting the gas bubbles to separate from the electrodes and ascend through the electrolyte, using centrifugal acceleration. The apparatus comprised a plurality of cells of annular form arranged around an axis of a hollow shaft having anodic and cathodic chmbers. The shaft communicated with the electrolytic cells by a plurality of ducts so arranged that hydrogen and oxygen could be delivered separately. A similar idea of rotary water electrolyser was also outlined in 1964 [9]. The idea related to improvements in process and apparatus for the production of oxygen

and/or hydrogen from water electrolysis. The patent claimed that the electrolyte decomposition, the gas and the electrolyte removal and recovery could be greatly enhanced in centrifugal fields. A rotary water electrolyser was patented in 1981 [10]. It was claimed that the cell could be used for supplying fuel (hydrogen) to an automobile and household. Unfortunately, no practical application for these ideas has been found. Moreover, since neither gave any performance data, it is not possible to estimate the energy savings that can be realised by their design.

1.3.2. The Rotary Electrodeposition Cells

Applying centrifugal fields in electrodeposition has attracted interest for many years. The earliest efforts appeared in the 1970s. A laboratory rotary cell was designed to synthesise composite materials of Ni and Al_2O_3 [11]. It was 5 inches in diameter with a capacity of 150 ml. The composite materials were formed in this cell according to the following procedure. The electrolyte slurry containing the reinforcing fibres were subjected to a centrifugal force field to press the fibres against the cathode and form a permeable mat for encapsulation by the deposited matrix metal. A typical laboratory demonstration was given in which the volume percentage of the Al_2O_3 whiskers was increased about 70% in the cell rotating at 1600 rpm, as compared to that achieved in the static cell. A similar cell was used to increase metal and alloy electrodeposition efficiency and produce high quality deposits of Ni and Al_2O_3 [12]. The apparatus comprises a centrifuge with a cylindrical housing constituting a cylindrical cell to hold the electrolyte. The process is suitable for nickel electrodeposition from a sulphamate bath. The required rotating speed is high for the cell operation, i.e., the minimum is 1500 rpm and the deposition rate of the nickle is three times higher when the cell was rotated at 2500-

3000 rpm than when the cell was stationary at a particular current density (not shown in the patent)

1.3.3. The Rotary Fused Salt Cells

Conventional molten salt electrowinning cells have poor energy consumption due to the large interelectrode spacing which causes high cell resistance. Under stationary conditions, reducing the interelectrode spacing can only be achieved at the detriment of increased back reaction of the products and a low current efficiency. Moreover, in some cases, the metal deposit droplets can adhere to the electrodes, causing an electrical short circuit and loss of production in the cell. The application of centrifugal fields through rotation of the cell can enhance the separation of the products of electrolysis, thereby allowing the interelectrode gap to be reduced. The centrifugal force would also encourage the metal droplets to be ejected away from the interelectrode spacing and so the chance of a short circuit was almost eliminated. From this idea, a rotary cell was fabricated to deposit Zn from the molten zinc chloride electrolytes [13]. It consisted of a silica beaker, 20 cm high and 14 cm in diameter, with plane graphite disc electrodes, 10 cm in diameter and 1 cm in thickness. The anode featured four 0.4-cm-diameter gas vents and was perforated to improve gas removal from the interelectrode gap, the rate-limiting step for the process. To facilitate the removal of the electrolytic products, conical electrodes were employed to take advantage of gravitational separation. The performance was reinforced by centrifugal force with the current efficiency almost 45% higher than the value obtained in the stationary cell at only 100 rpm (about 20 G).

A laboratory scale fused salt electrolysis cell for manufacturing Zn was constructed to further reduce large energy consumption and raise low space-time yields in fused

salt electrowinning [14]. The cell consisted of a recrystallised alumina crucible supported in a stainless steel container on a retractable arm. This allowed the cell to be easily placed in and removed from the furnace using an air-hydraulic system. Anode and cathode were both graphite. The cell was rotated by direct drive through the stainless steel rod and shaft system from an overhead electric motor. The upper anode plate was perforated to allow the chlorine gas to escape from the gap between the electrodes. The spacing between the electrodes was adjustable through the use of alumina spacer rings. The inter-electrode spacing was reduced from 100 mm (typical of commercial cells) down to less than 10 mm which served to significantly reduce the resistance between the electrodes. However, narrowing the spacing between the electrodes introduced the side reaction, i.e., the recombination of Zn and Cl_2. Application of a centrifugal field increased the current efficiency obviously, for example, from 43% to 93% when the rotating speed was increased from 0 to 100 rpm. The centrifugal force minimises turbulence effect and maximises physical separation of phases.

1.3.4. The Rotary Chlor-Alkali Cells

A rotating chlor-alkali membrane cell was designed at ICI [5]. In this cell, all but a 20 degree sector of the inter-electrode space was blanked off by a polypropylene spacer in order to restrict the current to the capacity of the slip ring assembly. When operated under the similar conditions as those encountered in commercial FM21 cells, very significant overall voltage savings was achieved in centrifugal fields[5]. Even at 25 G, the overall cell voltage reduced to 2.85 V at 3 kAm^{-2}, which is much lower than 3.17 V obtained in FM21 cells. The largest value of the cell voltage was attained at 200 G, i.e., about 2.8 V at the same current density.

The above pioneering work provided a very useful reference point for this work. Unfortunately, only the cell voltage behaviour was checked. The previous work did not mention the anodic behaviour itself, although this is very important from both a theretical and practical viewpoint.

1.3.5. The Rotary Air Cathode Cell

A new type of the rotating air cathode cell was designed [15]. The main components of the cell are Ag/carbon fibre cathode, anode, and Nafion membrane. The cell assembly was immersed in a rotating pool of electrolyte and the electrolyte was circulated through the cathodic and anodic chambers. Oxygen was supplied to the base (outer radius) of the cell and bubbled inwards through the cathode surface. This arrangement causes oxygen bubbles to split as they negotiate the cathode and stimulate excellent gas/electrolyte and electrolyte/electrode mass transfer. A cell voltage reduction of about 1 V could be achieved at a current density of 1 kAm^{-2}, when the oxygen (400 ml/min) was applied to the air cathode, rather than 400 ml/min nitrogen. This is due to the cathodic reduction of oxygen and corresponds remarkably closely to the maximum theoretical value under the prevailing conditions. A similar experiment was performed with a stationary equivalent of the rotating unit. In the unit, the electrolyte was pumped through the fibrous electrode, parallel to the current feeder. A maximum 0.8 V cell voltage reduction was achieved at a current density of only 0.1 kAm^{-2}. The good operating characteristics of the cell was attributed to the excellent mass transfer environment prevailing in the electrolytic cell operating in centrifugal fields. Although only cell voltage data are available in these work, it demonstrated the beneficial effect of centrifugal fields on the cell voltage. However, it is difficult to assess how centrifugal fields affect the

oxygen reduction reaction and to what extent. This knowledge is necessary because the cell voltage reduction resulted may not only be from the cathode potential reduction but also from the anode potential reduction.

The aforementioned research demonstrates that the aim of intensifying the electrochemical processes can be realised by using the intensified electrodes and high acceleration field. This thesis outlines the efforts made to reach the goal.

1.4. References for Chapter 1

[1] K. Scott, "Electrochemical Reaction Engineering", Academic Press, London, 1991.

[2]. F. Goodridge and K. Scott, "Electrochemical Process Engineering. A Guide", Plenum Press, New York, 1995.

[3]. D. J. Picket, "Electrochemical Reactor Design", 2nd Edition, Elsevier, Amsterdam, 1979.

[4]. F. C. Walsh, "A First Course in Electrochemical Engineering", The Electrochemical Consultancy, Hants, 1993.

[5]. C. Ramshaw, Heat Recovery Systems & CHP, 13, 493, 1993.

[6] D. R. Gabe and F. C. Walsh, I. Chem. E. Symp. Ser., 116, 219, 1990.

[7] D. R. Gabe and F. C. Walsh, Proc. Electrochem. Soc., 83-12, 167, 1983.

[8]. E. Thomson, US Patent, No.1,701,346, 1929.

[9]. T. B. Hoover, US Patent, No. 3,119,759, 1964.

[10]. N. Tsuji, Japan Patent, 81 96,084, 1981.

[11]. Iqbal Ahmad, US Patent, No. 3,716,461, 1973.

[12]. Iqbal Ahmad, US Patent, No. 3,783,110, 1974.

[13]. P. M. Copham and D. J. Fray, Met. Trans., 21B, 977, 1990.

[14]. A. Cox, J. W. A. Morris, and D. J. Fray, in "Electrochemical Engineering and Energy", Edited by F. Lapicque et al., p.109, Plenum Press, New York, 1995.

[15]. C. Ramshaw, European Patent, No. 207630, 1985.

Chapter 2. Experimental and Techniques

This chapter gives detailed information on the practical aspects and the experimental techniques used in this project. They are the centrifugal rig, the cell design, electrode fabrication and analysis techniques. Other specific aspects about experiments are covered in the related chapters.

2.1. Centrifugal Rig

The centrifugal rig is presented schematically in figure 2.1 (a) and its photo is given in figure 2 (b).

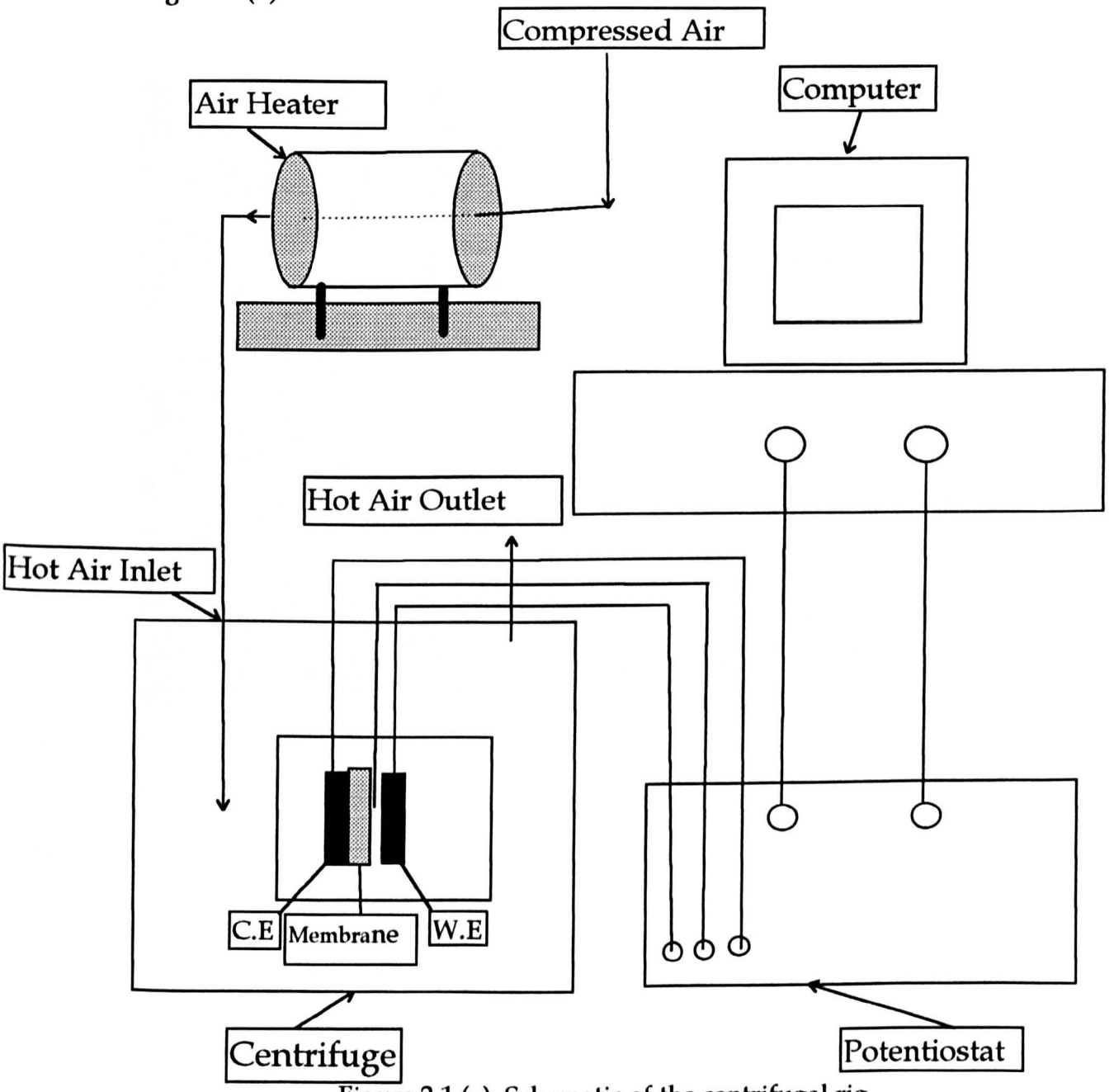

Figure 2.1 (a). Schematic of the centrifugal rig.

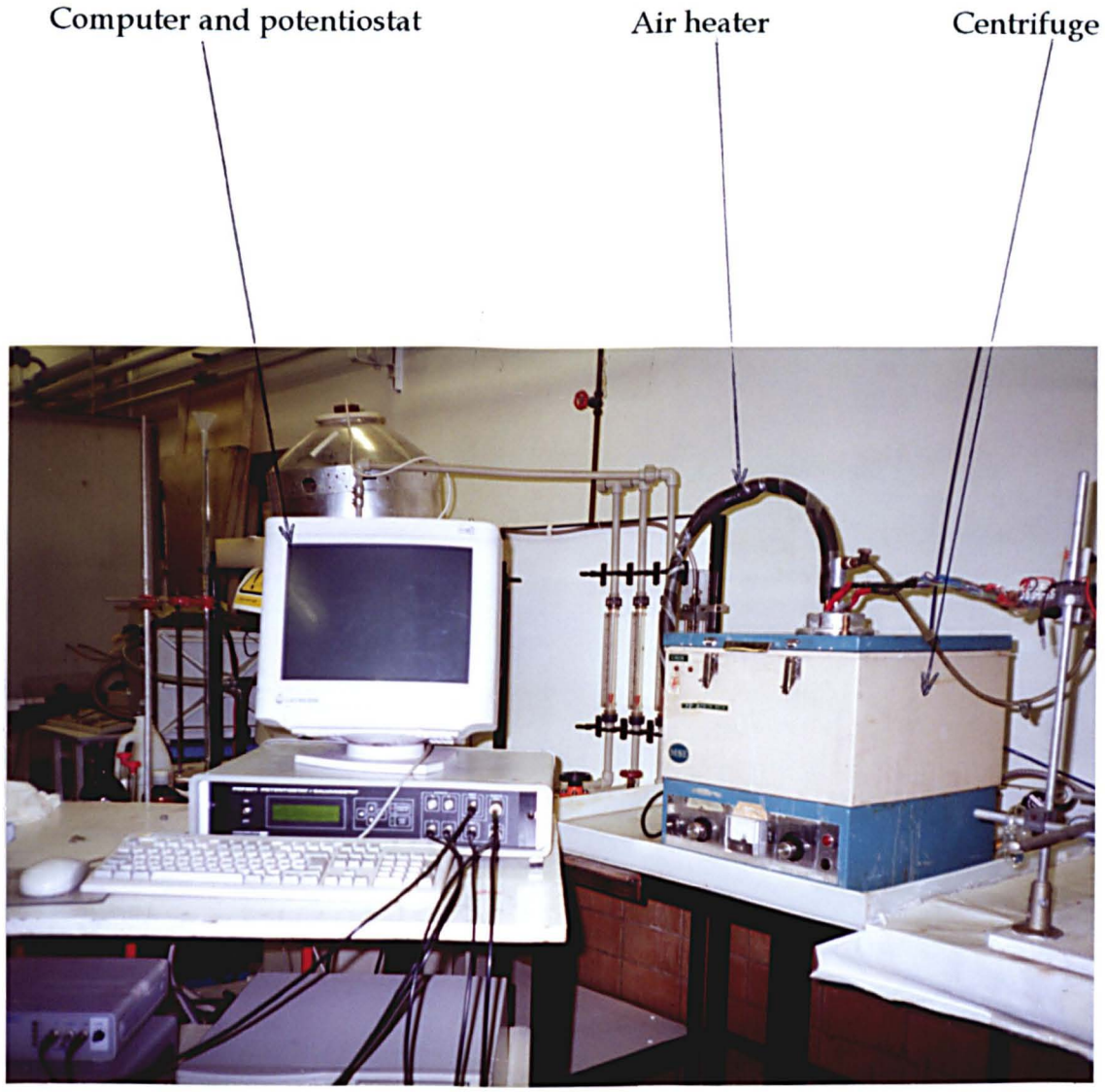

Figure 2.1 (b). Photograph of the centrifugal rig.

The electrochemical process intensification was realised in an acceleration field generated in a MSE Super Minor Centrifuge (England). To achieve constant higher temperature cell operation, the compressed air was introduced into the centrifuge using copper tubing. The tube was heated when required using 200 W barrel heaters. A thermocouple junction was attached to the air outlet tube to determine the temperature of the outlet air. The system was heated for 20 to 30 minutes before the measurements and the hot air was passed through the centrifuge pool during the experiments. The electrolytes were also preheated to the desired temperature before measurements.

The membrane cell (detailed in section 2.2) is housed within the centrifuge pool. The electrode is held between two electrically conducting meshes (usually made up of expanded Pt/Ti metal) into which channels are formed. The channels supply reactants to the respective side of the electrode. In the case when gaseous reactants were used, a subsystem outside of the electrode housing was introduced, which is responsible for delivering hydrogen, oxygen or air to the electrode surface. The gases were supplied from pressurised cylinders using a regulator and a needle valve to control the flow rate. The gases were directed into the working compartment of the cell through a 1 meter length of silicone rubber tubing. The exhaust outlet of the cell was located on the top of the cell.

The electrochemical set-up is presented in section 2.5.

2.2. Electrochemical Cells

This section describes the cells used for the studies in centrifugal fields, for routine electrochemical measurements, and for electrodeposition of catalyst.

2.2.1. The Rotary Cells

Design Considerations - The major goal of the cell design was the achievement of a large area for reaction in a compact space, especially for rotary cells. The distinctive feature of the electrolytic cell designed in this work is that both electrodes and electrolyte rotate at the same speed. There is no slip and negligible power dissipation and thus a low cost in operation. This is in marked contrast to other cells, for example, spinning disc or pump cell, in which there is a large electrolyte-electrode speed difference and a correspondingly high power loss. The design was made based on electrochemical engineering principles which integrate engineering concepts with electrochemistry theory [1-5]. The most important guidelines come from energy consumption consideration:

$$\Theta_{molar} = n\,F\,E_{cell}/\varnothing \tag{2.1}$$

$$E_c = E_A + |E_C| + V_A + V_C + V_M + V_{SA} + V_{SC} \tag{2.2}$$

where Θ_{molar} represents molar energy consumption, n is the number of electron transferred, F the Faraday constant, and $\varnothing$ is the current efficiency, E_{cell} is the cell voltage, E_A and E_C are the anodic and the cathodic electrode potential respectively and V_A, V_C, V_M, V_{SA}, and V_{SC} are the voltage drops caused by ohmic resistance on the anode, cathode, membrane, and in the anolyte, catholyte, respectively.

The following requirements should also be satisfied for good performance of the rotary cell:

(i) Low cell voltage at high current density. In principle, low cell voltage guarantees low energy consumption and high current density gives high productivity;

(ii) High catalytic activity of the working electrode to minimise the overpotential;

(iii) High mass transfer rate which will also lower the overpotential.

(iv) Low cell resistance. The design of cells with minimum resistance is a major concern in electrochemical engineering. A significant reduction in cell resistance was expected to be achieved in a high acceleration field. The internal cell resistance was also minimised in this work through "the zero interelectrode gap" design and using highly conducting electrolytes. The electrical circuit resistance was reduced by using high conducting current collector and connection wires;

(v) The cell must be constructed from low corrosion, thermally conducting and cheap material.

The Cell Sketch - According to the above principles, a rotary cell was designed and is shown schematically in figures 2.2 and 2.3.

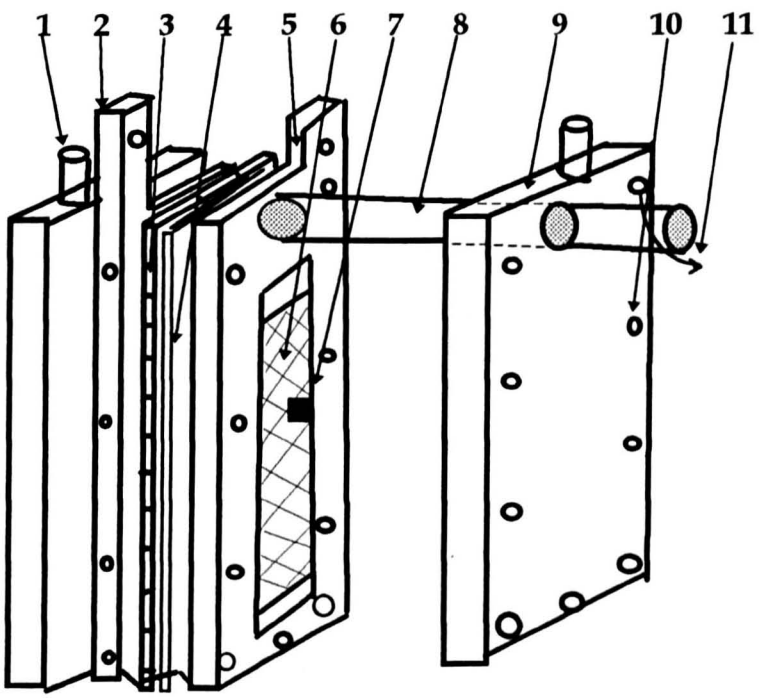

Figure 2.2. Schematic views of the components in the rotary cell.
1: Inlet and outlet; 2: Counter electrode current feeder (the counter electrode directly contacts the feeder); 3: Membrane; 4: Gasket; 5: Working electrode current feeder; 6: Working electrode; 7: Reference electrode; 8: Rotating axis; 9: Polypropylene block; 10: Belt hole; 11: Rotating direction.

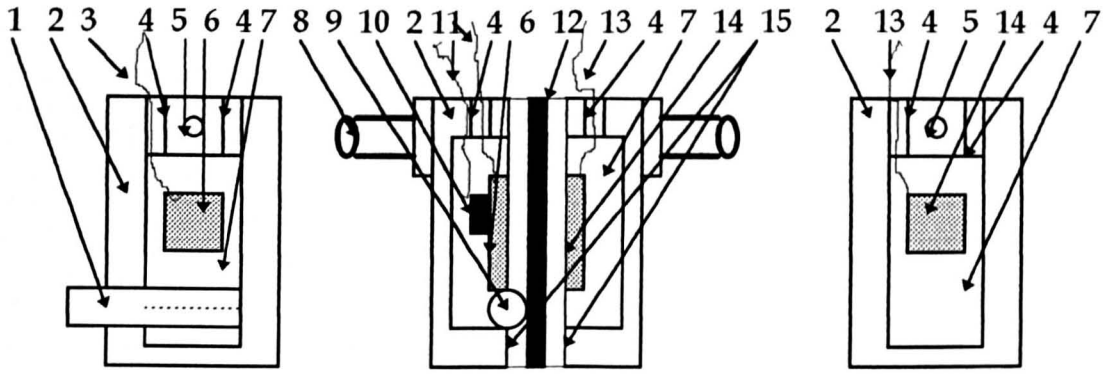

Figure 2.3 (a). Schematic views of the rotary cell.
1: Gas distributor (used for the gas consuming reactions only); 2: Polypropylene block; 3: Wire to the working electrode; 4: Inlet and outlet; 5: Hole for the cap; 6: Working electrode; 7: Electrode current feeders and electrolytes; 8: Cap; 9: Hole for the gas distributor; 10: Reference electrode; 11: Wire to the reference electrode; 12: Membrane; 13: Wire to the counter electrode; 14: Counter electrode; 15: Gaskets.

The centrifuge assembly including the position and rotating direction of the rotary cell are displayed in figures 2.4 and 2.5.

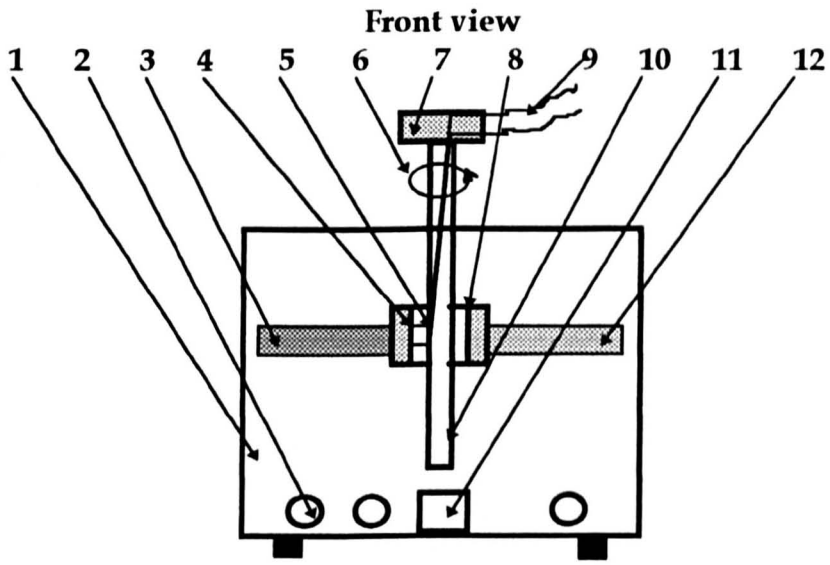

Figure 2.4 (a). The centrifuge assembly (front view).
1: Centrifuge; 2: Control key; 3: Rotary cell; 4: Cap; 5: Wires to electrodes; 6: Rotation direction; 7: Slip ring; 8: Screw; 9: To power supply; 10: Axis; 11: Revolution meter; 12: Counter part of the rotary cell.

The rotary cell, when operated at 0 rpm, was positioned in vertical direction while the cell was positioned in a horizontal plane at other rotation speeds. The cells and the position at 0 rpm were photograpged in figures 2.3 (b) and 2.4 (b).

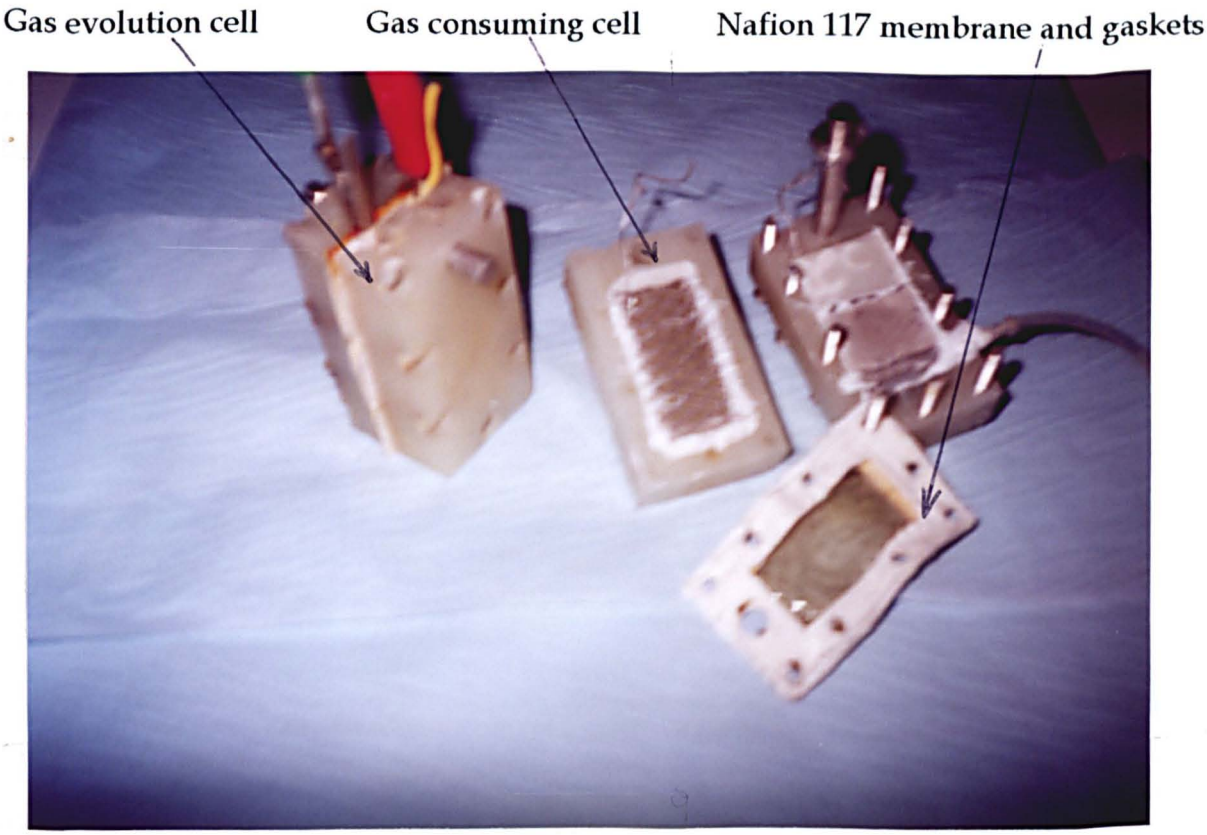

Figure 2.3 (b). Photographs of the rotary cells.

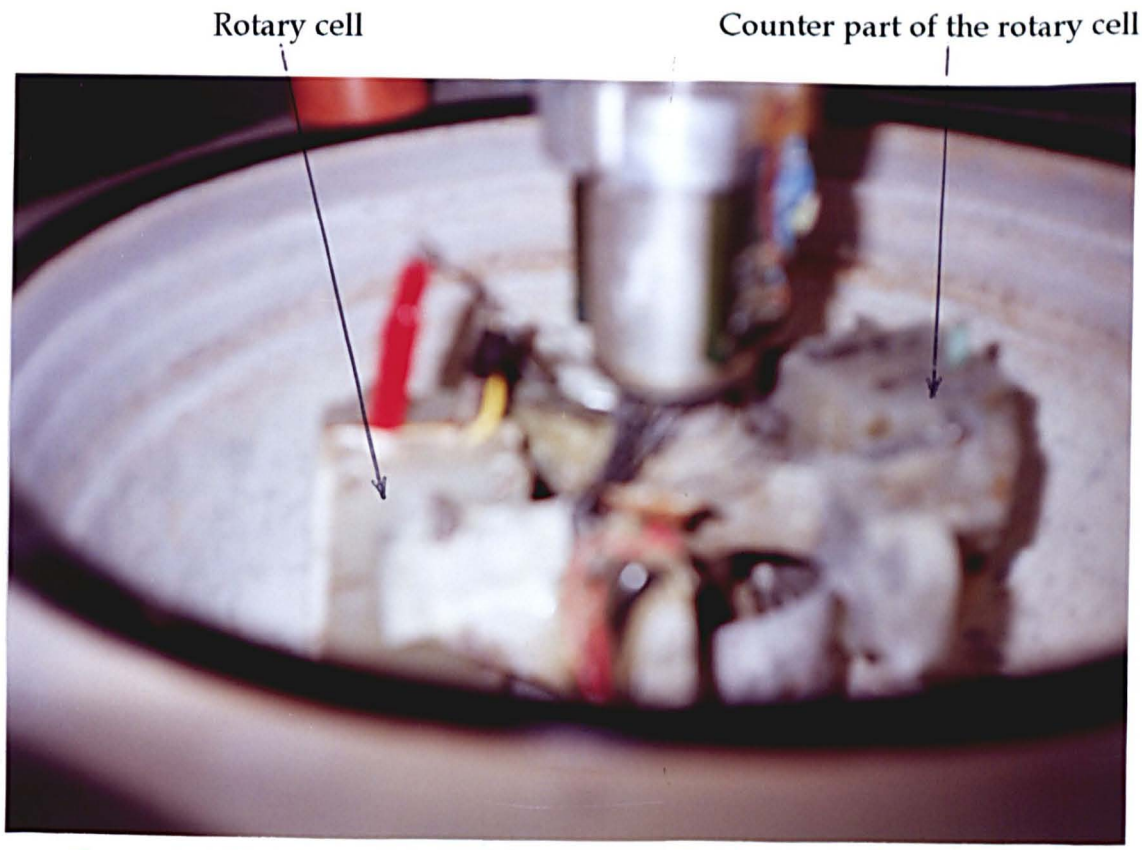

Figure 2.4 (b). The position of the rotary cell at 0 rpm in the centrifuge

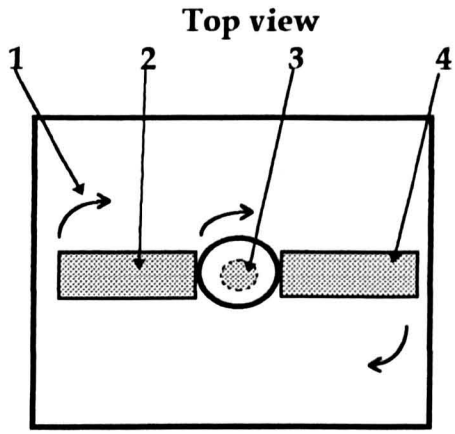

Figure 2.5. The centrifuge assembly (top view).
1: Rotation direction; 2: The rotary cell; 3: Axis; 4: Counter part of the rotary cell.

When gaseous reactants were used in the cell, a gas distributor system was constructed. This consisted of a hard plastic tube or a stainless steel tube with 24 holes as gas inlets within the rotary cell. A 20 cm long silicon tube (about 0.5 mm in diameter) was used as a gas supply, which serves to connect the inlets of the cell and the outside gas inlet on the axis. The gas was introduced from the gas cylinder to the inlet on the axis through a 2 m long silicon tube (about 4 mm in diameter).

A suitable gas distributor is important for the operation of the electrolytic cell, especially when operated in centrifugal fields where high pressure in the cell is often met. A good gas distributor will serve to achieve a high and uniform rate of mass transfer of material to or from the electrode surface. This improves the space-time yield and fractional conversion as well as minimises side reactions.

2.2.2. Polarisation Cells

Conventional three-electrode type glass cells with glass frit separator were adopted for measurements under static conditions. The cells have capacities of either 50, 100, 250, or 500 ml, for linear sweep voltammetric and steady-state measurements as well as bulk electrolysis, respectively. Working electrodes are described in the section 2.3.

Several counter electrodes were used, i.e., a platinum foil, a platinised carbon cloth, a platinised titanium (expanded metal), or a platinised titanium mesh. A commercial saturated calomel electrode was used as the reference, but all the potential values are reported on the RHE scale. For the measurements using three electrodes, a luggin probe was used to measure the electrode potential. The tip of the luggin probe was positioned within 0.5 mm of the surface of the working electrode. An agar salt bridge was used to connect the reference electrode and the luggin probe.

The details of electrochemical measurements are presented in the section 2.6.

2.2.3. Electrodeposition Cells

The electrochemical cell used during electrodeposition of Pt, Ag and Ru was similar to that used for polarisation studies and provided varying exposed electrode areas. The cell (100 ml) was fitted with a platinum foil counter electrode and a commercial saturated calomel reference electrode with a luggin probe and an agar salt bridge.

2.3. Intensified Electrodes

2.3.1. General Considerations and Materials

General Consideration: The following requirements are considered in manufacturing the intensified electrodes:

(i) Effective catalytic reactions of reactants to the desired products;

(ii) Effective dispersion of the catalyst throughout the electrode structure presenting the maximum possible catalyst surface area;

(iii) Open structure for efficient transportation of reactants and products at the catalyst surface;

(iv) Mechanical stability and flexibility.

(v) Chemical stability towards corrosive electrolytes and electrochemical redox conditions.

Materials: The following substrates were used: titanium mesh, expanded titanium metal, nickle foam, stainless steel mesh and foam, carbon cloth, carbon paper, and carbon fibre. The catalysts tested were platinum, silver, ruthenium, ruthenium dioxide. The catalysed titanium mesh is perhaps the most interesting because of its large catalytic surface area, short diffusion path of the reactants, chemical and mechanical stability, as well as its very open structure. The challenge was met in obtaining high dispersed catalyst particles while maintaining accessibility of the reactants to the electrode. The preparation of the catalysed electrodes is highlighted below.

2.3.2. Preparation Methods

This section describes the preparation of novel technical electrodes that are not commercially available but have potential application in the intensified electrochemical processes.

Chemical Methods - Of the many procedures that have been employed to prepare supported metal catalyst, the most commonly used has been impregnation of the support material with an aqueous solution of the catalyst compounds. Following a drying procedure, the support is heated under a gas-phase reductant, usually hydrogen, to give the metal. The interaction between metal salt and the support surface is of great importance. It determines the size of the metal particles obtained, as do the conditions used during adsorption of the metal salt onto the catalyst support. If the metal salt does not adsorb on the support, the salt will concentrate in the pores of the support during the drying step. The resulting catalyst will yield

metal crystallites. The number, and hence size of which, will be determined by the pore size and structure of the support [5]. Reduction of the metal salts carried out in-situ to form a colloid without the drying-in process yields smaller catalyst crystallites that are then strongly adsorbed onto the support. For carbon-type electrodes, the highest activity was attained by in-situ reduction of the metal salt with strong reducing agents such as formaldehyde. The higher activities attained by those electrodes was related to the smaller particle size which led to an increase in surface area. This is not surprising since smaller particles are likely to contain a larger proportion of low-co-ordination surface Pt atoms. These atoms have been associated with the enhanced activity of particles over that of the bulk material [5].

The Pt, Ru and RuO_2 catalysts were prepared using chemical deposition method. The Pt and Ru catalysts were prepared according to the literature method [6]. Appropriate volumes (15-25 ml) of the stock solution(s) were agitated and the pH of the solution was adjusted to 7.0 with 1 M $NaHCO_3$ before boiling for 1 hr. After this period of time, excess formaldehyde solution was added and the suspension further boiled for 1 hr until complete de-colourisation of the metal salt solutions occurred. After cooling, the suspension was filtered and the residue washed with copious quantities of boiling Millipore conductivity water until free of any chloride (detected by adding AgCl solution) and organic content.

An important step to achieve good coatings is substrate pre-treatment, which is usually carried out by chemical etching for thermally applied coatings. The etchant (10 wt/vol.% oxalic acid or 20 wt% HCl solution) preferentially attacks grain boundaries to form a micro-rough surface. This provides a reproducible and well defined surface that gives an adherent key for the coating. In practice, Ti mesh

surface was first abraded with emery paper and rinsed thoroughly with water. After drying, the Ti mesh was rinsed in acetone. Following etching with 20% HCl solution at 90°C for 1 min, a catalyst slurry was painted onto the substrates. The resulting paint was applied as a thin layer followed by thermal decomposition in air within a cubic furnace at 350~500°C for 1 hr. The process was repeated about 10 times to build up the desired coating thickness. Tight control of the furnace temperature is important to achieve the correct coating characteristics. For example, ruthenium trichloride requires a temperature in excess of 400°C to form the oxide but heating above 500°C will produce ruthenium metal leading to an electrode with inferior properties. Also the rate of substrate oxidation increases and a resistive layer of titanium dioxide is formed between the substrate and the coating at temperatures in excess of 500°C. For those electrodes obtained by gas phase reduction in a hydrogen atmosphere, a known weight of the catalyst salt solution was carefully painted onto the substrates. Samples were heated to either 300°C or 200°C for 1 hr in a steady stream of hydrogen atmosphere within a cubic furnace.

Electrochemical Methods: Electrodeposition techniques ensure that catalyst material is not deposited at electrically and ionically isolated positions within the electrode. Electrochemical deposition is a rather simple procedure for producing active catalyst material within an electrode when compared to some of the more complex chemical deposition techniques. Of course, deposition from chloride-containing metal salt requires scrupulous cleaning of the electrode following the deposition process. Moreover, extension of the electrochemical deposition technique to bimetallic catalysts was very difficult. Codepositon of bimetal materials is complex. Hence, it is difficult to control the composition of the deposit [6].

The important experimental factors that must be considered include: method of deposition, potentiostatic vs. galvanostatic; composition of the plating solution; temperature; pH of the plating solution; and the cathode efficiency.

In operation, the substrates were degreased in acetone and washed in Millipore conductivity water for nearly 15 min prior to mounting into the electrodeposition cell. The cell was then filled with N_2-saturated chloroplatinic acid or ruthenium chloride solution of known concentration and stirred mechanically. The catalyst was electrodeposited onto the substrate under potentiostatic control. The amount of charge required to deposit the catalyst was monitored through a computer-controlled potentiostat (Model 273 EG&G Princeton). During the deposition, the charge passed for the first 15 sec was not counted as it mainly consumed for charging the double-layer on the substrate and reducing adventitious oxygen. Following deposition, electrodes were extensively washed with boiling Millipore conductivity water until free from any chloride content. Electrochemical deposition was carried out with a number of electrodes to check reproducibility.

Some difficulties were founded initially in the co-electrodeposition of Pt-Ru bimetallic deposits. Since only Pt features were seen for the electrodeposited material, it is reasonable to assume that only a very small amount of Ru has been codeposited. This is not surprising since Pt is more noble than Ru, and hence, is more easily deposited. Therefore, a new deposition strategy was designed, i.e., depositing Ru followed by depositing Pt. Both carbon cloth-type and Ti mesh-type electrodes were prepared using this method. At first, the depositing potentials were chosen according to the linear voltammograms (e.g. figure 2.6):

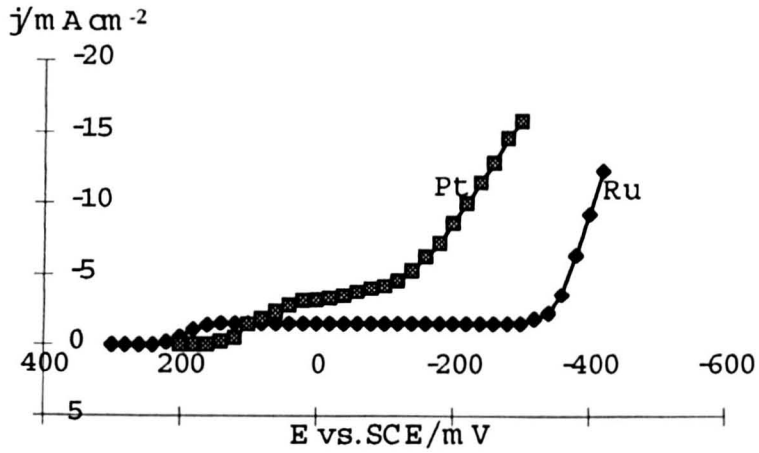

Figure 2.6. Linear voltammograms for evaluating the deposition potentials of platinum and ruthinium co-electrodeposition on titanium mesh.
Cathode: Ti mesh for Pt deposition and Pt/Ti mesh for Ru deposition; Catholyte: 0.02 M H_2PtCl_6 or $RuCl_3$ in 0.1 M HCl solution; Anode: Pt foil; Anolyte: 0.05 M H_2SO_4 solution; Scan rate: 5 mV/s; ambient temperature.

The linear voltammograms gives a clear indication of the suitable deposition potentials. For the platinum solution, a current plateau appears between 0.02 and -0.1 V vs SCE. The corresponding current densities vary from -3.1 to -4.6 $mAcm^{-2}$. At more negative potentials there was an evolution of molecular hydrogen. The behaviour in the ruthenium solution is different from that in the platinum solution, i.e., a well formed limiting current plateau (-1.54 mA cm^{-2}) was observed between 0.14 and -0.3 V vs SCE. Also, the hydrogen liberates at more negative potentials. The electrodeposition of the Ti mesh electrodes was therefore carried out under potentiostatic control at -0.05 V vs. SCE. Following the electrodeposition, electrodes were extensivly washed with boiling Millipore water until free from any chloride content.

The platinum deposits obtained by the above procedure were bright and the ruthenium deposit tended to be dark gray in colour. The deposits appeared uniform to the eye and appeared to adhere quite strongly to the Ti mesh, requiring forceful

scratching to remove them. More details were assessed by scanning electron microscopy described later. Electrodeposition was carried out with several electrodes to check reproducibility.

The electrochemical method gives better electrodes than the chemical method.

2.3.3. Characterising Methods

Scanning Electron Microscopy - Scanning electron microscopy (SEM) is often used to provide detailed knowledge of the physical nature and chemical composition of the solid surfaces on a submicrometer scale. It is especially useful to study surface topography and bulk microstructure [7, 8]. In such experiments, the surface of a solid sample is swept in a raster pattern with a finely focused beam of electron until a desired area of the surface has been scanned. Several types of signals, e.g. backscattered, secondary electrons, are produced from a surface when it is scanned with an energetic beam of electrons. In such a way, a map of the sample was produced, in which there is a one-to-one correlation between the signal produced at a particular location on the sample surface and a corresponding point on the cathode-ray tube display. Scanning electron microscopy (SEM) was performed using a Hitachi S-2400 scanning electron microscope at an acceleration voltage of 25 kV. The samples of the platinised carbon cloth and titanium mesh electrodes were prepared by cutting a piece of the platinised carbon cloth and titanium mesh electrodes and sticking them onto the specially made disks. Figure 2.7 gives the scanning electron micrographs of the Ti mesh and the catalysed Ti mesh prepared by the steady-potential method, with a loading of 1 mg Pt+0.5 mg Ru/cm^2.

(a)

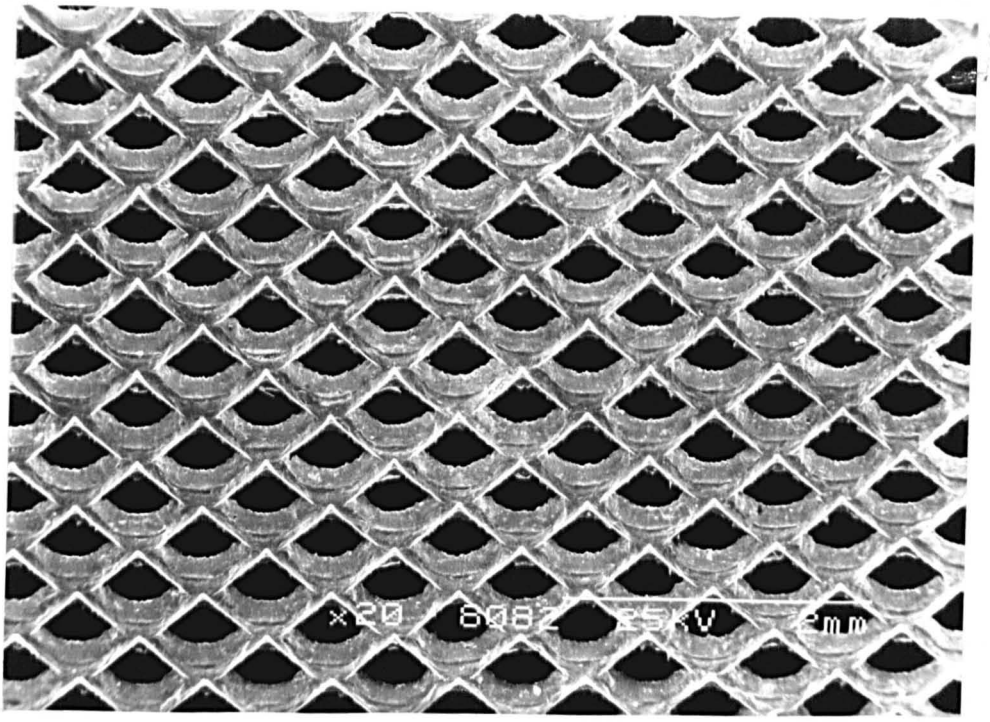

(b)

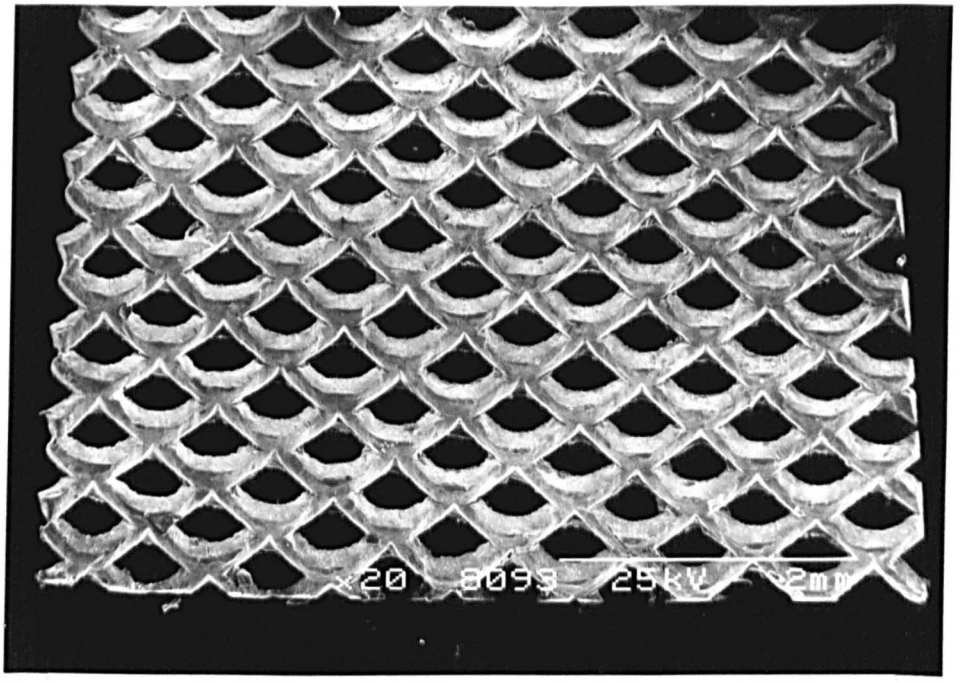

(c)

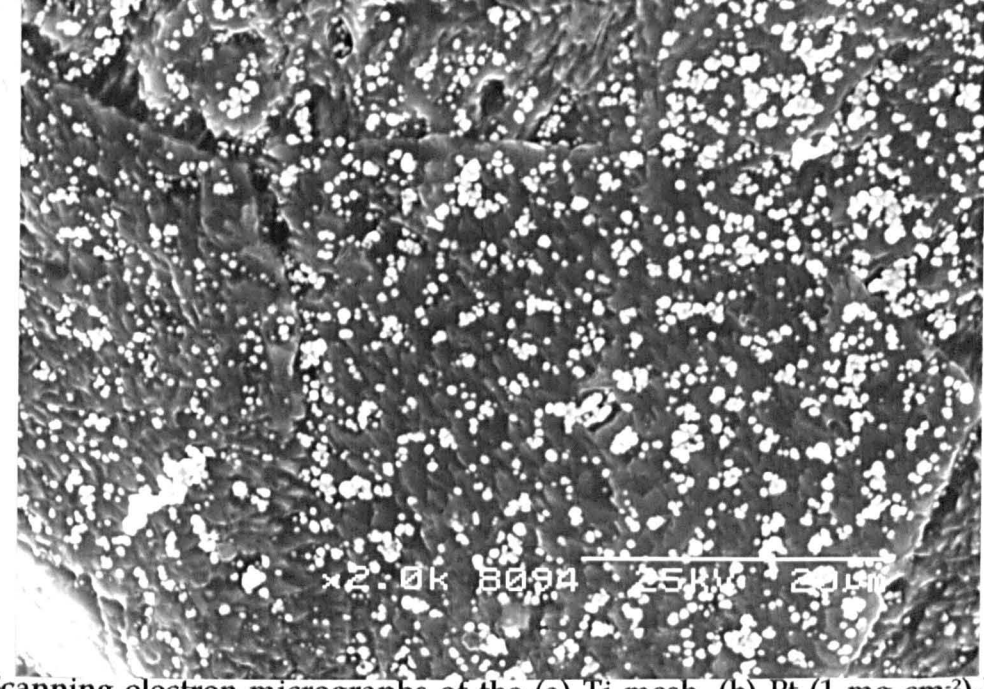

Figure 2.7. Scanning electron micrographs of the (a) Ti mesh, (b) Pt (1 mg cm^{-2})-Ru (0.5 mg cm^{-2})/Ti mesh, (c) Enlarged Pt-Ru/Ti mesh.

The SEM micrographs of the mesh show that the titanium mesh surface appears smoother after the deposition (figure 2.7, b). The Pt and Ru particles are distributed homogeneously across the matrix (figure 2.7, c). The electrode obtained using electrodeposition method shows significant phase segregation as illustrated in figure 2.7 (c). Discrete regions of substrate (dark) and Pt-Ru particles (white) are observed. The majority of the catalyst particles range from 250 to 500 nm in diameter and there are some bigger clusters (about 1.5 µm in diameter). These deposits are similar in size with those previously reported using the electrodeposition methods [10-12]. It is worthwhile to note that the catalysed titanium mesh after use in the methanol oxidation gave nearly the same SEM micrographs, i.e., there is no observable change resulting from use.

The electrode obtained using chemical deposition method show quite different characteristics to those obtained by electrodeposition, as shown in figure 2.8.

(a)

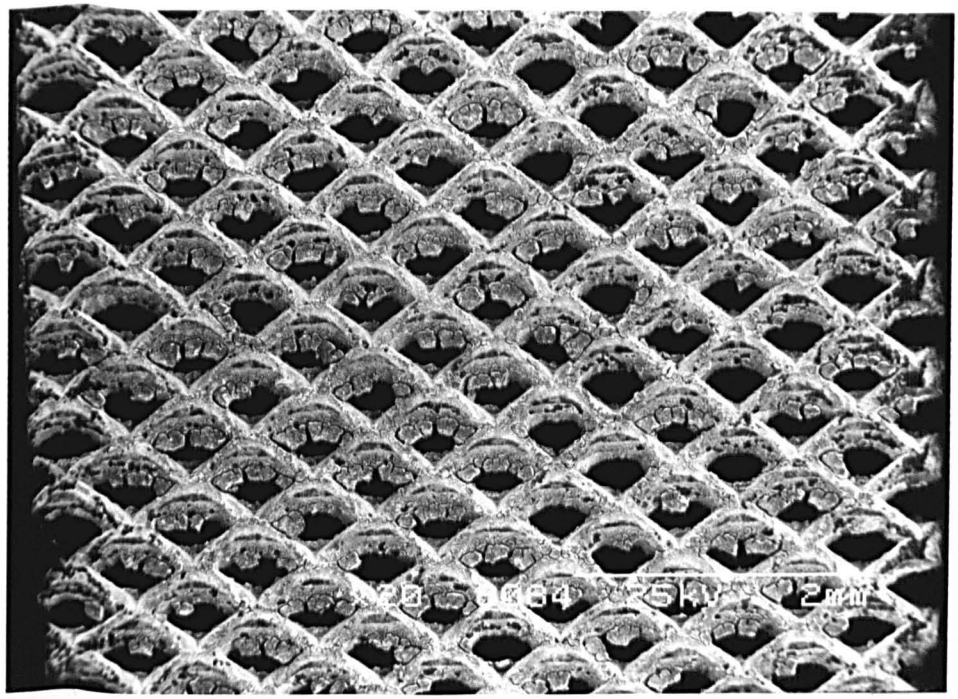

(b)

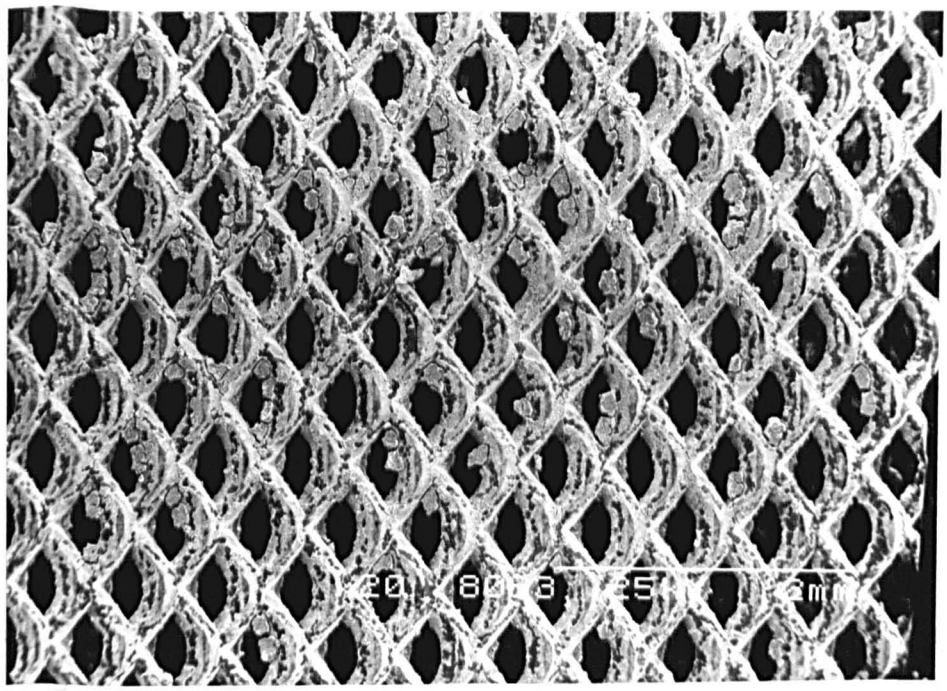

Figure 2.8. Scanning electron micrographs of the chemically prepared Pt (2 mg cm^{-2})-Ru (1 mg cm^{-2})/Ti mesh (a) before and (b) after using in methanol oxidation.

The SEM pictures show that the platinum and ruthenium particles are highly aggregated to form large clusters (75 to 200 μm diameter) which partly block the mesh holes(figure 2.8, a). After using in the methanol oxidation, the catalyst particles become detachal from the substrate matrix (figure 2.8, b).

Figure 2.9 displays scanning electron micrographs of the platinised carbon cloth.

(a)

(b)

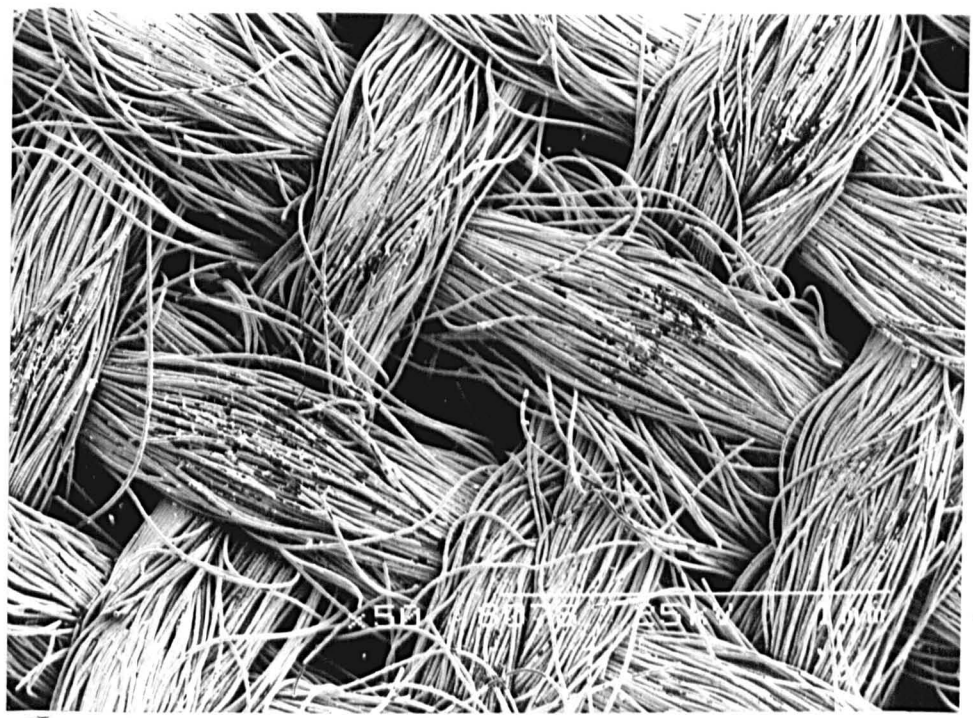

Figure 2.9. Scanning electron micrographs of the (a) carbon cloth, (b) Pt (2 mg cm^{-2})-Ru (1 mg cm^{-2})/carbon cloth before use.
When a carbon substrate was used, poorer adherence between the catalyst particles and carbon was observed, which are shown Chapter 6.

Electrochemical Characterising Technique - Most catalysed electrodes were characterised by electrochemical measurements which are presented in the related sections.

2.3.4. Electrode Pre-Treatment

The electrodes were treated before each experiment according to different procedures. For electrochemical pre-treatment of a Pt or Pt-based electrode used in collecting kinetic data, insert it, together with a saturated calomel reference electrode and a Pt counter electrode in 0.5 M sulphuric acid. Set the potential to 1.8 V vs. RHE for 30 seconds to oxidise impurities. Change to 1.2 V for 30 seconds to remove oxygen formed at the higher potential. Switch to 0.05 V for 30 seconds to reduce surface oxides formed in the previous steps. Repeat this procedure at least three times [6, 17, L. D. Burke and D. T. Buckley, J. Electroanal. Chem., 366, 239, 1994.]. The pretreatment method for the electrodes used was not found to be critical, but most electrodes were pretreated before experiments using chemical cleaning procedures, i.e., immese them in 2 M H_2SO_4 solution or 2 M NaOH solution for 5 minutes followed by rinsing with tap water and finally ultrapure water thoroughly.

2.4. Fabrication and Operation of Direct Methanol Fuel Cells

2.4.1. Catalyst and Electrode Preparation

Catalysts for both electrodes were prepared according to the procedure outlined elsewhere [12]. Pt-Ru catalysts used were: Electrochem. Inc (USA); Pt 20wt%, Ru10wt% on Vulcan XC-72R carbon or Johnson Matthey (UK); 35wt% Pt, 15wt% Ru or catalyst 40wt% Pt, 20wt% Ru on ketjen black carbon [13].

Each of the electrodes consists of a backing layer, a gas diffusion layer, and a reaction layer. A teflonised carbon cloth (E-TEK, type A) of 0.35 mm thickness was

employed as the backing layer in both electrodes. To prepare the gas diffusion layer, the required quantity of isopropanol was added to a pre-teflonised Ketjen Black carbon to make the paste required. The resulting paste was spread onto the carbon cloth and dried in an air oven at 85°C for five minutes. To prepare the reaction layer, the required quantity of Pt-Ru/C (anode) or Pt/C (cathode) was mixed with 10 wt% teflonised carbon. The required quantity of Nafion solution was added to the mixture with continuous stirring. The resulting paste was spread onto the gas diffusion layer of the electrode and dried in an air oven at 85°C for five minutes. The catalyst content on the anode was maintained at a level of 2 mg Pt cm^{-2} while that on the cathode was 1 mg Pt cm^{-2}. Finally, a thin layer of Nafion solution was spread onto the surface of each electrode.

2.4.2. Membrane Electrode Assembly

The membrane electrode assembly is housed within the mechanical framwork of the cell. The electrode is held between two electrically conducting field meshes (usually made of expanded Pt/Ti metal) into which channels are formed. The ridges between the channels are responsible for the electrical contact with the backs of the electrode and conduct the current to an external load. The channels between the ridges supply fuel and oxidant to the respective side of the electrode. The subsystems outside of the electrode housing are: An oxidant system, which is responsible for delivering oxygen or air to the electrode surface; a fuel injection system for fuel delivery to the electrode surface. The sandwiched membrane electrode assembly (MEA) was obtained by hot pressing the anode and cathode on either side of the pre-treated Nafion 117 membrane at 100 $kgcm^{-2}$ and 125°C for 3 minutes. The membrane pre-treatment involved boiling the membrane for 1 hr in 5 vol% H_2O_2 and 1 hr in 1 M

sulphuric acid before washing in boiling Millipore water (> 18 mΩ) for 2 hrs with regular changes of water. The thickness of the MEA is approximately 0.8 mm depending on the diffusion layer thickness. The resulting MEA was installed in the cell after pressing, and hydrated with water circulated over the anode at 75°C for 48 hrs. After allowing 48 hrs to condition a new MEA in the test fuel cell at 75°C and atmospheric pressure with continuous feed of 2 M methanol, the galvanostatic polarisation data were obtained at various operating conditions. Several MEAs were tested to ascertain reproducibility of the data. The extent of the conditioning period is of significance in the performance of the cells.

2.4.3. Fuel Cell Assembly

A liquid feed DMFC was assembled employing the MEA sandwiched between two graphite blocks with parallel channel flow paths cut out for methanol and oxygen/air flow. The cell was held together between two aluminium backing plates using a set of retaining bolts positioned around the periphery of the cell. Both electrodes were contacted on their rear with gas/liquid flow field plates machined from impregnated high density graphite blocks in which channels were formed. The ribs between the channels make the electrical contact to the back of the electrodes and conduct the current to the external circuit. Electrical heaters supplied by Watson Marlow were placed behind each of the graphite blocks in order to heat the cell to the desired operational temperature. The graphite blocks were also provided with electrical contacts and small holes to accommodate thermocouples. The fuel cells were used in a simple flow rig which consisted of a Watson Marlow perilstatic pump to supply aqueous methanol solution, from a reservoir, to a Eurotherm temperature

contoller to heat the methanol. Oxygen and air were supplied from the cylinders at ambient temperature,

and the pressure regulated at inlet by pressure regulating valves. All connections between the cells and equipment were with PTFE tubing, fittings and valves.

2.4.4. Rotary DMFC

The rotary fuel cells have been constructed by putting the fuel cell assembly into the rotary cell blocks described in previous section.

2.4.5. Measurement Set-Up

The measurement set-up was sketched in figure 2.9.

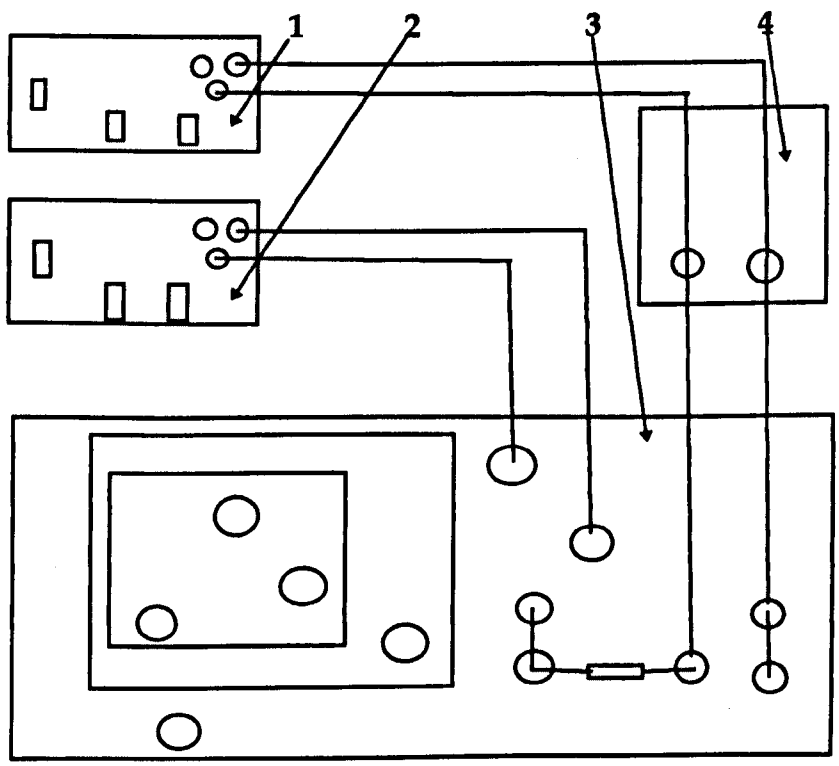

Figure 2.9. The Fuel Cell Measurement rig. 1: Electrometer for current measurement; 2: Electrometer for cell voltage measurement; 3. Ministat precision potentiostat; 4: Fuel cell.

2.5. Reference Electrodes

Saturated Calomel Electrode: For those measurements using stationary electrochemical cells, a commercial saturated calomel electrode was used and

potentials are also reported relative to the reversible hydrogen electrode. A double-junction SCE reference electrode, immersed in saturated KCl, was connected to the cell through a luggin capillary salt bridge that was filled with the same electrolyte solution used in the working chamber of the cell as the supporting electrolyte.

Special care was taken in positioning the reference electrodes or the luggin capillary with respect to the working electrode. This is due to a substantial iR drop may distort the shape of the polarisation curves, particularly in the vicinity of the peak or high current density range.

Nafion Membrane Electrode: The electrochemical measurements in the rotary cells with routine reference electrode were tried and failed. It was clear that commercial SCE reference electrodes could not use in the rotary cells due to the easy damage by powerful centrifugal force generated in the centrifuge. An alternative reference electrode, a Nafion membrane reference electrode, was designed and used for the measurements in centrifugal fields in this work.

In practice, the Nafion membrane reference electrode utilizes a small thin piece of Nafion 117 membrane having a surface area about 0.5 cm^2. A stainless steel wire was sealed to the membrane and acted as the internal conducting lead. The evaluation of such a reference electrode is necessary because this type of electrode has rarely been used in electrochemical measurements and no rerefence about its use in rotary cell was found, although other types of membrane reference electrodes have been preliminarily evaluated [14, 15].

The thorough assessments of the Nafion 117 membrane electrodes were carried out by comparing the electrochemical response towards the investigated processes using this reference with that of a commercial SCE reference. This was first checked in the

stationary cell both in the blank solution as well as in the electrolyte with electrochemical active species. The interference of acidic, neutral, and alkaline solution was investigated up to a concentration corresponding to the value used in experiments; there is no notable interference within experimentally permitted error during a moderate operation period. The response to the variation in temperature of the medium was also studied. The results were also satisfactorily, compared to those referred to the commercial SCE reference. However, the deviation of the electrochemical measurements using the Nafion 117 membrane reference electrodes from those referred to the SCE was observed for long term tests. Most of the Nafion membrane electrodes used in this work are not good for long term operation. For example, the stabiblity of the Nafion membrane reference electrodes towards hydrogen and oxygen evolution reactions was studied for a period of about 72 hours in the sulphuric acid, sodium sulphate, or potassium hydroxide solution, respectively. During the first 24 hours, there was no notable fluctuation in the linear sweep voltammetric responses for the processes, compared to the results obtained using the commercial SCE reference. However, the deviation became larger later and developed to an unacceptable extent at last. The deviation become severe in centrifugal fields for long term usage, although the results suggest that such a reference electrode could be reliable for a moderate operation period even at high rotating speeds. The problem arose from eventual mechanical damage of the sealing stainless steel conducting wire of the electrode, which was exposed partly or completely to the electrolytes.

The direct measurement of electrochemical parameters in centrifugal fields was achieved by placing this type of reference electrode near the working electrode. To

get reliable and reproducible data, the new reference electrode was used for every experiment and the reference electrodes were regularly calibrated against a commercial saturated calomel reference electrode. All anode potentials are corrected, and quoted against the Reversible Hydrogen Electrode (RHE) by adding about 5 mV to the potential values measured against the Nafion membrane reference. All measurements were repeated with fresh solution at least twice under the same conditions to ensure reproducibility.

Potential drift is a common source of inaccuracy during direct potentiometric measurements with membrane electrodes. Inherent defects or "poisoning" of the membrane by other constituents of the solution and temperature heterogeneity within the electrode body are the main causes of potential drift. Miniaturisation of the membrane reference electrodes was recommonded as an effective way to improve their thermal hysteresis characteristics, i.e., reach a target of a small temperature coefficient [7]. In our case, the membrane reference electrodes were minimised and very simple structure was adopted, the accuracy for a moderate measuring period satisfactorily agreed with that obtained using the commercial SCE reference, regardless of changes in the rotating speed, concentration, and temperature. It is possible to improve the long term stability of Nafion membrane reference electrode. However, this is beyond the range of this work.

2.6. Electrochemical Measurement Techniques

This section describes the basic electrochemical technique used in this work. More complete descriptions about practical operations and theoretical treatments may be found elsewhere [16, 17]. In the electrochemical measurements, current densities refer to a superficial area, i.e., a geometric surface of the electrode projected onto the

membrane. To get meaningful and consistent data, a standard testing procedure was adopted as described in the following sections. All data are reproducible and are the average of at least two, and usually three or more, trials.

2.6.1. Linear Sweep Voltammetric Technique

The linear sweep voltammetric technique has been employed in most of the work described in this thesis for the evaluation of electrodes and the effects of centrifugal fields. The technique involved sweeping the electrode potential or cell voltage continuously between two pre-set limits (initial potential and final potential) at a known scan rate. The current response was measured as a function of potential or cell voltage; scan rates can vary from less than 1 mV/s to several hundred V/s depending on the experimental need. A scan rate of 5 mV/s was chosen throughout this work, as the results obtained using 1 mV/s show the same features as those at 5 mV/s.

The currents are reported in accord with IUPAC convention (anodic current is positive and cathodic current is negative). For the reactions investigated in this thesis, examinations of the curves obtained in the blank solutions are used to reveal any competing currents in the potential range of interest. Generally, the background currents were insignificant and were therefore neglected.

2.6.2. Steady-State Polarisation Measurements

Steady-state polarisation measurements were carried out in a conventional three-electrode cell or the rotary cell with the Nafion membrane reference for the data comparison between the static cell and the rotary cell. Two methods were used, i.e., galvanostatic polarisation technique and potentiostatic polarisation technique.

Galvanostatic Polarisation Measurements - Galvanostatic polarisation measurements were performed. The technique can avoid gas bubble inteference and is more suited to higher currents where large quantities of gas are evolved.

A current was applied to the working electrode or the cell assembly and the potential monitored until it remained constant for a specified time (5 to 10 minutes) and monitors the resulting potentials. For half-cells, the electrode polarisation was measured at current densities of 0, 5, 20, 40, 60, 80, 100, 120, or 150 $mAcm^{-2}$ for most temperatures and reactant concentrations. The current density was automatically controlled by a computer.

Potentiostatic Polarisation Measurements - Potentiostatic polarisation technique was also used for steady state polarisation curves. For half-cells, constant anode potentials applied to the electrodes, and the current density of the electrode recorded as a function of time. This was also automatically controlled by a computer. In these measurements, the current-time transient typically showed an initial sharp rise associated with double-layer charging and then the current decayed with time in a hyperbolic fashion as a result of depletion of the reactant near the electrode surface.

Tafel Constant Measurements - The Tafel plots were constructed in order to determine if the kinetic parameters of Tafel slope b and exchange current density j_0 for the investigated reactions, i.e., the oxygen reduction and evolution, hydrogen oxidation and evolution, chlorine evolution and methanol oxidation, are affected by the experimental conditions. First, the experiments were done galvanostatically or potentiostatically with a conventional three-electrode glass cell. and the curves converted into the corresponding Tafel plots. This has been done by plotting average

overpotentials versus logarithmic current density. Tafel parameters were obtained from these plots according to the Tafel equations:

$$\text{Cahtodic: } E_C - E_{C,e} = a_C + b_C \log |j_C| \tag{2.3}$$

$$\text{Anodic: } E_A - E_{A,e} = a_A + b_A \log j_A \tag{2.4}$$

where Tafel constants are

$$\text{Anodic: } a_A = -(2.3\ R\ T/\alpha_A\ n\ F) \log j_{A,0} \qquad b_A = 2.3\ R\ T/\alpha_A\ n\ F \tag{2.5}$$

$$\text{Cathodic: } a_C = (2.3\ R\ T/\alpha_C\ n\ F) \log |j_{C,0}| \qquad b_C = -2.3\ R\ T/\alpha_A\ n\ F \tag{2.6}$$

and n is the number of electron transferred, F the Faraday constant, and ø is the current efficiency, E_A and E_C are electrode potentials for the anodic and the cathodic reactions respectively, $E_{C,e}$ and $E_{A,e}$ are equilibrium potentials for the anodic and the cathodic reactions respectively, j_A and $|j_C|$ are the anodic and the modula of the cathodic current density respectively, $j_{A,0}$ and $j_{C,0}$ are exchange current densities for the anodic and the cathodic reactions respectively, α_A and α_C are the transfer coefficients for the anodic and the cathodic reactions respectively. The equilibrium potentials were replaced by the rest potentials observed after polarisation measuring. This method was claimed as the most reasonable potential at which to determine the intercepts of Tafel plots [3, 17].

The Tafel data are reported in the related chapters.

2.6.3. Controlled Potential Coulometry

Controlled potential coulometric experiments were carried out to determine the electrolysis products in methanol oxidation. In the experiments, the potentiastat steps the potentials from the open circuit potential to a programmed potential while stirring the sample solution and monitors the current that follows. The technique was used to determine the total charge passed in the experiments. The methanol

samples were added after pre-electrolysis of the blank solution. The background current was subtracted from all subsequent current measurements.

2.6.4. Mass Transfer Measurements

As usual, the mass transfer coefficients in the rotary cell were determined using the diffusion limiting current technique [2-4, 18-20]. The reduction of ferricyanide at a platinised titanium cathode was chosen as a model reaction

$$Fe(CN)_6^{3-} + e^- = Fe(CN)_6^{4-} \qquad (2.7)$$

Current density versus cell voltage curves were recorded at each rotation speed. The application of the ferricyanide reduction with cell voltage values, rather than electrode potential measurements, is considered as a very useful method for the determination of mass transfer rates in electrochemistry which avoid the experimental difficulties associated with the incorporation of a reference electrode [21]. The limiting current densities, j_{lim}, were obtained from the limiting current plateau and used to calculate the mass transfer coefficients, k_L, according to

$$k_L = j_{lim}/(n\,F\,C_b) \qquad (2.8)$$

where n is the number of electrons involved in the reduction, F the Faraday constant and equals 96485 C/mol, and C_b the bulk concentration of ferricyanide (mol m^{-3}).

The limiting current is obtained from steady state polarisation curve which showed a clear limiting current plateau. The cell was charged with 50 ml fresh catholyte and 30 ml fresh anolyte for each run. High ratio of ferrocyanide to ferricyanide (0.05 M:0.01 M) was used to ensure that the cathode reaction is under electron transfer control and the reduction of ferricyanide to ferrocyanide will occur efficiently. The use of KOH solution ensured that the contribution of migration to mass transfer was

negligible. The catholyte was purged with nitrogen for 20 min before measurements were taken to avoid the effect of oxygen reduction.

The mass transfer data are reported in Chapter 7.

2.7. Gas Chromatography

Gas chromatography is a technique for separating mixtures of relatively volatile compounds into their components. The sample is injected into the carrier gas. The vapour is then carried through a column which is usually prepared by deactivating the sillica surfaces prior to coating with the stationary phase, such as dimethylsiloxane and polyethylene glycol. This stationary phase was immobilised by surface bonding and/or cross-linking. As each component reaches the end of the column it is detected and the detector issues an electrical signal to the recorder. The gas-liquid and gas-gas GC were used.

All the gas samples produced by the electrolysis were analysed using GC - 8A Gas Chromatography controlled by C - R6A Chromatopac computer Apparatus (Shimadzu Corporation, Kyoto, Japan). The amounts of CO_2 and O_2 evolved from the anodes were determined using standard calibration curves for CO_2 and O_2, respectively. The peak area values in the gas chromatographic reports were used for these determination.

2.8. Membrane

General Considerations - Use of a membrane causes IR loss in a cell and increases the cost and complexity of cell construction. But this is essential for the rotary cell for two reasons: (i) to prevent physical contact between the anode and cathode as the electrodes are closely spaced; this also serves to separate gases in the cathodic and

anodic chambers; (ii) to guarantee good contact between reactant and the working electrode surface so as to make full utilisation of reactant.

Membrane Pretreatment - Prior to use, membranes were cleaned by the following procedure [22, 23]. First, membranes were heated at 80°C in 5% H_2O_2 solution for 1 hr to remove any residual organic species present. The membranes were thoroughly washed with Millipore conductivity water and boiled in 1 M aqueous sulphuric acid for 2 hrs. Following washing, the electrodes were then boiled in Millipore conductivity water for a further 2 hrs. Membranes were stored in a glass container and were boiled for 1 hr in Millipore conductivity water prior to use.

2.9. Reagents and Electrolytes

Reagents - The chemical reagents and materials with their respective suppliers are: Nafion 117 membrane (Aldrich); Carbon paper (PC 206) (Stackpole); Carbon cloth(GC-14) (E-Tek Inc.); Carbon fibre felt; Hydrogen hexachloroplatinate (H_2PtCl_6, Janssen); Ruthenium(III) chloride ($RuCl_3$, Aldrich); Sodium carbonate (Na_2CO_3, BDH AnalaR); Sodium hydroxide (NaOH, BDH AnalaR); Hydrochloric acid (HCl, BDH AnalaR); Sulphuric acid (H_2SO_4, BDH AnalaR); Methanol (CH_3OH, Fisons HPLC-grade). Millipore water, obtained from a Milli-U 10 water purification system, was used during all electrochemical experiments.

Electrolyte Pretreatment - Bubble the electrolytes with purified nitrogen for 10 minutes and continue passing nitrogen over the solutions during the experiments for routine electrochemical measurements.

2.10. References for Chapter 2

[1] K. Scott, "Electrochemical Reaction Engineering", Academic Press, London, 1991.

[2]. F. Goodridge and K. Scott, "Electrochemical Process Engineering. A Guide", Plenum Press, New York, 1995.

[3]. D. J. Pickett, "Electrochemical Reactor Design", 2nd Edition, Elsevier, Amsterdam, 1979.

[4]. F. C. Walsh, "A First Course in Electrochemical Engineering", The Electrochemical Consultancy, Hants, 1993.

[5]. J. B. Goodenough, A. Hamnett, B. J. Kennedy, R. Manoharan and S. A. Weeks, Electrochim. Acta, 35, 199, 1990.

[6]. M. P. Hogarth, PhD Thesis, Newcastle University, Newcastle upon Tyne, 1995.

[7] J. A. Dean, "Analytic Chemistry Handbook", McGraw-Hill, Inc., New York, 1995.

[8] D. A. Skoog and J. J. Leary, "Principles of Instrumental Analysis", Fourth Edition, Saunders College Publishing, Chapter 16, New York, 1992.

[9]] K. Shimazu, H. Kita and U. Nodasaka, J. Electroanal. Chem., 256, 481, 1988.

[10] J.-H. Ye and P. S. Fedkiw, Electrochim. Acta, 41, 221, 1996.

[11] W. J. Basirun and D. Pletcher, J. Appl. Electrochem., 28, 167, 1998.

[12] M. K. Ravikumar and A. K. Shukla, J. Electrochem. Soc., 143, 2601, 1996.

[13] J. M. Leger and C. Lamy, Ber. Busenges. Phys. Chem., 94, 1021, 1990.

[14] C. E. Efstathiou, J. G. Pentari, and T. P. Hadjiioannou, Anal. Chem., 58, 233, 1986.

[15] H. H. Lee, B. C. Lee, D. H. Cho, S. S. Jeung, and P. M. Yong, Bull. Electrochem., 11, 597, 1995.

[16]. A. J. Bard and L. R. Faulkner, "Electrochemical Methods: Fundamentals and Applications", John Wiley & Sons, New York, 1980.

[17]. The Southampton Electrochemistry Group, "Instrumental Methods in Electrochemistry", T. J. Kemp (Editor), Ellis Horwood Limited, New York, 1985.

[18] J. R. Selman and W. Tobias, Adv. Chem. Eng., 10, 211, 1978.

[19] U. Landau, in "Tutorial Lectures in Electrochemical Engineering and Technology", (Edited by R. C. Alkire and T. Beck), AIChE Symp. Ser. No. 204, 77, 75, 1981.

[20] J. R. Selman, in "Tutorial Lectures in Electrochemical Engineering and Technology", (Edited by R. C. Alkire and T. Beck), AIChE Symp. Ser. No. 204, 77, 88, 1981.

[21] T. R. Ralph, M. L. Hitchman, J. P. Millington and F. C. Walsh, Electrochim. Acta, 41, 591, 1996.

[22] V. A. Paganin, E. A. Ticianelli and E. R. Gonzalez, J. Appl. Electrochem., 26, 297, 1996.

[23] Y. W. Rho, O. A. Velev, S.Srinivasan and Y. T. Kho, J. Electrochem. Soc., 141, 2084, 1994.

Chapter 3. Gas Consuming Reactions

3.1. Introduction

Two industrially important electrochemical gas consuming reactions, i.e., oxygen reduction and hydrogen oxidation are investigated in this chapter.

Oxygen reduction and hydrogen oxidation have generated much interest and a significant amount of research due to their importance both for the basic electrochemical theory development and for the technical applications [1-5]. Their potential technical applications particularly attract us to explore the possibility of intensifying both processes in centrifugal fields.

3.2. The Past Work On Oxygen Reduction And Hydrogen Oxidation

It appears that there is only one piece of research which considered centrifugal fields for gas consuming reaction, i.e., oxygen reduction [6]. Among a large amount of work in static cells, the technical aspects are of interest in this review.

3.2.1. Oxygen Reduction

Cathode - To be suitable for technical applications, oxygen reduction should proceed at suitably low overpotentials. This is determined to a great extent by the catalytic activity of the cathode. Efficient catalysts for oxygen reduction accelerate the rate of charge transfer and increase the reduction current. Platinum has been found a material of preference, although in order to save cost, other materials have been exploited.

- Pt and Pt Alloys - Platinum is considered an active electrocatalyst for oxygen reduction. It provides maximum activity and long term stability. To balance the efficiency and cost, platinum is often used in a highly dispersed form on various conductive supports or as Pt alloys. The typical substrates used for dispersing

platinum are high surface area carbon and titanium [7-10]. The electrochemical reduction of oxygen were reported to be a 4e process in alkaline electrolytes:

$$O_2 + 2\,H_2O + 4\,e^- = 4\,OH^- \qquad (3.1)$$

For example, this 4e reduction proceeded on Pt/TiO_2 electrodes as a 4e process in 1 M NaOH commencing at potentials of about -0.8 V vs. SCE [11, 12]. Tafel plots with two different slope regions were observed for oxygen reduction at Pt/Ti cathodes in 0.1 M KOH solution [13]. At low current densities the slope was around -60 mV/dec, whereas at high current densities the slopes ranged from -260 to -490 mV/dec when the Pt film thickness increased from 1 nm to 20 nm [13]. This transition in Tafel slope was analogous to those observed on Pt/Glass carbon cathodes and was caused by the slow oxygen adsorption, a rate determining step [13]. The exchange current densities of the low current density region changed from about $2x10^{-10}$ to $9.4x10^{-10}$ Acm^{-2} corresponding to the increase of Pt film thickness from 1 to 20 nm [13].

As for Pt alloys, some interesting examples include Pt-Ir-Au [14] and Pt-Cobalt oxide [15]. These electrodes display improved performance for oxygen reduction in alkaline solution. Using Pt-Cr-Cu or Pt-Cr-Cu alloy, oxygen reduction in solid polymer electrolyte fuel cells was greatly improved [16].

•Au - Oxygen reduction on gold is remarkably influenced by crystallographic orientation. Notable examples of such an influence are a complete 4e reduction on the Au(100) face, and a 2 e process on the Au(111) face with a Tafel slope of - 175 mV/dec [17, 18]. The well ordered strcture of the Au(111) flat surface was found unsuitable for a stronger adsorption of O_2, reaction intermediates and OH^- anions. The slow H_2O_2 desorption partially blocked the surface for oxygen reduction. In

contrast to this, the chemisorption of the OH^- anions, giving the $AuOH_a$ (a is a structure constant) layer, catalysed a 4e reduction on Au(100) surface [17, 18].

•Ag and Ag Alloys - Silver is also an effective catalyst for oxygen reduction in alkaline electrolyte [19]. A great deal of work has been done on this topic. Both the direct 4e pathway (equation (3.1) and the sequential pathway

$$O_2 + H_2O + 2e = HO_2^- + OH^- \quad (3.2)$$

$$HO_2^- + H_2O + 2e = 3\,OH^- \quad (3.3)$$

have been shown to occur simultaneously on silver [20]. In 6.5 M NaOH solution at 25°C, the sequential pathway dominates the direct 4 e pathway prevails on silver [19].

It was reported that silver containing very low percentages of Sb or Bi was very active for oxygen reduction in alkaline solutions [21]. Silver containing 2 to 5 atom% Sb and 2 to 5 atom% Bi was fabricated as smooth solid disc electrodes for oxygen reduction. For example, the Tafel slopes changed from 85 mV/dec on the Ag cathode to 55 mV/dec on the Ag-Sb (2 atom%) and to 50 mV/dec on the Ag-Bi (2 atom%). The exchange current densities decreased from 7.0×10^{-7} Acm^{-2} on the Ag cathode to 2.0×10^{-7} Acm^{-2} on the Ag-Sb (2 atom%) and to 4.5×10^{-7} Acm^{-2} on the Ag-Bi (2 atom%) [21]. Based on the kinetic analysis, it was proposed that the oxygen reduction kinetics on these electrodes was controlled by the diffusion of the dissolved oxygen from the bulk to the electrode surfaces and the transfer of the second electron to the absorbed oxygen is the rate determining step of the oxygen reduction [21].

• Stainless Steel Composite - In fabricating high surface area carbon electrodes, problems of catalyst support were often experienced. Carbon black is usually used

in a powdered form but it cannot be easily supported unless polytetrafluorethelene or other types of binders are employed. To overcome this limitation stainless steel-carbon composite electrodes were produced [22-27]. The approach chosen was to combine dissimilar and normally incompatible materials, i.e., high aspect ratio carbon fibres , conductive metal fibres, and cellulose fibres. These materials form a highly porous yet physically stable and highly conductive structure. The performances of various composite fibre electrodes without the use of Pt catalyst were examined for oxygen reduction in 45 wt% KOH electrolyte at ambient temperature. The tested composite electrodes exhibited Tafel slopes ranged from 40 to 50 mV/dec, which is similar to that obtained on a commercial Teflon bonded platinum gas diffusion electrode (Prototech electrode with 0.45 mg Pt cm^{-2}, Electrosynthesis, Inc.), i.e., 40 mV/dec. However, exchange current densities derived from the composite electrodes ranged from $1.1x10^{-4}$ Acm^{-2} to $9.4x10^{-4}$ Acm^{-2} which is larger than that obtained on the Prototech electrode, i.e., $4.0x10^{-6}$ Acm^{-2}. Furthermore, the composite provided about seven times higher current per electrode weight than the commercial electrode, i.e., 8.13 A/g for the composite and 1.15 A/g for the commercial electrode at - 525 mV vs. SCE [27]. The sintered metal fibre networks in the composite structure provide a highly conductive three dimensional current collecting medium as well as a structure support to the active carbon within the electrode. The dual functionality reduces electrode weight and is more efficient than other forms of current collectors such as perforated metal foil or wire screens and meshes. The electrode material was considered as a suitable candidate for applications in various air electrodes.

• Other Materials - Porous gas diffusion electrodes prepared by using amorphous Ni-Zr or Ni-Ti alloys+Pt-Ru, or Pt-Rh, or Pt catalyst powders [28]. They were employed for electrochemical reduction of oxygen and oxidation of hydrogen in 1 M H_2SO_4 solution [28]. The Tafel slope of the Pt- and Rh-containing amorphous alloy electrodes coincided with these previously reported values for the Pt group metals, i.e., about -120 mV/dec. The Tafel slopes were about - 180 mV/dec for the Ru- and Ir-containing electrodes and about - 60 mV/dec for Pd-containing electrode. The overpotential of the Pt-containing electrodes for oxygen reduction was about 250 mV, while that of the electrodes without Pt is higher than about 350 mV.

Semiconducting elctrocatalysts containing clusters of transition metal atoms provide the reservoir of charges for the multi-electron charge transfer. They can avoid the so-called relaxation of the electronic states to a great extent. Therefore, oxygen reduction proceeds mostly via four-electron transfer reaction to water [29-30]:

$$O_2 + 4\,H^+ + 4\,e^- = 2\,H_2O \qquad (3.4)$$

For example, the chalcogenide materials based on Mo-Ru-Se was used for oxygen reduction in 0.5 M H_2SO_4. The electrocatalytic activities of the material was improved through reducing the overpotential.

Applications

•Fuel Cells - Most research work in O_2 reduction are related to fuel cell development. This is due to the fact that the performance of fuel cells is limited by the slow kinetics of the oxygen reduction. The problem is much more significant when air is used as the cathodic reactant.

Polymer electrolyte fuel cells have especially high power density compared with other fuel cell systems. Oxygen reduction and hydrogen oxidation proceed very

efficiently in such systems. For example [31], a cell with only 0.4 mg Pt cm^{-2} can achieve a current density of 20 kAm^{-2} at the cell voltage of 0.5 V with H_2/O_2 at 5 atm pressure without any mass transfer limitation. The excellent performance of the cell was attributed to the superior electrode structure with highly porous catalyst layer. This facilitates good electrolyte uptake and establishment of the maximum three phase boundary. Also the catalyst layer, facilitates fast transport of reactants, in the gaseous form and in the dissolved form, to the catalyst site leading to minimum mass transfer and ohmic overpotentials. The excellent performance of the fuel cell was attributed to significant improvements in oxygen reduction.

Various methods have been tried to improve the performance of oxygen cathodes. These include: improving the wettability of the gas diffusion electrodes [32] or improving the structure of the catalyst layer [33]. Another approach is through the use of different electrolytes. A typical example is in the phosphoric acid fuel cell, where performance is often limited by polarisation of the oxygen cathode. Replacing phosphoric acid with perfluoroethlene-1,2-bis-phosphonic acid, the cathode performance was improved [34, 35]. This is due to modification of the interfacial dielectric properties by the fluorocarbon moiety thereby favouring oxygen adsorption at the platinum electrolyte interface. On the other hand, the high ionic conductivity was still retained thereby avoiding resistive voltage losses.

• Chlor-Alkali Industry - From the viewpoint of electrochemical engineering, replacement of the hydrogen reduction reaction with the reduction of oxygen in chlorine cells can produce a theoretical reduction in cell voltage up to 1.2 V. This voltage reduction was nearly realised in modern membrane chlor-alkali cells and is

one of the promising ways to reduce the power consumption in chlor-alkali electrolysis [36, 37].

• Waste Water Treatment - Oxygen-fed cathode have been used in electrochemical treatment of waste water [38]. The oxygen-fed cathode electrogenerates H_2O_2 from the reduction of pure O_2 via reaction:

$$O_2 + 2\,H^+ + 2\,e^- = H_2O_2 \qquad (3.5)$$

The method showed high decontaminating power in degradations of the acidic aniline solutions. The degradations were performed in an undivided cell with an Fe anode and a carbon-polytetrafluoroethylene O_2 - fed cathode which continuously generated H_2O_2. Benzoquinone, nitrobenzene, NH_4^+, and NO_3^- were detected in electrolysed solutions. For example, in a solution of 0.05 M Na_2SO_4+H_2SO_4 solution with 1000 ppm aniline at initial pH 3.0 and 25°C, total organic removal from a 120 minutes electrolysis at a current density of 45 mAcm-2 are 91% for the oxygen-fed cathode and 12% for the graphite cathode [38].

3.2.2. Hydrogen Oxidation

Mechanisms and Kinetic Data - Hydrogen oxidation is a very important reaction occurring in some kinds of fuel cells and electrochemical sensors [68] and has received renewed attention recently with respect to electrode kinetics and reaction mechanisms. The accepted mechanism of hydrogen oxidation reaction is formed by a Tafel reaction

$$H_2 + 2\,M = 2\,MH^- \qquad (3.6)$$

and/or a Heyrosky adsorption reaction

$$H_2 + M = MH + H^+ + e^- \qquad (3.7)$$

followed by a Volmer reaction

$$MH = M + H^+ + e^- \quad (3.8)$$

where M is an active site on electrode surface [39, 40]. The mechanism is dependent on electrode material and electrolyte. For example, a Tafel/Volmer mechanism, with Tafel being the rate determining step and a Tafel slope of about 70 mV/dec, has been proposed for the hydrogen oxidation reaction on Pt electrode and strong acid media [39, 40]. In 0.5 M K_2SO_4 solution, the Heyrovsky/Volmer mechanism, with Volmer being the rate determining step and a Tafel slope of about 40 mV/dec has been proved [41]. With a CW 87.8 Mo12.2 electrode in 0.5 M H_2SO_4 solution, a Tafel/Volmer mechanism is also suitable but the Tafel slope changed to 170 mV/dec and the exchange current density was 5.2×10^{-7} A cm^{-2} [42].

Fuel Cells - Most research of H_2 oxidation at high surface area electrodes is related to fuel cell development. A major application is the use of hydrogen in hydrogen/oxygen fuel cells for static power generation, transportation and compact power supplies [5]. Recently the use of hydrogen to power buses and automobiles has seen major investment by multinational companies determined to overcome the environmental problems with the use of petroleum and diesel fuels [43].

Very high chemical-to-electrical conversion efficiencies have been achieved in hydrogen-driven fuel cells. Highly dispersed noble metals (e.g. platinum alloys) on high surface area supports (e.g. carbon blacks) are currently the most favourable electrocatalysts for applications in phosphoric acid fuel cell systems [44, 45].

Zinc Electrowinning - A novel high speed zinc electrowinning cell using a hydrogen anode was developed [46-49]. The cell consists of an Al rotating disc cathode driven by a motor via a shaft and a Pt gas diffusion anode (0.56 mg cm^{-2} Pt). An electrolyte containing 60 g/l Zn+160 g/l H_2SO_4 was fed to the cell through a pump, while

hydrogen gas was supplied to the anode through a mass flow controller. Hydrogen oxidation took place at such an anode with high rate and a low overpotential in a sulphuric acid solution. The cell not only replaced the oxygen evolution reaction at the anode but also reduced the gap between the anode and cathode to 4 mm. This leads to high operating current densities up to 10 kAm^{-2} which was eighteen times higher than that in conventional zinc electrowinning cells. At a current density of 5 kAm^{-2} the cell operated at a cell voltage of 1.8 V, which is only half of that of the conventional cell. The current efficiency (86%) and the purity of the zinc (at least 99.999%) are also high. The energy consumption of the system reached as low as 1400 kWh per tonne of zinc, compared to 3300 kWh per tonne of zinc in the conventional cell, at the expense of 380 m^3 H_2 gas, of course. During a 200 h continuous operation, no noticeable decrease in activity of the hydrogen anode and change in the overpotential of the hydrogen oxidation reaction were observed. Moreover, the zinc deposit formed was uniform and no nodular or dentritic phase formation was observed.

Salt Splitting - Salt splitting is a relatively new technology to produce caustic soda without the co-production of chlorine so as to reduce the cost for disposing of heavily laden salt solutions. Using a hydrogen depolarised anode, the cell voltage can be over 1 V lower, as realised in the Hydrina™ process piloted by DeNora [50]. A similar process was also developed in The Electrosynthesis Company [51]. It takes advantage of gas diffusion electrode technology to accomplish low cell voltage. The key step in the process is hydrogen oxidation at a platinum catalysed gas diffusion electrode. The process is able to produce high purity and high concentrations (up to 32%) caustic soda at current densities of 2.5 kAm^{-2} and a cell voltage of less than 1.6

V. This corresponds to a total power consumption of less than 1200 kWh/ton of caustic which is much lower than in conventional processes (2000 to 4000 kWh/ton of caustic).

Waste Treatment - The destruction of low-level radioactive waste containing species such as nitrites and nitrates is a difficult task. The operating current required to achieve an economic reduction of nitrate results in the generation of hazardous ammonia, which also can combine with the oxygen generated at the anode to form an explosive mixture. Moreover, the anodic evolution of oxygen consumes a high amount of energy. An attempt was made to avoid the high energy consumption associated with oxygen evolution and to use the hydrogen generated at the cathode [52]. Using a commercial hydrogen gas diffusion electrode with 30 ml/min hydrogen, a substantial cell voltage reduction from 0.4 to 1.8 V at 2.5 kAm^{-2} was observed, compared to that obtained in the absence of a hydrogen gas diffusion electrode.

Anode Catalysts - As platinum is relatively expensive, the practical application of such an electrode is unlikely, where cost effectiveness is a concern. Therefore, hydrogen anodes with low Pt loading are highly desirable. One way of achieving this is based on the gas diffusion concept, using high surface area catalysed carbon. The reaction at such anodes takes place within the pores of the anode at the three phase interface formed between the gas, liquid electrolyte and anode surface. So high efficiency can be achieved with low Pt loadings. It was also found that the catalysis of H_2 oxidation reaction is usually promoted by the platinum catalyst dispersed as fine particles (about 20 μm in diameter) on high surface area carbon supports [45, 53] in acid media.

Another way to efficiently use platinum is through Pt alloys. Teflon bonded Pt-Ir bimetal catalyst - based porous carbon electrodes were fabricated and found applications in chlor-alkali industry [54]. The Pt alloys electrodes, Ni-40Zr-Pt, Ni-40Ti-Pt, Ru-Pt, and Rh-Pt, have higher electrocatalytic activity for H_2 oxidation and O_2 reduction reactions than Pt black catalyst [55]. The gas diffusion electrodes made of the alloys, such as Co-Mo, Ni-Mo, Ni-Zr, Ni-Ti, and Pd-H_2MoO_4 have also been investigated for H_2 oxidation [56, 57].

Electrodeposition is another method to improve the catalyst use. Pt catalyst particles can be selectively deposited in electrode regions with both ionic and electronic accessibility [58, 59]. The increased utilisation of Pt catalyst was attributed to the selective location of the Pt catalyst only in electrode region with ionic and electronic conductivity. Moreover, this approach enables operation, with hydrogen saturated electrolyte, in a flow through arrangement with a dispersion of hydrogen in solution to promote good mass transport to the electrode surface. This type of electrode is simple to operate and can in principle extend the reaction zone to a significant depth of the electrode, thereby increasing the surface area for oxidation.

3.3. Experimental

The general aspects of the experimental equipments were described in Chapter 2. Some special considerations for the the gas consuming processes are highlighted in this section.

Gas Path - In the early experiments of oxygen reduction, the reduction current was small and almost independent of the gas flow rates. A simple experiment using a transparent cell in which the gas bubbles could be clearly observed was designed to check whether oxygen passed on the cathode surface or not. It was found that the

most oxygen was by-passing the electrolyte rather than the cathode surface, as shown in figure 3.1.

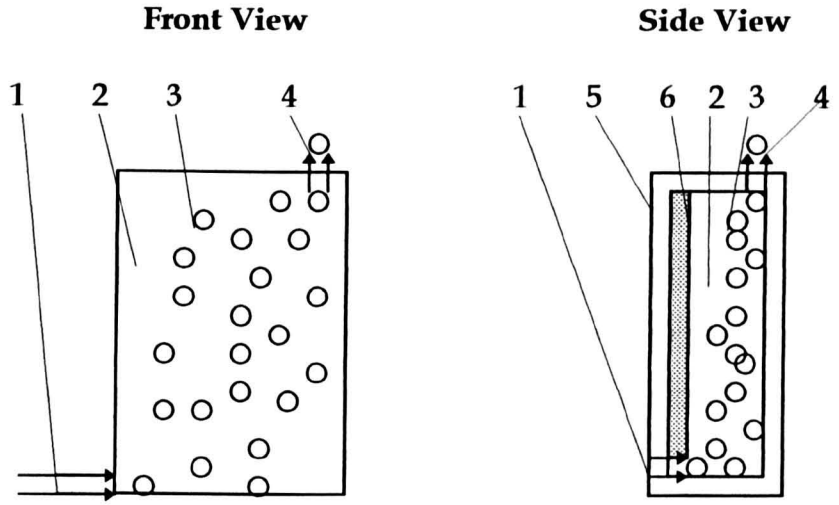

Figure 3.1. Schematic views of the transparent cell for observing the bubblr paths. 1: Gas inlet; 2: electrolyte; 3: Gas bubbles; 4: Gas outlet; 5. Transparent cell frame; 6. Electrode.

Through blocking the gas by-pass, using a PVC separator and reducing the distance between the cathode and the membrane, the gas utilisation was greatly increased.

The Separator - The PVC separator was used to support the membrane, which was situated between the cathode and anode, and to guarantee efficient use of the oxygen, increased the cell resistance due to the enlarged gap between the cathode and the anode. When a dimensionally stable anode (DSA) was introduced instead of the PVC separator, the cell resistance was reduced dramatically. In addition, the gas evolved on the anode surface during oxygen reduction was therefore easily removed. Consequently, the cell resistance was reduced drastically. A cell voltage reduction of about 1.5 V was achieved at a current density of 2 kAm^{-2} when the PVC separator was replaced by DSA.

3.4. Electrochemical Characteristics In The Static Cell

As a starting point, electrochemical measurements were carried out in a static cell to identify the key factors which promote process intensification. High purity oxygen or hydrogen (BOC) was bubbled at a rate of 400 ml/min continuously through the electrolytes during the experiments. Most data were collected at ambient temperature between 21 and 25°C. Typical results are reported in this section.

3.4.1. Oxygen Reduction

Pt and Ag were tested as the catalysts for oxygen reduction. As shown in figure 3.2, the Pt catalysts gave slightly better performance for oxygen reduction compared to Ag catalyst. Under same conditions and at a cathode potential range of -0.9 to -1.1 V vs. RHE, the oxygen reduction current density at the Pt/carbon cloth anode was only 1 to 2 $mAcm^{-2}$ higher than at the Ag/carbon cloth anode.

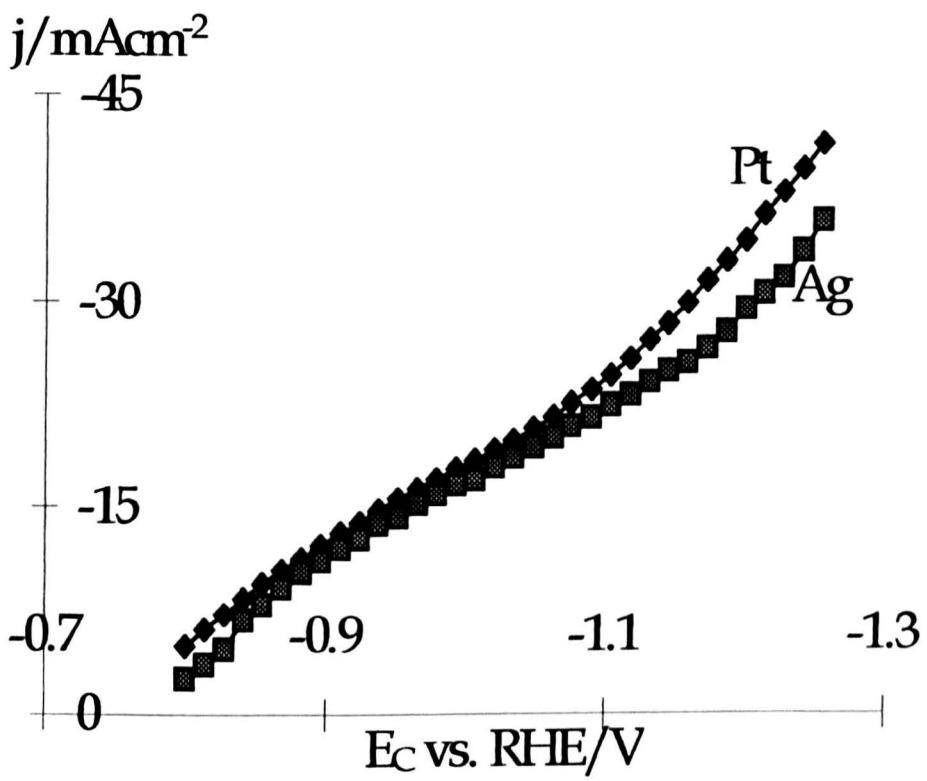

Figure 3.2. Linear sweep voltammograms of oxygen reduction on Pt/carbon cloth and Ag/carbon cloth anodes (10 mg Pt or Ag cm^{-2}). Scan rate: 5 mV/s; Cathode: Stainless steel foam; Gas bubbling rate: 400 ml/min O_2; Temperature: 20.5°C; The rotary cell (static mode).

After about 20 hour operation, a peel-off of the Ag layers from the carbon cloth substrate was observed, while no obvious change for the Pt anode was observed. This demonstrates that the Pt cathode is better than the Ag cathode under the experimental conditions.

Two ways were adopted to change the catalyst loading. One was changing catalyst loading on a single layer substrate; the second way was using the multilayer catalised cathode, i.e., the catalyst was deposited on each substrate and two or more deposited layers were contacted each other and constituted cathodes for oxygen reduction. Figure 3.3 shows the effect of catalyst loading (designated as d in a unit of mg Pt or Ag cm^{-2}) on the current density for oxygen reduction.

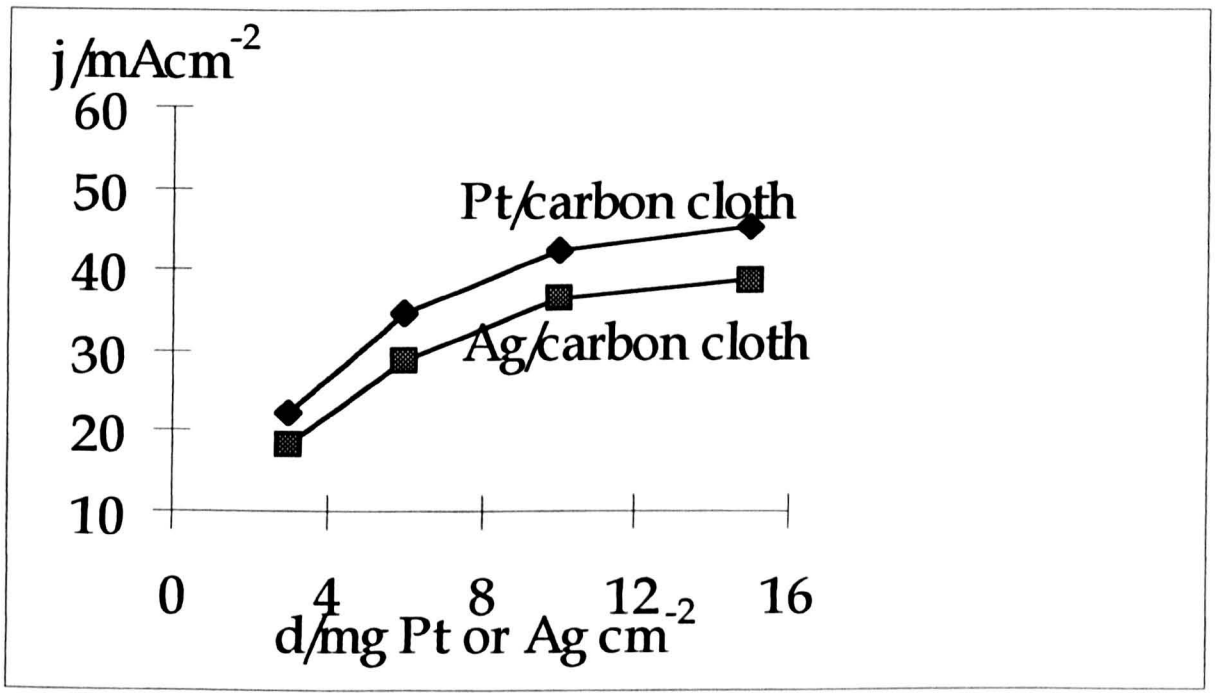

Figure 3.3. Current density (j at -0.8 V vs. RHE)-catalyst loading (d) plots for oxygen reduction at a single layer cathode. Anode: DSA; O_2 flow rate: 400 ml/min; Electrolyte: 1 M NaOH solution; Temperature: 21°C; The rotary cell (static mode).

The data was collected at -0.8 V vs. RHE to avoid the interference of the current from hydrogen evolution. The major effect of the increased catalyst loading is a

steady increase in electrochemical active area and therefore increase in reduction current. In the range 3 to 6 mg Pt or Ag cm^{-2}, a significant increase in current density was observed for the both cathodes. Further increase of catalyst loading gave better performance. Above a catalyst loading of 10 mg cm^{-2}, the effect of catalyst loading on the current density was small, as seen from figure 3.3.

The multi-layer cathodes gave better performance than single layer cathode. However, the improvement is relatively small. An example is given in figure 3.4 where one, two or three layer electrode, constituted by the Pt/carbon cloth with 10 mg Pt cm^{-2}, were used. This means that the catalyst loadings are 10, 20, and 30 mg Pt cm^{-2} for one, two or three layer electrode respectively.

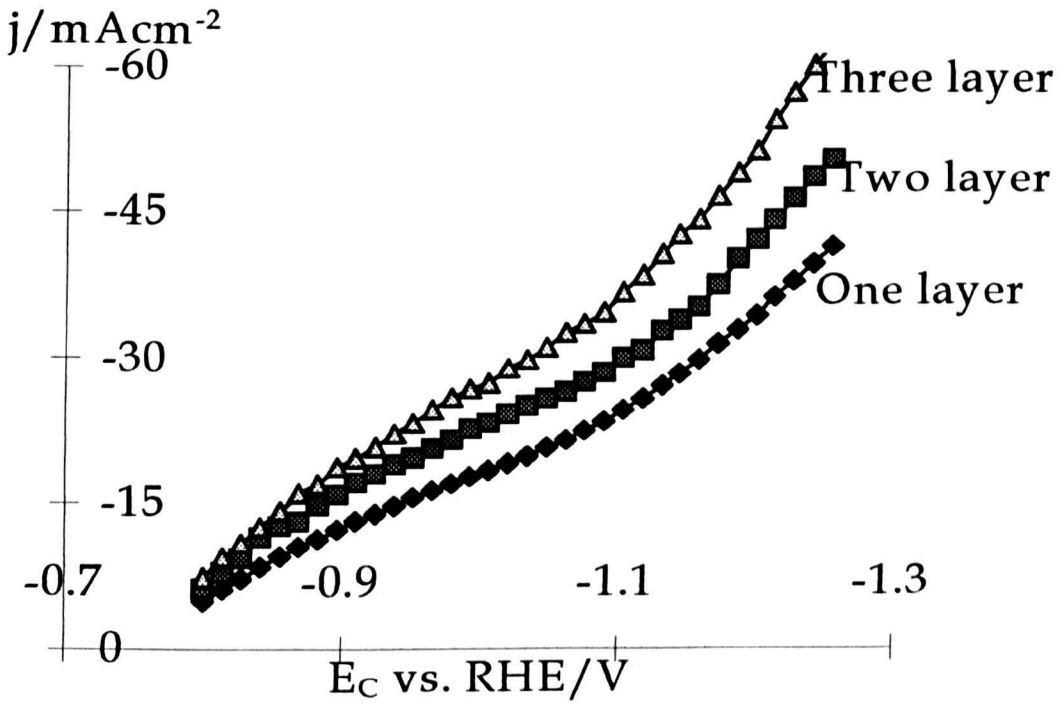

Figure 3.4. Linear sweep voltammograms of oxygen reduction on Pt/carbon cloth cathodes. Cathode catalyst loading: 10, 20, and 30 mg Pt cm^{-2} for the one-, two- and three-layer electrode respectively; Anode: DSA; Scan rate: 5 mV/s; Gas bubbling rate: 400 ml/min O_2; Temperature: 20.5°C; The rotary cell (static mode).

It can be seen from figure 3.4 that increase in current density at a constant potential is not proportional to electrode layer. For example, current densities at a cathode potential of -0.95 V vs. RHE are -15.52, -19.55 and -23.24 mA cm^{-2} for the one-, two- and three-layer electrode respectively. For the multilayer electrode, catalysts between each layer could not be completely used for the oxygen reduction. Also, electrolytes could not pass through a small gap between electrode layers. Theerefore, the performances of the multilayer electrodes were poorer than single layer electrode. Considering the effectiveness and cost, one-layer cathode seems the best choice.

3.4.2. Hydrogen Oxidation

Effect of Anode Material - As expected from the literature, the anode material had a big effect on hydrogen oxidation in the experiments. Some results are shown in figure 3.5. In order to establish an electrochemical effectiveness rating of each anode for hydrogen oxidation, the current density (in mA cm^{-2}) at an anode potential of -0.05 V vs. RHE, which was or nearly corresponding to maximum current densities for hydrogen oxidation at the anodes tested, was evaluated from figure 3.5.The data shows the following order was found in 1 M NaOH solution at 25°C:

Pt/carbon cloth (6. 56) > Stainless steel foam (3.35) > Ni foam (2.25)

> TYSAR foam (2.20) > Carbon cloth (1.50).

As would be expected, platinised carbon cloth gave the best performance due to the efficient use of the catalyst and the high surface area structure. According to the measurements, the foam materials also show high effectiveness for the hydrogen oxidation reaction due to their high catalyst loading per unit volume.

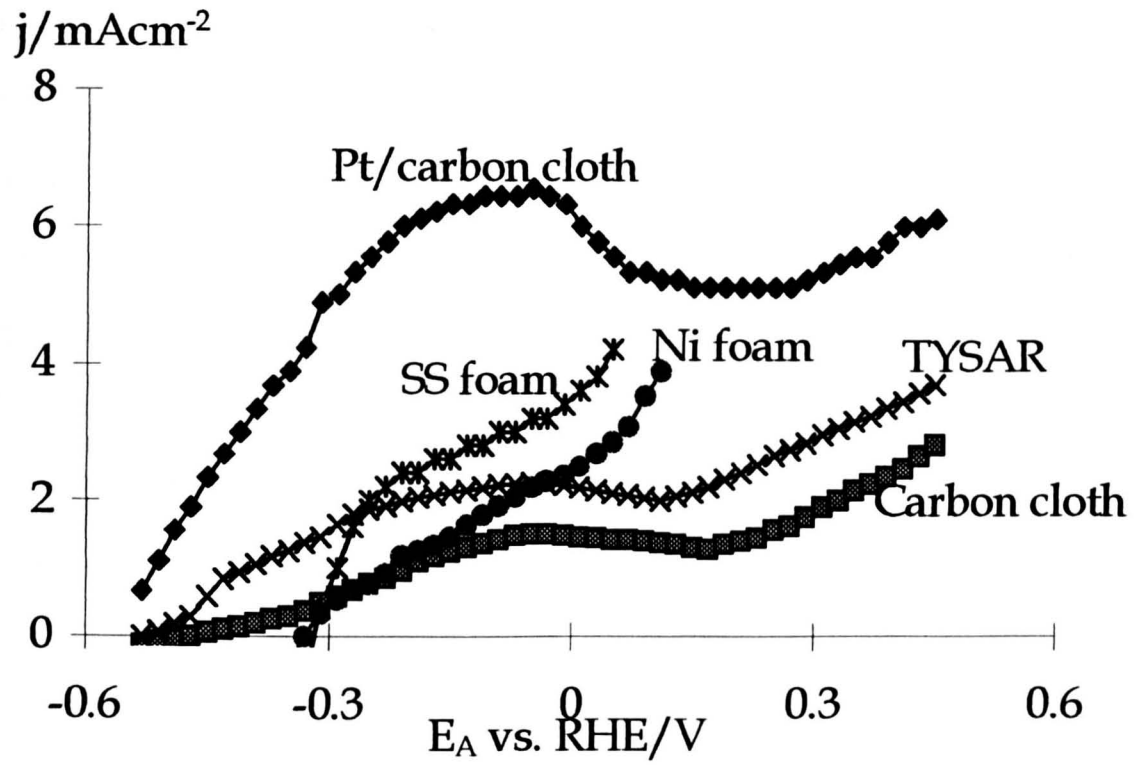

Figure 3.5. Linear sweep voltammograms of hydrogen oxidation on several anodes. Electrolytes: 1 M NaOH solution; Catalyst loading of Pt/carbon cloth anode: 10 mg Pt cm^{-2}; Scan rate: 5 mV/s; Cathode: Stainless steel foam; Gas bubbling rate: 400 ml/min H_2; Temperature: 21.5°C; The rotary cell (static mode).

It is interesting to compare the behaviour of the platinised carbon cloth with that of a commercial platinised high surface anode made from titanium fibre TYSAR™ (The Electrosynthesis Co. Inc., USA). This material has a specific area of 60 cm^2/cm^3 and a platinum loading of 7.8 mg cm^{-2} when purchased. It only gave a peak current density of 2.20 $mAcm^{-2}$ at -0.05 V, with a scan rate of 5 mV/s. This is only about one-third of that obtained using platinised carbon cloth anode. The Pt loading seems lower than the value when purchased.

Effect of Electrolyte - The behaviour of hydrogen oxidation depends on the electrolyte chosen, in this case, 1 M H_2SO_4, 1 M Na_2SO_4, or 1 M NaOH solution. Figure 3.6 shows the influence of electrolyte on the linear sweep voltammograms for operation in acidic, neutral, and alkaline electrolytes at a potential sweep rate of 5

mV/s. For comparision, the polarisation curves obtained in the blank solutions, i.e., used nitrogen rather than hydrogen, are also given in the figure.

No oxidation peak was observed when nitrogen was used (Curves d, e, and f, Figure 3.6). However, when hydrogen was used to replace nitrogen, the oxidation of hydrogen ocurred in the three electrolytes (Curves a, b, and c, Figure 3.6). A current density peak responsible for hydrogen oxidation, resulting from mass transport limitation associated with dissolved hydrogen, was observed in all solutions, as shown in figure 3.6.

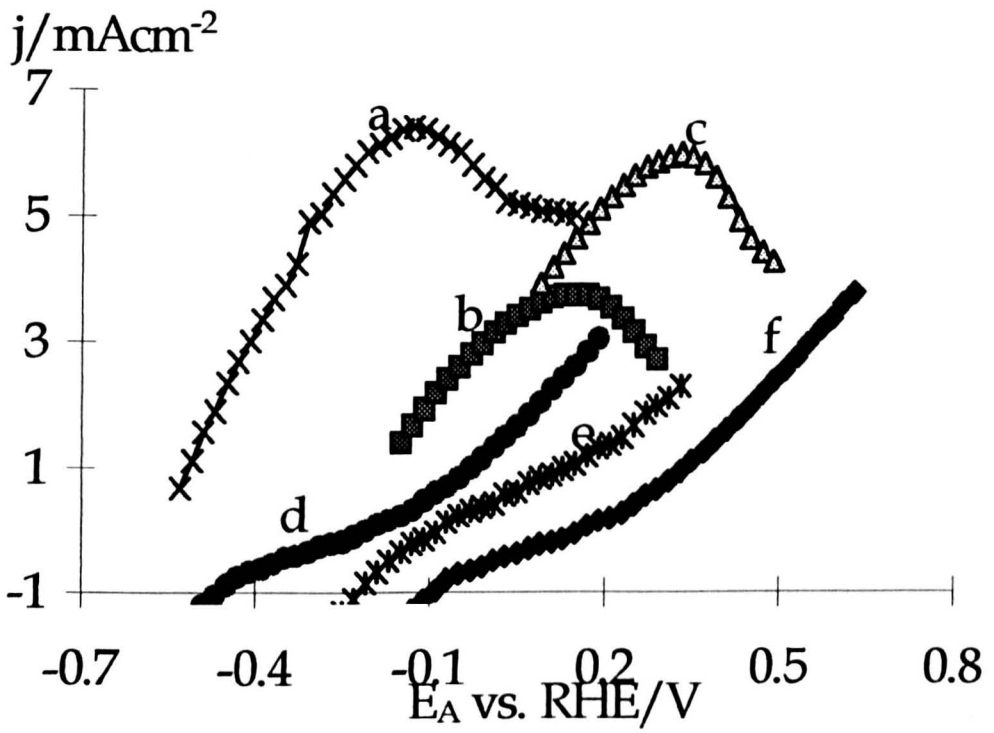

Figure 3.6. Linear sweep voltammograms of hydrogen oxidation on Pt/carbon cloth anode (10 mg Pt cm^{-2}). (a, d): 1 M NaOH solution; (b, e): 1 M Na_2SO_4 solution; (c, f): 1 M H_2SO_2 solution; Cathode: Stainless steel foam; Scan Rate: 5 mV/s; Gas bubbling rate: 400 ml/min H_2 (a, b, and c) or N_2 (d, e, f); Temperature: 21.5^{0}C; The rotary cell (static mode).

The electrocatalysis benefits from operation in an alkaline environment, by operating at several hundred millivolts lower peak potentials, i.e., about -130, 150,

and 330 mV vs RHE for alkaline, neutral, or acidic medium, respectively. This effect has previously been reported for the oxidation using different electrode material [60].

Effect of Potential Scan Rate - Figure 3.7 shows the effect of sweep rate on the linear sweep voltammograms for hydrogen oxidation in alkaline solution.

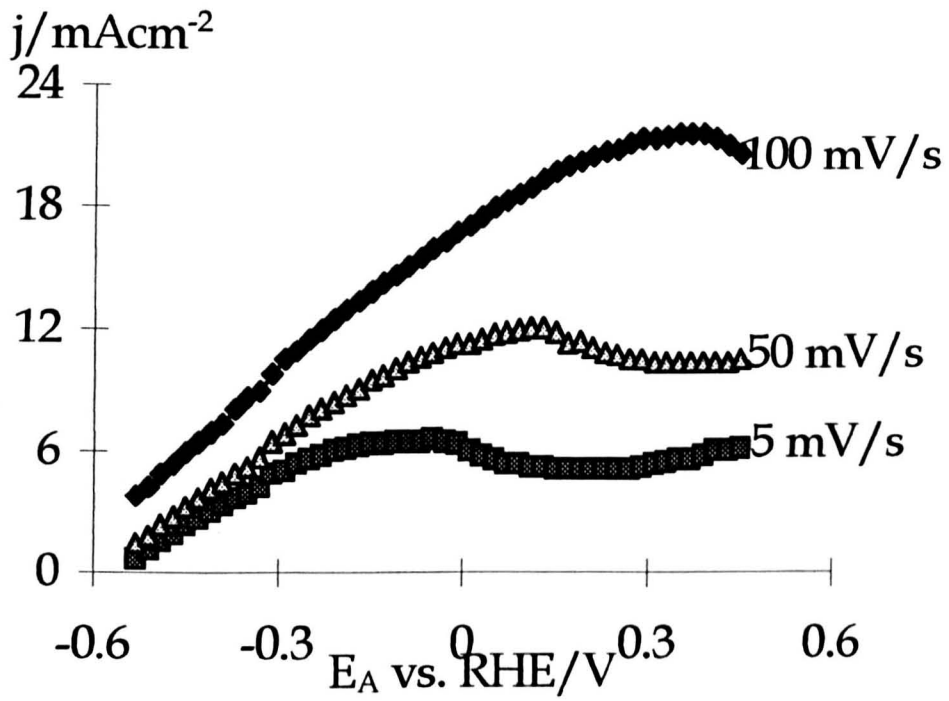

Figure 3.7. Linear sweep voltammograms of hydrogen oxidation on Pt/carbon cloth anode (10 mg Pt cm^{-2}) as a function of scan rate. Cathode: Stainless steel foam; Gas bubbling rate: 400 ml/min H_2; Temperature: 21.5°C; The rotary cell (static mode).

The linear sweep voltammograms exhibit mass transport limitations associated with the diffusion limitations related to the stationary electrolyte solutions used. This can be explained by considering the concentration profiles of the reactants, i.e., hydrogen in this case [62]. Within the region next to the electrode, known as the nernst diffusion layer, the concentration gradients are essentially linear. As the potential was made more positive the surface concentration of the reactant must be progressively decreased. The concentration gradient is thereby increased, and hence

the current also increased until the surface concentration of the reactant approached zero and then the current reached a maximum value. When the sweep rate was increased, the diffusion layer did not have sufficient time to relax to its equilibrium state and did not extend as far into solution, and the concentration profiles were not yet linear. However, the electrode potential was still increasing, and therefore the surface concentration of the reactant is further decreased until it reached zero. Once the surface concentration of the reactant reached zero the concentration gradient started to decrease, due to the relaxation effect and hence the current flowing also decreased. Overall, this behaviour have rise to a peak shaped current-potential responseas shown in figure 3.7. A clear current peak was observed for three scan rates at a range of anode potential between 100 mV vs RHE and about 360 mV vs RHE. The peak current density also increases with increasing scan rate, i.e., 6.6, 11.8, and 21.56 $mAcm^{-2}$ at 5, 50, and 100 mV/s, respectively. At higher potentials the polarisation curves were influenced by the simultaneous evolution of oxygen at the surface as mass transport limitations, for hydrogen oxidation, in the porous electrode become apparent.

3.5. Electrochemical Behaviour In The Rotary Cell

3.5.1. Oxygen reduction

The results of effect of centrifugal fields on the cell voltage and the cathode potential during oxygen reduction are described. The effect of the other operating conditions is also discussed.

Cathode Polarisation - The cathode polarisation behaviour was dramatically changed in centrifugal fields, as shown in figure 3.8 for oxygen reduction at a Pt/carbon cloth electrode.

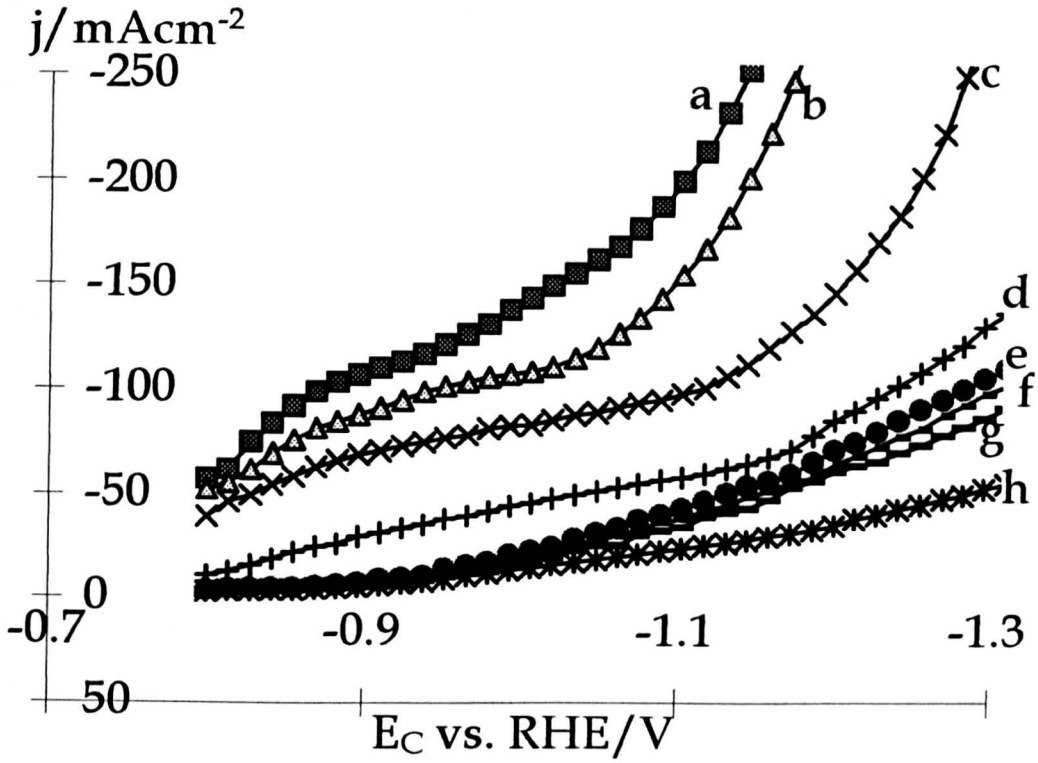

Figure 3.8. Cathode polarisation curves for oxygen reduction - Effect of rotating speed. (a, e)1100, (b, f) 800, (c, g) 400, and (d, h) 0 rpm; Pt/carbon cloth cathode (10 mg Pt cm^{-2}); DSA anode; Gas flow rate: 400 ml/min O_2 (a, b, c, d) or N_2 (e, f, g, h); 1M NaOH electrolytes; Temperature: 21.5°C; Temperature: 21.5°C; The rotary cell.

Three features of the effect of rotating speed are apparent. Firstly, at less negative potential range, the polarisation curves obtained from nitrogen is almost independent of rotating speed while larger difference can be seen for the polarisation curves obtained from oxygen. This indicates that although oxygen reduction, which occured at the low potential range, can be intensified in centrifugal fields, the intensification degree decreased with increasing rotating speed which may be due to some chemical and physical problems, which need to be identified. Secondly, at more negative values, the difference between the polarisation curves obtained from the oxygen systems at high potential range became very significant. Bear in mind that the hydrogen evolution took place at a significant rate at the high

potential range. This suggests that centrifugal force affects the process of gas removal (hydrogen evolution in this case) from the electrode surface more significantly than the gas consuming process (oxygen reduction in this case). Thirdly, in the oxygen saturated solutions, the hydrogen evolution potential shifted to less negative values, compared to the nitrogen systems.

In alkaline media and at less negative potential, the main reaction at the cathode is:

$$O_2 + 2\,H_2O + 4\,e^- = 4\,OH^- \qquad (3.9)$$

Due to mass transfer limitation for oxygen reduction, a current plateau in the stationary cell (curve at 0 rpm, figure 3.8) can be seen. The oxygen reduction and the hydrogen evolution processes are clearly distinguished in figure 3.8 (the curve d at about -1.1 V vs. RHE). Of course, hydrogen evolution becomes a dominant reaction at more negative potential. These two reactions are quite different processes. One involves reduction of oxygen on the cathode and the other evolution of hydrogen gas from the cathode surface. It seems that centrifugal force has bigger effect on the gas removing process than on the gas adherence process. This may be the possible reason responsible for the difference between the results obtained at the high current density (the hydrogen evolution was a major process) and at low current density (the oxygen reduction was a major process). Similar observation was reported on an oxygen cathode [61]. It is worthwhile to point that the setup used in the above work was not optium. Also, a further work is needed to know the bubble paths in the rotary cell and the electrolyte circulation over the electrode, which have not been clear yet. Therefore, more investigation is needed to obtain conclusion about the above observation.

Quantitatively, it is safe to analyse the effect of centrifugal fields on the oxygen reduction process by using the data obtained at less negative potentials. As expected, the reduction current increases with increasing rotating speeds. For example, at a potential of -0.92 V vs. RHE, the current density is -33.5, -72.9, -94.5, and -112.9 $mAcm^{-2}$ at 0, 400, 800, 1100 rpm, respectively. This means that the magnitude of the cathode current density at 1100 rpm was about 3-fold higher than that at 0 rpm.

Figure 3.9 shows the Tafel plot obtained on Pt/carbon cloth cathode in 1 M NaOH solution.

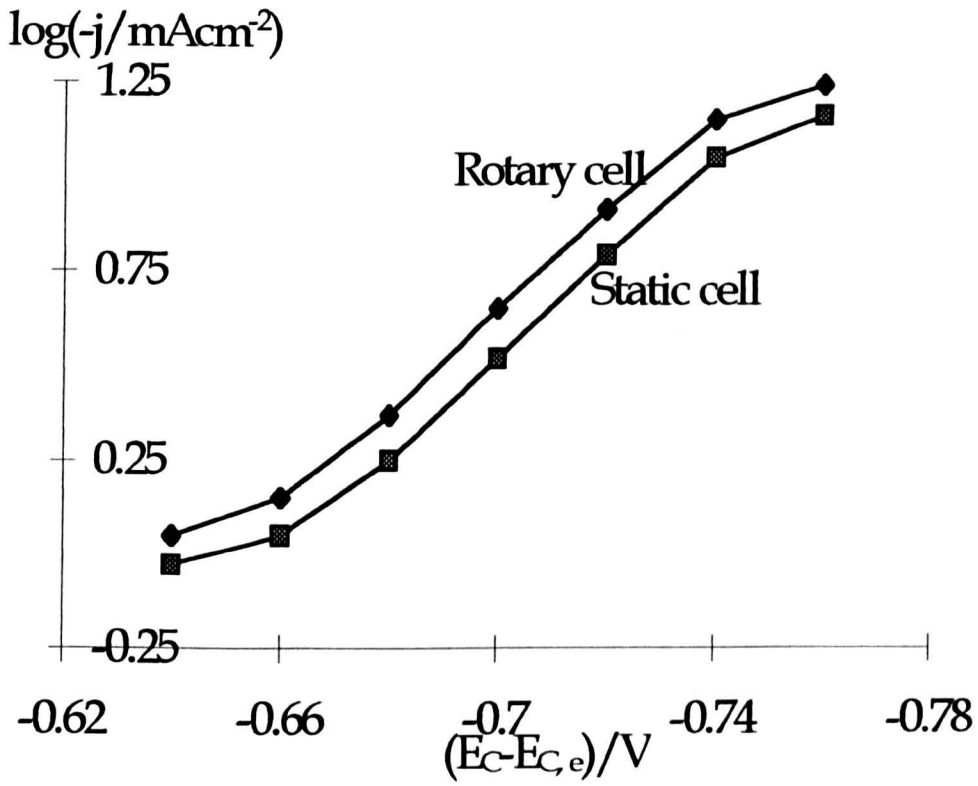

Figure 3.9 Tafel plots for oxygen reduction reaction on Pt/carbon cloth electrode. Pt/carbon cloth cathode (5 mg Pt cm^{-2}); DSA anode; 400 ml/min O_2; 1M NaOH electrolytes; Temperature: 20.5°C; The Rotary cell.

The Tafel slopes in an overpotential range of 0.67 and 0.72 V obtaining from figure 3.9 are about 65 mV/decade; the exchange current densities by extrapolating to (E_C-

$E_{C,e}$)=0 are 10^{-7} A cm^{-2} for both the rotary cell and the static cell. The reported Tafel slopes range from 40 to 70 mV/decade [63, 64]. The reported exchange current densities are 10^{-4} A cm^{-2} on Pt/carbon black electrodes [63, 65, 66] and 10^{-3} Acm^{-2} on Pt black electrode [67] and 10^{-11} A cm^{-2} on Pt electrodes [64]. The data of this work exhibit that the Tafel parameters keep constant in an acceleration field.

It is common for a Tafel slope to be observed over three orders of magnitude of current [62]. Only about one order of magnitude of current could be observed in these experiments due to hydrogen evolution at more negative potentials. Also, the exchange current density based on geometric projected are greater than those based on real electrode area (up to several orders of magnitude) [63] Thus, the Tafel slopes and exchange current densities obtained here should not be considered as rigorous quantitative data.

Cell Voltage - When air cathodes are used in industrial cells, cell polarisation characteristics are important. The effect of centrifugal fields on the cell voltage reduction with oxygen bubbling cathode is reported in Figure 3.10.

The values of cell voltage reduction were obtained by subtracting the cell voltage at 0 rpm from the values at different rotating speeds. Several features can be seen in figure 3.10. The cell voltage reduction increased rapidly from 200 rpm to 400 rpm, after which the rate of increase slows. The maximum reduction in cell voltage of 740 mV was realised in a cell with the Pt/carbon cloth cathode at 1100 rpm (190 G). From the previous section, it was known that the effect of centrifugal fields on the oxygen reduction is relatively small. Also, one of the major intrinsic properties of centrifugal force is that it can disengage gas bubbles from the electrode surface very effectively. Therefore, the major contribution for the cell voltage reduction comes

from the improvement in anodic oxygen evolution process, although the cathode performance improvement in centrifugal fields contributed to the cell voltage reduction.

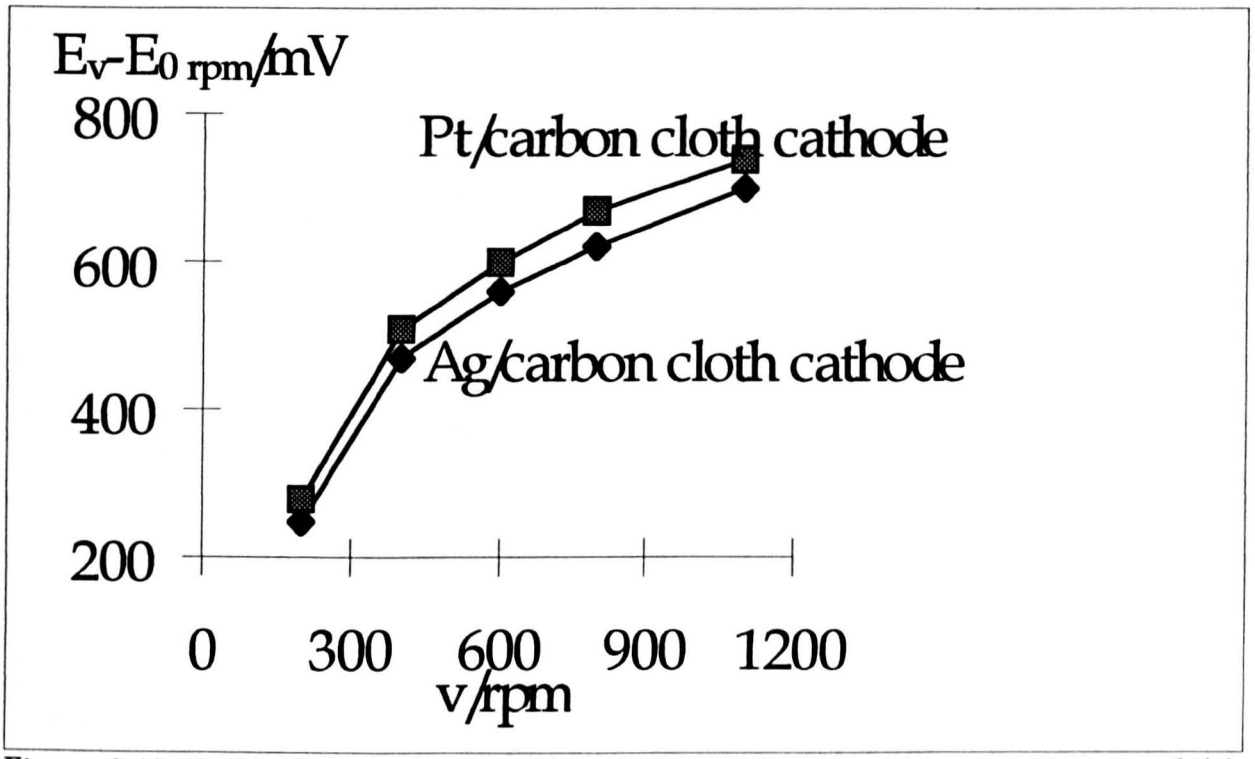

Figure 3.10. Cell voltage reduction ($E_{0\ rpm}$ - E_v at 1 kAm^{-2}) versus rotating speed (v) plots for oxygen reduction. Cathode catalyst loading: 10 mg Pt or Ag cm^{-2}; Anode: DSA; O_2 flow rate: 400 ml/min; Electrolyte: 1 M NaOH solution; Temperature: 20.5°C; The Rotary cell.

Effect of the Partial Pressure of Oxygen - Figure 3.11 shows the effect of oxygen pressure on the oxygen reduction process in an acceleration field of 190 G.

The effect of oxygen partial pressure can be discerned by comparing the current data collected at -0.9 V vs RHE in figure 3.11. Namely, -52.9, -75.4, -84.1, and -112.9 mA cm^{-2} for air, 50% O_2+50% N_2, 80% O_2+20% N_2, and O_2, respectively. This is a steady increase in j with oxygen partial pressure.

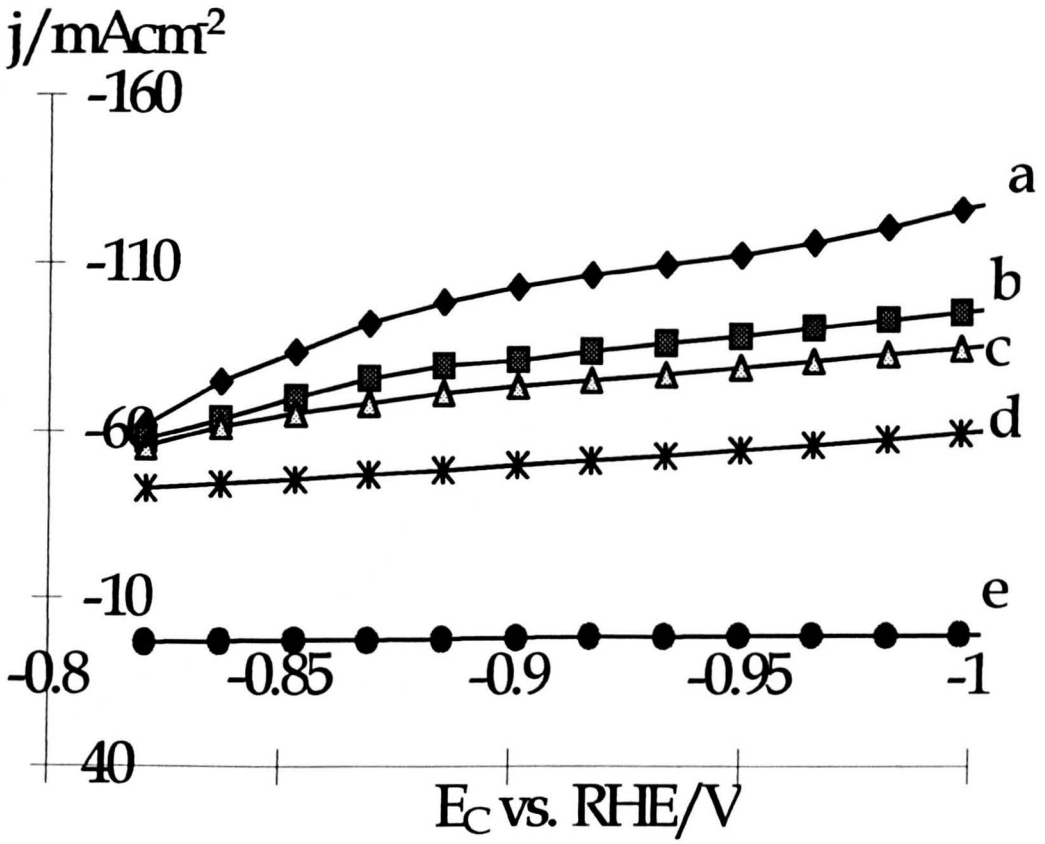

Figure 3.11. Cathode polarisation curves for oxygen reduction in an acceleration field of 190 G-Effect of the partial pressure of oxygen. (a) O_2; (b) 80% O_2+20% N_2;; (c) 50% O_2+50% N_2; (d) air; (e) N_2; Cathode: Pt/carbon cloth (10 mg Pt cm^{-2}); Anode: DSA; Scan rate: 5 mV/s; Gas flow rate: 400 ml/min; Electrolyte: 1 M NaOH solution; Temperature: 20.5°C; The rotary cell.

3.5.2. Hydrogen Oxidation

Relative Acceleration Rate - Figure 3.12 presents data for the effect of relative acceleration rate on the anode polarisation behaviour of hydrogen oxidation at a Pt/carbon cloth electrode.

An increase in rotating speed increases the current density at a fixed potential. For example, at a anode potential of -0.1 V vs. RHE, i.e., corresponding to the peak potential in a stationary cell, current density is 6.40, 19.14, 22.04, 24.88, and 28.75 $mAcm^{-2}$ at 0, 400, 600, 800, 1100 rpm, respectively. The magnitude of the anode

current density at 400 rpm was more than three times greater than that at 0 rpm. The current density increase was relatively small for further increase in rotating speed.

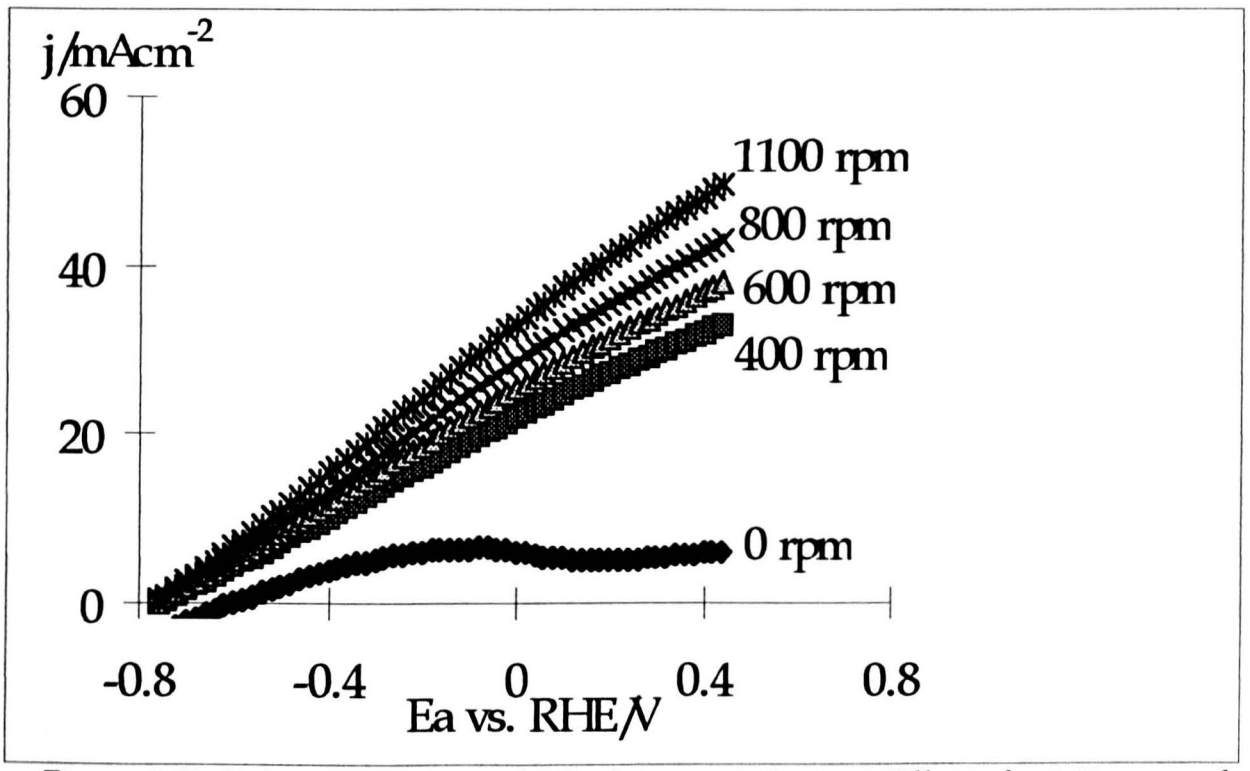

Figure 3.12. Polarisation curves for hydrogen oxidation - Effect of rotating speed. Anode: Pt/carbon cloth (10 mg Pt cm^{-2}); Cathode: Stainless steel foam; Electrolyte: 1 M NaOH; Scan rate: 5 mV/s; 400 ml/min H_2; Temperature: 21.5°C; The rotary cell.

The Tafel plot obtained from the rotary cell as well as from the static cell, are shown in figure 3.13. The data in the figure 3.13 gives Tafel slope of 60 mV/decade in an overpotential range of 0.15 to 0.19 V. The literature Tafel slopes vary from 40 to 120 mV/decade depending on oxidation mechanisms [68-71]. The Tafel data obtained in this work qualitatively agree with the literature data for Heyrovsky/Volmer mechanism with a Heyrovsky rate determining step [68]. The exchange current densities by extrapolating to $(E_A-E_{A,e})=0$ from figure 3.12 are $10^{-5.2}$ and $10^{-5.3}$ A cm^{-2} for the rotary cell and the static cell respectively which are smaller than the literature value (about $10^{-3.8}$ A cm^{-2} on Pt/carbon cloth electrodes [72]).

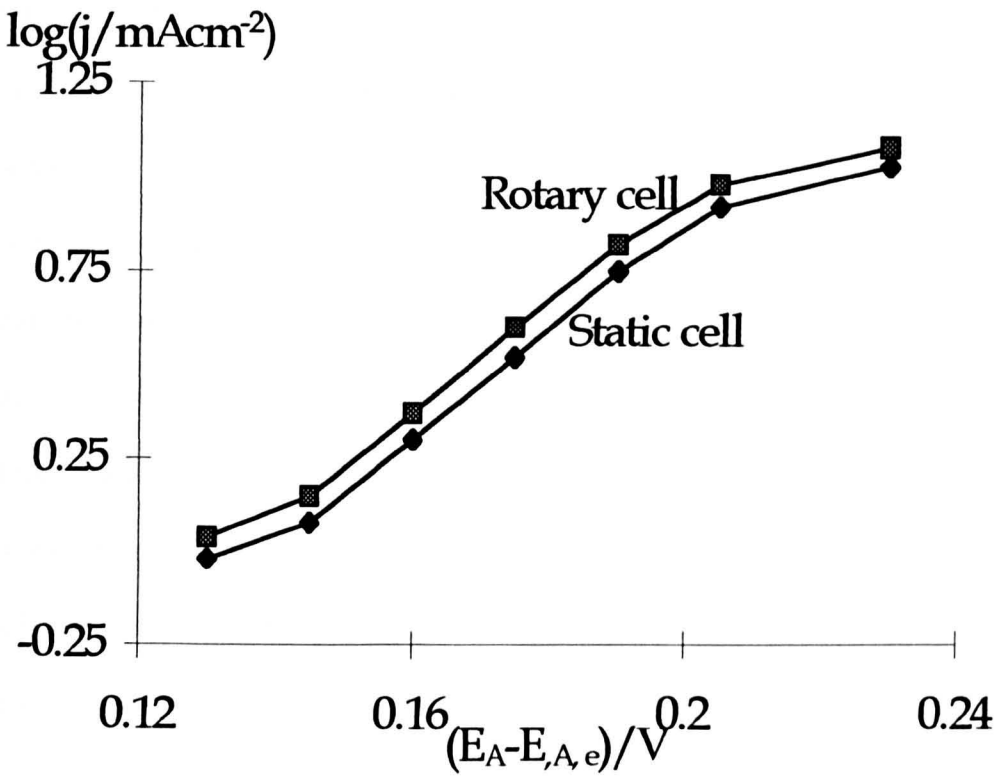

Figure 3.13. Tafel plots for hydrogen oxidation reaction on Pt/carbon cloth electrode. Anode: Pt/carbon cloth (5 mg Pt cm^{-2}); Cathode: Stainless steel foam; Electrolyte: 1 M NaOH; 400 ml/min H_2; Temperature: 21.5°C; The rotary cell at 1100 rpm.

As mentioned in section 3.5.1, a Tafel slope should be observed over three orders of magnitude of current [62]. Only about one order of magnitude of current could be observed in this work due to oxygen evolution at more positive potentials. Also, the exchange current densities based on geometric area are greater than those based on real electrode area (up to several orders of magnitude) [63] Thus, the Tafel slopes and exchange current densities obtained here should not be considered as rigorous quantitative data.

It is obvious that the major effect of an centrifugal field if any is from enhanced mass transport at the anode rather than change in kinetic parameters. As described in the section 3.5.1, high G can produce finer bubbles and reduce boundary layer thickness

which tend to increase hydrogen oxidation current. However, centrifugal force can not fully overcome hydrogen solubitity and kinetics obstacles. Also, as mentioned above, the setup used in the above work was not optium and a further work is needed to know the bubble paths in the rotary cell and the electrolyte circulation over the electrode, which have not been clear yet. Therefore, more investigation is needed to know why the limited degree of intensification was observed.

More significantly, at higher potentials, an increase in current density with increasing rotating speed was observed. Of course, the increase in current density includes the influence of oxygen evolution which simultaneously occured at the anode surface.

Electrolyte - Figure 3.14 shows the influence of electrolyte on the anode potential-current density behavioure for hydrogen oxidation. Different responses to centrifugal fields were observed in acidic, neutral, and alkaline media.

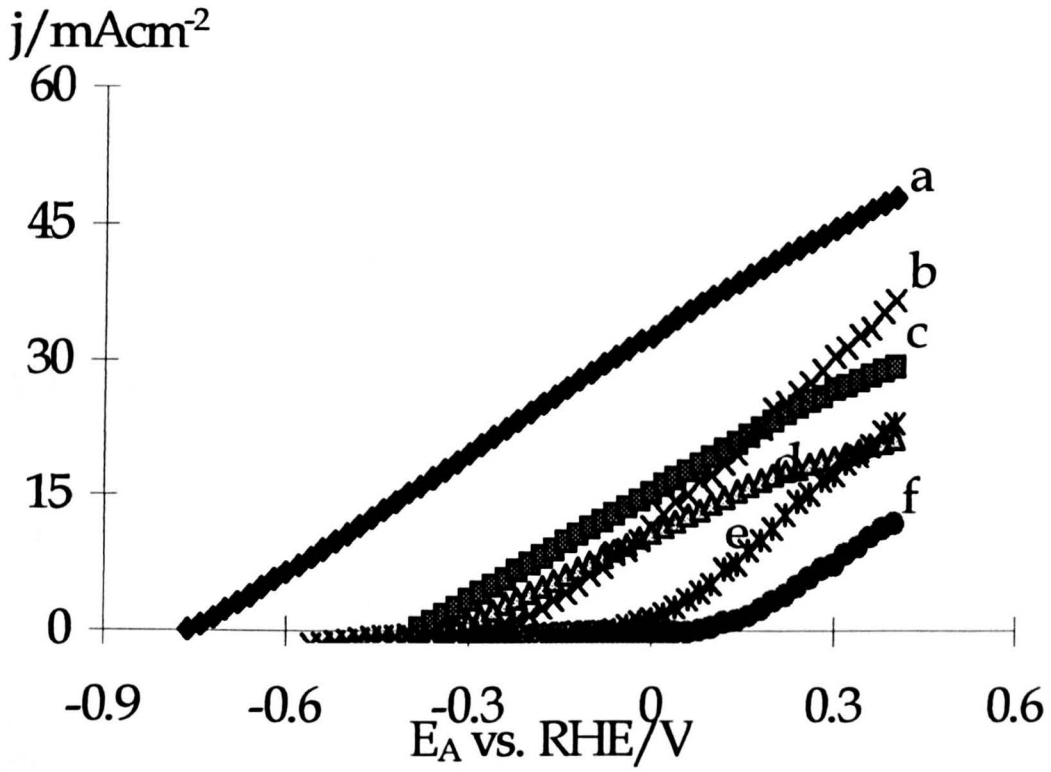

Figure 3.14. Linear sweep voltammograms of hydrogen oxidation at a rotating speed of 1100 rpm on Pt/carbon cloth anode (10 mg Pt cm^{-2}). (a, b): 1 M NaOH solution; (c, e): 1 M H_2SO_4 solution; (d, f): 1 M Na_2SO_4 solution; Cathode: Stainless steel foam; Scan Rate: 5 mV/s; Gas bubbling rate: 400 ml/min H_2 (a, c, and d) or N_2 (b, e, f); Temperature: 21.5°C; The rotary cell.

Figure 3.15 shows the influence of applied G on the current density obtained at the anode potential corresponding to the anodic peak potentials in the static cell. The anode current densities increase significantly with a centrifugal field of 25 G for the three electrolytes. Increase the applied "G" up to 200, show further improvement but beyond 200 G little enhancement is achieved. Overall, the effect of centrifugal fields on hydrogen oxidation can be discerned in all these media.

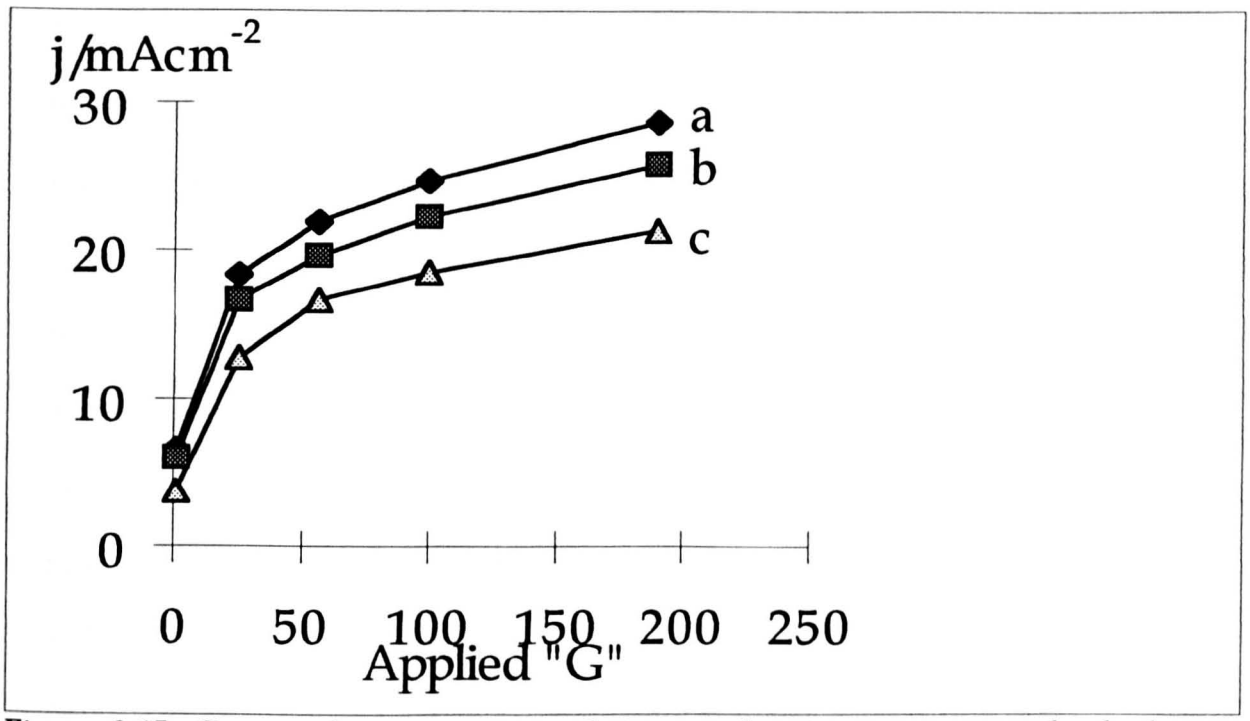

Figure 3.15. Current density against relative acceleration rate curves for hydrogen oxidation - Electrolyte effect. (a). 1 M NaOH solution; (b): 1 M H_2SO_4 solution; (c): 1 M Na_2SO_4 solution; Anode: Pt/carbon cloth (10 mg Pt cm^{-2}); Cathode: Stainless steel foam; Scan rate: 5 mV/s; 400 ml/min H_2; Temperature: 21.5°C.; The rotary cell.

3.6. Conclusions

The results for the gas consuming reactions leads to the following conclusions:

•The oxygen reduction and hydrogen oxidation processes are moderately intensified in centrifugal fields. The current density for oxygen reduction is about three times that at 200 G than that at 0 rpm. For hydrogen oxidation, the anode current density at 1100 rpm is about 4 times higher than that at 0 rpm in all electrolytes used. But the absolute amplitudes are small and of limited value for industrial application. The relatively slow kinetics for oxygen reduction and hydrogen oxidation as well as low oxygen and hydrogen solubilities can not overcome by means of centrifugal acceleration field.

•Centrifugal fields affect the cell voltage of the rotary air cathode cell to a greater extent than reported in literature. More importantly, this work identifies the cause of

the cell voltage reduction as a reduction in the anode potential rather than the oxygen reduction reaction.

•A catalysed cathode with high surface area was necessary to intensify the gas consuming processes. The catalyst utilisation was the most efficient in the cell with the single layer cathode. Pt and Ag catalyst showed similar catalytic activity for the oxygen reduction process. Although Pt is more expensive than Ag, it has better adhesion with the substrate. Carbon cloth is a more suitable substrate than carbon fiber. Platinised carbon cloth exhibits the best activity for hydrogen oxidation.

•The partial pressure of oxygen affects the oxygen reduction process in centrifugal fields. The hydrogen oxidation reaction gives superier polarisation characteristics in an alkaline environment compared to an acidic electrolyte.

3.6. References for Chapter 3

[1] J. C. Huang, R. K. Sen, and E. Yeager, J. Electrochem. Soc., 126, 786, 1979.

[2] C. C. Wang, K. S. Goto, and S. A. Akbar, J. Electrochem. Soc., 138, 3673, 1991.

[3] C. Oloman and A. P. Watkinson, J. Appl. Electrochem., 9, 117, 1979.

[4] H. Wendt (Editor), "Electrochemical Hydrogen Technologies. Electrochemical Production and Combustion of Hydrogen", Elsevier, Amsterdam, 1990.

[5] L.J.M.J. Blomen and M. N. Mugerwa, "Fuel Cell Systems", Pluem, New York, 1993.

[6] C. Ramshaw, Heat Recovery Systems & CHP, 13, 493, 1993.

[7] J. A. Poirier and G. E. Stoner, J. Electrochem. Soc., 141, 425, 1994.

[8] K. Tammeveski, T. Tenno, J. Claret and C. Ferrater, Electrochim. Acta, 42, 893, 1997.

[9] Y.-K. Choi, S.-S. Seo, K.-H. Chjo, Q.-W. Choi and S.-M. Park, J. Electrochem. Soc., 139, 1803, 1992.

[10] L. He, H. F. Franzen and D. C. Johnson, J. Appl. Electrochem., 26, 785, 1996.

[11] V. B. Baez and D. Pletcher, J. Electroanal. Chem., 382, 59, 1995.

[12] V. B. Baez, J. E. Graves and D. Pletcher, J. Electroanal. Chem., 340, 273, 1992.

[13] K. Tammeveski, M. Arulepp, T. Tenno, C. Ferrater and J. Claret, Electrochim. Acta, 42, 2961, 1997.

[14] Y. J. Li, C. C. Chang, and T. C. Wen, J. Appl. Electrochem., 27, 227, 1997.

[15] S. Wada et al., Chem. Lett., (1), 45, 1993.

[16] G. Tamizhmani and G. A. Capuano, J. Electrochem. Soc., 141, 968, 1994.

[17] R. R. Adzic and N. M. Markovic, J. Electroanal. Chem., 138, 443, 1982.

[18] S. Strbac, N. A. Anastasijevic and R. R. Adzic, Electrochim. Acta, 39, 983, 1994.

[19] P. K. Adanuvor and R. E. White, J. Electrochem. Soc., 135, 2509, 1988.

[20] P. R. Trevellick, PhD Thesis, Oxford University, Oxford, 1985.

[21] A. I. Raj and K. I. Vasu, J. Appl. Electrochem., 23, 728, 1993.

[22] D. Kohler, J. Zabasajja, A. Krishnagopalan, and B. J. Tatarchuk, J. Electrochem. Soc., 137, 136, 1990.

[23] D. Kohler, J. Zabasajja, A. Krishnagopalan, and B. J. Tatarchuk, J. Electrochem. Soc., 137, 1750, 1990.

[24] B. J. Tatarchuk, M. F. Rose, A. Krishnagopolan, and D. A. Kohler, U. S. Patent, No. 5,080,963, 1992.

[25] B. J. Tatarchuk, U. S. Patent, No. 5,096,663, 1992.

[26] B. J. Tatarchuk, M. F. Rose, and A. Krishnagopolan, U. S. Patent, No. 5,102,745, 1992.

[27] S. Ahn and B. J. Tatarchuk, J. Appl. Electrochem., 27, 9, 1997.

[28] Y. Hayakawa, A. Kawashima, H. Habazaki, K. Asami, and K. Hashimoto, J. Appl. Electrochem., 22, 1017, 1992.

[29] N. Alonso-Vante ,M. Giersig, and H. Tributsch, J. Electrochem. Soc., 138, 639, 1991.

[30] Alonso-Vante and H. Tributsch, in" Electrochemistry of Novel Materials, Vol. III (Edited by J. Lipkowski and P. Ross), VCH Publishers, Inc., p. 1, 1994.

[31] G. S. Kumar, M. Raja, and S. Parthasarathy, Electrochim. Acta, 40, 285, 1995.

[32] D. B. Zhou and H. V. Poorten, Electrochim. Acta, 40, 1819, 1995.

[33] M. Watanabe, H. Igarashi. and K. Yosioka, Electrochim. Acta, 40, 329, 1995.

[34] K. Kanamura, A. Tanaka, D. Gervasio, V. Kennedy, R. Adzic, E. B. Yeager, D. Burton, and R. Guneratne, J. Electrochem. Soc., 143, 2765, 1996.

[35] M. Razaq, A. Razaq, D. DesMarteau, S. Singh, and E. Yeager, J. Electrochem. Soc., 136, 385, 1989.

[36] V. H. Thomas and E. J. Rudd, in "Modern Chlor-Alkali Technology", Volume 2, (Edited by C. Jackson), E. Horwood, Chichester, p.168, 1983.

[37] F. Goodridge and K. Scott, "Electrochemical Process Engineering", pp.360-361, Plenum Press, New York, 1995.

[38] E. Brillas, R. Sauleda, and J. Casado, J. Electrochem. Soc., 144, 2374, 1997.

[39] W. Vogel, J. Lundquist, P. Ross and P. Stonehart, Electrochim. Acta, 20, 79, 1975.

[40] S. Shuldier, J. Electrochem. Soc., 107, 452, 1960.

[41] R. M. Q. Mello and E. A. Ticianelli, Electrochim. Acta, 42, 1031, 1997.

[42] G. Bronoel, E. Museux, G. Leclercq, L. Leclercq and N. Tassin, Electrochim. Acta, 36, 1543, 1991.

[43] V. Raman, Chem. and Ind., 771, 1997.

[44] S. C. Chang, J. R. Setter, and C. S. Cha, Talanta, 40, 461, 1993.

[45] V. A. Paganin, E. A. Ticianelli, and E. R. Gonzalez, J. Appl. Electrochem., 26, 297, 1996.

[46] N. Furuya and T. Sakakibara, J. Appl. Electrochem., 26, 58, 1996.

[47] N. Furuya and N. Mineo, J. Appl. Electrochem., 20, 475, 1990.

[48] N. Furuya and S. Motoo, J. Electroanal. Chem., 174, 297, 1984.

[49] S. Motoo, M. Watanabe, and N. Furuya, J. Electroanal. Chem., 160, 351, 1984.

[50] G. Faita, "Caustic Soda without Chlorine Production", Seventh Forum Proceedings, published by The Electrosynthesis Company, Inc., 1993.

[51] D. Pletcher, J. D. Genders, N. L. Weinberg, and E. F. Spiegel, "Electrochemical Methods for the Production of Alkali Metal Hydroxides without the Co-production of Chlorine", U. S. Patent No. 5,246,551, 1993.

[52] E. E. Kalu, R. E. White, and D. T. Hobbs, J. Electrochem. Soc., 143, 3094, 1996.

[53] S. C. Chang, J. R. Setter, and C. S. Cha, Talanta, 40, 461, 1993.

[54] S. M. Shibli and M. Noel, Int. J. Hydrogen Energy, 18, 141, 1993.

[55] Y. Hayakawa et al., J. Appl. Electrochem., 22, 1017, 1992.

[56] C. Fan, D. L. Piron, and M. Rojas, Int. J. Hydrogen Energy, 19, 29, 1994.

[57] O. Savadogo, New Mater. Fuel Cell Syst. I, Proc. Int. Symp., 1st, 212, 1995.

[58] E. J. Taylor, E. B. Anderson, and N. R. K. Vilambi, J. Electrochem. Soc., 139, L45, 1992.

[59] E. J. Taylor, E. B. Anderson, and N. R. K. Vilambi, U.S. Patent, No. 5,084,144, 1992.

[60] D. Gender, Watts News, 1, No.1, 1995.

[61] N. Furuya, T. Maeda, and A. Uchimura, The Electrochemical Society Meeting Abstracts, Vol. 96-1, p. 1188, Los Angeles, Calofornia, May 1996.

[62] The Southampton Electrochemistry Group, "Instrumental Methods in Electrochemistry", T. J. Kemp (Editor), Ellis Horwood Limited, New York, 1985.

[63] S. Ahn and B. J. Tatarchuk, J. Electrochem. Soc., 142, 4169, 1995.

[64] K. Kinoshita, "Electrochemical Oxygen Technology", John Wiley & Sons, Inc., New York, 1992.

[65] R. Holze and W. Vielstich, Electrochim. Acta, 29, 607, 1984.

[66] R. Holze and W. Vielstich, J. Electrochem. Soc., 131, 2298, 1984.

[67] I. Morcos and E. Yeager, Electrochim. Acta, 5, 953, 1970.

[68] R. M. Q. Mello and E. A. Ticianelli, Electrochim. Acta, 42, 1031, 1997.

[69] J. A. Harrison and Z. A. Khan, J. Electroanal. Chem., 30, 327, 1971.

[70] J. O'M Bockris and N. Reddy, "Modern Electrochemistry", Plenum Press, New York, 1970.

[71] B. E. Conway, "Theory and Principles of Electrode Processes", The Ronald Press Company, New York, 1965.

[72] S. Mukerjee and J. McBreen, J. Electrochem. Soc., 143, 2285, 1996.

Chapter 4. Chlorine Evolution

4.1. Introduction

Chlor-alkali production is the largest scale industrial inorganic electrosynthesis at a rate of 3.5~4.0x10^7 tons Cl_2 per year world-wide[1, 2]. The primary reactions in a chlor-alkali membrane cell are:

Anode: $2NaCl = Cl_2+2Na^++2e^-$ (4.1)

Cathode: $2H_2O+2e^- = H_2+2OH^-$ (4.2)

Membrane: $2Na^+(anolyte) = 2Na^+(catholyte)$ (4.3)

Overall reaction: $2NaCl+H_2O = Cl_2+H_2+2NaOH$ (4.4)

Under typical operating conditions the reversible potentials are, at the anode 1.247 V (versus reversible hydrogen electrode, RHE), at the cathode -0.797 V (vs. RHE), giving a total reversible cell voltage of 2.23 V [3]. At the very high current densities were used, i.e., 1 to 5 kAm^{-2}, one of the major issues confronting the chlor-alkali industry is the high power consumption, about 10^8 MWh of electricity per year [2]. This is becoming more significant in an environment of rising energy costs. It was estimated that the power consumption accounts for 35% to over 50% of the operating costs [4]. More recent estimations indicate that electrical energy is the major cost factor in production, typically up to 60-70% of plant running costs [5]. Significant improvement of the electrolytic process would be tremendously beneficial, both economically and environmentally and has stimulated extensive research works of the brine electrolysis process. The introduction of two technologies, i.e., substituting DSA anodes for graphite anode and replacing the traditional mercury and/or diaphragm cells with membrane cells, has revolutionized the chlor-alkali industry. It was reported [6] that a 1.07 V decrease in cell voltage, in mercury cells, resulted

when RuO_2-based anodes replaced graphite anodes at 10 kAm^{-2}. This cell voltage reduction is a result of

(i) the decrease of 0.1 V in overvoltage on going from graphite to RuO_2;

(ii) 0.2 V due to reduction in ohmic loss because anodes can be moved closer to the cathodes; and

(iii) 0.77 V related to gas bubble effects. This means that 90% of the total reduction in cell voltage is due to certain properties that may not be directly related to the electrocatalytic properties.

It is possible to reduce gas bubble effects further when the chlor-alkali cells are operated in centrifugal fields. In addition, the mass transport in the chlor-alkali cell will be enhanced in a high acceleration field. In other words, there is the opportunity for the use of high acceleration field to reduce power consumption through improved mass transport and reduced gas bubble effects. Furthermore, considering that the cells can run at a very high operating intensity, the plant modules will be severely reduced in size, thereby contributing to further reductions in plant system costs [7]. The idea was demonstrated by pioneering work at ICI with a rotating chlor-alkali membrane cell [7]. The present work has been done to continue the progress in development of chlor-alkali technology.

4.2. Literature Review

The progress in chlor-alkali technology has been reviewed extensively in literature[e.g. 2, 8-16], which will be briefly covered in this section with particular interest in electrodes, membrane and electrolytes. The only work in rotary chlor-alkali cells has been described in Chapter 1.

Mechanism and Kinetic Data - Chlorine evolution on RuO_2-based anodes has several possible mechanisms based on the following reaction [17-20]:

Discharge reaction	$Cl^- = Cl_{ad} + e^-$	(4.5)
Recombination reaction	$2Cl_{ad} = Cl_2$	(4.6)
Electrochemical desorption reaction	$Cl_{ad} + Cl^- = Cl_2 + e^-$	(4.7)

Industrial electrolysis is carried out in about 5 M NaCl solution at a pH of 2 and a temperature of 90°C. Plots of E (anode potential) versus logj (current density) with Tafel slopes of 30-40 mV/decade were observed in such solutions corresponding to intensive chlorine evolution (j>20 mA cm^{-2}) [2, 18-23]. The theoretical Tafel slopes are 30 and 40 mV/decade for DR, i.e., the mechanism consisted of the discharge and recombination reactions (rate determining step), and DE, i.e., the mechanism made upon of the discharge and the electrochemical desorption reactions (rate determining step) respectively. Thus, for chlorine evolution under the industrial electrolysis conditions with a Tafel slope of 30 or 40 mV/decade, DR or DE are accepted mechanisms [2, 16, 18-23].

The reported exchange current densities range from $10^{-6.3}$ (on a DSA anode in 3.0 M NaCl + 0.01 M HCl solution at 25°C [24]) to 10^{-4} (on a DSA anode in 4.3 M NaCl with pH=1.6 at 87°C [21]) mA cm^{-2}.

The DR mechanism requires a reaction order of 2 with respect to Cl^- and of 0 with respect to H^+ at concentrations of NaCl between 0.5 and 5.0 M at constant pH (0.01 M HCl) [25]. Reaction orders of 1 to 2 with respect to Cl^- for the DE mechanism was also reported [16, 19]. The experimental reaction order of 1.5 for Cl^- for chlorine evolution on RuO_2 anode, independent of composition, was explained in terms of specific chloride adsorption, i.e., the adsorbed negative charge retarding the

discharge of Cl^- ions [26]. A reaction order of 1 with respect to Cl^- for chlorine evolution on RuO_2 anode in 5 M NaCl + 0.01 M HCl at 25°C was also reported [27].

Anode - The anode plays a very important role in chlor-alkali cells. The selection of the anode material for chlor-alkali cells should take account of the corrosion environment in the anode chamber of chlor-alkali cells, the requirements of high efficiency and low energy consumption. A variety of metal/metal oxides have been examined as anode materials [10, 11, 28, 29], usually consisting of valve metals (e.g., Ti, Zr, Hf, Nb, Ta, W, Al, Bi), noble metals (e.g., Pt, Ir, Ru, Rh, Os, Pd, Au), and nonnoble metals (e.g., Cu, Ag, Fe, Co, Ni, Sn, Si, Pb, Sb, As, Cr, Mn). The patents that describe the composition of anodes containing these metals are summarized in [29].

Oxide-coated titanium anodes consisting of RuO_2 and TiO_2, usually with > 50% RuO_2 (registered trade name DSA for Dimensionally Stable Anode, Diamond Shamrock Technologies, S.A., Geneva, Switzerland), have great advantages over other anode materials. They are recognized as the best anodes for Cl_2 evolution for two reasons:

(i) excellent catalytic activity for Cl_2 evolution reaction. The lower overpotential for Cl_2 evolution on DSA compared to carbon has enabled the cell voltage reductions of the order of 0.5 V. So these anodes possess very low operating voltage, acceptable efficiency and cost.

(ii) excellent stability in very strong corrosive environment. They do not undergo passivation and detectable dissolution phenomena so that overvoltage may be kept constant over long periods of operation. Also, they are not wetted by Cl_2 gas so that wear and gas bubble effects are minimised [6, 29, 30].

RuO_2-based anodes have replaced graphite as the preferred material for anodes in chlor-alkali cells, which has led to a reduction of the energy consumption by 10-15%

[2]. For example, in the early of 1980s, about 60% of the world production of Cl_2 (36 ktons/day) used metal anodes of the DSA type. It was estimated that the use of the DSA electrodes in USA and Canada resulted in energy savings of 3.2 billion kWh during the year 1977 [31].

About 30 to 40 mol % of RuO_2 seems to be a critical composition for RuO_2-TiO_2 mixed oxide films. For lower RuO_2 content the performance of the electrodes deteriorates [32, 33]. The titanium support is also very important to obtain the rutile structure of such electrodes [34].

Other metal oxides, such as Pt-Ir coated on Ti [35, 36], cobalt spinel coatings [37], and PdO [38], have also been evaluated as alternatives to RuO_2-TiO_2 coatings for high performance anodes in chlor-alkali cells.

Cathode - With the tremendous development in the anode and separator technologies, the cathode is one of the last remaining areas for significant cell voltage improvement [39].

Industrial cathodes, such as mild steel and nickel plate cathodes, have significant overpotentials for hydrogen evolution. They have been gradually replaced by precious-metal/Ni or high area nickel cathodes. The overpotentials for hydrogen evolution using these cathodes are as low as 50 mV, which gave about 10% energy saving [2].

Catalysed with Pt, Pd, Ru, Ir, Rh, or Os show good performance in minimizing overpotential losses. To fully utilise the chlor-alkali cells, they should be operated at increasingly high current densities. This led to side effect, such as increased rate of heat evolution in the cells due to ohmic resistance and overpotential losses.

Catalysed cathodes not only increase cell efficiency but minimise heat evolved as a by-product of the electrolysis process [39].

Membranes - Membrane-cell technology, almost unknown in 1970, has advanced rapidly. It was responsible for about 10% of the total world production in 1987 and was considered as the dominant technology within the chlor-alkali industry by the year of 2000 [2]. In addition to other advantages, such as high purity products, easier operation, and elimination of environmental problems, the membrane cell has more compact cell room design and therefore very low total energy consumption [40], e.g., 2770 kWh/MT Cl_2, which is much lower than that in diaghragm cell (3638 kWh/MT Cl_2) [8]. Energy savings in membrane cells will be achieved by addressing the cathode overpotential, the membrane voltage, electrolyte ohmic losses and structural ohmic losses. The power consumption for the ion exchange membrane cells of Asahi Chemical is quoted at approximately 2200 kWh/t NaOH at a current efficiency of 95% and a current density of 4 kAm^{-2} [41].

Electrolytes - It is well known that the low oxygen polarisation of metal oxide electrodes in chlor-alkali cells reduces the current efficiency for Cl_2 generation as a result of parasitic generation of oxygen. Oxygen generation can be minimized when chlor-alkali cells operate with concentrated NaCl solutions. For example, the current efficiency of a RuO_2-TiO_2 anode (Ru/Ti mole ratio = 0.5) for Cl_2 evolution was reported to be higher than 99% in 4 M NaCl, 97% in 1 M NaCl, and 92% in 0.4 M NaCl solutions [42, 43]. In more dilute solution, at stationary electrodes, the current efficiency for Cl_2 evolution may decrease at higher currents because chloride ion discharge produces chloride depletion at the electrodes, thus favoring O_2 production. Also, as such electrodes are sensitive to O_2 evolution, their stability is

thus reported to decrease as the chloride ion concentration decreases as a result of a decreased current efficiency[39, 44, 45].

Using acidified brine solutions is another way to improve the performance of chlor-alkali cells. In industrial operation, hydrochloric acid is added to the feed brine to improve chlorine purity by reducing oxygen discharge at the anode. The oxygen levels declined from around 1.5%, a typical level in commercial chlorine plants operated at high current efficiency, to well below 1% by hydrochloric acid addition [46]. In acidified 3 M NaCl solution of pH 1, the current efficiency is >98% over a wide range of current densities 20 to 150 $mAcm^{-2}$. In dilute, acidified NaCl solutions, polarisation curves for both the chlorine and oxygen evolution reactions, as well as the overall polarisation curve in 0.5 M NaCl of pH 1 at 70°C were obtained. The results show that the Tafel slope for oxygen evolution is higher than that of the chlorine reaction, especially at low current densities. Consequently, the current efficiency increases with an increase in current density and stays at a level about 90% for 1 M and 2 M NaCl solutions [46]. However, in dilute acidified 0.5 M NaCl solution of pH 1, a current efficiency of <80% was obtained at low current densities.

4.3. Design Of The Rotary Chlor-Alkali Cell

This section describes the design and fabrication of the rotary chlor-alkali cell.

The Cell Design - The designed rotary chlor-alkali cell was presented in Chapter 2. The basic design criteria are to fabricate a membrane cell which can be conveniently operated in the centrifuge (could be simply assembled or dismantled) and combine the need for a low energy consumption unit with low cost. Thus, a two compartment "zero-gap" ion-exchange membrane cell of 50 ml capacity was designed and used for most measurements. The anode and cathode were separated by a Nafion-117 ion-

exchange membrane (Aldrich) and sandwiched between two polypropylene cell bodies, which were joined by bolting. A pair of rubber gaskets was used to avoid liquid leaking.

Anode - The anodes used in this work were one of the the following materials: nickel foam (60 pores per inch, 6 cm^2), carbon cloth (3 cm^2, GC-14, E-Tek Inc.), carbon fiber paper (6 cm^2, PC 206, Stackpole) with a thickness of 0.5 mm, carbon fiber felt (8 cm^2, SPC 7011, SIGRATEX Carbon Group) with a thickness of 8 mm, platinum/titanium mesh (6 cm^2), TYSAR™ EP mesh (The Electrosynthesis Co., Inc., USA; designated as TYSAR), commercial dimensionally stable mesh anode (2 cm^2, consists of thin metal rods) with a thickness of about 0.5 mm (designated as DSA thereafter). The "anode area" used to calculate the current density is the overall anode area projected onto the membrane.

The RuO_2-TiO_2/Ti mesh anode was prepared according to published methods [47, 48]. Ti mesh, pretreated by mechanical and chemical methods, was painted with a solution of $RuCl_3$ and $Ti(OC_4H_9)$ in n-butyl alcohol containing a few drops of 20% HCl. The typical catalyst loading of the Ru component was 2 $mgcm^{-2}$. After drying below 100°C and heating at 450°C for 10 minutes, the coated Ti mesh was painted again, and the procedure was repeated until the desired catalyst loading was achieved. The final annealing treatment was carried out at 450°C for 1 hour.

Considerable difficulty was experienced in finding a suitable current feeder material for the anode which would work in a strong corrosive environment. Stainless steel mesh was chosen first. It was difficult to give reproducible results and even dissolved in the anolyte. As platinized titanium mesh anode only gave low current density for the chlorine evolution reaction, i.e., very low background current was

produced when using this material as a current collector, and to date no evidence of surface corrosion, under the experimental conditions, was found, it was therefore used as the current collector.

Cathode - Nickel foam, stainless steel mesh, and TYSAR platinised mesh were tested as the cathodes of the rotary chlor-alkali cell.

Electrolytes - Most experiments used NaCl solutions as the electrolytes. For comparison purpose, the acidified NaCl anolytes and the NaOH catholytes were using for several runs.

4.4. Polarisation Behaviour In the Static Cell

This section highlights the polarisation characteristics of the rotary cell operated in a static mode.

4.4.1. Anode

Tafel Plots and Reaction Order - Figure 4.1 displays typical steady-state Tafel plots for the chlorine evolution in different NaCl solutions.

The Tafel slope obtained at a overpotential range of 0.02 to 0.06 V from figure 4.1 is 36 mV/decade for all solutions. The exchange current densities are $10^{-3.35}$, $10^{-3.45}$, $10^{-3.60}$, and $10^{-3.80}$ A cm^{-2} for the 6.2, 4.5, 1, and 0.5 M NaCl respectively. These data qualitatively agree with the literature data, which are 35 to 40 mV/decade and $10^{-4.20}$ to $10^{-3.30}$ Acm^{-2} in a about 5 M NaCl solution at a pH of 2 and a temperature of 90°C [21, 22, 49, 50]. These data show that the concentration affect the Tafel parameters.

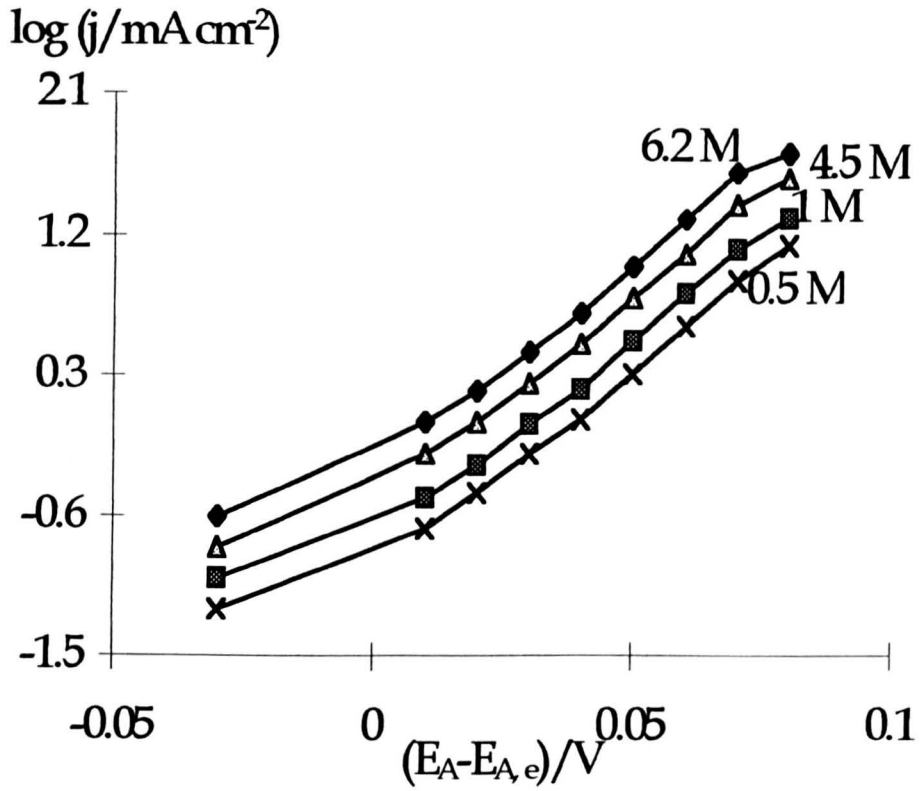

Figure 4.1. Tafel plots for chlorine evolution reaction on DSA anode - Concentration effect. Cathode: Pt/Ti mesh (2 mg Pt cm^{-2}); Electrolyte: NaCl solutions; Temperature: 80°C; The rotary cell (static mode).

Figure 4.2 shows the dependence of the reaction rate at constant potentials on the chloride ion concentration. The order of reaction with respect to Cl^- determined at a constant potential, as resulting from the linear section of the logj vs. $\log C_{NaCl}$ (C_{NaCl} in mol dm^{-3}) curves (figure 4.2) is about 1.2. the reported reaction order are 1.5 with respect to Cl^- in 0.5 to 5.0 M NaCl solutions at 90°C [25] and 1 in 5 M NaCl + 0.01 M HCl at 25°C [27].

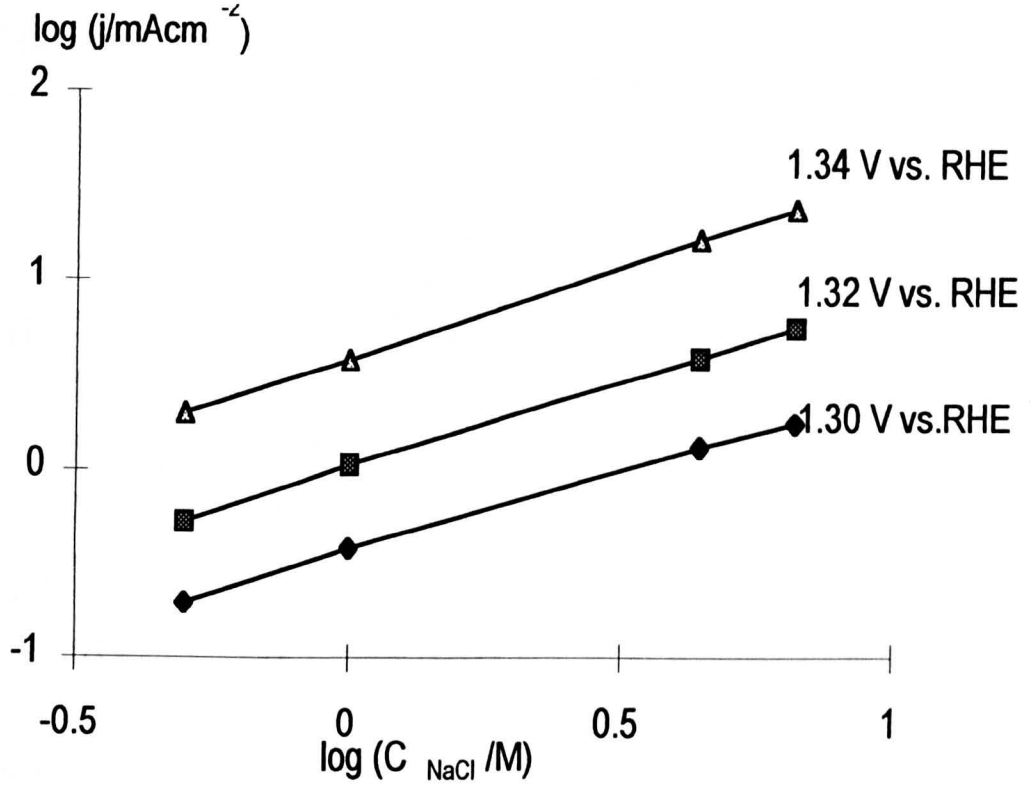

Figure 4.2. Reaction rate for chlorine evolution on DSA anode at variable Cl^- concentration (in mol dm^{-3}) solutions. Cathode: Pt/Ti mesh (2 mg Pt cm^{-2}); Electrolyte: NaCl solutions; Temperature: 80°C; The rotary cell (static mode).

The cell temperature had a large influence on the Tafel intercepts, as shown in figure 4.3. The Tafel slope obtained from figure 4.3 is about 36 mV/decade at the three temperatures and exchange current densities are $10^{-3.35}$, $10^{-3.55}$, and $10^{-4.0}$ A cm^{-2} at 80, 50, and 25°C respectively. These data also qualitatively agree with the literature data which are about 36 mV/decade and $10^{-4.2}$ A cm^{-2} at 80°C [21, 22, 50]; 31 mV/decade and 10^{-5} A cm^{-2} at 25°C [25, 26, 50].

It is worthwhile to note that, during the anodic polarisation of all electrodes used here in NaCl solutions, two major processes take place: (i) chlorine evolution reactions; (ii) oxygen evolution reactions. The latter and/or other side reactions, if had, only occupy a very small proportion of the total current, especially at high current densities and in concentrated NaCl solutions [42, 44, 45]. Therefore, the effect of O_2 evolution and other possible reactions on the polarisation curves is assumed negligible.

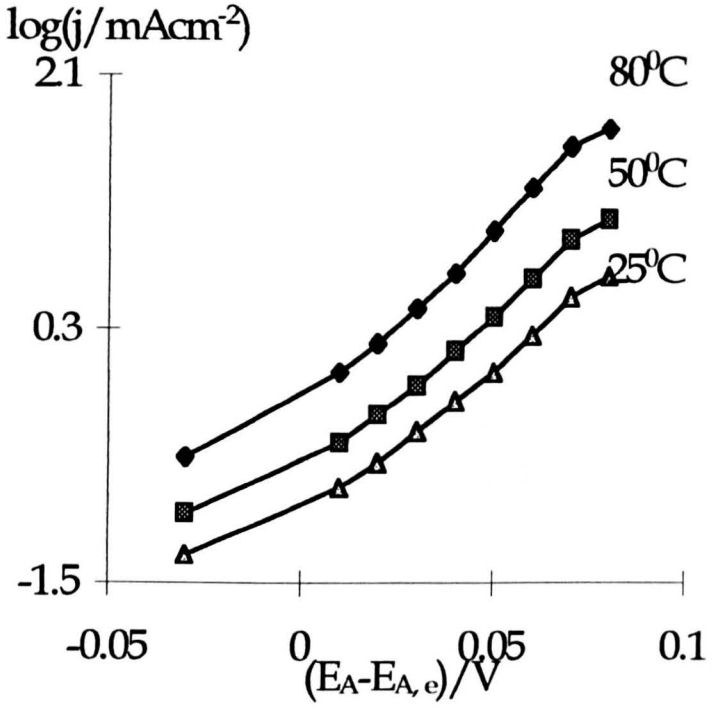

Figure 4.3. Tafel plots for chlorine evolution reaction on DSA anode - Temperature effect. Cathode: Pt/Ti mesh (2 mg Pt cm^{-2}); Electrolyte: 6.2 M NaCl solutions; The rotary cell (static mode).

Anode Material - The anode in chlor-alkali cells should preferentially evolve chlorine at low overpotential and not support the oxidation of water to oxygen. Figure 4.4 shows polarisation curves obtained at different anodes.

Anode material affects the anodic polarisation behaviour obviously. For example, in 6.2 M NaCl solution at 80°C, the current density is 224, 218 and 49 mA cm^{-2} at an anode potential of 2.2 V vs RHE for the RuO_2/Ti mesh, commercial DSA and carbon paper anode respectively. The TYSAR foam, carbon cloth and Pt/Ti anode gave 36, 21 and 3 mA cm^{-2} at an anode potential of 2.7 V vs RHE respectively. The data gave the following order about the effectiveness of the anodes for the chlorine evolution:

Pt/Ti expanded metal < Carbon cloth < TYSAR mesh

< Carbon paper < Commercial DSA < RuO_2/Ti mesh

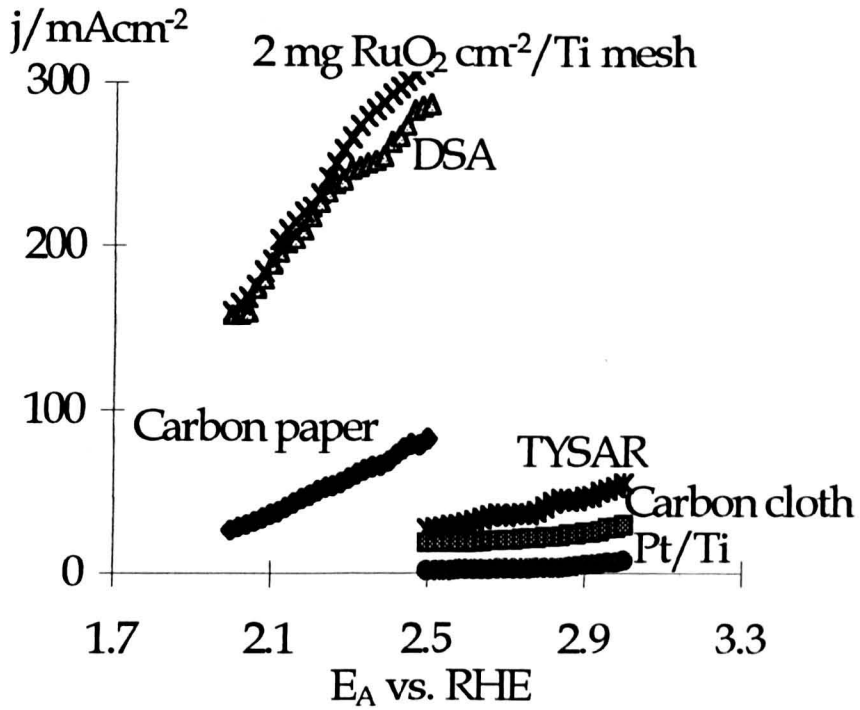

Figure 4.4. Anode polarisation curves for Cl_2 evolution reaction. Cathode: Pt/Ti mesh (2 mg Pt cm^{-2}); Electrolyte: 6.2 M NaCl solution; Scan rate: 5 mV/s; Temperature: 80°C; The rotary cell (static mode).

From these results, two factors emerge immediately: (i) The most important quality as an anode is the effectiveness for Cl_2 evolution reaction. RuO_2/Ti mesh anodes and commercial DSA anodes display excellent Cl_2 evolution behaviour; (ii) Effective surface area is a major factor in determining the electrode catalytic activity and therefore the operating efficiency for the same material. Among the anodes made up of the same material and with same geometric surface area, the anode with high specific surface area gives better performance. For example, carbon paper is better than carbon cloth; TYSAR is better than Pt/Ti expanded metal; and RuO_2/Ti mesh is better than commecial DSA.

Catalyst Loading - Figure 4.5 exhibits the effect of catalyst loading on the anode polarisation behaviour. It is seen that there is an increase in current density from 1 to 3.35 kA m^{-2} with increasing catalyst loading from 1 to 5 mg Ru cm^{-2}. Above this

value, no significant improvement is seen with a greater loading of the catalyst (Figure 4.5).

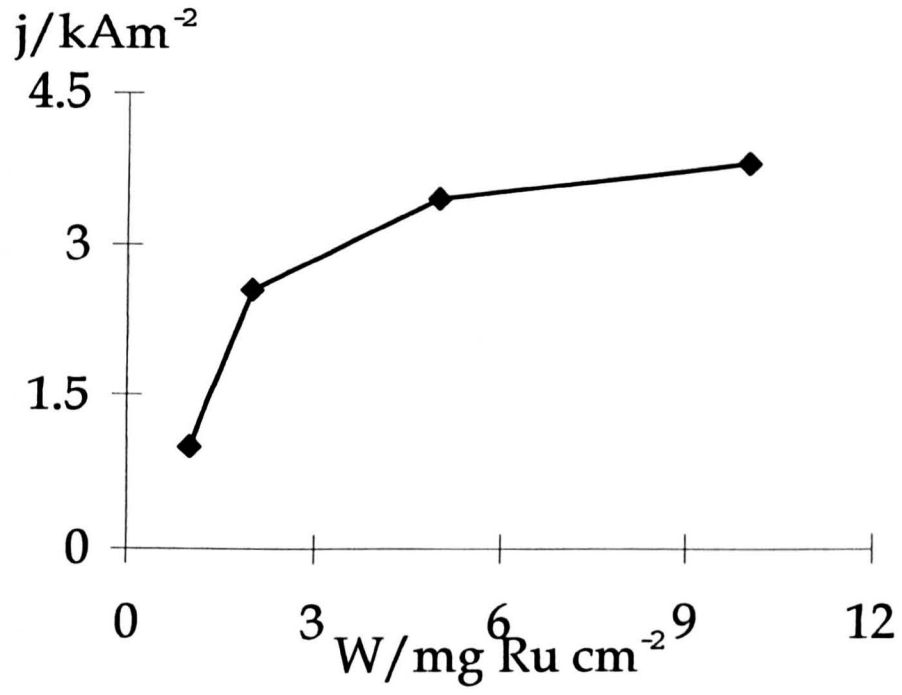

Figure 4.5. Anode current density as a function of catalyst loading for Cl_2 evolution reaction. Anode potential: 1.5 V vs. RHE; Anode substrate: Ti mesh; Cathode: Pt/Ti mesh (2 mg Pt cm^{-2}); Electrolyte: 6.2 M NaCl solutions; Scan rate: 5 mV/s; Temperature: 80°C; The rotary cell (static mode).

The performance improvement using multi-layer anodes is not as significant as expected. For instance, in a static cell using the anode with 2 mg Ru m^{-2}, at 1.5 V vs. RHE, the increase in current density was small from one layer to double layers (2.08 to 2.85 kAm^{-2}) and even lower for a further increase in the anode layer (only 0.3 kA m^{-2}). The average rate of increasing current density for the single layer anode is about 0.54 kAm^{-2}/mg Ru cm^{-2}, which is greater than that achieved (0.15 kAm^{-2}/mg Ru cm^{-2}) for the three layer anode, between the catalyst loading of 1 and 5 mg Ru cm^{-2}. It is clearly that better catalyst utilisation is realised using a single layer electrode with moderate catalyst loading. The possible explanation can be reached from three

aspects. Firstly, the diffusion path length within the anode of the cell was increased by using the multi-layer anodes due to increased anode thickness and decreased porosity due to blocking the mesh holes. Thus the rate of transport of chloride ions to the electrode may be insufficient to sustain the high cell current by discharge of chloride ions to produce chlorine, minimising co-evolution of oxygen. Secondly, the true surface area of catalysed anode can not be proportional to increasing the anode layers due to blocking the catalyst active sites during using the multi-layer electrodes. Finally, poor current distribution and resisitivity may be problems for the multi-layer electrodes. Even for compact films, which exhibit resisitivities of the order of 10^{-4} ohm cm^2, the resistance may amount to 0.1 ohm cm^2 with a 10 μm thickness. This value would not be negligible at very high current densities. Theoretical calculation [49] and the industrial cell performance [51, 52] show the close relationship between the polarisation curves and the ohmic resistances, especially at high cell voltage or high cell current, e.g., when cell ohmic resistance increases from 2.1×10^{-4} to 4.1×10^{-4} ohm cm^2, the cell current density decreases from 1.5 to 0.85 kAm^{-2} at a cell voltage of 3 V; the value drastically decreases from about 8 to 4.1 kAm^{-2} at 4.5 V [53]. It is thus seen the significant effect of cell ohmic resistances on the cell polarisation behaviour. For a membrane gap cell, it was reported that a significant portion of the electrolysis occurs at the inner walls and back of the electrode structure [54].

4.4.2. Cathode

Figure 4.6 shows effect of the cathode on the chlor-alkali cell performance.

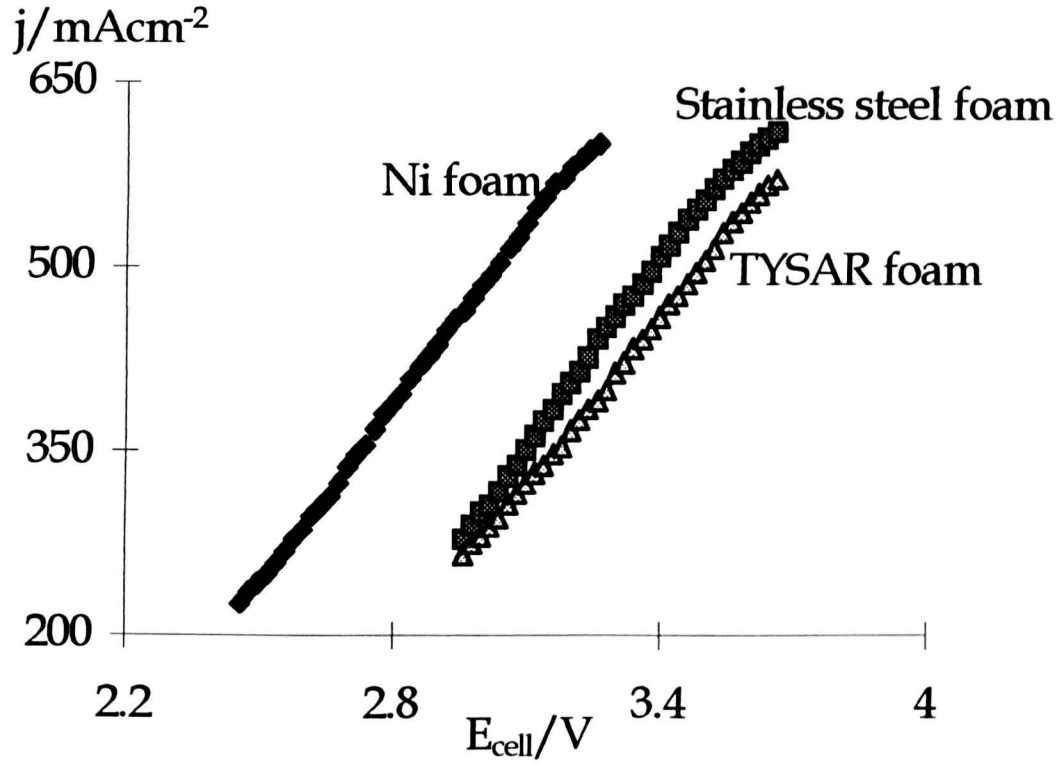

Figure 4.6. Cell voltage against current density curves for Cl_2 evolution reaction in a cell with different cathodes. Anode: DSA; Electrolyte: 6.2 M NaCl solution; Scan rate: 5 mV/s; Temperature: 80°C; The rotary cell (static mode).

Nickel foam cathode is better than stainless steel foam and TYSAR foam cathodes for the cell performance, as shown in figure 4.6. For example, at a current density of 400 mA cm^{-2} the cell voltage are 2.82, 3.18 and 3.28 V for the Ni foam, stainless steel and TYSAR cathode respectively.

4.4.3. Effect of Electrolyte

NaCl Concentration - Figure 4.7 records the anode polarisation curves as a function of NaCl concentration.

The anode potential decreases rapidly at a fixed current density, e.g., about 3.81, 2.92, 2.54, and 2.16 V at 3 kAm^{-2} for 0.1, 1, 4.5, and 6.2 M NaCl solutions, respectively. At about 3.1 V vs. RHE, a current plateau appeared in 0.1 M NaCl solution, indicating mass transport limitating conditions. Much better performance

in the concentrated NaCl solutions was observed. Evidently, concentrated electrolyte should be utilized in chlor-alkali cells in order to maximise operating current density at low cell voltage and/or low anode potential.

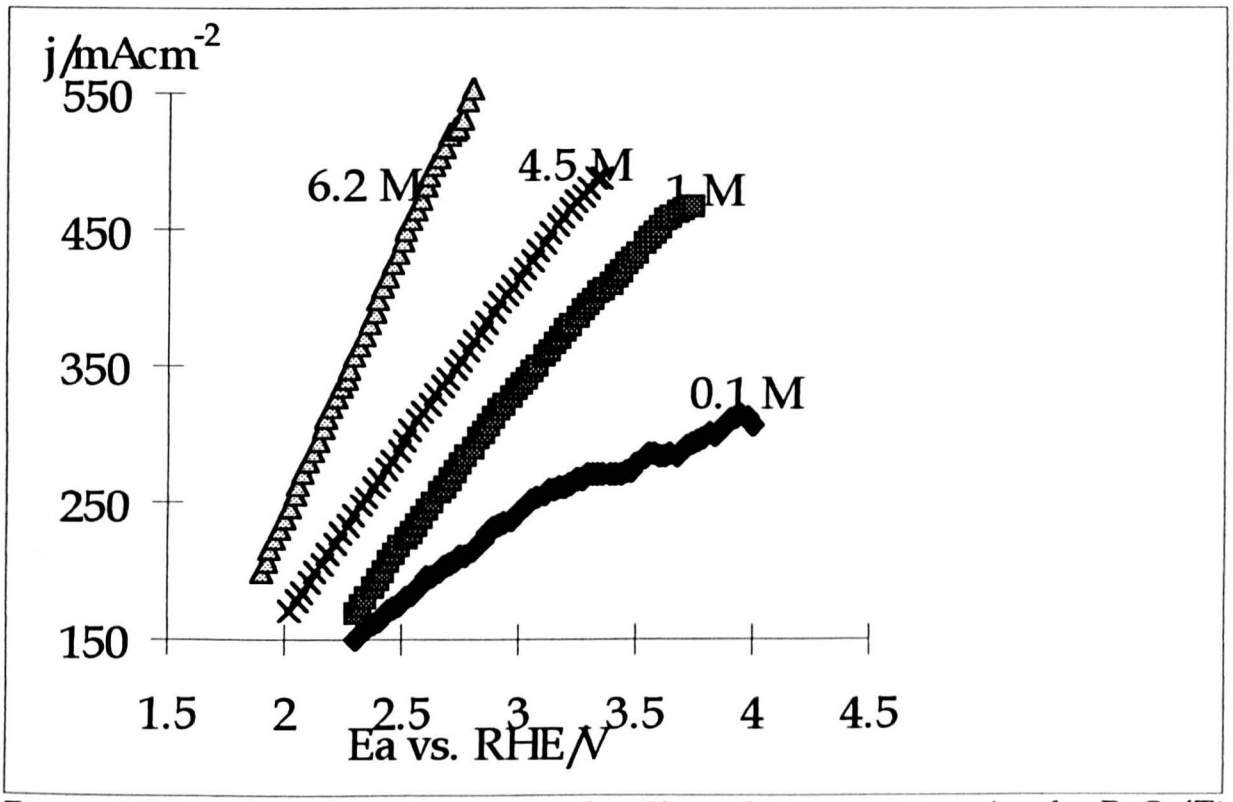

Figure 4.7. Anode polarisation curves for Cl_2 evolution reaction. Anode: RuO_2/Ti mesh (2 mg Ru cm^{-2}); Cathode: Pt/Ti mesh (2 mg Pt cm^{-2}); Electrolyte: NaCl solutions concentration: indicated above the curves); Scan rate: 5 mV/s; Temperature: 80°C; The rotary cell (static mode).

Electrolyte Type - As mentioned above, in industrial operation, hydrochloric acid is added to the feed brine to improve chlorine purity by reducing oxygen discharge at the anode. In a slightly acid solution, the hydrolysis of the chlorine to hypochlorite can be prevented. This also reduces the oxygen evolved in competing water oxidation at the anode and accelerate the anodic process. Chronoamperograms obtained at a RuO_2/Ti mesh anode in 0.5 M HCl+6.2 M NaCl solution are shown in figure 4.8. A curve for 6.2 M NaCl solution is also presented for comparison.

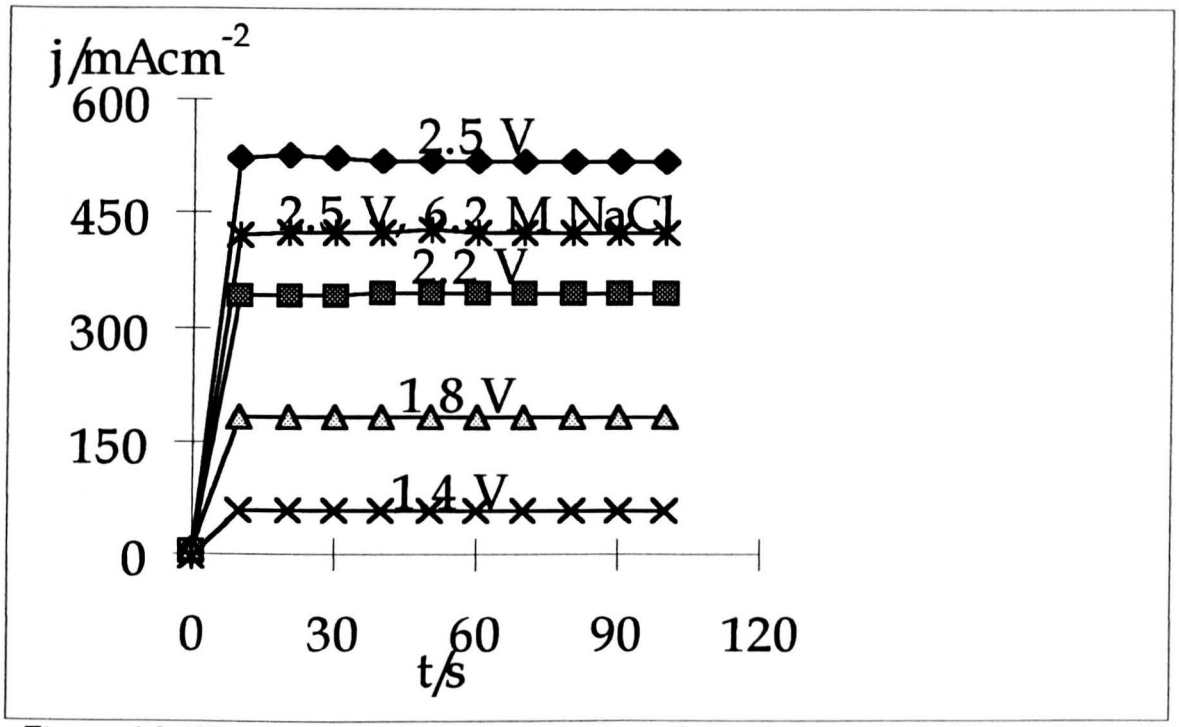

Figure 4.8. Chronoamperometric curves for Cl_2 evolution reaction. Anode: RuO_2/Ti mesh (2 mg Ru cm^{-2}); Cathode: Pt/Ti mesh (2 mg Pt cm^{-2}); Anolyte: 0.5 M HCl+saturated NaCl solution; Catholyte: 10% NaOH solution; Scan rate: 5 mV/s; Temperature: 80°C; The rotary cell (static mode).

It can be seen that the current density at 2.5 V vs. RHE is about 1 kAm^{-2} higher with the acidified anolyte rather than the 6.2 M NaCl solution.

4.4.4. Temperature

Electrochemical measurements were carried out at varying cell temperatures from 25 to 80°C. Representative data about temperature effect, are given in the steady-state polarisation curves (figure 4.9), obtained using the chronoamperograms of figure 4.8. A systematic increase in the current density at a constant anode potential with temperature was noted in figure 4.9. The best performance was achieved at 80°C which is the typical chlor-alkali plant operating temperature.

It was well known that an increase in the electrolyte temperature to about 70°C results in faster reaction kinetics for Cl_2 evolution reaction. The reaction proceeds at a much higher rate when the temperature is increased, due to an increase in the

reaction and/or mass transfer rate. The results obtained here about temperature effect confirm the faster rate of chlorine evolution due to increase the temperature.

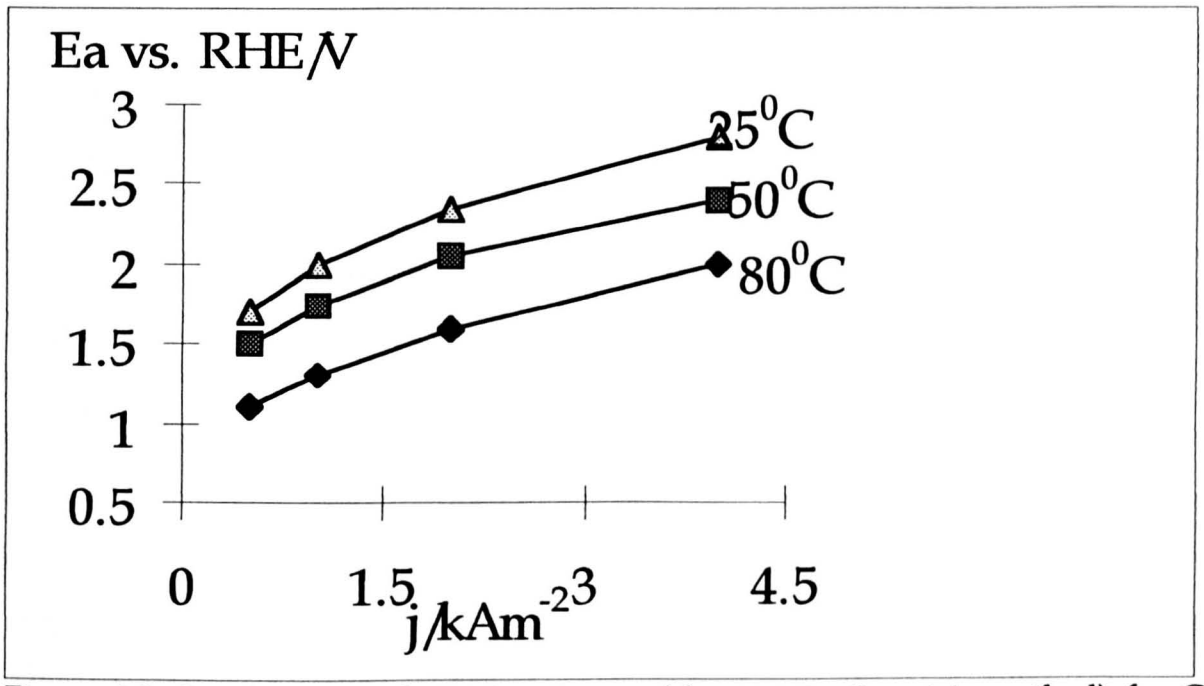

Figure 4.9. Steady-state polarisation curves (chronopotentiometric method) for Cl_2 evolution reaction. Anode: RuO_2/Ti mesh (2 mg Ru cm^{-2}); Cathode: Pt/Ti mesh (2 mg Pt cm^{-2}); Electrolyte: 6.2 M NaCl solution; Scan rate: 5 mV/s; Temperature: as shown above the curves; The rotary cell (static mode).

4.5. Electrochemical Characteristics In The Rotary Cell

As stated above, the chlor-alkali process is energy-intensive and should be intensified to reduce the energy consumption. Low power consumption is determined by the current efficiency and the cell voltage. Centrifugal acceleration field provides a means to minimise cell voltage and increse current efficiency.

The energy consumption of chlor-alkali industry were reduced drastically through the introduction of membrane cells. However, even in ordinary membrane cell, it was found that a realistic linear velocity cannot remove gas from the perfluorocarbon membrane surface [55]. One of major effects of this is that the cell

voltage increases only about 0.04 V when the linear velocity of electrolyte changes from 5 up to 20 cm/sec [55], as shown in figure 4.10.

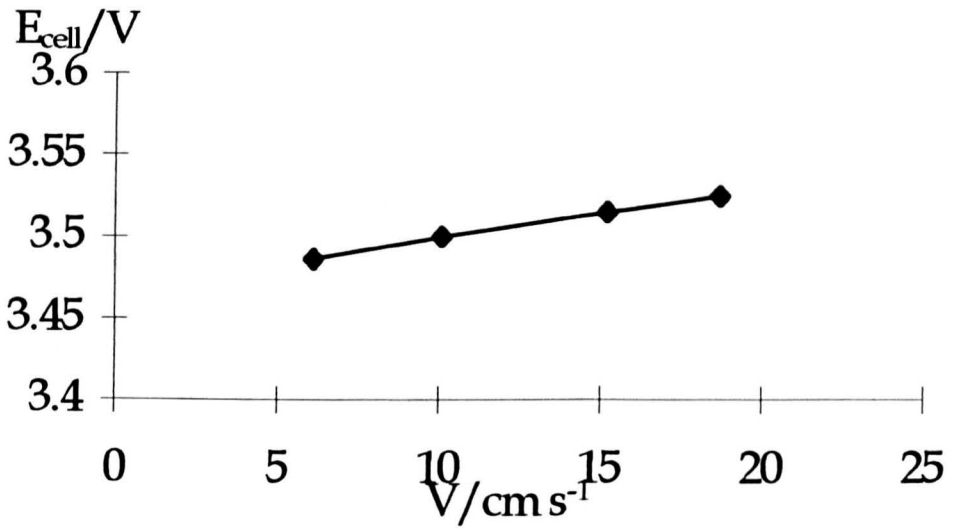

Figure 4.10. Dependence of chlor-alkali cell voltage on electrolyte linear velocity (from [55]).

Obviously, only an increase of the flow rate could not overcome mass transport limitation. On the other hand, putting the cell into a centrifugal field provides an effective way to intensify chlor-alkali process. The work presented here was therefore carried out based on these considerations and the early promising work in rotary chlor-alkali cell.

4.5.1. Cell Voltage

Cell Polarisation Curves - Figure 4.11 shows a representative comparison of the voltammetric responses of the rotary cells at various rotating speeds. The cell polarisation behaviour changed rapidly in centrifugal fields. All polarisation curves obtained in centrifugal fields were moved to lower cell voltages. For example, at a current density of 4 kAm^{-2}, the cell voltage decreased from 3.2 V at the static cell to 2.81, 2.68, and 2.63 V at 400, 800, and 1100 rpm, respectively.

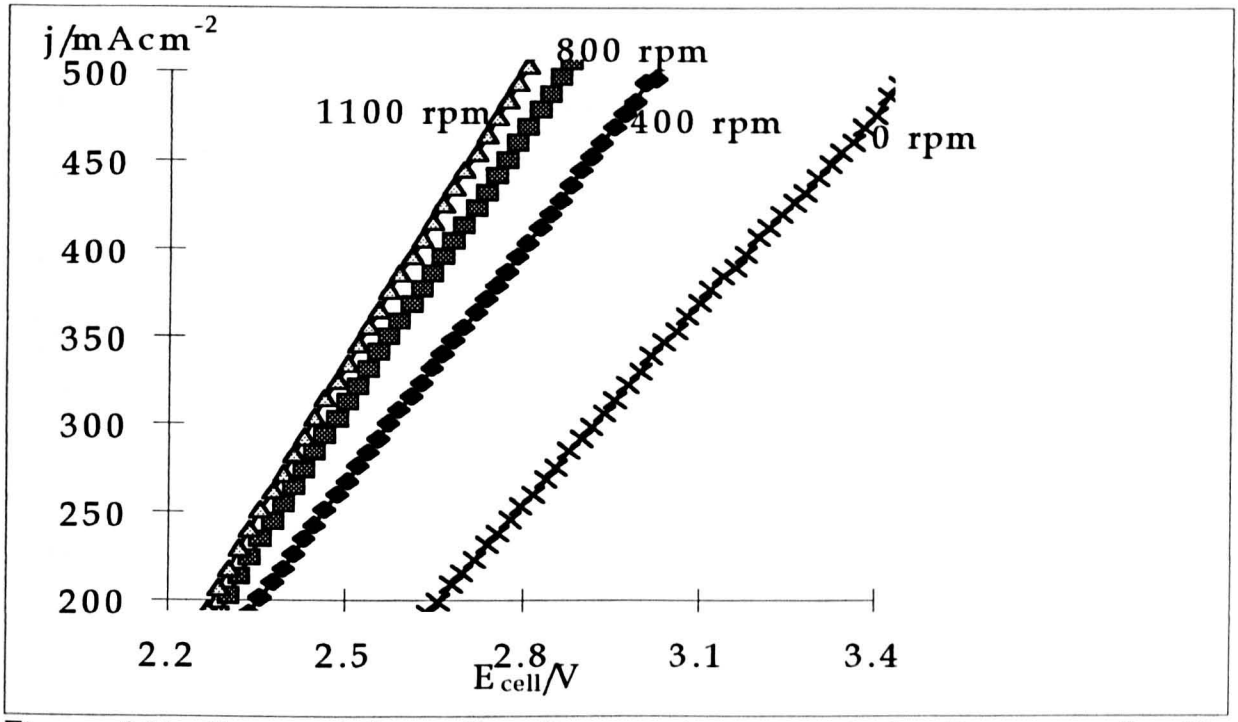

Figure 4.11. Representative cell voltage against current density curves for Cl_2 evolution reaction in centrifugal fields. Rotating speed: Indicated above the curves; Anode: RuO_2/Ti mesh (2 mg Ru cm^{-2}); Cathode: Pt/Ti mesh (2 mg Pt cm^{-2}); Anolyte: 0.5 M HCl+saturated NaCl solution; Catholyte: 10% NaOH solution; Scan rate: 5 mV/s; Temperature: 80°C; The rotary cell.

Cell Voltage Reduction - The pronounced dependence of the cell voltage reduction on rotating speed, which directly reflects the effect of centrifugal fields, is shown in figure 4.12. It was strongly related to NaCl concentration and temperature (figures 4.12 and 4.13). The cell voltage reduction increased with increasing rotating speed at all tested temperatures, as shown in figure 4.12.

Typical chlor-alkali plant operates at between 80 and 90°C. It was reported that the membrane cell voltage decreased 50 to 100 mV with each ten-degree increase in temperature, while no effect on current efficiency was observed [46]. In commercial static cells, the high temperature operation can generate internal forces beyond the interlayer bond of the polymer membrane and separate the two polymer layers, which are intimately bonded in the manufacturing process, and thereby forming

blisters. This will increase electrical resistance and distribute more current to unblistered areas [46]. At higher temperatures, the gas bubbles produced on the electrode surfaces are more easily removed than at lower temperatures, which leads more pronounced effect.

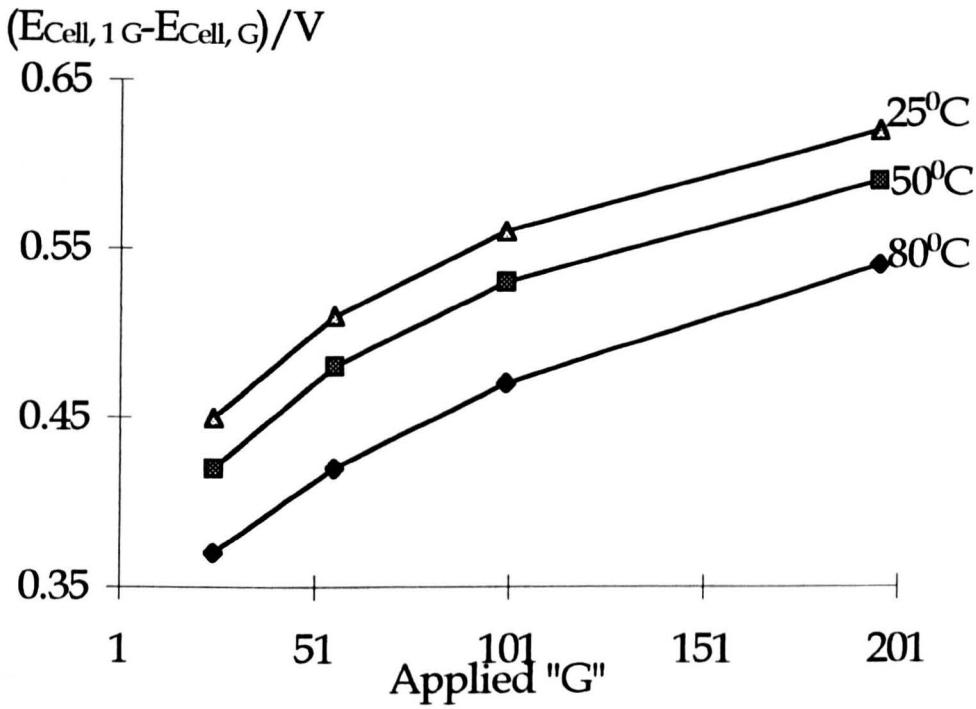

Figure 4.12. Cell voltage reduction against applied "G" curves for Cl_2 evolution. Current density: 4 kAm^{-2}; Anode: RuO_2 /Ti mesh (2 mg Ru cm^{-2}); Cathode: Pt/Ti mesh (2 mg Pt cm^{-2}); Anolyte: 0.5 M HCl+saturated NaCl solution; Catholyte: 10% NaOH solution; Scan rate: 5 mV/s; The rotary cell.

The concentration of NaCl has a significant effect on the polarisation behaviour, as presented in figure 4.13. At a fixed current density, cell voltage decreases with the increase of NaCl concentration.

It is noteworthy that a more significant cell voltage reduction was achieved in the dilute than concentrated solutions at higher operating current densities. The cause appears to be that centrifugal acceleration field promotes mass transport as well as the disengagement of gas bubbles from the electrode surface. Both functions of

centrifugal fields enhance the cell process and therefore greater intensification for the process can be expected in the dilute solutons. Of course, in industry, concentrated solution is used to minimise the cell voltage.

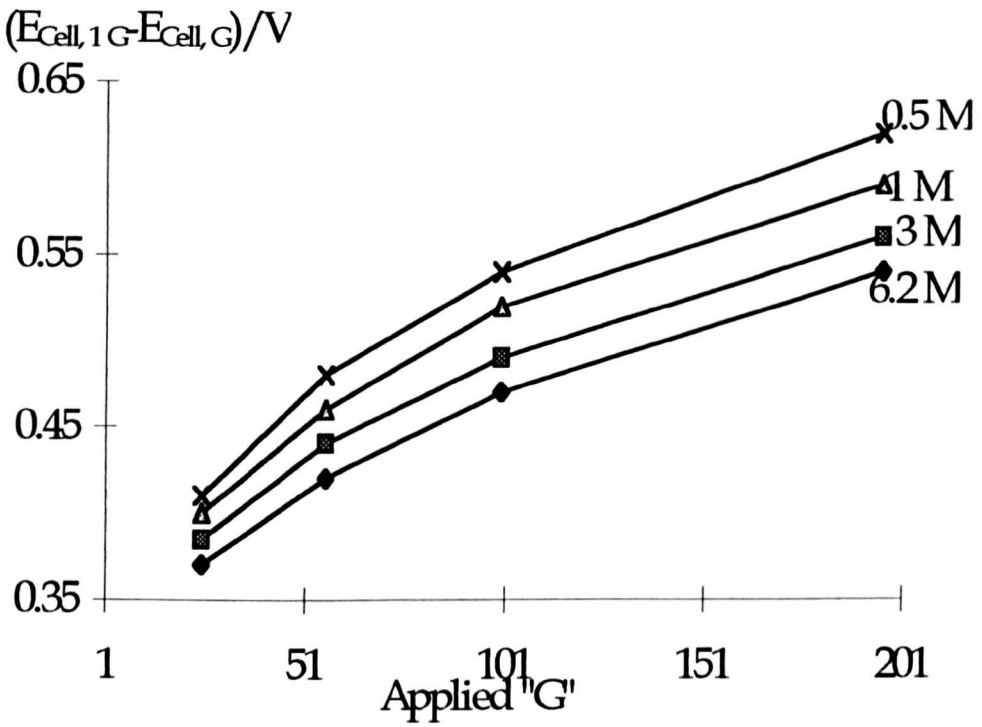

Figure 4.13. Cell voltage reduction against applied "G" curves for Cl_2 evolution. Current density: 4 kAm^{-2}; Anode: RuO_2/Ti mesh (2 mg Ru cm^{-2}); Cathode: Pt/Ti mesh (2 mg Pt cm^{-2}); Electrolyte: NaCl solution (concentration: indicated above the curves); Scan rate: 5 mV/s; Temperature: 80^0C; The rotary cell.

The reduction in cell voltage in centrifugal acceleration field can lead the major savings in power consumption. This reduction comes mainly from the anodic behaviour, which is discussed below.

4.5.2. Anode Potential

Anode Polarisation Curves - Anode potential changes radically with rotating speed at a constant current density, as shown in figure 4.14.

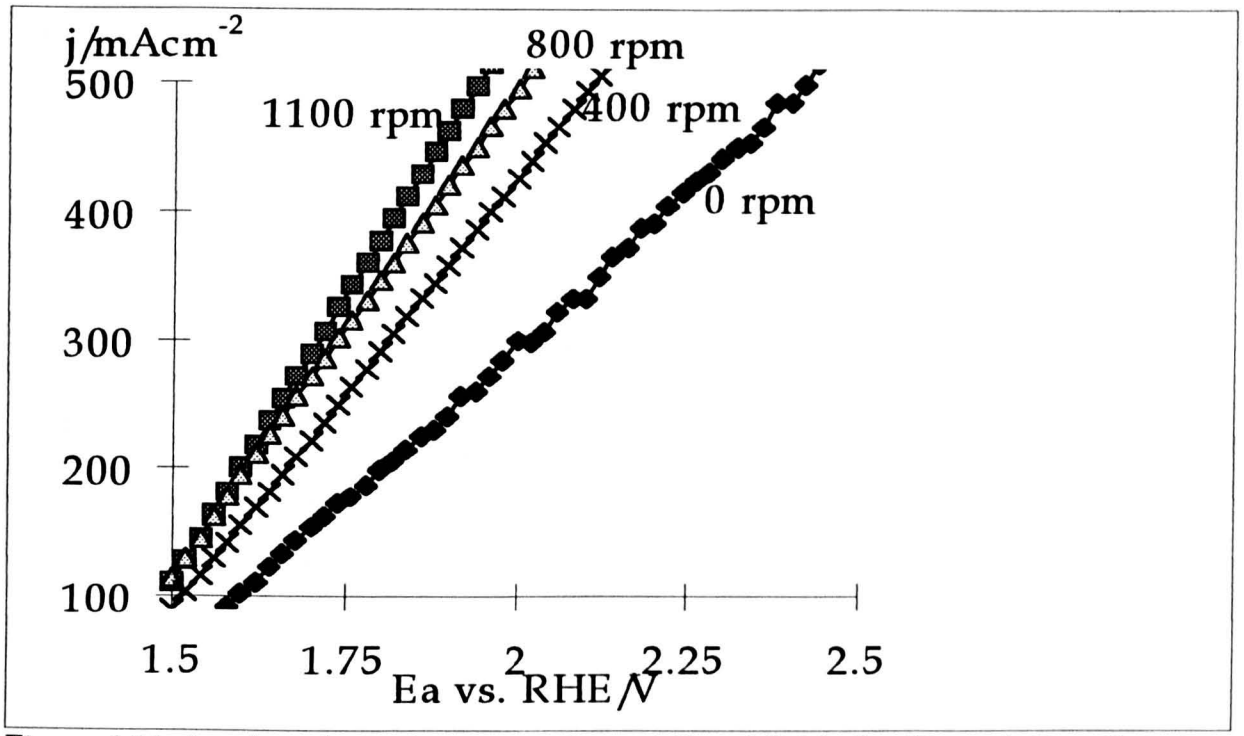

Figure 4.14. Anode polarisation curves in centrifugal fields for Cl_2 evolution. Rotating speed: Indicated above the curves; Anode: RuO_2/Ti mesh (2 mg Ru cm^{-2}; Cathode: Pt/Ti mesh (2 mg Pt cm^{-2}); Anolyte: 0.5 M HCl+saturated NaCl solution; Catholyte: 10% NaOH solution; Scan rate: 5 mV/s; Temperature: 50°C; The rotary cell.

At a current density of 5 kAm^{-2}, the anode potential is reduced from 2.42 V at 0 rpm to 2.12, 2.01, and 1.94 V at 400, 800, 1100 rpm, respectively. This confirms that the performance improvement of the rotary cell, as described in the previous section, majorly results from the anode performance enhancement.

Tafel Plots - Figure 4.15 gives a representive steady-state Tafel plot for the rotary cell as well as the static cell. The Tafel slopes obtained from figure 4.15 is 40 mV/decade both for the static cell and the rotary cell. The exchange current densities are $10^{-3.15}$ and $10^{-3.35}$ A cm^{-2} for the rotary cell and the static cell respectively. The static cell data qualitatively agree with the literature data which are quoted in the sections 4.2 and 4.4 [21, 22, 49].

These data show the acceleration field has a small effect, on the Tafel parameters. The possible reason for this may be due to different anode surface concentrations in the rotary cell and the static cell, however, this needs further investigation.

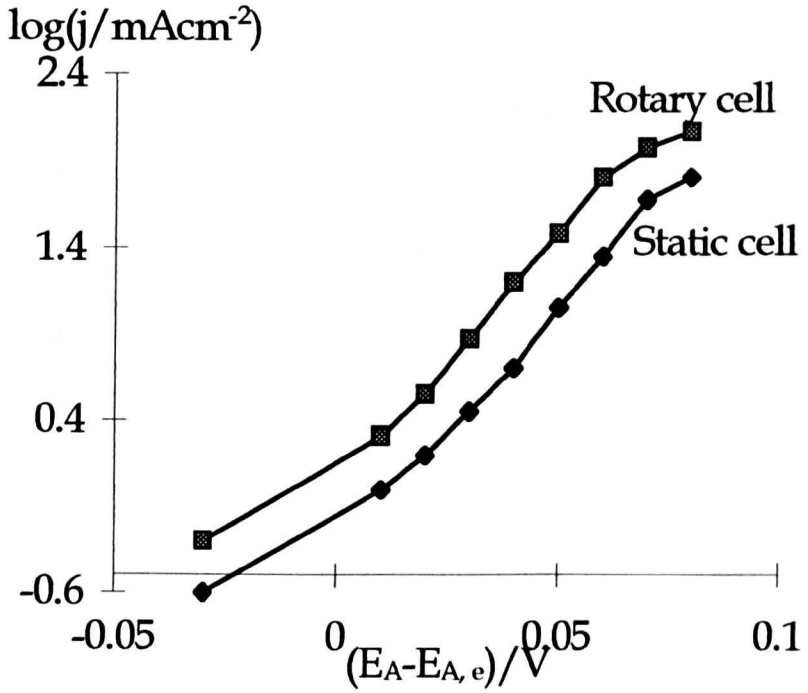

Figure 4.15. Tafel plots for chlorine evolution reaction on DSA anode - Effect of relative acceleration rate. Cathode: Pt/Ti mesh (2 mg Pt cm^{-2}); Electrolyte: 6.2 M NaCl solutions; Temperature: 80°C; The rotary cell.

Effect of Temperature - Temperature has a large effect on the chlorine evolution reaction. Interestingly, this effect was intensified in centrifugal fields as shown in figure 4.16.

It is clear that the increase in current density with temperature in centrifugal fields is greater than in the stationary cell. The slope is about 43 $Am^{-2}/^{0}C$ at 1100 rpm, compared to 24 $Am^{-2}/^{0}C$ obtained in the stationary cell. This demonstrates that the temperature effect was intensified in centrifugal fields.

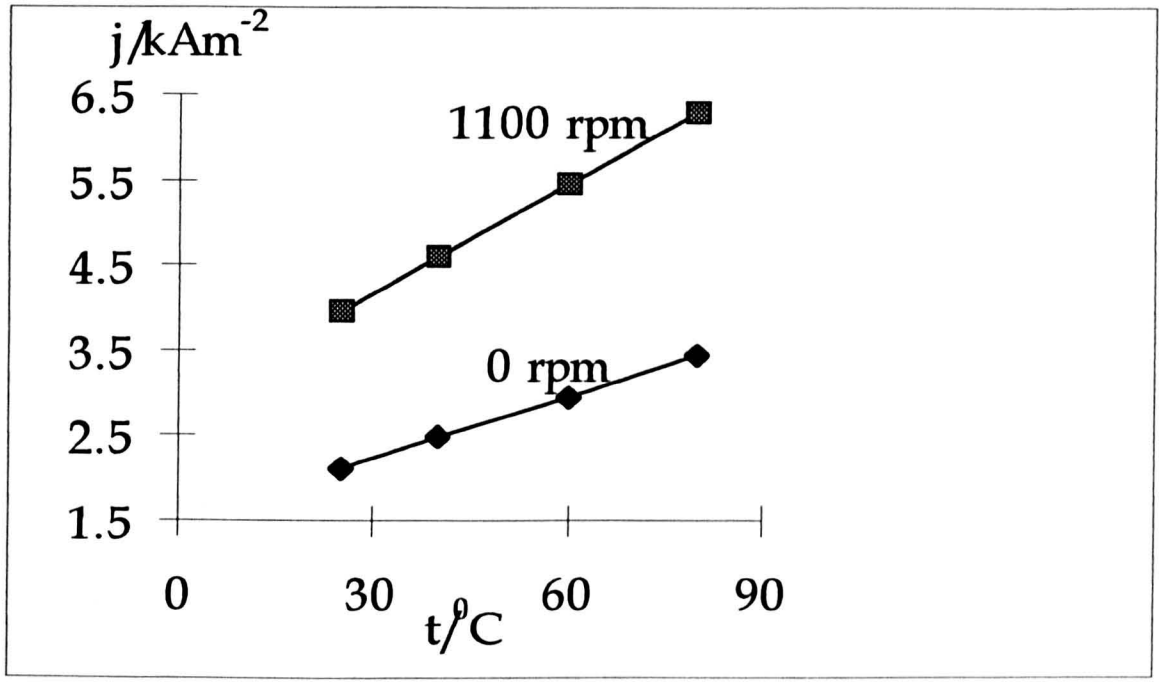

Figure 4.16. Anode current density against temperature curves for Cl_2 evolution reaction. Anode potential: 1.9 V vs RHE; Anode: RuO_2/Ti mesh (2 mg Ru cm^{-2}); Cathode: Pt/Ti mesh (2 mg Pt cm^{-2}); Anolyte: 0.5 M HCl+saturated NaCl solution; Catholyte: 10% NaOH solution; Scan rate: 5 mV/s; The rotary cell.

Effect of Concentration - The anode potential in centrifugal fields is also concentration sensitive; the concentration effect was also intensified in centrifugal fields, which are shown in figure 4.17. The anode potential increased rapidly with increasing electrolyte concentration at lower concentrations. The rate slowed at higher concentration. More importantly, the current density increased more rapidly in the rotary cell than in the static cell. The average slope is about 0.49 kAm^{-2}/M at 1100 rpm, compared to 0.28 kA m^{-2}/M obtained in the stationary cell. It is evident that centrifugal fields not only reduce mass transport limitation but also disengage gas bubbles from the electrode surface. Both factors intensified the concentration effect.

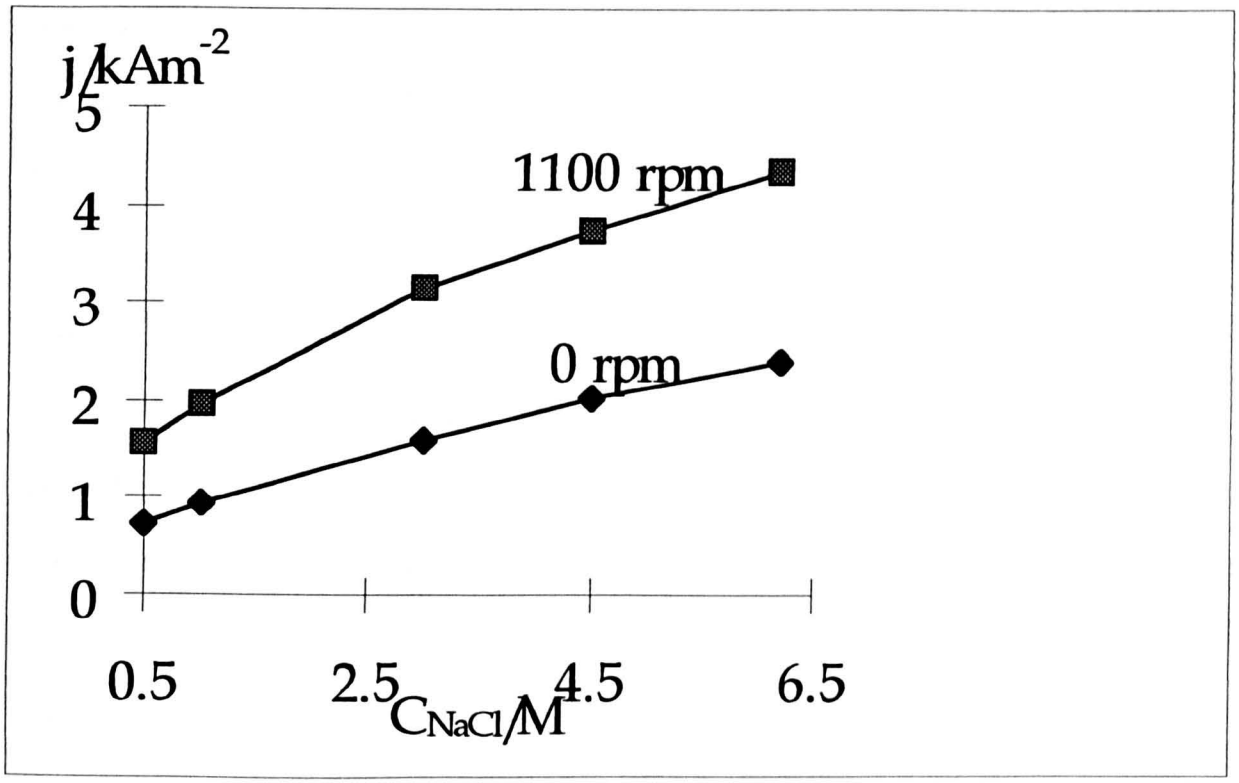

Figure 4.17. Anode current density against NaCl concentration curves for Cl_2 evolution reaction. Anode potential: 1.8 V vs RHE; Anode: RuO_2/Ti mesh (2 mg Ru cm^{-2}); Cathode: Pt/Ti mesh (2 mg Pt cm^{-2}); Scan rate: 5 mV/s; Temperature: 23.5°C; The rotary cell.

4.5.3. Summary

In a gas-evolving process, gas bubbles block the electrode and membrane surfaces and increase the solution resistivity, and therefore introduce large energy losses [56, 57]. These effects are largely eliminated in the rotary cell. The most striking feature of this work is that the higher the current density, the more significant the the effect of centrifugal field on the anode potential as well as cell voltage. Apart from the peculiarity of gas-evolving electrodes, this results from the fact that the reaction on RuO_2 anode demands the generation of higher oxidation state surface species, essentially surface-bonded strong oxidants [58]. These species can be obtained only at higher anode current densities. The above results also corroborate that

intensification of the chlor-alkali process mainly comes from improving mass transport environment and reducing the cell resistance.

It was reported that the overall rate of the chlorine evolution reaction is strongly influenced by slow transfer of produced Cl_2 away from the interface [59]. As is well known, under intensive gas evolution on the electrode the mass transfer of reaction product into the bulk solution is strongly affected by the convection fluxes existing near the electrode surface, determined not only by breaking-off and removal of the gas bubbles from the surface, but also by the process of their growth occuring both at the surface and after their break-off in the supersaturated bulk solution in the vicinity of the electrode [60-62]. These processes, as well as the accompanied mass transport limitations, should be sharply affected by a powerful centrifugal acceleration field due to its function of promoting mass transport. Consequently, the significant process intensification would be achieved. For example, a cell voltage reductions of 500-650 mV at 3-5 kAm^{-2} was derived in an acceleration field of 190 G at 80°C in acidified NaCl solutions, compared with a static cell. Under similar conditions, the reported cell voltage reduction is about 400 mV, compared to the industrial FM21 chlor-alkali cells, at 3-5 kAm^{-2} [7].

On the other hand, the cell resistance also plays important role for the process. It was determined in Hoechst-Uhde membrane flow cell at a current density of 3 kAm^{-2}, both electrode chambers was completely filled with gas-electrolyte mixture. The average gas bubble content was 9-10% in the cathode chamber and 29% in the anode chamber [63]. At higher current density, the gas content will definitely increase. Undoubtedly, these bubbles will be efficiently removed from the electrode surfaces as well as from the electrolytes by a powerful centrifugal acceleration field due to its

function of disgaging gas bubbles from the electrode surface. This, in turn, reduces the cell resistance drastically and therefore greatly intensified the process.

As already noted, at ambient temperature, the partial pressure of water vapour over the brine is low. However, in industrial practice the cells operate at about 90°C at which the water partial pressure is relatively high (about 0.67 Atms). This results in a larger volumetric flux of gas being generated from an electrode operating at a given current density and makes the electrode more susceptible to gas blinding. Therefore, for the current densities explored in this study the impact of higher acceleration fields, as expected, is even more marked when the cells are operated under practical conditions. Interestingly, both effects of temperature and electrolyte concentration were intensified in centrifugal fields.

4.6. Conclusions

The following conclusions can be drawn from the above results:

• Not surprisingly, the chlor-alkali process under industrial chloralkali electrolysis conditions can be significantly intensified in centrifugal fields, particularly at high current densities and in concentrated solutions. The outstanding performance was demonstrated by subjecting the electrolytes to centrifugal force to promote the separation of gas bubbles from the electrodes. The high acceleration field exerts an effect on the cell voltage and the anode and cathode potentials. Cell voltage reductions of 500-650 mV at 3-5 kAm^{-2}, an anode current density of 2.5-3.8 kAm^{-2} at 1.8 V vs RHE were derived in an acceleration field of 190 G at 80°C in acidified NaCl solutions, compared with a static cell. These results show that the centrifugal force provides the following benefits for the rotary cell: (i) Maximising mass transport

rate; (ii) Minimising ohmic resistance by removing gas bubble faster than it was formed.

The results also demonstrate that an application of high acceleration field in commercial chlor-alkali cells can lead to a substantial reduction in electric energy and, consequently, in the operational cost of the system.

• Centrifugal fields affect a gas evolution process much more significantly than a gas consuming process, in particular at high current densities, as can be seen from the comparison between this Chapter and Chapter 3. In the other words, centrifugal force accelerates the gas bubble removal more easily and efficiently than promotes the reactant gas adhesion on the electrodes or diffusion in aqueous solution. This is also hardly surprising because of the peculiarity of the electrode process with gas evolution. In these processes, the removal of the end product from the electrode surface may proceed not only through its diffusion into the bulk solution, but also by gas bubbles formation at the electrode surface. Thus, if the rate of the electrochemical step of the overall process, say, anodic reaction, is very high, and the preceding diffusion step does not affect its kinetics (e.g., under chlorine evolution from concentrated chloride solution), then its rate-determining step is the removal of reaction product from the electrode surface. At relatively low current densities this removal will proceed only through diffusion of the reaction product molecules into the bulk solution; at high current densities, however, under supersaturation of the near-electrode solution layer by the reaction product and intensive evolution of gas bubbles, its removal would preferentially go through gas evolution. Obviously, centrifugal fields play very significant role in this aspect and leads the above observations.

• Apart from using high acceleration field, the most important factor affecting the the intensification is the effectiveness of the anodes for the chlorine and hydrogen evolution processes. RuO_2/Ti mesh anode showed the best performance in acidified NaCl solutions due to its high density of the catalysts and low electrode resistivity. Commercial DSA also gave encouraging results.

• Concentrated electrolyte solution and high temperature are necessary for high efficiency performance, i.e., operating chlor-alakli cells at low cell voltage and high current density. An increase in the electrolyte concentration can lead to a dramatic reduction of the cell resistance. On the other hand, an increase in working temperature also benefits the operational characteristics of the cells, although the effect is smaller than powerful centrifugal acceleration field. Both effects of temperature and concentration were intensified in centrifugal fields.

4.7. References for Chapter 4

[1] Published annually in J. Electrochem. Soc.

[2] D. Pletcher and F. C. Walsh, Industrial Electrochemistry, 3rd Edition, Chapman & Hall, London, Chapter 3, 1993.

[3] R. D. Varjian, in "Tutorial Lectures in Electrochemical Engineering and Technology", AIChE Symposium Series No. 204, Volume 77 (R. Alkire and T. Beck, Editors), p.219, American Institute of Chemical Engineers, New York, 1981.

[4] M. M. Silver, in "Tutorial Lecturers in Electrochemical Engineering and Technology", AIChE Symposium Series No. 204, Volume 77, R. Alkire and T. Beck (Editors), p.234. American Institute of Chemical Engineers, New York, 1981.

[5] D. S. Cameron, R. L. Phillips, and P. M. Willis, in "Modern Chlor-Alkali Technology", Volume 4, N. M. Prout and J. S. Moorhouse (Editors), Elsevier, London, 1990.

[6] O. de Nora, Chem.-Ing.-Techn., 42, 222, 1970.

[7] C. Ramshaw, Heat Recovery Systems & CHP, 13, 493, 1993.

[8] Kim Kinoshita, "Electrochemical Oxygen Technology", John Wiley & Sons, Inc., New York, pp. 342-348, 1992.

[9] D. L. Caldwell, in "Comprehensive Treatise on Electrochemistry", Vol. 2, J. O'M. Bockris, B. E. Conway, E. Yeager, and R. E. White (Editors), Plenum Press, New York, pp. 105-166, 1981.

[10] "Modern Chlor-Alkali Technology", Volume 1, M. O. Coulter (Editor), Ellis Horwood, Chichester, 1980.

[11] "Modern Chlor-Alkali Technology", Volume 2, C. Jackson (Editor), Ellis Horwood, Chichester, 1983.

[12] "Modern Chlor-Alkali Technology", Volume 3, K. Wall (Editor), Ellis Horwood, Chichester, 1986.

[13] "Modern Chlor-Alkali Technology", Volume 4, N. M. Prout and J. S. Moorhouse (Editors), Elsevier, London, 1990.

[14] "Modern Chlor-Alkali Technology", Volume 5, T. Wellington (Editor), Elsevier, London, 1993.

[15] "Modern Chlor-Alkali Technology", Volume 6, R. Corry (Editor), Wiley, Chichester, 1995.

[16] "Advances in Electrochemistry & Electrochemical Engineering", Volume 12, H. Gerischer and C. W. Tobias (Editors), John Wiley & Sons, New York, 1981.

[17] T. Arikado, C. Iwakura, and H. Tamura, Electrochim. Acta, 23, 9, 1978.

[18] L. J. J. Janssen, L. M. C. Starmans, J. G. Visser and E. Barendrecht, Electrochim. Acta, 22, 1093, 1977.

[19] I. R. Burrows, J. H. Entwisle and J. A. Harrison, J. Electroanal. Chem., 77, 21, 1977.

[20] G. Faita and G. Fiori, J. Appl. Electrochem., 2, 31, 1972.

[21] V. V. Losev, N. Y. Bune, and L. E. Chuvaeva, Electrochim. Acta, 34, 929, 1989.

[22] J. A. Harrison, D. L. Caldwell, and R. E. White, Electrochim. Acta, 29, 203, 1984.

[23] I. R. Burrows, D. A. Danton and J. A. Harrison, Electrochim. Acta, 23, 493, 1978.

[24] C.-C. Hu, C.-H. Lee and T.-C. Wen, J. Appl. Electrochem., 26, 72, 1996.

[25] T. A. F. Lassali, J. F. C. Boodts and S. Trasatti, Electrochim. Acta, 39, 1545, 1994.

[26] S. Trasatti, Electrochim. Acta, 32, 369, 1987.

[27] V. Consonni, S. Trasatti, F. Pollak and W. E. O'Grady, J. Electroanal. Chem., 228, 393, 1987.

[28] "Proceedings of the Symposium on Advances in the Chlor-Alkali and Chlorate Industry", M. M. Silver and E. M. Spore (Editors), The Electrochemical Society, Inc., Pennington, New York, 1984.

[29] V. de Nora and A. Nidola, Paper No. 270, Extended Abstr., Electrochm. Soc. Meeting, Los Angeles, 1970.

[30] D. M. Novak, B. V. Tilak, and B. E. Conway, in "Modern Aspects of Electrochemistry", Volume 14, J. O'M. Bockris, B. E. Conway, and R. E. White (Editors), p. 195, Plenum Press, New York, 1982.

[31] K. J. O'Leary and T. J. Navin, in "Chlorine Bicentennial Symposium", T. C. Jeffrey, P. A. Nanna, and H. S. Holden (Editors), The Electrochemical Society, Princeton, New Jersey, p. 174, 1974.

[32] W. A. Gerrard and B. C. H. Steele, J Appl. Electrochem., 8, 417, 1978.

[33] A. T. Kuhn and C. J. Mortimer, J. Electrochem. Soc., 120, 231, 1973.

[34] F. Hine, M. Yasuda, and T. Yoshida, J. Electrochem. Soc., 124, 500, 1977.

[35] P. C. S. Hayfield and W. R. Jacob, in "Modern Chlor-Alkali Technology", Volume 1, p.103, M. O. Coulter (Editor), Ellis Horwood, Chichester, 1980.

[36] G. Faita, G. Fiori, and J. W. Augustynski, J. Electrochem. Soc., 116, 928, 1969.

[37] D. E. Caldwell and M. J. Hazelrigg, in "Modern Chlor-Alkali Technology", Volume 1, p.121, M. O. Coulter (Editor), Ellis Horwood, Chichester, 1980.

[38] S. Saito, in "Modern Chlor-Alkali Technology", Volume 1, p.138, M. O. Coulter (Editor), Ellis Horwood, Chichester, 1980.

[39] D. S. Cameron, R. L. Phillips, and P. M. Willis, in "Modern Chlor-Alkali Technology", Volume 4, N. M. Prout and J. S. Moorhouse (Editors), Elsevier, London, 1990.

[40] E. Pearson, in "Modern Chlor-Alkali Technology", Volume 2, p177, C. Jackson (Editor), Ellis Horwood, Chichester, 1983.

[41] Y. Tominaga, T. Kanke, K. Takagi, and T. Miyazaki, in "Modern Chlor-Alkali Technology", Volume 4, p.143, N. M. Prout and J. S. Moorhouse (Editors), Elsevier, London, 1990.

[42] E. A. Kalonovskii, R. U. Bondar, and N. N. Meshkova, Elektrokhimiya, 8, 1468, 1972.

[43] A. T. Kuhn and C. J. Mortimer, J. Appl. Electrochem., 2, 283, 1972.

[44] R. U. Bondar, A. A. Borisova, and E. A. Kalonovskii, Elektrokhimiya, 10, 44, 1974.

[45] L. M. Elina, V. M. Gitneva, V. I. Bystrov, and N. M. Shmygul, Elektrokhimiya, 10, 68, 1974.

[46] J. H. Austin, in "Modern Chlor-Alkali Technology", Volume 3, K. Wall(Editor), pp.137-142, Ellis Horwood Limited, 1986.

[47] M. Shen and Y. Chen, in D. S. Cameron, R. L. Phillips, and P. M. Willis, in "Modern Chlor-Alkali Technology", Volume 4, N. M. Prout and J. S. Moorhouse (Editors), p.149, Elsevier, London, 1990.

[48] D. Galizzioli, F. Tantardini, and S. Trasatti, J. Appl. Electrochem., 4, 57, 1974.

[49] J. A. Harrison, in "Modern Chlor-Alkali Technology", Volume 4, N. M. Prout and J. S. Moorhouse (Editors), p.85, Elsevier, London, 1990.

[50] C.-C. Hu, C.-H. Lee and T.-C. Wen, J. Appl. Electrochem., 26, 72, 1996.

[51] D. Bergner, in "Modern Chlor-Alkali Technology", Volume 3, K. Wall(Editor), p.162, Ellis Horwood Limited, 1986.

[52] R. J. Horvath, in, "Modern Chlor-Alkali Technology", Volume 3, K. Wall(Editor), p.218, Ellis Horwood Limited, 1986.

[53] J. A. Harrison, in "Modern Chlor-Alkali Technology", Volume 4, N. M. Prout and J. S. Moorhouse (Editors), p.88, Elsevier, London, 1990.

[54] R. J. Horvath, in, "Modern Chlor-Alkali Technology", Volume 3, K. Wall(Editor), p.222, Ellis Horwood Limited, 1986.

[55] N. Kawasaki, M. Murakami, M. Akazawa, and T. Sato, in "Modern Chlor-Alkali Technology", Volume 3, K. Wall(Editor), p.212, Ellis Horwood Limited, 1986.

[56] P. J. Sides and C. W. Tobias, J. Electrochem. Soc., 127, 288, 1980.

[57] P. J. Sides and C. W. Tobias, J. Electrochem. Soc., 129, 2715, 1982.

[58] L. D. Burke and J. F. Healy, J. Electroanal. Chem., 124, 327, 1981.

[59] L. D. Burke and J. F. O'Neill, J. Electroanal. Chem., 101, 341, 1979.

[60] H. Vogt, Electrochim. Acta, 29, 167; 175, 1984.

[61] L. Muller, M. Krenz, and R. Landsberg, J. Electroanal. Chem., 180, 453, 1984.

[62] L. J. J. Janssen and J. G. Hoogland, Electrochim. Acta, 15, 1013, 1970.

[63] D. Bergner, Chem.-Ing.-Tech., 62, 409, 1990.

Chapter 5. Water Electrolysis

5.1. Introduction

Water electrolysis is an attractive process for the production of oxygen and hydrogen in aqueous solutions, particularly for the small-scale production of the high-purity gases. The process involves the splitting of water into ionic charged components and finally to hydrogen and oxygen:

Anode (alkaline medium):	$4OH^- = 2H_2O+O_2+4e^-$	(5.1)
Anode (acidic and neutral medium):	$2H_2O = O_2+4H^++4e^-$	(5.2)
Cathode (alkaline medium):	$4H_2O+4e^- = 4OH^-+2H_2$	(5.3)
Cathode (acidic and neutral medium):	$4H^++4e^- = 2H_2$	(5.4)
Overall:	$2H_2O = O_2+2H_2$	(5.5)

All conventional commercial electrolysers use alkaline electrolyte (~30 wt% KOH) and operate at temperatures ranging from 70 to 90°C and 1 atm pressure [1,2]. Due to high overpotentials of anode and cathode, the typical cell voltages of water electrolysers (about 1.8-2.0 V at operating current densities of 1~3 kAm^{-2}) are considerably higher than the thermodynamic decomposition voltage (1.229 V at 25°C and 0.1 M Pa) [1,2]. This high energy comcumption has limited the production of hydrogen and oxygen using electrolysis. Only ~5% of the world hydrogen production was accomplished by electrolysis [3]. Oxygen is produced for commercial and industrial use primarily also by nonelectrochemical processes [1].

The high anode and cathode overpotentials are the major factors attributed to high energy consumption [1,2]. The ohmic potential drop due to the presence of the gas bubbles in the solution and the electrode surfaces enhances the energy losses. The overpotentials can be lowered by using effective catalysed electrodes and operating

the cell at elevated temperature. Part of this work will be concentrated on this aspect. On the other hand, the high ohmic drop can only be overcome to a limited extent in the commercial water electrolysers. A reason for this is that cells have been dependent upon normal gravitational force for separation of the evolved gas bubbles from liquid electrolyte, i.e., a limitation imposed by the slowness with which gas bubbles separate from the electrodes and ascend through the electrolyte. When the current density is increased to speed up the production of gas, then the collection of gas bubbles at the electrodes unduly increases the electric resistance of the cells. To overcome this difficulty, one option is designing equipment wherein the electrolyte is subjected to centrifugal force to promote the separation of gas bubbles from the electrodes. In this way, the significant intensification of the water electrolysis process can be reasonably expected. It was therefore decided to investigate the behaviour of a water electrolysis cell in a simple laboratory centrifuge, in order to provide the basis for a more realistic cell design.

5.2. Literature Review

The past work in water electrolysis is briefly reviewed in this section.

Mechanistic Study - Oxygen and hydrogen evolutions have been studied both in acidic and alkaline solutions. The representative mechanisms of oxygen and hydrogen evolution are listed in Tables 5.1 and 5.2.

Table 5.1. Mechanisms of Oxygen Evolution

Media	Mechanism		Refrence(s)
Acidic solutions (M is active site of electrode)	$M+2H_2O = MOH+H^++e^-$	(5.6)	[4]
	$MOH = MO+H^++e^-$	(5.7)	
	$MOH+MOH = MO+M+H_2O$	(5.8)	
	$MO+MO = 2M+O_2$	(5.9)	
Alkaline solutions	$M+OH^- = MOH+e^-$	(5.10)	[5]
	$MOH+OH^- = MO+H_2O+e^-$	(5.11)	
	$2MO = 2M+O_2$	(5.12)	

Table 5.2. Mechanisms of Hydrogen Evolution

Media	Mechanism		Refrence(s)
Acidic solutions	$M+H^++e^- = MH$	(5.13)	[6]
(M is active site of electrode)	$MH+H^++e^- = M+H_2$	(5.14)	
Alkaline solutions	$M+H_2O+e^- = MH+OH^-$	(5.15)	[7]
	$MOH+ H_2O+e^- = H_2+M+OH^-$	(5.16)	
	$2MH = 2M+H_2$	(5.17)	

The Tafel slopes and exchange current densities of oxygen and hydrogen evolution change with different conditions, which are shown in Tables 5.3 and 5.4.

Table 5.3. Tafel Slope (b) and Exchange Current Density (j_0) of Oxygen Evolution

Electrode	Media	Temperature/°C	b/mVDec^{-1}	j_0/Acm^{-2}	Refrence(s)
Pt	1 M NaOH	25	55	1.0×10^{-11}	[1]
Pt	0.5 M H_2SO_4	20	107	7.6×10^{-10}	[1]
Pt	0.5 M H_2SO_4	80	90	1.3×10^{-11}	[1]
RuO_2	1 M H_2SO_4	80	30-40	$(5\text{-}15)\times10^{-9}$	[1]
RuO_2	30% KOH	80	68	9.3×10^{-7}	[1]
Ni	50% KOH	70	48	6.0×10^{-8}	[5]
Ni	50% KOH	100	57	4.0×10^{-7}	[5]
Ni	50% KOH	150	98	3.0×10^{-4}	[5]
Ni-Co	50% KOH	70	41	5.4×10^{-8}	[5]
Ni-Co	50% KOH	100	54	3.6×10^{-7}	[5]
Ni-Co	50% KOH	150	77	4.0×10^{-4}	[5]

Table 5.4. Tafel Slope (b) and Exchange Current Density (j_0) of Hydrogen Evolution

Electrode	Media	Temperature/°C	-b/mVDec^{-1}	j_0/Acm^{-2}	Refrence(s)
Ni	50% KOH	70	142	4.8×10^{-4}	[5]
Ni	50% KOH	100	178	3.2×10^{-3}	[5]
Ni	50% KOH	150	194	9.7×10^{-3}	[5]
Ni-Fe	50% KOH	70	93	2.1×10^{-3}	[5]
Ni-Fe	50% KOH	100	97	6.0×10^{-3}	[5]
Ni-Fe	50% KOH	150	73	1.2×10^{-2}	[5]
Pt	0.5 M NaOH	25	117	$1.0\times10^{-3.5}$	[8]
Pt	0.5 M H_2SO_4	25	30	1.0×10^{-4}	[8]

Rotary Electrolyser - Literature records on rotary water electrolysis cells are scant. The first description of this type apparatus, a rotary water electrolyser comprising a

plurality of annular cells arranged around an axis of a hollow shaft, appeared in 1920s [9]. The shaft has two compartments communicating with the cells by a plurality of ducts for delivering hydrogen and oxygen.

A similar proposal was patented in 1964 where in the cell, the electrolysis proceeds in concert with a rotary motion induced therein to ensure efficient separation of the liquid and gas phases [10]. The liquid electrolyte was thrown towards the periphery of the apparatus while the product gases were withdrawn along the axis of rotation. The entrained droplets of liquid electrolyte can be removed in the centrifugal field.

More recently, a rotary water electrolyser, for supplying hydrogen and oxygen to an automobile or household, was patented [11]. It was said that the membrane cell was adapted to rotate about an central axis and the fuels would be efficiently produced in a centrifugal acceleration field and directly conducted to an automobile.

Unfortunately, these patents neither gave any experimental data, nor found any practical application.

Electrodes - It is estimated that, at current densities of the order of 1.5 kAm^{-2}, the practical voltage efficiency of conventional water electrolysers is around 65-75%. The anode and cathode polarisations are major contributors to the energy losses in water electrolysers and depend strongly on electrode materials [12, 13]. So exploring electrodes for water electrolysis has received considerable attention, particularly in the development of improved electrocatalysts. While some improvement in overall cell efficiency has been obtained in recent years, the problem of long-term stability of the electrodes under the rather severe operating conditions still remains to be solved. To date, the commercialy available water electrolysers are largely based on nickel and steel electrodes [1]. Other materials were also studied but have not found

use yet as technical water electrolysis cells due to either high cost or poor long-term stability.

• Anode - Because the oxygen electrode is highly irreversible, high anodic potentials were encountered during oxygen evolution. This demands the use of highly stable anodes. The goals in the development of practical anodes are to find stable, electro-conducting oxides with low overpotential for oxygen evolution and long life. Currently, nickel and nickel-based materials are typically used for anodes in alkaline water electrolysers [14-18].

However, the anodic overpotential at nickel electrodes increases with time due to the growth of poorly conducting nickel oxide layers [19] and so noble metal oxides have been evaluated. The Tafel intercepts, which represent the experimental activation overpotential at a current density of 1 A cm^{-2}, were measured and taken as a criteria of the effectiveness of various metal oxides for oxygen evolution. In 30 wt% KOH at 80°C, this effectiveness decreases in the order Ru oxide (0.37 V) > Ir oxide (0.41 V)~Pt oxide (0.41 V) > Rh oxide (0.43 V) > Pd oxide (0.45 V)~Ni oxide (0.45 V) > Os oxide (0.49 V) >> Co oxide (0.69 V) >> Fe oxide (0.91 V) [18].

Although RuO_2 is highly active for oxygen evolution due to the presence of reactive surface groups [20], it lacks long-term stability. By adding a controlled amount of an inactive oxide, e. g., SnO_2, both the long-term stability and electrocatalytic activity of RuO_2 electrodes can be improved. For example, an anode composing 40:60 RuO_2/ SnO_2 mol% has a service life of 220 hours, compared to 50 hours of the RuO_2 electrode. The service life was determined by recording the time required for total removal of the electro-active surface layer during continuous electrolysis in 6 M NaOH at 0.75 A cm^{-2} and 80°C.At this time, a large increase in anode potential was

observed which was associated with the formation of a poorly conducting oxide on the Ti substrate. These electrodes remain in contention as possible candidates for large-scale water electrolysis cells [21].

• Cathode - The cathode materials used in commecial water electrolysers nowadays are smooth nickel, Raney-nickel, nickel sulphide, steel, and nickel coated or painted steel [18, 22]. In order to reduce the high electric energy demand of alkaline water electrolysers, the structure of Ni cathodes was improved by using highly porous electrodes. The performance of such cathodes is further improved by adding active Raney Ni catalysts and/or other metals. The cathodic polarisation at 2 kAm^{-2} for hydrogen generation by electrolysis of 6 M NaOH was decreased by about 230 mV when using Ni/Al coated electrode compared with pure Ni ones for water electrolysis [23]. A further decrease of the polarisation voltage by 80-100 mV was obtained by alloying with Ti, B, Zr, and Mo [23]. RuO_2 coated Ni electrodes were also prepared and tested for the hydrogen evolution reaction in alkaline media [7]. Transition metal oxides are claimed to have good electrocatalytic performance for hydrogen evolution [24-26]. Platinum group metals or their oxides were also used as cathodes for hydrogen evolution [27-29].

5.3. Design Of The Rotary Water Electrolyser

General Aspects - The electrolytic flow circuit and the rotary cell are descibed in Chapters 2 and 4. Most experiments were carried out in KOH solutions at 80°C and atmosphere pressure. Before starting the elevated temperature experiments a warming-up period of about 30 minutes was required to reach a desired constant temperature. Many series of experiments were carried to optimise the system and some results are given below.

Effect of Anode Material - Anode materials have an obvious effect on the anode potentials and therefore on the cell voltages. Figure 5.1 shows anodic polarisation curves obtained on different electrodes.

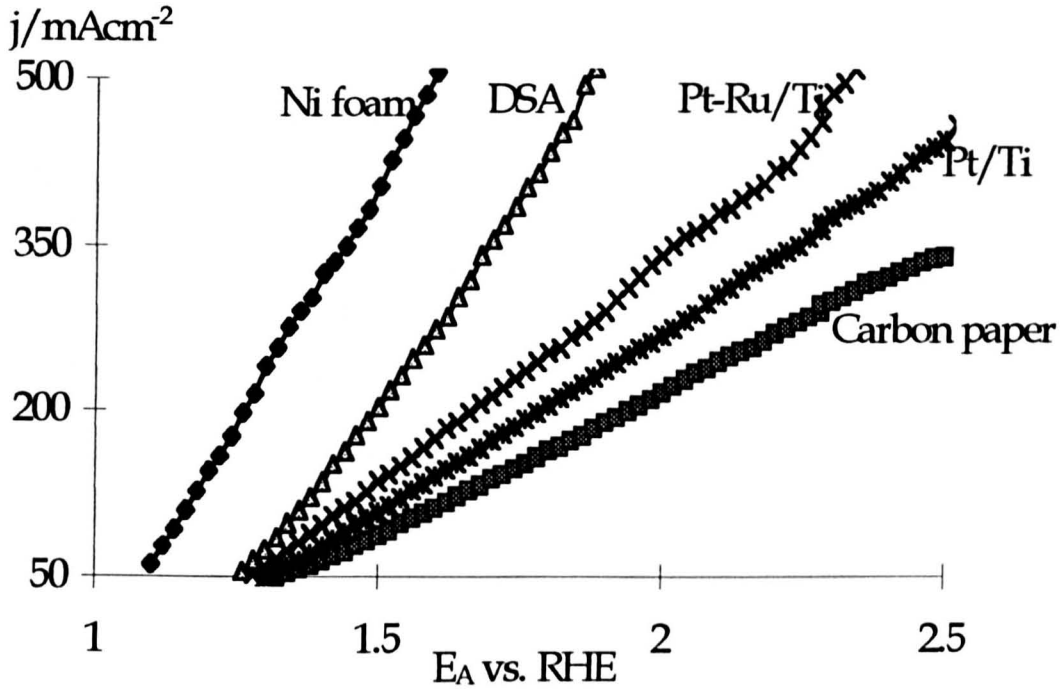

Figure 5.1. Steady-state anodic polarisation curves for oxygen evolution reaction - Effect of anode material. Electrolyte: 4.5 M KOH solutions; Cathode: Pt/Ti mesh (2 mg Pt cm^{-2}); Scan rate: 5 mV/s; Temperature: 80°C; The static cell.

At 300 mA cm^{-2}, the anode potential is 1.38, 1.63, 1.92, 2.09 and 2.30 V vs. RHE for Ni foam, DSA, Pt-Ru/Ti mesh, Pt/Ti mesh, and carbon paper anodes, respectively. The value for Ni foam anode is in the range of those from polymer-electrolyte water electrolysers [9, 12]. These data clearly shown that the effectiveness of the materials for oxygen evolution followed the order:

Ni > DSA > Pt-Ru/Ti mesh > Pt/Ti mesh > Carbon paper.

The high efficiency of the nickel foam resulted in its high Ni loading in a unit volume. From the viewpoint of electrochemical engineering, an increase in electrode activiity can be achieved through: (a) increase of intrinsic activity and (b) increase in

the real surface area. Because the main contribution to the total activity arises from an increase of the real surface area [30]. Therefore, the active reaction sites were tremondously increased by using this material.

Effect of Cathode Material - Several materials were tested as cathode for water electrolysis and results are shown in figure 5.2.

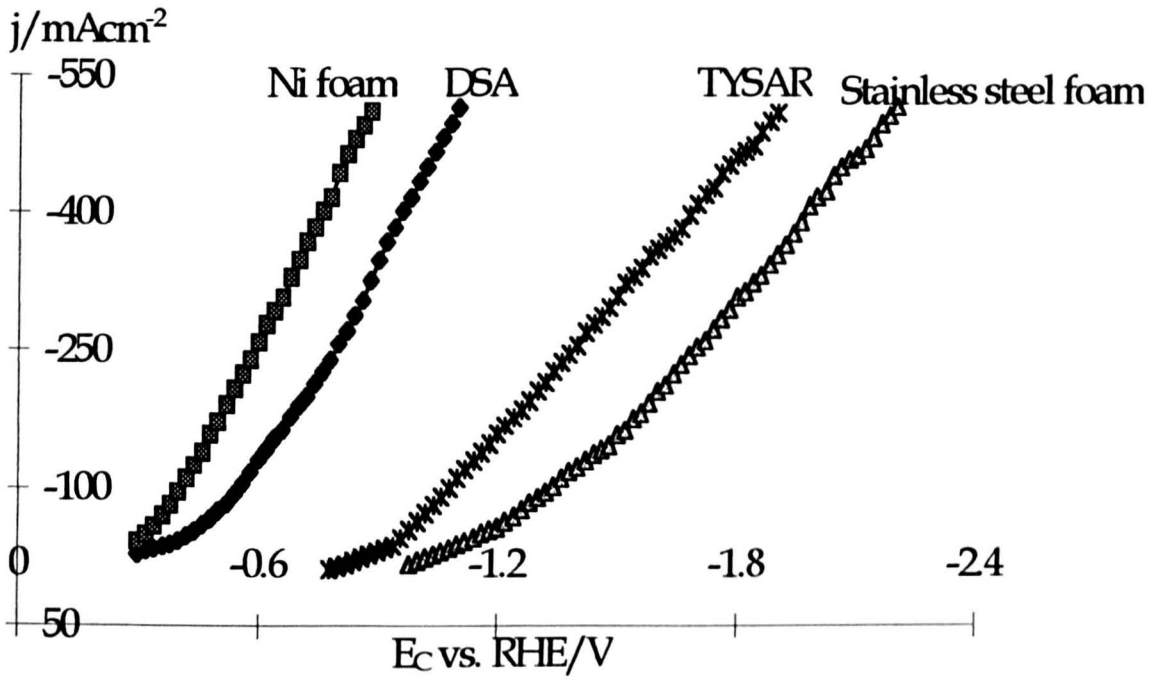

Figure 5.2. Steady-state cathodic polarisation curves for hydrogen evolution reaction - Effect of cathode material. Electrolyte: 4.5 M KOH solutions; Anode: Ni foam; Scan rate: 5 mV/s; Temperature: 80°C; The static cell.

From figure 5.2, the cathode potential at -300 $mAcm^{-2}$ is -0.65, -0.85, -1.50, and -1.79 V vs. RHE for Ni foam, DSA, TYSAR foam and stainless steel cathode, respectively. The values for Ni foam anode and DSA are in the range of those from polymer-electrolyte water electrolysers [5, 7]. According to these data, the cathodic effectiveness of these materials for the hydrogen evolution decreased showed the following order:

Nickel foam > DSA > Tysar > Stainless steel

Again, the nickel foam cathodes gave the minimum cathode potential at a fixed current density. As stated in the anode section, the high efficiency of the nickel foam resulted in its high density of the catalyst per unit volume and therefore the high density of active surface sites. Of course, nickel can only be used in alkaline media.

Electrolytes - Electrolyte type and concentration affect the polarisation behaviours of the anode, cathode, and cell. For nickel electrodes, the electrolyte is limited to neutral and alkaline media. Using Pt/Ti mesh electrodes rather than Ni foam allows the selection of a wide range of electrolytes. Thus, most experiments examining the enfluence of electrolytes were carried out using Pt/Ti mesh electrodes and/or stailess steel cathode. When the Pt/Ti mesh electrodes were used, KOH seemed the best anolyte.

5.4. Electrochemical Behaviour In The Stationary Cell

This section summarises the polarisation behaviours of the static water electrolyser.

5.4.1. Cell Voltage

Cell voltage is a critical parameter for the water electrolysis industry. The cell voltage is closely related the electrode used. Ni foam electrodes gave the best performance for water electrolysis process in a static cell. This is due to high total surface area of the Ni foam electrodes which effectively decreased anodic and cathodic overpotentials with KOH electrolytes [30]. In addition, the cell voltage was affected by electrolyte concentration, pH, and temperature.

Effect of Concentration - Figure 5.3 shows the effect of electrolyte concentration on the cell polarisation curves. The cell polarisation decreases with increase in concentration. For example, at a cell voltage of 3 V, the cell current density is 2, 3.7, 4.1, and 4.9 kAm^{-2} for 0.5, 1, 4.5, and 6.3 M KOH solution, respectively. The

maximum increase in current density at the given cell voltage was observed when the concentration changed from 0.5 to 1 M. Both reduction in a cell resistance and mass transport improvement are responsible for this.

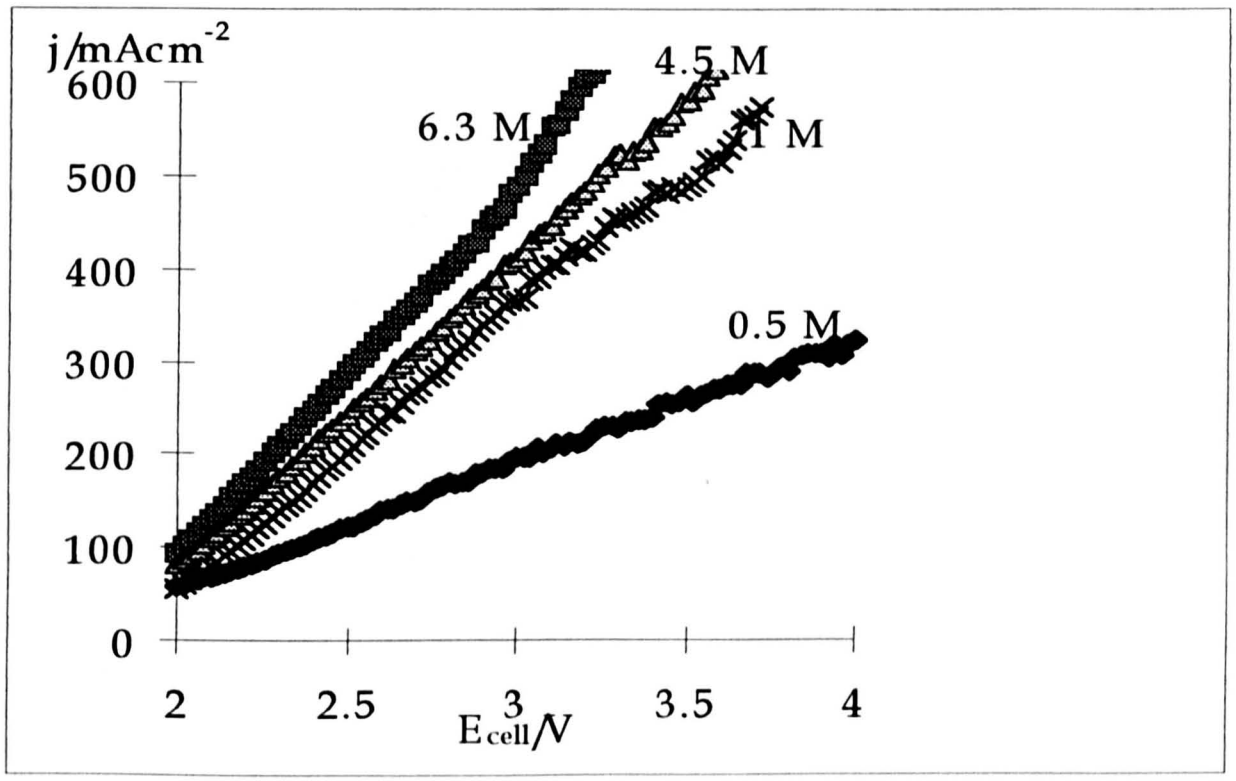

Figure 5.3. Cell polarisation curves for water electrolysis. Anode and cathode: Ni foam; Electrolyte: KOH solutions; Scan rate: 5 mV/s; Temperature: 23.6°C; The static cell.

Effect of pH - The electrolyte has a significant effect on the cell voltage, as shown in figure 5.4. At 200 $mAcm^{-2}$, the cell voltage is 2.22, 2.6, and 3.36 V for 1 M H_2SO_4, KOH, and Na_2SO_4 electrolyte, respectively. Sulphuric acid gave the best performance.

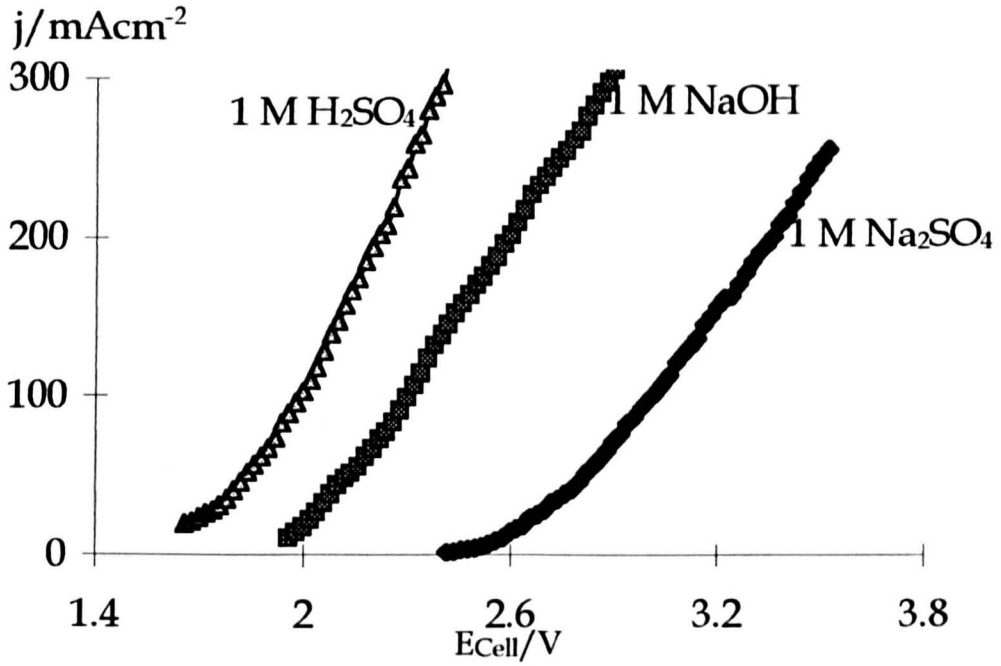

Figure 5.4. Cell polarisation curves for water electrolysis - Effect of pH. Anode and cathode: Pt/Ti mesh (2 mg Pt cm^{-2}); Scan rate: 5 mV/s; Temperature: 23.6°C; The static cell.

Effect of Temperature - The cell voltage decreased with increasing cell temperature, as shown in figure 5.5.

The reduction of about 280 mV was realised when the temperature changed from 25 to 80°C. Obviously, higher operating temperatures increase electrolyte conductivity and reduce overpotentials, facilitating a lower cell voltage.

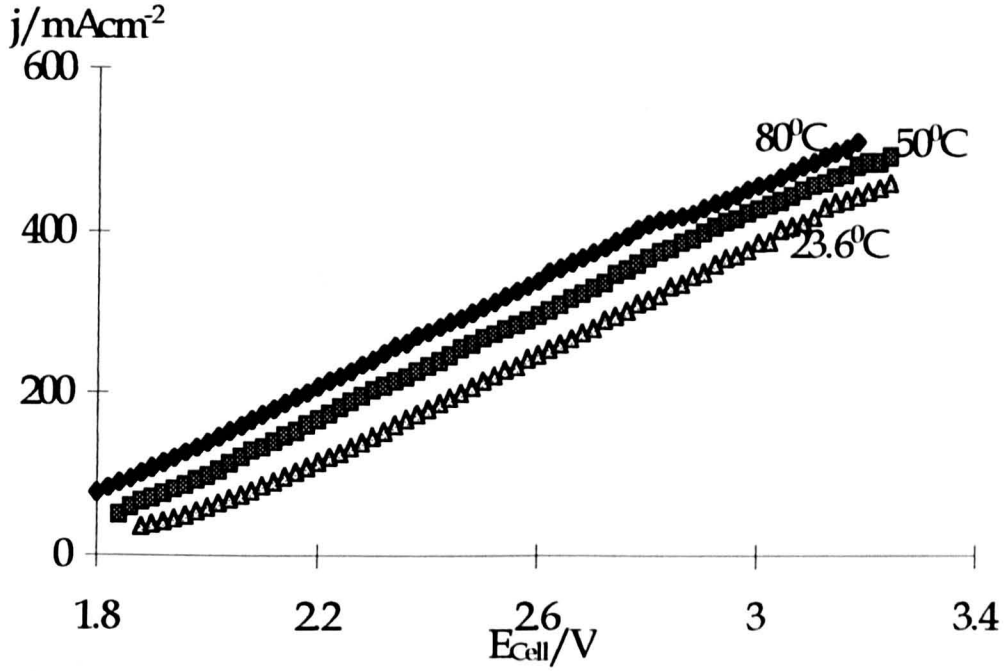

Figure 5.5. Cell polarisation curves for water electrolysis - Effect of temperature. Anode and cathode: Ni foam; Electrolyte: 4.5 M KOH solutions; Scan rate: 5 mV/s; The static cell.

5.4.2. Oxygen Evolution

The anodic evolution of oxygen in electrolysis cell, is affected by the concentration, pH, and temperature of the anolyte.

Effect of Concentration - Figure 5.6 exhibits effect of electrolyte concentration on the polarisation behaviour for oxygen evolution in alkaline media. It can be seen that the anode potential decreases, at a constant current density, with increasing concentration and is more significant at higher current density. For example, at 300 $mAcm^{-2}$, the anode potential is about 2.6, 2.5, 2.1, and 1.8 V vs RHE in 0.5, 1, 4.5, and 6.3 M KOH solutions respectively. The anode potential changes in a smaller extent at low current density say 50 $mAcm^{-2}$, i.e., 1.05, 0.96, 0.90 and 0.82 V vs. RHE in 0.5, 1, 4.5, and 6.3 M KOH solutions respectively.

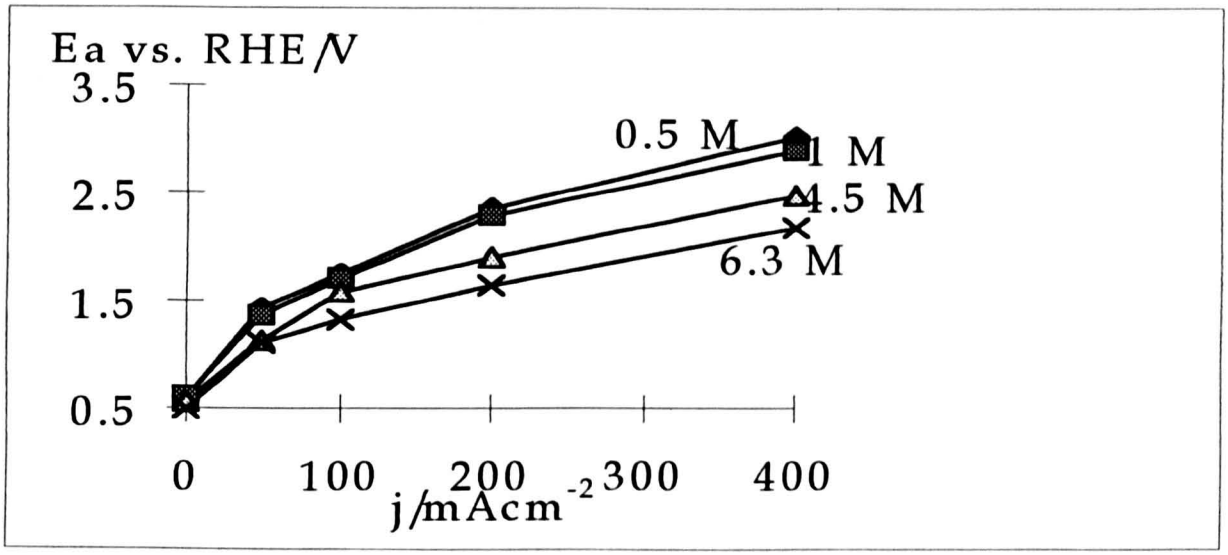

Figure 5.6. Steady-state anodic polarisation curves for water electrolysis-concentration effect. Electrolyte: KOH solutions; Anode and cathode: Pt/Ti mesh (2 mg Pt cm^{-2}); Temperature: 80°C; The static cell.

Concentration affects the oxygen evolution kinetics, as exhibited in the Tafel data (figures 5.7 and table 5.5).

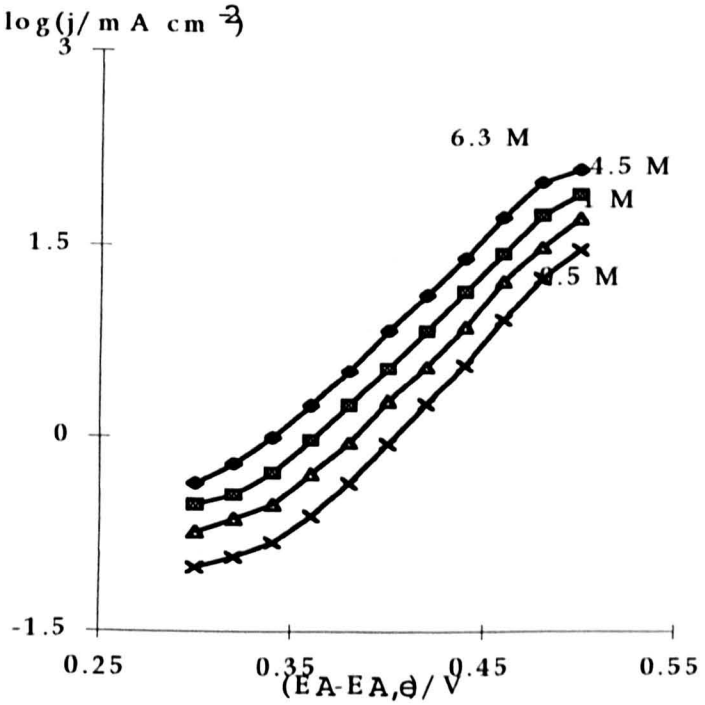

Figure 5.7. Tafel plots for oxygen evolution reaction on Pt/Ti electrode - Concentration effect. Electrolyte: KOH solutions; Anode and cathode: Pt/Ti mesh (2 mg Pt cm^{-2}); Temperature: 80°C; The static cell.

The Tafel slope b in an overpotential range of 0.35 to 0.45 V and exchange current densities j_0 obtained by extrapolating to $(E_A - E_{A,e})=0$ from figure 5.7 are listed in table 5.5.

Table 5.5. Tafel parameters for oxygen evolution under different conditions

C_{KOH}/M	t/°C	b/mVdecade^{-1}	j_0/Acm^{-2}
0.5	80	66	$10^{-7.84}$
1	80	66	$10^{-7.63}$
4.5	80	66	$10^{-7.40}$
6.3	80	66	$10^{-7.35}$
4.5	50	66	$10^{-7.60}$
4.5	25	66	$10^{-7.65}$

As shown in Table 5.5, the Tafel slope is same in the four solutions. There is a small improvement in the exchange current density corresponding increasing the concentration. Increasing the KOH concentration from 0.5 to 6.3 M leads to an increment in the exchange current densities from $10^{-7.84}$ to $10^{-7.35}$ A cm^{-2}. The reported Tafel slope and the exchange current density are 55 mV/decade and 1.0×10^{-11} A cm^{-2} for oxygen evolution on Pt electrode in 1 M NaOH solution at 25°C [1]. The exchange current density obtained in this work is higher than that reported which may be due to different electrode surface concentration. Further work is needed to clarify this. As can be seen above, the concentration effect on the Tafel parameters is small and only has qualitative sense, as aforementioned, in this work.

. It was worthwhile to point out that our experiments were run at high currents and the uncompensated IR potential drop may be large, although the tip of the reference electrode was designed for very close placement to the working electrode. The potentiostat lost control completely over the cell when we tried to measure and correct this IR drop during the measurements. It is difficult to correct the quantities during the analysis of the data because the uncompensated resistance is unknown and the geometric complexity of the electrodes used, which introduced nonuniform distribution of current density. However, these data can still give a qualitative picture about the effect of concentration on the oxygen evolution kinetics.

Figure 5.8 shows the dependence of current density at constant potential on KOH concentration.

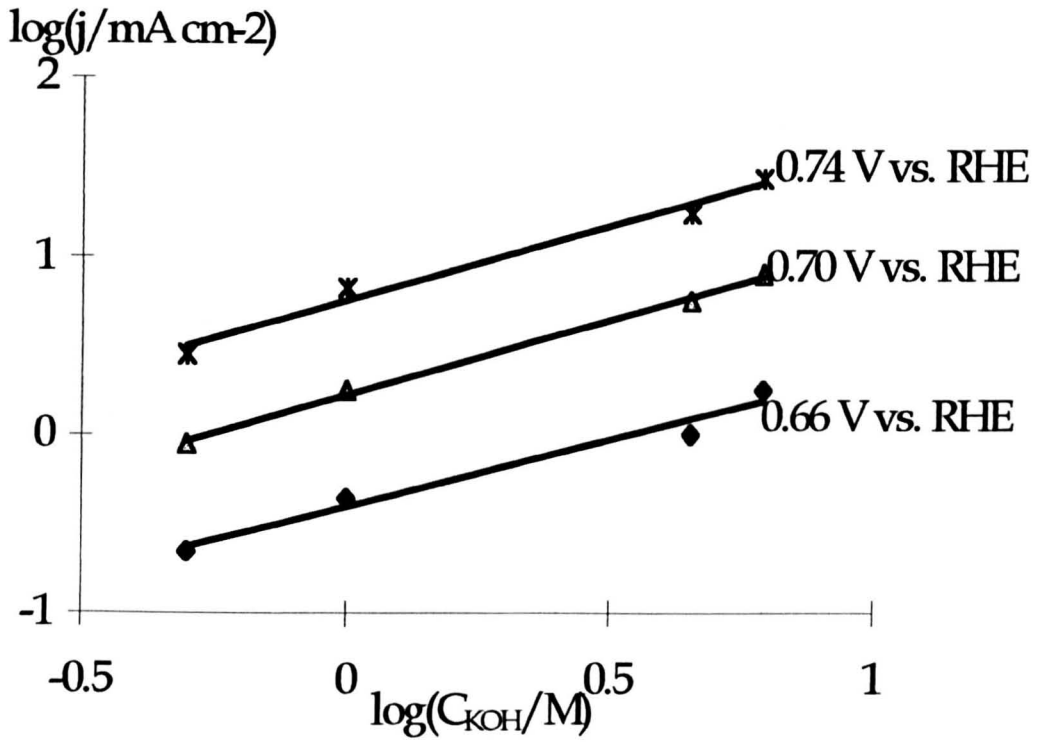

Figure 5.8. Dependence of current density at different anodic potentials on KOH concentration for oxygen evolution reaction on Pt/Ti electrode. Electrolyte: 4.5 M KOH solutions; Anode and cathode: Pt/Ti mesh (2 mg Pt cm^{-2}); Temperature: 80°C; The static cell.

The reaction order with respect to OH^- obtained from figure 5.8 are 0.7, 0.85 and 1.85 at 0.66, 0.70 and 0.74 V vs. RHE respectively.

Effect of Temperature - Figure 5.9 shows the influence of temperature on the oxygen evolution reaction. The anode potential decreases approximately at a rate of 5 mV per degree.

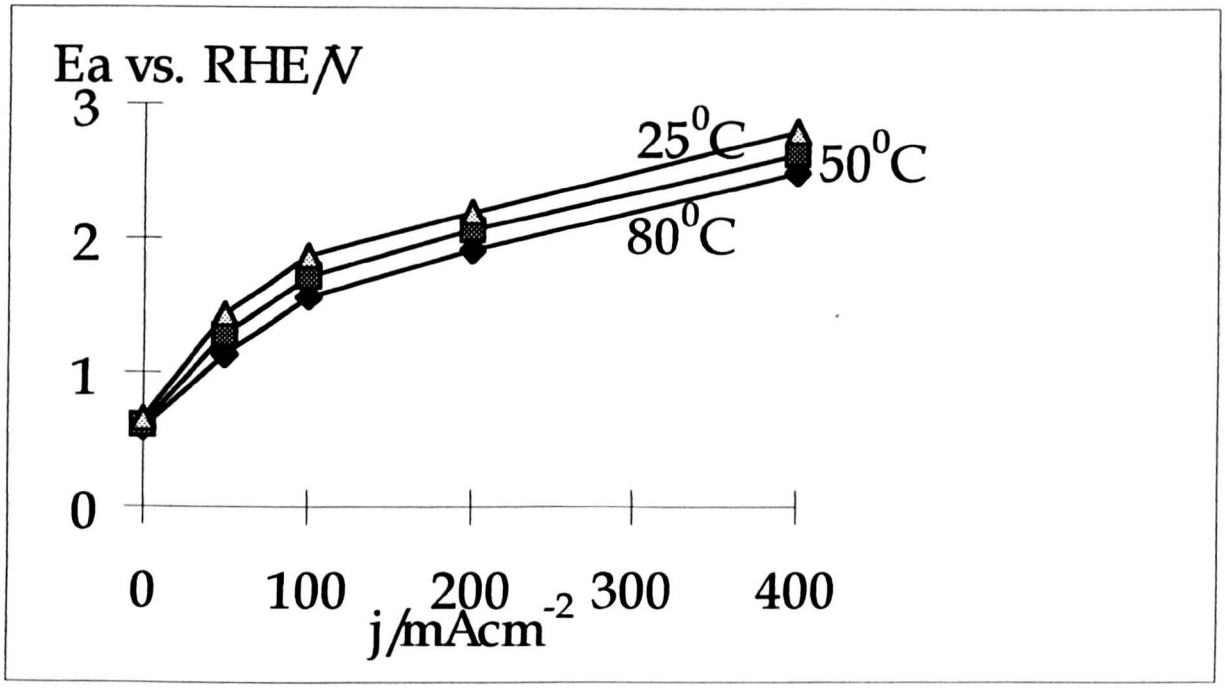

Figure 5.9. Steady-state anodic polarisation curves for water electrolysis-temperature effect. Anode and cathode: Pt/Ti mesh (2 mg Pt cm^{-2}); Electrolytes: 4.5 M KOH solutions; The static cell.

The effect of temperature on the oxygen evolution Tafel behaviour is shown in figures 5.10 and table 5.5.

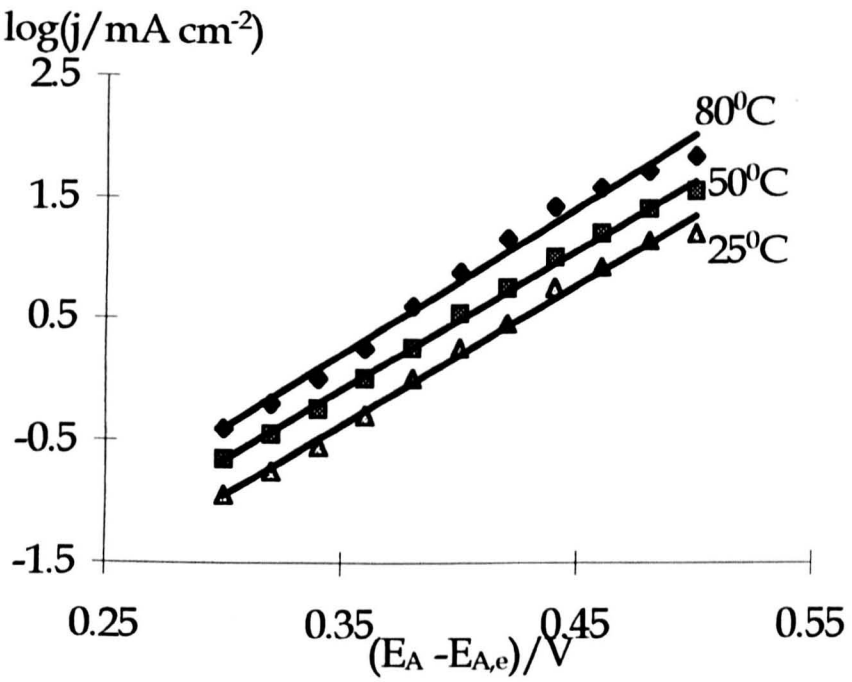

Figure 5.10 Tafel plots for oxygen evolution reaction on Pt/Ti electrode - Temperature effect. Electrolyte: 4.5 M KOH solutions; Anode and cathode: Pt/Ti mesh (2 mg Pt cm^{-2}); The static cell.

Raising the cell temperature has similar effect on the kinetics as that of increasing the concentration. The Tafel slope is constant, i.e., 66 mV/decade at all temperatures. The exchange current densities increase from $10^{-7.65}$ to $10^{-7.40}$ A cm^{-2} when the temperature increases from 25 to 80°C. There are different reports about temperature effect on Tafel parameters for oxygen evolution, e.g., at Pt electrode in 0.5 M H_2SO_4 solution, the Tafel slopes decrease only from 107 to 90 mV/decade and the exchange current densities from $7.6x10^{-10}$ to $1.3x10^{-11}$ A cm^{-2} when the temperature increases from 20 to 80°C [1]; on the other hand, the Tafel slopes increase only from 48 to 98 mV/decade and the exchange current densities from $6.0x10^{-8}$ to $3.0x10^{-4}$ A cm^{-2} when the temperature increases from 70 to 150°C at Ni electrode in 50% KOH [5].

Effect of pH - The oxygen evolution is affected by pH, as shown in figure 5.11.

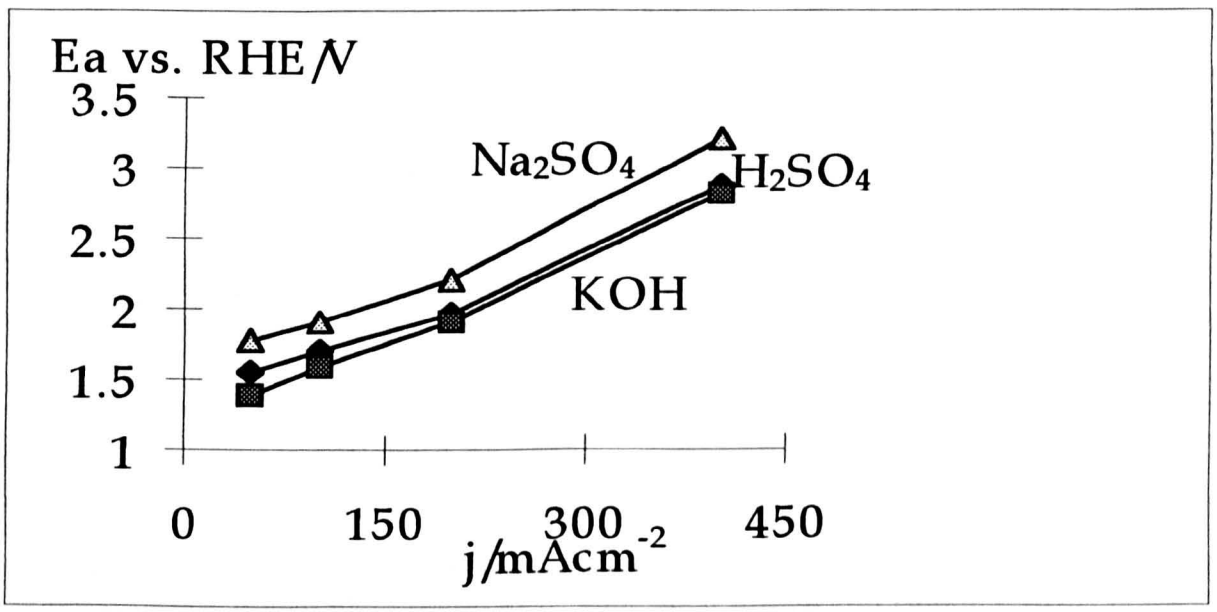

Figure 5.11. Steady-state anodic polarisation curves for water electrolysis-pH effect. Electrolyte concentration: 1 M; Anode and cathode: Pt/Ti mesh (2 mg Pt cm^{-2}); Temperature: 80°C; The static cell.

The anodic current density was about 200, 190, and 140 $mAcm^{-2}$ at 2.0 V vs RHE for KOH, H_2SO_4 and Na_2SO_4 anolyte, respectively. The difference between alkaline and acidic media is small, although at the concentration of 1 M, alkaline medium gave the best performance.

5.4.3. Hydrogen Evolution

The hydrogen evolution reaction is also sensitive to the operation conditions and some steady-state measurement data are given in this section.

Effect of Concentration - The effect of electrolyte concentration on the hydrogen evolution is displayed in figure 5.12. The cathode potential shifts to less negative values with increasing concentration at a given current density. The effect is more pronounced at higher current density.

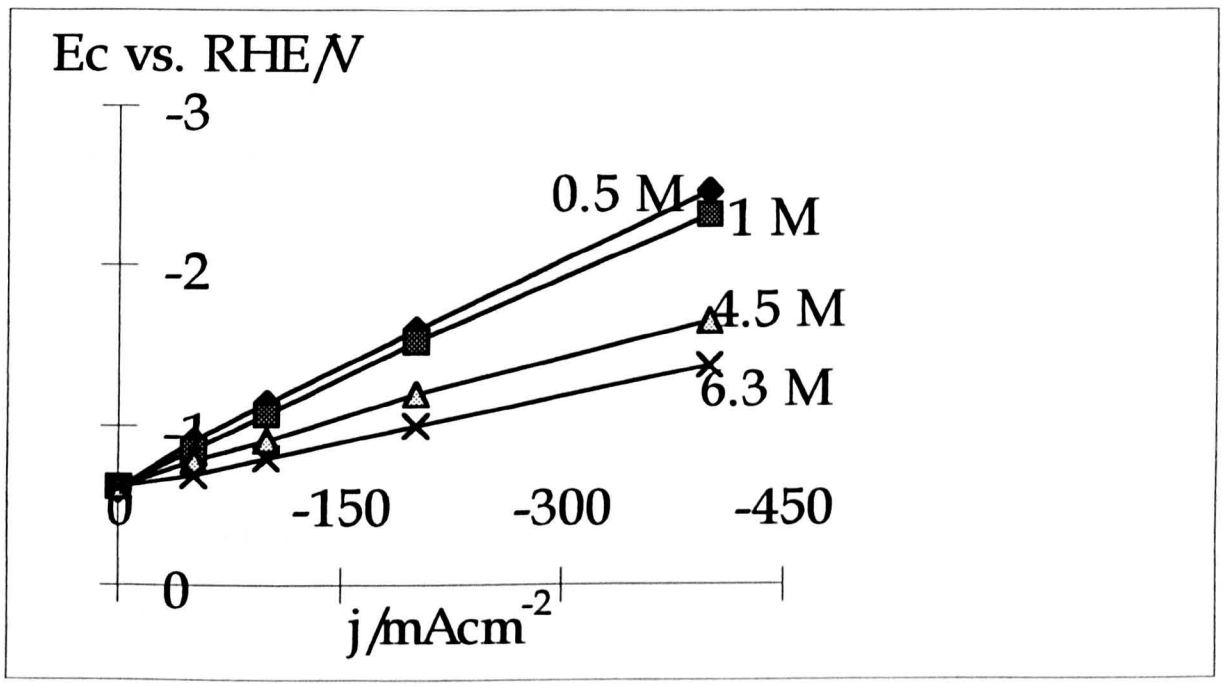

Figure 5.12. Steady-state cathodic polarisation curves for water electrolysis-Concentration effect. Electrolyte: KOH solutions; Anode and cathode: Pt/Ti mesh (2 mg Pt cm^{-2}); Temperature: 80°C; The static cell.

The effect of concentration on the hydrogen evolution kinetics is shown in figure 5.13 and table 5.6. Similar as oxygen evolution, there is improvements in the hydrogen evolution kinetics when increasing concentration. Quantitatively, increasing the KOH concentration from 0.5 to 6.3 M leads no effect on the Tafel slope, i.e., 90 mV/decade. The exchange current densities increase from $10^{-4.05}$ $10^{-3.60}$

A m^{-2} in an overpotential range of 0.11 to 0.16 V. At Pt electrode in 0.5 M NaOH solution, the reported Tafel slope is 117 mV/decade and the exchange current density are $1.0x10^{-3.5}$ A m^{-2} [8]. These differences cannot be explained at the moment.

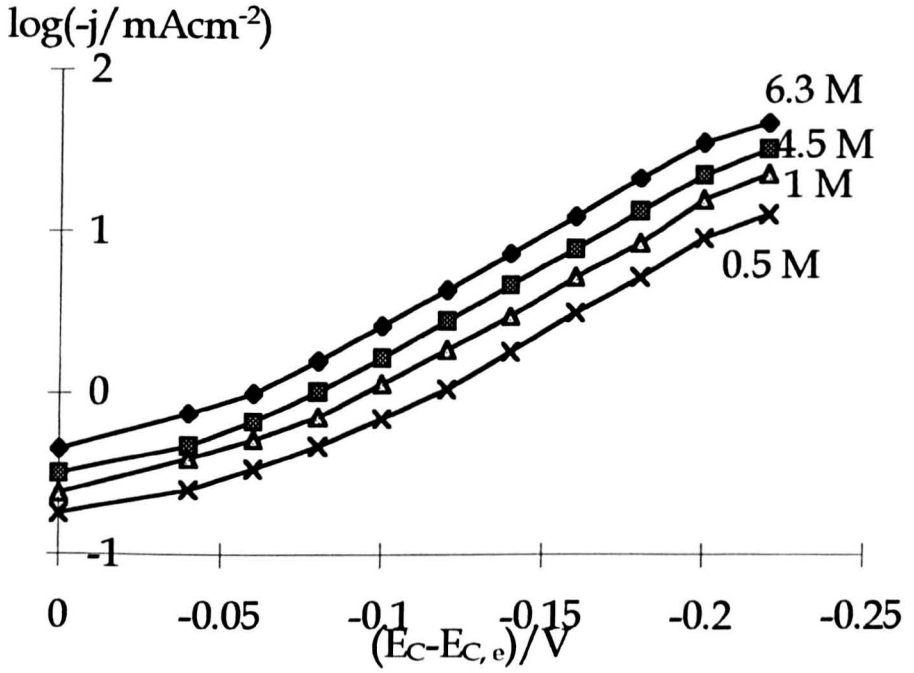

Figure 5.13. Tafel plots for hydrogen evolution reaction on Pt/Ti electrode - Concentration effect. Electrolyte: KOH solutions; Anode and cathode: Pt/Ti mesh (2 mg Pt cm^{-2}); Temperature: 80°C; The static cell.

Table 5.6. Tafel parameters for hydrogen evolution in different conditions

C_{KOH}/M	t/°C	-b/mVdecade^{-1}	-j_0/Acm^{-2}
0.5	80	90	$10^{-4.05}$
1	80	90	$10^{-4.12}$
4.5	80	90	$10^{-3.88}$
6.3	80	90	$10^{-3.60}$
4.5	50	90	$10^{-3.95}$
4.5	25	90	$10^{-4.00}$

As discussed above, the uncompensated IR potential drop may be large and it was difficult to measure and correct during the measurements and the analysis of the data. The above data, therefore, can only give a qualitative picture about the effect of concentration on the hydrogen evolution kinetics.

Effect of Temperature - Increasing the temperature shifts the cathode potential to less negative values at a constant current density (figure 5.14).

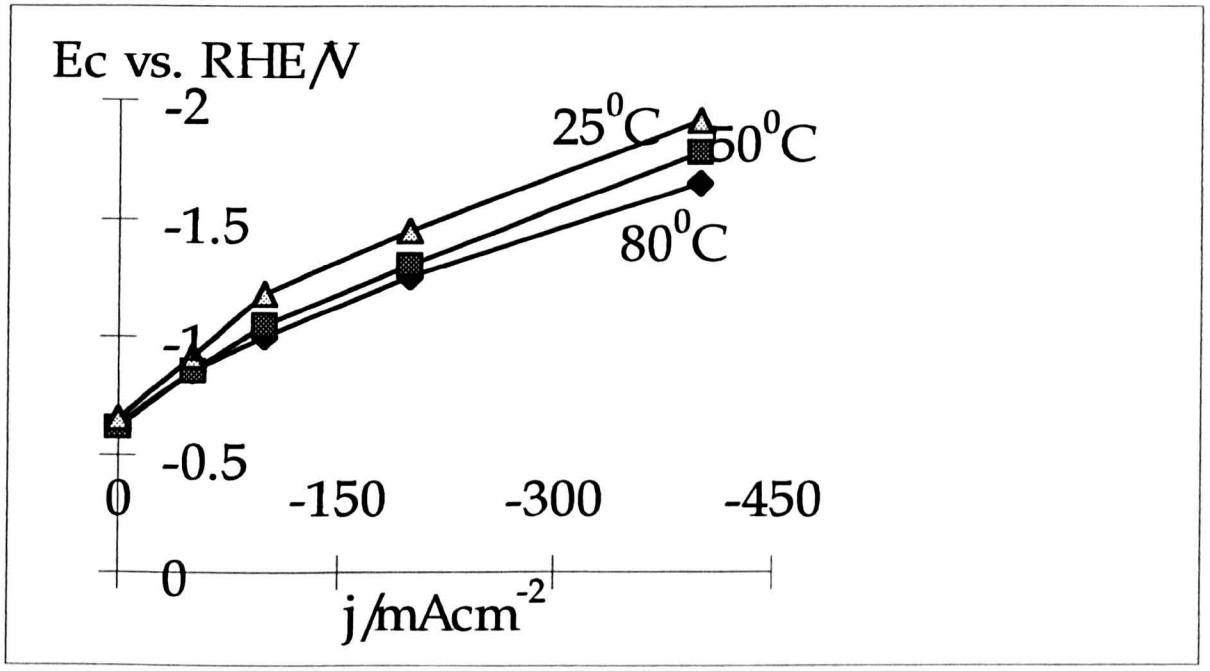

Figure 5.14. Steady-state cathodic polarisation curves for hydrogen evolution-Temperature effect. Anode and cathode: Pt/Ti mesh (2 mg Pt cm^{-2}); Electrolyts: 4.5 M KOH solutions; The static cell.

The Tafel plots for the effect of temperature effect are presented in figure 5.15 and Tafel parameters are recorded in table 5.6.

The Tafel slope is constant at 90 mV/decade. The exchange current densities increase from $10^{-4.0}$ to $10^{-3.88}$ A m^{-2} when the temperature increases from 25 to 80°C. The reported Tafel slopes increase from 142 to 194 mV/decade and the exchange current densities from 4.8×10^{-4} to 9.7×10^{-3} A cm^{-2} when the temperature increases from 70 to 150°C at Ni electrode in 50% KOH [5]. The difference between the reported data and the data of this work may be partily due to different conditions used. Further investigation is needed to complete understanding this difference.

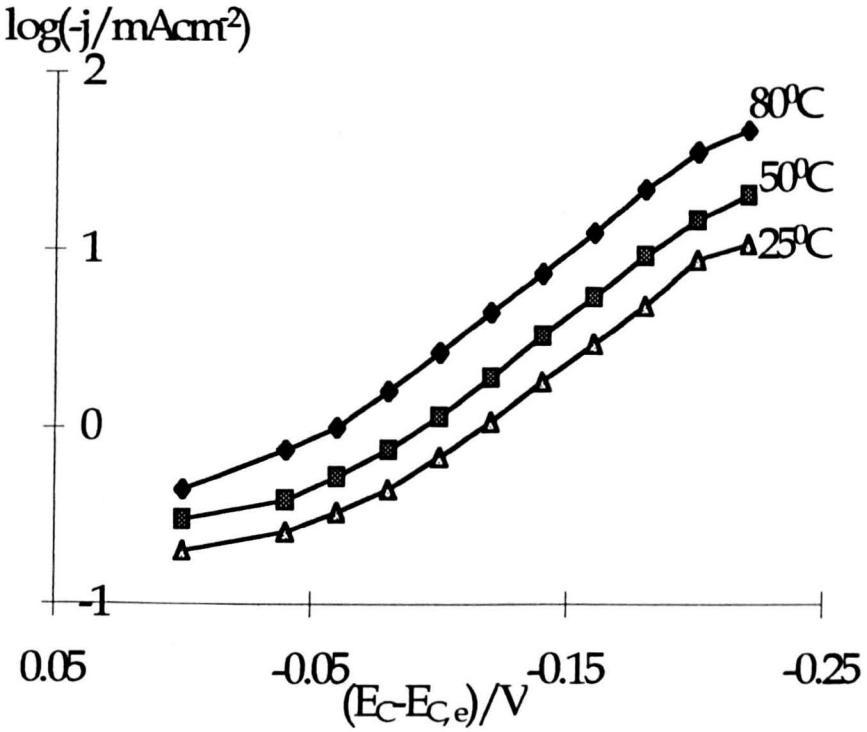

Figure 5.15 Tafel plots for hydrogen evolution reaction on Pt/Ti electrode - Temperature effect. Electrolyte: 4.5 M KOH solutions; Anode and cathode: Pt/Ti mesh (2 mg Pt cm^{-2}); The static cell.

Effect of pH - Figure 5.16 records the effect of electrolyte on the polarisation curves.

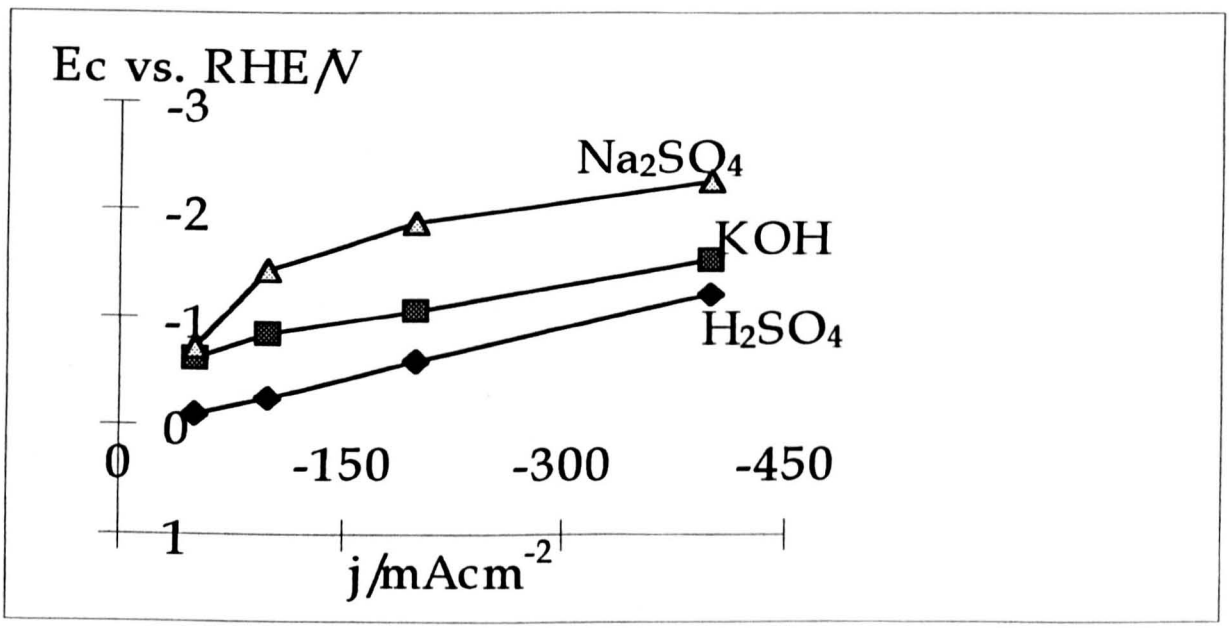

Figure 5.16. Steady-state polarisation curves for hydrogen evolution -pH effect. Electrolyte concentration: 1 M; Anode and cathode: Pt/Ti mesh (2 mg Pt cm^{-2}); Temperature: 80°C; The static cell.

Large difference can be seen in the cathodic polarisation curves. For example, at a current density of 300 $mAcm^{-2}$, the cathode potential is -0.9, -1.4, and -2.1 V vs RHE for H_2SO_4, KOH and Na_2SO_4 catholyte, respectively. Sulphuric acid appears to be the best medium for the hydrogen evolution reaction.

5.5. Electrochemical Behaviours In The Rotary Cell

The water electrolysis process was intensified using centrifugal fields in a relatively simple cell, with a stationary pool of electrolyte, far from being optimised to reduce cell voltage for water electrolysis. The focus of the work is to assess the impact of the application of an acceleration field on the cell voltage and on the electrode potentials. Effects of concentration and temperature were investigated.

5.5.1. Cell Voltage

Effect of a Relative Acceleration Rate - Figure 5.17 illustrates typical cell voltage-current density plots obtained with the rotary cell using 4.5 M KOH solution at 80°C. It can immediately be seen that there is a marked beneficial effect of an increase in rotating speed on the performance of the cell. The application of acceleration field drastically increases the current at fixed cell voltage or diminishes the cell voltage for a constant current density, e.g., at 4 kAm^{-2}, the cell voltage reduction (based on the cell voltage obtained in the static cell) is 230 mV, 390 mV, and 450 mV at 400, 800, and 1100 rpm, respectively.

The effect was more significant at high current densities than at low current densities. For example, at 2 kAm^{-2}, the cell voltage reduction is only 80 mV, 140 mV, and 190 mV at 400, 800, and 1100 rpm, respectively.

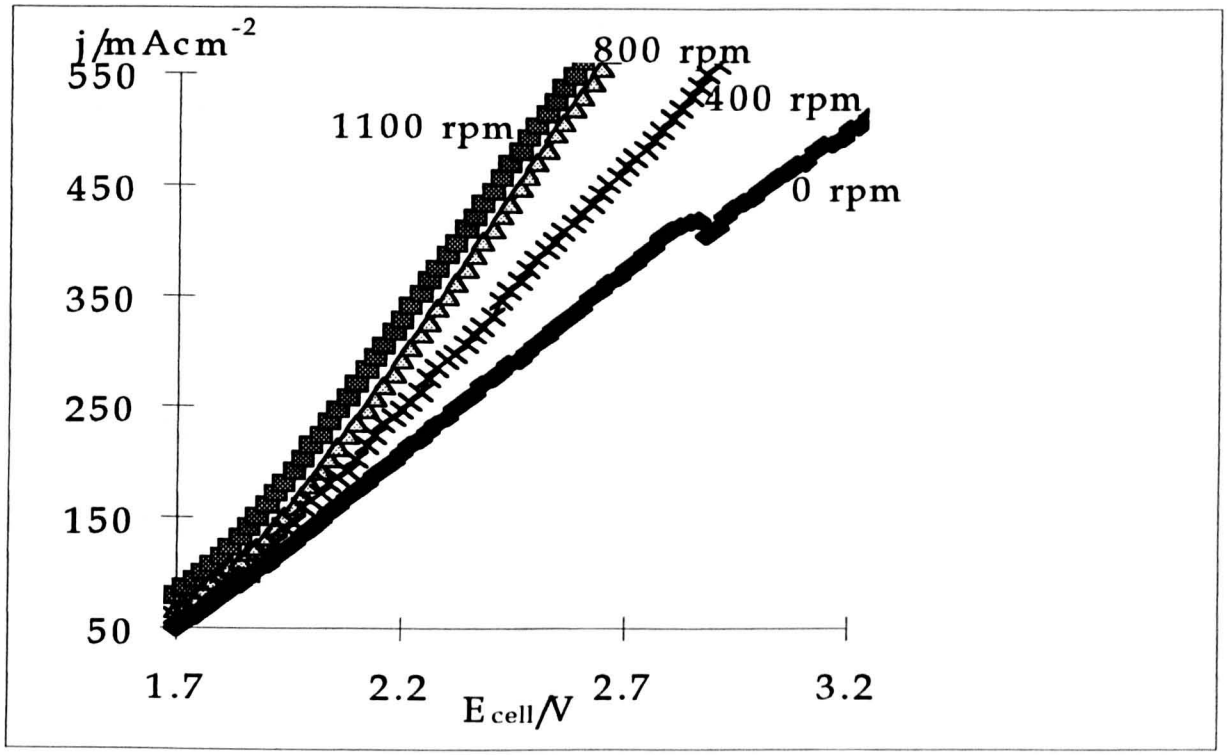

Figure 5.17. Typical cell voltage versus current density curves for water electrolysis. Anode and cathode: Ni foam; Electrolytes: 4.5 M KOH solutions; Scan rate: 5 mV/s; Temperature: 80°C; The rotary cell.

Effect of Concentration - In a centrifugal field, the performance of the rotary cell voltage is concentration sensitive, as shown in figure 5.18.

The cell voltage falls dramatically at a fixed current density, as shown in figure 5.18. For example, at 3 kAm^{-2} and 0 rpm, about 3.80, 3.10, 2.80, 2.55, 2.46 V in 0.1, 0.5, 1, 4.5, and 6.3 M KOH solutions, respectively. This is a result of a reduction in the electrode potentials and the increase in the electrolyte conductivity.

The cell voltage reduction, due to the effect of centrifugal fields, is also related to the KOH concentrations. At a fixed current density, the reduction in cell voltage with rotating speed decreases as the concentration of KOH increases. The maximum cell voltage reduction, of approximately 1.0 V, was achieved in 0.1 M KOH solution. It is

noteworthy that more significant cell voltage reduction was achieved in the concentrated solutions at higher operating current densities.

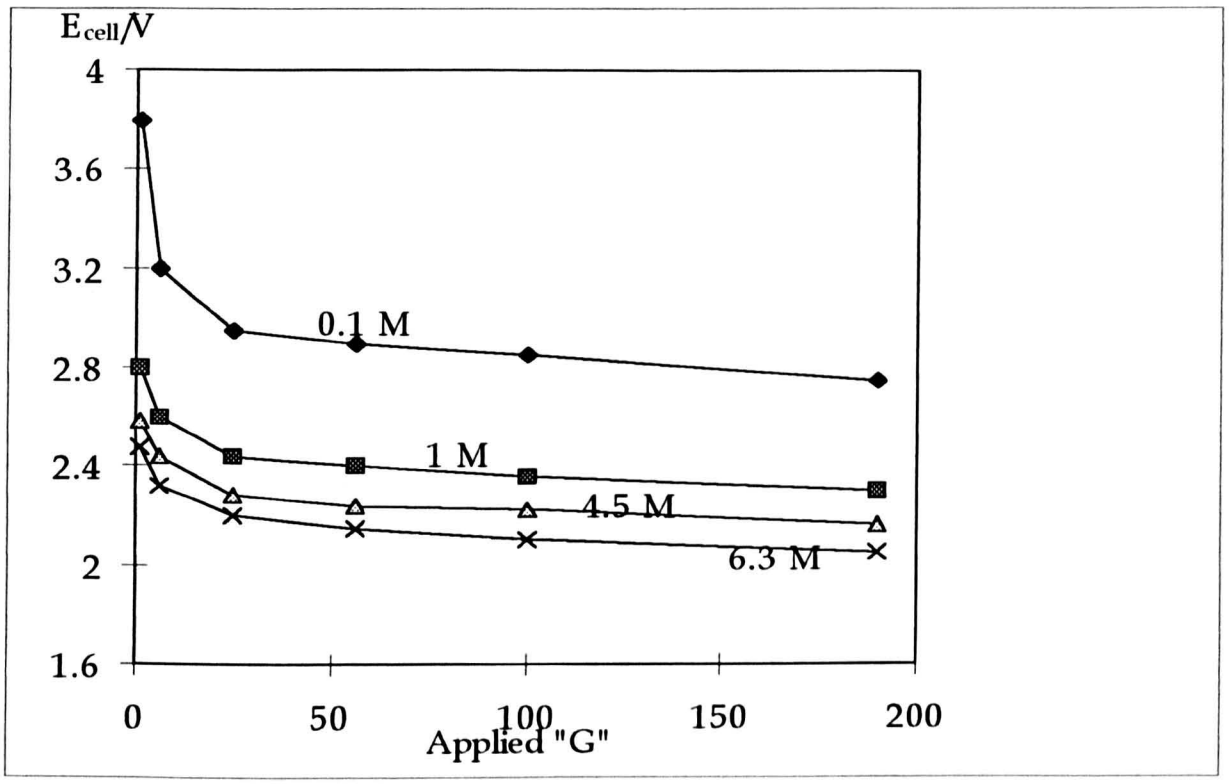

Figure 5.18. Cell voltage (at 3 kAm^{-2}) as a function of KOH concentration.
Anode and cathode: Ni foam; Scan rate: 5 mV/s; Temperature: 80°C; The rotary cell.

The performance enhancement of the rotary cell is mainly attributed to the effects of centrifugal fields on the mass transfer rate of the electrolytes and on gas disengagement. In dilute electrolyte, the supply of the electrolytes was significantly enhanced in centrifugal fields and therefore the gas evolution processes were significantly enhanced. Also, the high acceleration field efficiently removes the gas bubbles from the electrode surfaces. This reduces the cell resistance and therefore the ohmic potential drop in the cell.

Effect of Temperature - An increase in cell temperature reduces the cell voltage as shown in figure 5.19.

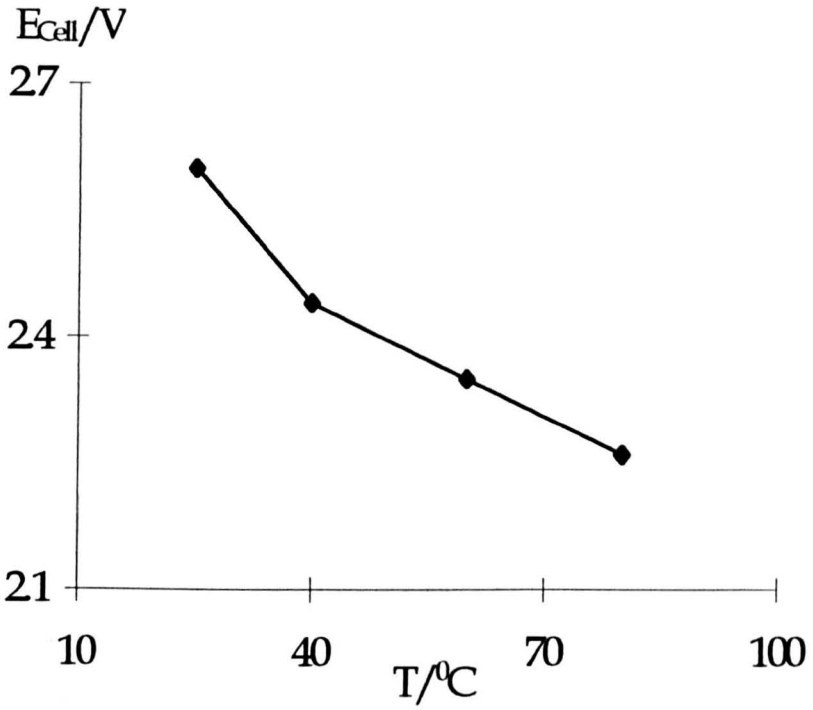

Figure 5.19. Cell voltage as a function of temperature. Anode and cathode: Nickel foam; Electrolyte: 6.3 M KOH; Current density: 3 kAm^{-2}; Scan rate: 5 mV/s; The rotary cell.

The cell voltage decreases by about 200 mV at 3 kAm^{-2} in the static cell when the temperature is increased from 25 to 80°C. Correspondingly, the cell voltage reduction, as shown in figure 5.20, increases to about 300 mV at 1100 rpm. It is clear that high temperature will benefit the intensification of water electrolysis.

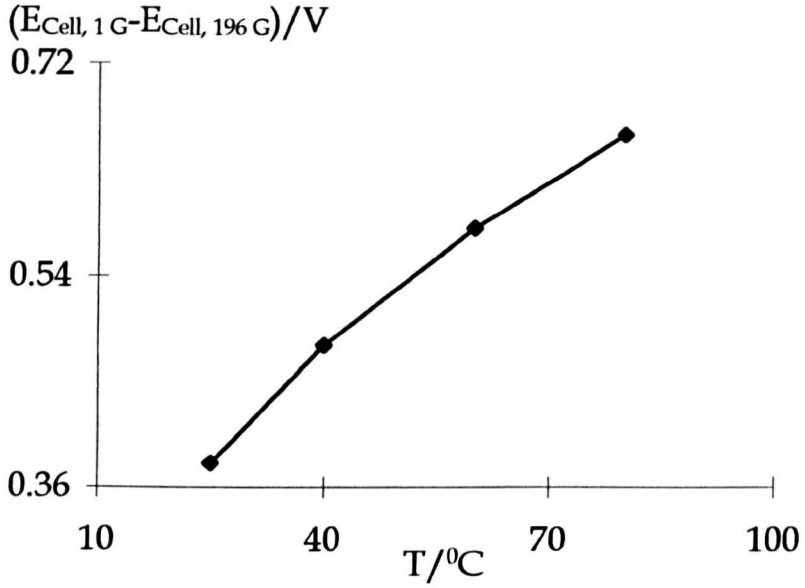

Figure 5.20. Cell voltage reduction as a function of temperature. Anode and cathode: Nickel foam; Electrolyte: 6.3 M KOH; Current density: 3 kAm^{-2}; Scan rate: 5 mV/s; The rotary cell.

Effect of Gap Between the Electrodes - The cell with the finite gap of 2 mm between electrodes and membrane was compared with zero gap cell. For the stationary cells, the zero gap cell gave larger current density than the finite-gap cell for water electrolysis, as shown in figure 5.21.

For example, at 300 mA cm^{-2}, the cell voltage reduction when the rotating speed changed from 0 rpm to 1100 rpm was 400 and 280 mV for the 2 mm-gap and no-gap cell, respectively. This means that centrifugal fields will give much more benifit when a finite-gap cell was used. This may be due to the lower resistance of the zero gap cell in which the electrodes and membrane were directly contacted. More investigations are needed to clarify the reasons responsible for the above observation.

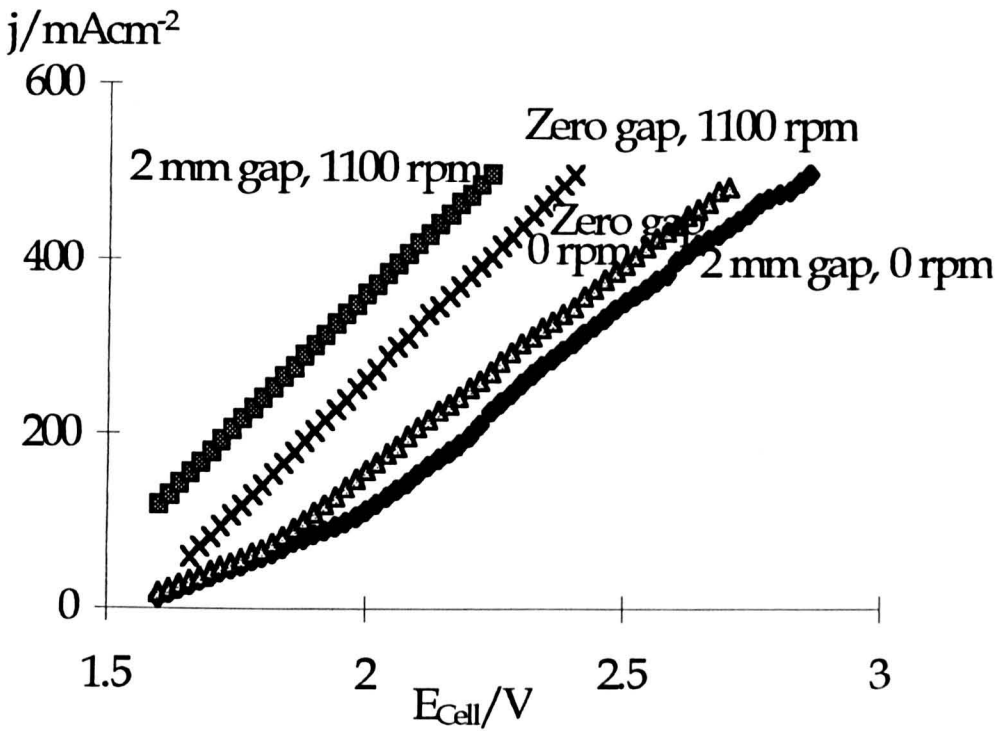

Figure 5.21. Typical cell voltage versus current density curves for water electrolysis. Anode: DSA; Cathode: Stainless steel foam; Electrolytes: 4.5 M KOH solutions; Scan rate: 5 mV/s; Temperature: 80°C; The rotary cell.

5.5.2. Oxygen and Hydrogen Evolution Reactions

The cell behaviour is determined by the individual electrode behaviours which are also strongly related to the rotating speed as briefly described in the following sections.

Effect of a Acceleration Rate - The O_2 or H_2 evolution potentials change dramatically in a centrifugal field (figure 5.22). Both anode and cathode polarisation curves at 0 rpm are similar to those reported in the literature [6, 19, 31]. The results obtained in the rotary cell demonstrate that centrifugal fields increase the current densities at a constant electrode potentials. For example, at 1.25 V vs. RHE, the anode current density is 340, 455, 530, and 570 mA cm^{-2}; at -1.45 V vs. RHE, the cathode current

density is -383, -552, -605, and -650 mA cm^{-2} at 0, 400, 800, and 1100 rpm, respectively.

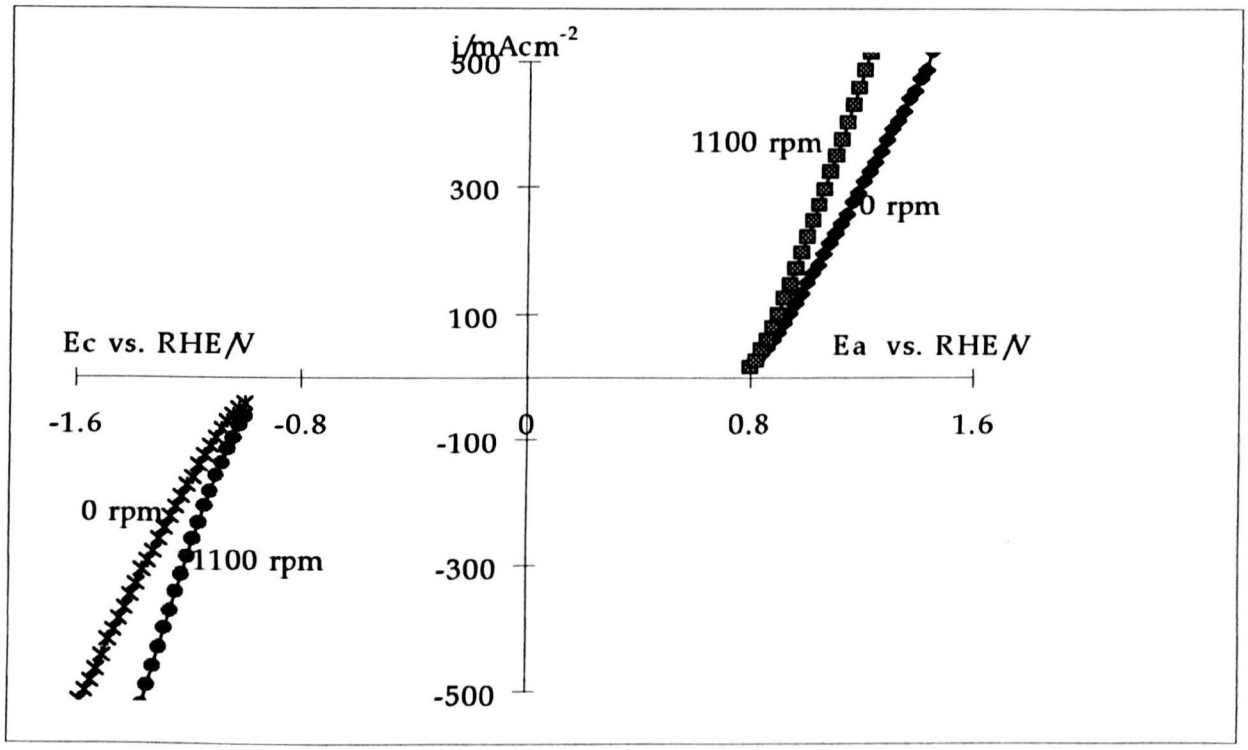

Figure 5.22. Electrode polarisation curves at differentd rotating speeds for water electrolysis. Anode and Cathode: Nickel foam; Electrolyte: 4.5 M KOH solution; Scan rate: 5 mV/s; Temperature: 25°C; The rotary cell.

The electrode potential reductions are also influenced by the applied acceleration field, as shown in figure 5.23. The data demonstrate that centrifugal fields have a large effect on the oxygen and hydrogen evolution reactions; electrode potentials are reduced by several hundred millivolts over the range of applied relative acceleration rate of 10 to 200 G. The large interphase buoyancy force, which controls the fluid dynamic behaviour of the water electrolysis cell operating in a centrifugal field, causes a very high interphase slip velocity and therefore increases the gas disengagement. This increases the exposed electrode area and leads to lower anode and cathode overpotentials. Evidently, it is the reduction in electrode potential that are mainly responsible for the cell voltage reduction of the rotary cell.

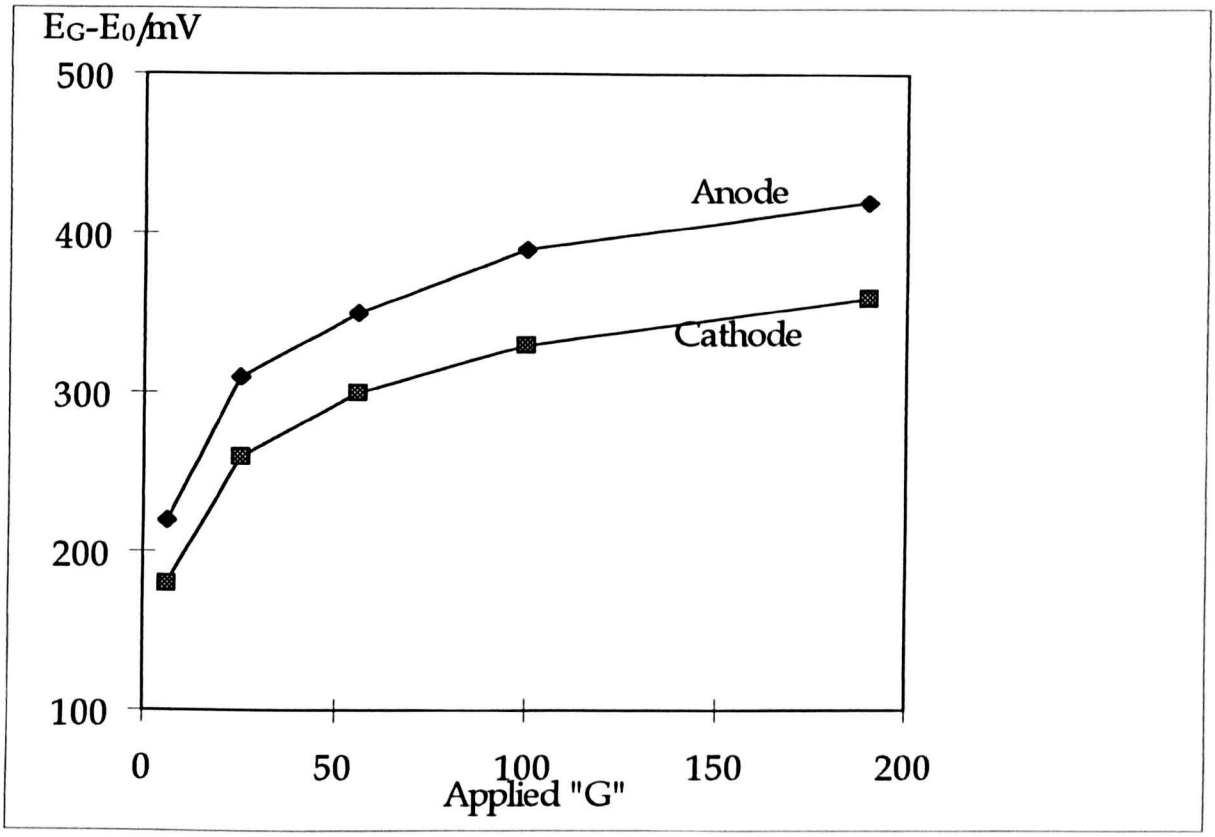

Figure 5.23. Electrode potential reduction (at 3 or -3 kAm^{-2}) as a function of applied "G" values. Anode and cathode: Pt/Ti mesh (2 mg Pt cm^{-2}); Electrolyte: 4.5 M KOH solution; Scan rate: 5 mV/s; Temperature: 80°C; The rotary cell.

Figures 5.24 shows typical Tafel plots for oxygen evolution reaction. The Tafel slope of the oxygen evolution obtained in an overpotential range of 0.5 to 0.55 V from figure 5.24 is 68 mV/decade both in the static cell and in the rotary cell. The exchange current densities obtained by extrapolating to $(E_A-E_{A,e})=0$ are $10^{-7.4}$ and $10^{-7.66}$ A cm^{-2} for the rotary cell and the static cell respectively. The reported data for oxygen evolution in a static cell with Ni electrodes in 50% KOH at 70°C are 48 mV/decade and $6x10^{-8}$ A cm^{-2} [5].

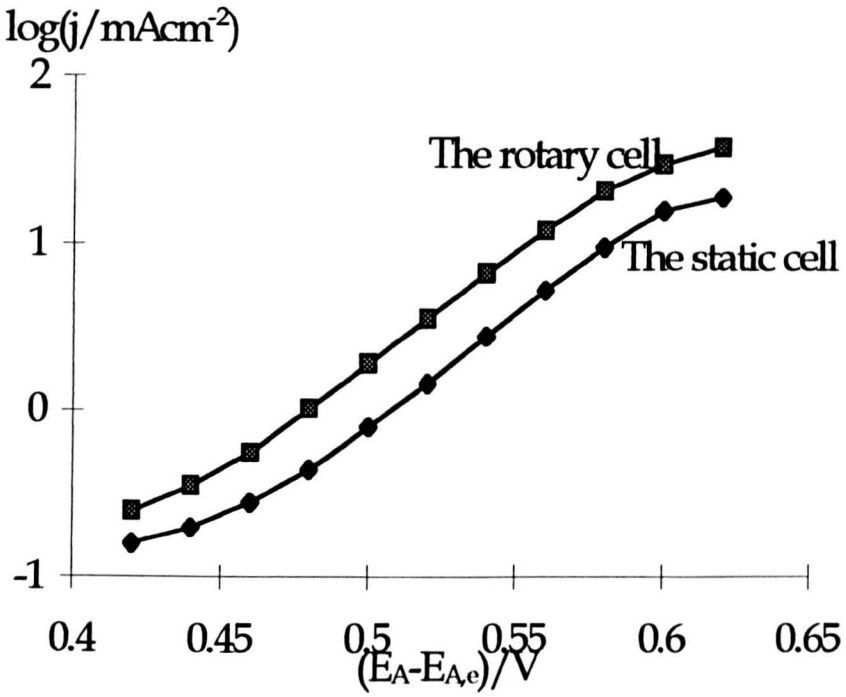

Figure 5.24. Tafel plots for oxygen evolution reaction on Ni foam electrode - Effect of acceleration rate. Anode and Cathode: Nickel foam; Electrolyte: 4.5 M KOH solution; Temperature: 80°C; The rotary cell.

Figures 5.25 shows typical Tafel plots for hydrogen evolution reaction. The Tafel slopes of the hydrogen evolution obtained in an overpotential range of - 0.1 to - 0.17 V from figure 5.25 is - 90 mV/decade. The exchange current densities obtained by extrapolating to $(E_C-E_{C,e})=0$ are $10^{-3.6}$ and $10^{-3.9}$ A cm^{-2} for the rotary cell and the static cell respectively. The data show the effect of acceleration fields on the Tafel parameters for hydrogen evolution reaction. The reported data for hydrogen evolution in a static cell with Ni electrodes in 50% KOH at 70°C are 142 mV/decade and 4.8×10^{-4} A cm^{-2} [5].

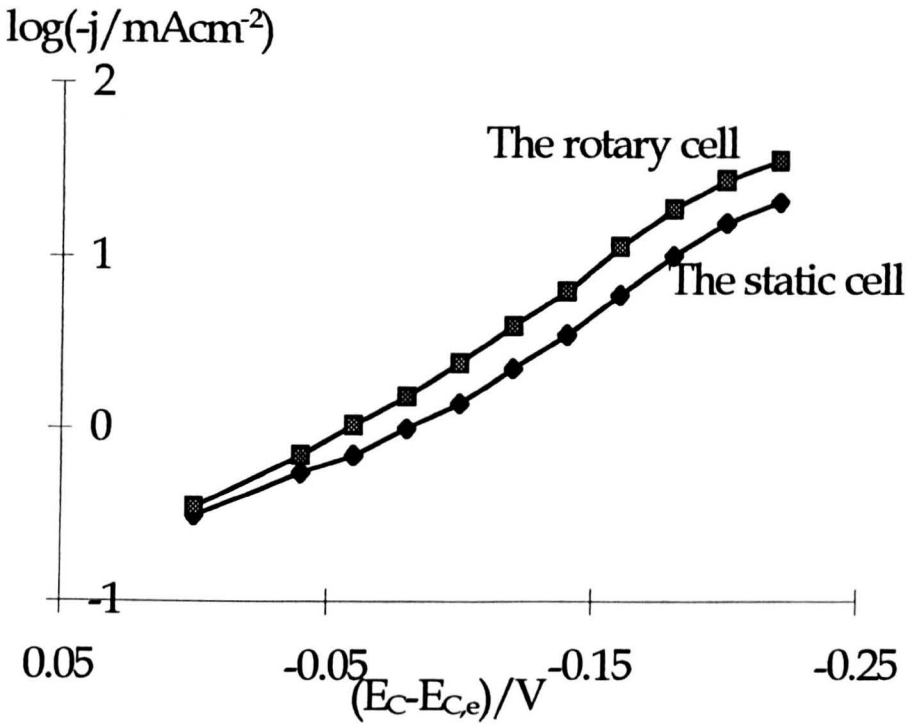

Figure 5.25. Tafel plots for hydrogen evolution reaction on Ni foam electrode - Effect of acceleration rate. Anode and Cathode: Nickel foam; Electrolyte: 4.5 M KOH solution; Temperature: 80°C; The rotary cell.

The improved performance in an electrolytic cell may arise from an increase in the real/apparent area factor or from an increase in rate constant and/or changes of reaction mechanism [32]. The different measuring potential range can lead varying Tafel parameters due to mechanism change [6]. These factors may result in difference between the reported data and the data of this work. Further investigation is needed to complete understanding this difference.

The improvement in the rotary cell performance, as indicated by the Tafel data, is small and can be partly explained by the increase in exposed electrode area arising from the centrifugal force. A complete understanding these results needs further research.

The Effect of Electrolyte Concentration - The anode and cathode potentials exhibit the similar trend to that for cell voltage. Data obtained at a constant anode potential of 1.25 V vs. RHE or cathode potential of -1.45 V vs. RHE are reported in figure 5.26.

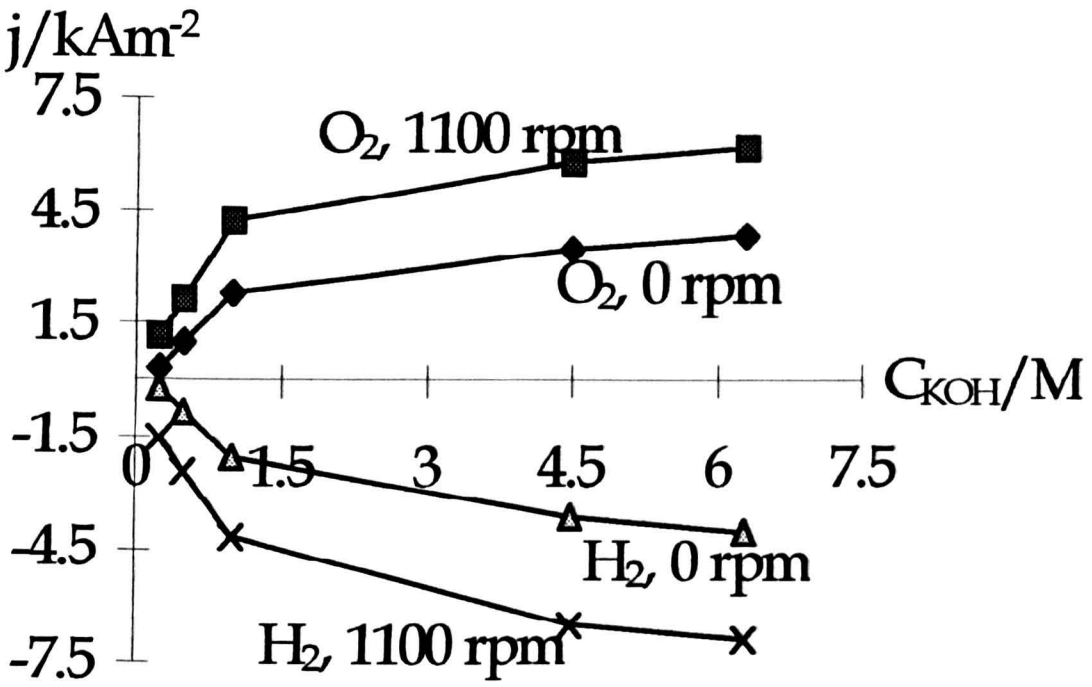

Figure 5.26. Electrode current densities as a function of KOH concentration for water electrolysis. Anode and cathode: Nickel foam; Anode potential: 1.25 V vs RHE; Cathode potential: -1.45 V vs. RHE; Scan rate: 5 mV/s; Temperature: 80°C; The rotary cell.

The anodic and cathodic current densities for the both cells increase rapidly when the electrolyte concentration increases from 0.25 M to 1 M, while with further increase in the concentration, the increase in current densities is slower. The much better performance in the concentrated KOH solutions, compared to that in the dilute solutions, is predominantly due to a decrease in ohmic resistance of the electrolytes. More importantly, at a constant potential, the current density increased in the rotary cell at a greater rate than in the static cell. At 1100 rpm, the average

increases in anode current density are 3.87 kAm^{-2}/M from 0.25 M to 1 M and 0.47 kAm^{-2}/M from 1 M to 6.3 M compared to 2.81 and 0.26 kAm^{-2}/M obtained in the static cell. Similarly, the cathode current density rate are 3.63 kAm^{-2}/M from 0.25 to 1 M and 0.50 kAm^{-2}/M from 1 to 6.3 M, which compared to 2.84 and 0.32 kAm^{-2}/M for the static cell.

Although the concentrated KOH solutions made the cell performance improvement less than that of the dilute solutions, concentrated electrolyte should be utilized in water electrolysis cells to achieve high operating current density at low cell voltage and to achieve a higher intensification.

Effect of Temperature - Figure 5.27 records the effect of temperature on the oxygen and hydrogen evolution at Pt/Ti mesh electrodes in 4.5 M KOH solutions.

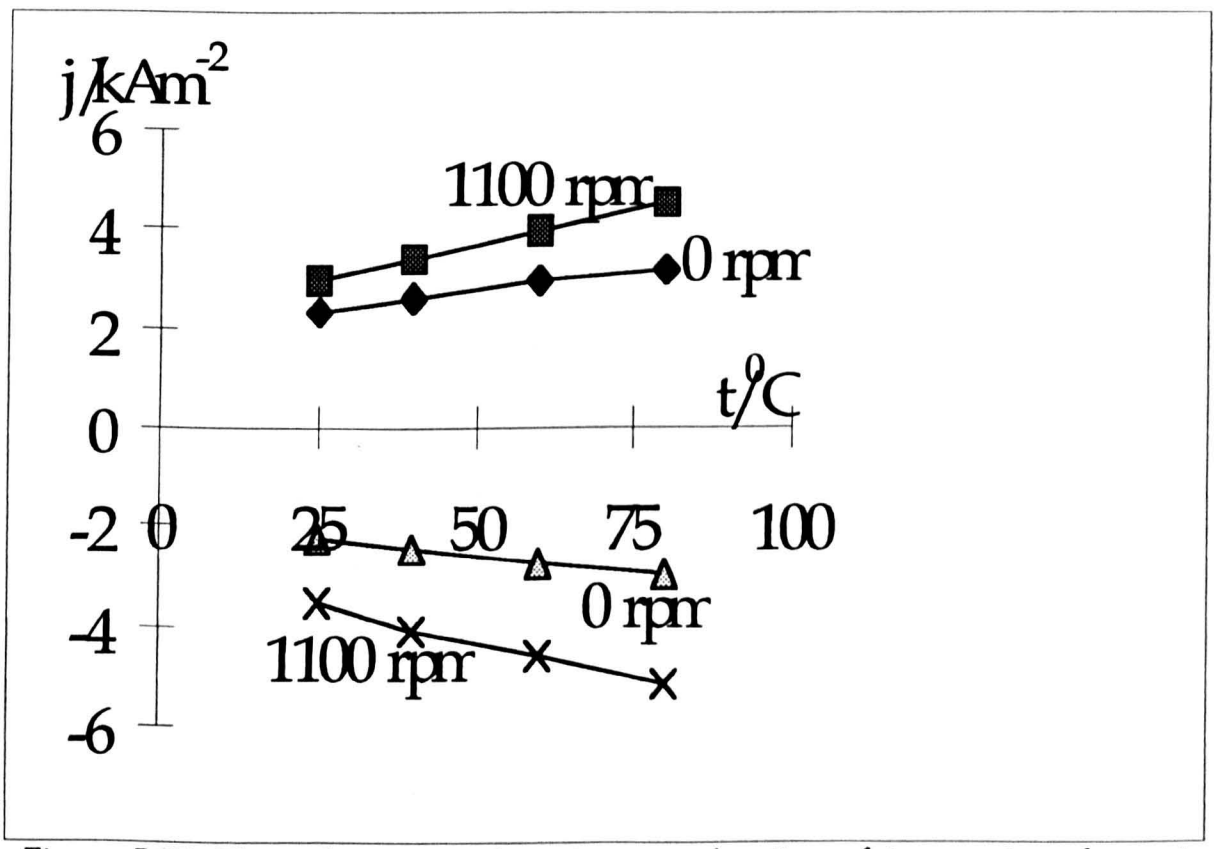

Figure 5.27. Electrode current densities as a function of temperature for water electrolysis. Anode and cathode: Pt/Ti mesh (2 mg Pt cm^{-2}); Anode potential: 1.40 V vs RHE; Cathode potential: -1.70 V vs. RHE; Electrolytes: 4.5 M KOH solutions; Scan rate: 5 mV/s; The rotary cell.

Anode and cathode current density both increase with increasing cell temperature in both the static and the rotary cell. The new discovery in this work is that the temperature effect is intensified in an acceleration field, i.e., the current density increases faster with temperature in the rotary cell than in the static cell, as indicated in figure 5.27. The rates of current density increase are 28.9 $Am^{-2}/^{0}C$ for the anode and 29.3 $Am^{-2}/^{0}C$ for the cathode at 1100 rpm in the rotary cell. In the static cell, the values are 14.6 $Am^{-2}/^{0}C$ for the anode and 12.9 $Am^{-2}/^{0}C$ for the cathode. This means that high temperatures are better for efficient performance of process intensification in a rotary water electrolysers.

5.5.3. Summary

The results described in this section demonstrate that centrifugal fields provide a powerful means for intensifying water electrolysis. Most of the improvements arise directly from the improvement in mass transport and from the removal of gas bubbles from the electrodes in the high acceleration field. The relative acceleration rate, i.e., rotating speed, has significant effect on the cell voltage. The maximum benefits were resulted at high currents where much more O_2 as well as H_2, was evolved at the anode or the cathode, respectively. This proves again that centrifugal field affects the gas evolution processes in a much more significant extent than the gas consuming reactions.

5.6. Conclusions

The results cited above testify the following conclusions:

• The water electrolysis process can be significantly intensified in centrifugal fields. The outstanding performance was demonstrated by subjecting of the cell, including the electrolytes, to a centrifugal field to promote mass transport and to disengage

gas bubbles from the electrode surfaces. The high acceleration field affects not only the cell voltage, but also the anode and cathode potentials. A cell voltage reduction of up to 700 mV , an anode potential reduction of up to 500 mV and a cathode potential reduction of up to 350 mV at 3 kAm^{-2} were achieved in an acceleration field of 190 G at 80°C, compared with a static cell. These benefits result from the centrifugal force in the rotary water electrolyser, which maximise mass transport rate of the reactants and minimise ohmic resistance. It is obvious that an application of high acceleration field in commercial water electrolysis cells can lead to a substantial reduction in electric energy and, consequently, in the operational cost of the system.

- The results demonstrate again that centrifugal fields affect gas evolution processes more significantly than gas consuming process.
- Apart from using high acceleration field, the most important factor affecting the the intensification is the effectiveness of the electrodes for the oxygen and hydrogen evolution reactions. Nickel foam shows the best performance in alkaline media due to its high density of catalyst. Platinised titanium mesh also gave encouraging results and could be used in acidic as well as alkaline media.
- Concentrated electrolyte solution and high temperature are important for high efficiency performance, i.e., operating water electrolysers at low cell voltage and high current density. An increase in the electrolyte concentration can lead to a dramatic reduction in the cell resistance. Interestingly, both the effect of concentration and of temperature were intensified in centrifugal fields.

5.7. References for Chapter 5

[1] Kim Kinoshita, "Electrochemical Oxygen Technology", Chapter 7, John Wiley & Sons, Inc., New York, 1992.

[2] D. Pletcher and F. C. Walsh, "Industrial Electrochemistry", 3rd Edition, Chapter 5, Chapman & Hall, London, 1993.

[3] A. Yildiz and K. Pekmez, NATO ASI Ser., Ser. E, 295, 45, 1995.

[4] G. Lodi, E. Sivieri, A. de Battisti and S. Trasatti, J. Appl. Electrochem., 8, 135, 1978.

[5] A. C. Ferreira, E. R. Gonzalez, E. A. Ticianelli, L. A. Avaca, and B. Matvienko, J. Appl. Electrochem., 18, 894, 1988.

[6] T.-C. Wen and C.-C. Hu, J. Electrochem. Soc., 139, 2158, 1992.

[7] N. Spataru, J.-G. Le Helloco, and R. Durand, J. Appl. Electrochem., 26, 397, 1996.

[8] C. F. Zinola, A. M. Castroluna, W. E. Triaca and A. J. Arvia, J. Appl. Electrochem., 24, 531, 1994.

[9] E. Thomson, US Patent, 1,701,346, 1929.

[10] T. B. Hoover, US Patent, 3,119,759, 1964.

[11] N. Tsuji, Japan Patent, 81 96,084, 1981.

[12] E. A. Chapman, Chem. Process Eng., 387, 1965.

[13] D. H. Smith, in "Industrial Electrochemical Process", (Edited by A. T. Kuhn), Elsevier, Amsterdam, p.127, 1971.

[14] H. Wendt and G. Imarisio, J. Appl. Electrochem., 18, 1, 1988.

[15] H. Wendt and V. Plzak, Electrochim. Acta, 28, 27, 1983.

[16] F. Gutmann and O. J. Murphy, in "Modern Aspects of Electrochemistry", Volume 15 (R. E. White, J. O'M. Bockris, and B. E. Conway, Editors), p.1, Plenum, New York, 1983.

[17] D. E. Hall, J. Electrochem. Soc., 128, 740, 1981.

[18] M. H. Miles, Y. H. Huang, and S. Srinivasan, J. Electrochem. Soc., 125, 1931, 1978.

[19] T. Schmidt and H. Wendt, Electrochim. Acta, 39, 1763, 1994.

[20] L. D. Burke and J. F. Healy, J. Electroanal. Chem., 124, 327, 1981.

[21] M. E. G. Lyons and L. D. Burke, J. Chem. Soc., Faraday Trans. 1, 83, 299, 1987.

[22] B. V. Tilak, P. W. T. Lu, J. E. Coleman, and S. Srinivasan, in "Comprehensive Treatise of Electrochemistry", Volume 2 (J. O'M. Bockris, B. E. Conway, E. Yeager, and R. E. White, Editors), p.1, Plenum, New York, 1981.

[23] H. Kronberger, Chem.-Ing.-Tech., 63, 399, 1991.

[24] J. Clerc-Renaud, F. Leroux and D. Ravier, Eur. Patent Appl. 240,418, 4 June 1988.

[25] A. Nidola, PCT Int. Appl., 8,603,790, 20 April, 1986.

[26] J. F. Cairns, D. A. Denton and P. A. Izard, Eur. Patent 129,374, 5 August 1984.

[27] V. Plzak and H. Wendt, Chem. Ing. Tech., 58, 415, 1986.

[28] D. E. Grove, Platinum Met. Rev., 29, 98, 1985.

[29] M. M. Jaksic, Electrochim. Acta, 29, 1539, 1984.

[30] A. Lasia, Curr. Top. Electrochem., 2, 239, 1993.

[31] H. E. G. Rommal and P. J. Morgan, J. Electrochem. Soc., 135, 343, 1988.

[32] M. Vukovic, H. A.-Kozlowska and B. E. Conway, J. Appl. Electrochem., 12, 193, 1982.

Chapter 6. Methanol Oxidation And Direct Methanol Fuel Cells

6.1. Introduction

There is a growing world-wide interest in the development of hydrocarbon fuel cells for mobile applications because of environmental and legislative considerations. Such a cell would combine both the convenience of the internal combustion engine in terms of ease of fuel handling and the efficiency advantages of an electrochemical conversion device. The strategic goal is a fuel cell operating at low temperature and utilising a liquid fuel. Methanol would be an ideal fuel for fuel cell powered vehicles owing to its low cost, good availability, liquid form and high volumetric energy density. The direct methanol fuel cell (DMFC), in which methanol is directly electrooxidized at the anode, could possibly lead to simplified design and reduced weight and cost as compared with a power system having external methanol reformation and a hydrogen fuel cell. Thereby the DMFC is being considered as one of the most desirable fuel cells for small scale power units (<15 kW) [1,2]. The methanol oxidation reaction has therefore been an attractive topic since the 1960s.

Methanol Oxidation - The overall methanol oxidation reaction is simple:

$$CH_3OH+H_2O = CO_2+6H^++6e^- \quad \text{(acidic media)} \quad (6.1)$$

$$CH_3OH+8OH^- = CO_3^{2-}+6H_2O+6e^- \quad \text{(alkaline media)} \quad (6.2)$$

An acidic electrolyte is generally preferred for practical application since carbonate residues are formed in alkaline media but not in acidic electrolyte [3].

In this work, the initial target is to select and optimise the anodes for methanol oxidation and then, the process was expected to be intensified in a high acceleration field. The idea comes from the fact that CO_2 bubbles, the products of methanol oxidation, will stick to the anode surface, block the access of methanol to the anode

surface, reduce the contribution of the catalysts to the oxidation reaction, as well as increase the cell resistivity. Also, keep in mind that mass transport limitations were often observed in conventional methanol fuel cells. The use of centrifugal acceleration field should play some role in removing the bubbles from the electrode surface and enhancing mass transport for the system therefore improving the overall efficiency of the cells.

Direct Methanol Fuel Cells - Fuel cells were initially investigated by Sir William Grove in 1839. They are one type of Galvanic cell in which the free energy change of a chemical reaction is converted directly into electrical energy. For a fuel cell based on CH_3OH and O_2:

$$CH_3OH/Pt/\text{acid electrolyte}/Pt/O_2 \qquad (6.3)$$

the overall cell reaction is:

$$CH_3OH(l)+3/2O_2\,(g) = 2H_2O(l)+CO_2\,(g) \qquad (6.4)$$

for which E^0 = 1.212 V. In reality, fuel cells do not behave ideally due to several factors. Firstly, electrode kinetics are a major factor for voltage deviations. At increased current densities, both the anode and cathode potentials deviate from their ideal thermodynamic values, due to a number of thermodynamically irreversible processes, and lead to lower cell voltage. Secondly, the mass transport limitations will also lower the power output. Under the extreme conditions, reactants are consumed and products accumulated in amounts that may begin to exceed the rates at which reactants can be supplied or products removed, and the cell potential can fall dramatically to zero. Finally, the cell ohmic resistivity also contributes to reduce cell voltage.

Fuel cells experienced a rapid development in the sixties and seventies because they offer a number of environmental and engineering advantages as well as the maximum achievable energy efficiency. One of the most notable fuel cells is the direct methanol fuel cell (DMFC). It was pioneered by Shell and separately by Exon-Alsthom and attracted extensive investigation world-wide [4].

In the direct methanol fuel cell, the liquid methanol fuel is supplied directly to the anode where it is electro-oxidised to carbon dioxide. Such a low temperature power delivery device, at least in principle, offers the possibility of rapid start-up with a very rapid response to external demand [5]. The power levels of fuel cells depend on heat and mass transport rates, conduction of electrons and ions in the electrode, and charge transfer rates across the interface [6]. One of the primary disadvantages of the DMFC is related to the poor electrode kinetics at the anode side, which is responsible for substantial inefficiencies within the cell. The electro-oxidation of methanol only occurs at a sensible rate in the presence of platinum or a platinum-based electrocatalyst. The surface adsorbed species present throughout its useful potential range are responsible for the poor catalytic activity of platinum towards methanol electro-oxidation. Another problem of DMFC is related to the removal of CO_2 from the anode surface. In the proton exchange membrane fuel cell, a highly optimised electrode will not function to its full potential if this problem can not be overcome. The function of centrifugal fields in disengaging gas bubbles from the electrode surface should be effective in this aspect. With this in mind, this work has been undertaken to consider the feasibility of a rotary methanol fuel cell.

6.2. Literature Review

To our best knowledge, no paper has been published about methanol electro-oxidation or DMFC operation in centrifugal fields, although a wealth of literature has contributed to methanol oxidation and DMFC under ordinary conditions. This review highlights the mechanism of methanol oxidation, the developments in the electrodes and the DMFC.

6.2.1. Mechanism of Methanol Oxidation

The typical mechanisms of methanol oxidation are listed in Tables 6.1.

Table 6.1. Mechanisms of Methanol Oxidation

Media	Mechanism		Refrence(s)
Acidic electrolytes, Pt Anode	$CH_3OH = PtCOH+3H^++3e^-$	(6.5)	[7, 8]
	$PtCOH+OH_{ads} = PtC=O+H_2O$	(6.6)	
	$PtC=O+OH_{ads} = PtCOOH$	(6.7)	
	$PtCOOH+Pt = CO_2+H_2O$	(6.8)	
where OH_{ads} are absorbed radicals and formed by			
	$H_2O = OH_{ads}+H^++e^-$	(6.9)	
Acidic electrolytes, Pt-Ru Anode	$CH_3OH_{sol} = CH_3OH_{ads}$	(6.10)	[9]
	$CH_3OH_{ads} = PtCO_{ads}+4H^++4e^-$	(6.11)	
	$Ru+H_2O = RuOH_{ads}+H^++e^-$	(6.12)	
	$PtCO_{ads}+RuOH_{ads} = CO_2+H^++e^-$	(6.13)	
Carbonate Electrolytes	$CH_3OH+3CO_3^{2-} = 4CO_2+2H_2O+6e^-$	(6.14)	[10]
	$3CO_2+3H_2O+3CO_3^{2-} = 6HCO_3^-$	(6.15)	
Alkaline solutions	$CH_3OH+3OH^- = HCO_{ads}+3H_2O+3e^-$	(6.16)	[11]
	$OH^- = OH_{ads}+e^-$	(6.17)	
	$HCO_{ads}+OH_{ads} = HCOOH$	(6.18)	
	$HCOOH+OH^- = HCOO^-+H_2O$	(6.19)	

There remains substantial controversy regarding the composition of surface species. For example, COH [7, 8] and CO [12] were proposed.

A reaction order of 0.5 was usually reported in both acidic and alkaline solutions [9, 11]. However, higher reaction orders, i.e., 0.7-1, were reported which is due to the beginning of the influence of the rate of methanol adsorption [13]. At higher

potentials, when methanol adsorption becomes the rate determining step, a first order reaction kinetics was observed for methanol oxidation on Pt electrode [13]. Some reported Tafel slopes and exchange current densities of methanol oxidation are shown in Table 6.2.

Table 6.2. Tafel Slope (b) and Exchange Current Density (j_0) of Methanol Oxidation

Electrode	Media	Temperature/°C	b/mVDec^{-1}	j_0/Acm^{-2}	Refrence(s)
Pt	0.1 M CH_3OH+0.5 M H_2SO_4	25	118	$1.0x10^{-5.6}$	[14]
Pt	0.1 M CH_3OH+0.5 M H_2SO_4	75	120	$1.0x10^{-5.6}$	[14]
Pt-Ru/C	1 M CH_3OH+0.5 M H_2SO_4	25	120	$1.0x10^{-5.15}$	[15]
Pt-Ru/C	1 M CH_3OH+0.5 M H_2SO_4	45	120	$1.0x10^{-5.2}$	[15]
Pt-Ru/C	1 M CH_3OH+0.5 M H_2SO_4	60	110	$1.0x10^{-5.2}$	[15]
Pt	0.3 M CH_3OH+1 M NaOH	22	120	$1.0x10^{-10.1}$	[11]
Pt	0.3 M CH_3OH+0.1 M NaOH	22	120	$1.0x10^{-10.3}$	[11]
Pt	0.3 M CH_3OH+0.01 M NaOH	22	120	$1.0x10^{-10.5}$	[11]

6.2.2. Anode

It was well known that the practical application of the direct methanol-fuel cells is hindered by the need to use relatively large quantities of precious platinum-group metal catalysts, in particular Pt, the only materials suitable for the electrocatalytic oxidation of methanol to date, owing to the inherent kinetic sluggishness of both the anodic and cathodic reactions in acid solution. Moreover, although the overall methanol oxidation reaction is simple, it proceeds in a quite complicated way in which surface intermediates play an important role [6, 9, 16]. In particular, the CO_{ad} produced in the reaction forms passive CO islands on the platinum surfaces, thus blocking the surface for further adsorption of methanol [6, 9, 17, 18]. Therefore, solving the poisoning of the anode catalysts by the reaction intermediates such as CO_{ad}. becomes one of the fundamental problems in development of direct methanol fuel cells. An intense search has been initiated to improve catalysts, with particular

attention paid to solving the catalyst poisoning problem, since the late of 1980s. The most important progress in this area is covered in this section.

Porous Carbon Supported Platinum Anodes - In order to enhance the performances of the platinum electrode, one possibility is to increase the active surface area, by dispersion of the catalyst as small particles on a conducting support. A notable method is using platinum supported on various porous-carbon electrodes [19]. Platinum (3 $mgcm^{-2}$) was dispersed on high surface area carbon supports with the aid of polytetrafluorethelene binder. It was demonstrated that the methanol oxidation in 1 M CH_3OH+2.5 M H_2SO_4 solution is catalysed on this type of electrodes in the presence of oxygen, shifting the onset potential of CO_2 production 100 mV more cathodic [20].

The use of carbon paper as the support has ameliorated several materials related problems . With the carbon cloth collectors, the previous problems encountered with carbon paper such as fragility have been solved. Pt/ carbon cloth anodes show similar results for methanol oxidation as those of using other supports [21].

The Pt particle size affects the methanol oxidation activity. Unexpectedly, a decrease in platinum particle sizes from 4.3 to 1.2 nm results in a decrease in current density of methanol oxidation from 0.08 to 0.032 mA cm^{-2} at a potential of -0.05 V vs. MSE and 23°C in 0.1 M CH_3OH+0.5 M H_2SO_4 solution In the range of 4.5-10 nm, the current density of methanol oxidation remains almost constant [3].

Polymer Supported Platinum Anodes - To obtain an efficient dispersion of the catalyst, porous carbon is typically choosen as a conducting support. Nafion membrane, a perfluorinated membrane, with inert chemical property and good stability, is another alternative support. Apart from its use as a solid polymer

electrolyte for hydrogen/oxygen fuel cells, the membrane can be highly dispersed with small Pt particles, on both sides, and used as the main part of the proton exchange membrane fuel cell. The Pt loading can be as low as 1 mg Pt cm^{-2} without losing the catalytic activity [22]. A new method of fabricating composite polymer anodes was introduced [14]. In this method, the metallic Pt particles were deposited from cationic salts, using chemical reduction which was carried out through the membrane by means of a reducing agent in contact with the opposite side. Anodes obtained in this way gave a maximum current density of 46 $mAcm^{-2}$ at 0.89 V vs. RHE in 0.1 M CH_3OH+2.5 M $HClO_4$ solution at 25°C. Feeding with gaseous methanol in a nitrogen flow, also at 25°C, the maximum current density reaches 150 $mAcm^{-2}$. At 45°C, the maximum current density can increase to 250 $mAcm^{-2}$ [14]. Moreover, the poisoning effects for methanol oxidation using such a anode is reduced. The enhanced electrocatalytic activity on such electrodes was attributed to the uniform dispersion of Pt microparticles and synergistic effects of Pt microparticles and the polypyrrole films [22].

Platinum Alloy Anodes - One successful approach to overcome the poisoning effects is using composite catalysts, i.e., by the combination of Pt with other metal elements having sites that play a different role from that of the Pt sites, i.e., form surface oxides at lower potentials than Pt alone thus being able to oxidise the poisoning species at more cathodic potentials [23, 24]. Pt/Ru [25-27], Pt/Sn [28, 29], Pt/Mo [30, 31], etc., catalysts impregnated, or electrodeposited, onto carbon paper, or carbon cloth, have shown superior performance than Pt alone for methanol oxidation. For example, at a catalyst loading of 0.5 mg cm^{-2}, current density is about 5, 10 and 70

mA cm^{-2} at 0.5 V vs. RHE in 1 M CH_3OH+0.5 M H_2SO_4 solution at 45°C for Pt/C, Pt-Sn/C and Pt-Ru/C anode respectively [15].

Recently, Pt-Ru was electrodeposited on gold foil at a controlled potential of 0.002, 0.05 and 0.1 V vs. RHE from 0.005 M H_2Cl_6Pt and 0.005 M $RuCl_3$ solutions at 25°C [32]. An electrode, obtained by passing a deposition charge of 74 C, with 80% Pt and 19% Ru, gave a current density of about 15 mA cm^{-2} at 0.6 V vs. RHE in 2 M CH_3OH+1.5 M H_2SO_4 solution at 70°C [32].

Other Composite Anodes -

Pt-WO_3 and Pt-Ru-WO_3 electrodes show a high activity for methanol oxidation [33]. For example, Pt-WO_3 gave a current of 200 mA/mg Pt at 0.4 V vs. RHE in 1 M CH_3OH+0.05 M H_2SO_4 solution at 60°C. Under similar experimental conditions, the data for the oxidation of methanol on optimised Teflon-bonded Pt/C electrode is 50 mA/mg Pt at 0.55 V vs. RHE [19] and Pt-Ru/C electrode is 50 mA/mg Pt+Ru at 0.4 V vs. RHE [28]. The superior performance was attributed to: (i) keeping the Pt sites clean for chemisorption of methanol; and (ii) destroying the poisons. But the stability and catalytic activity of this type of catalyst needs to be improved, particularly in acidic media and at a high temperature above 60°C.

6.2.3. Direct Methanol Fuel Cells

Development of DMFC - The benefit of the DMFC was demonstrated at a single cell. In general, the cell was based on a Nafion membrane electrolyte and Pt-Ru anodes and Pt catalysed air/oxygen cathodes. Although considerable progress has been made in achieving high energy efficiencies (about 50%) and high energy densities (>1 Wcm^{-2}) in hydrogen-oxygen fuel cells, for methanol-oxygen fuel cells, the

reported power output density is lower (≤ 0.2 Wcm^{-2}) [15, 34]. The power output density is even lower (≤ 0.1 Wcm^{-2}) for the multiple cell stacks [35, 36].

Oxygen Cathode for DMFC - Oxygen reduction kinetics is very slow and limits the performance of oxygen based fuel cells [37]. This is because oxygen reduction proceeds primarily through a polyatomic intermediate [38, 39]. The oxygen-containing species strongly adsorb on the cathode surface and decrease the electrocatalytic activity of the cathode towards oxygen reduction. Moreover, in the Nafion based DMFC, methanol crossover to the cathode, due to high methanol permeability in the membrane [40, 41], results in a mixed cathode potential and causes polarisation losses due to the simultaneous oxygen reduction and methanol oxidation. Pt based catalysts seem to be the prefered choice for oxygen reduction [15, 20, 42].

6.3. Methanol Oxidation In The Stationary Cell

This section describes the experimental data collected in a static cell, which is same as that shown in Chapter 2, with Pt-Ru deposited Ti mesh electrodes under various conditions.

6.3.1. General Characteristics

A typical linear sweep voltammogram of Pt-Ru/Ti mesh anode for methanol oxidation is shown in figure 6.1. As can be seen, methanol was effectively oxidized in the potential range of 200 to 700 mV vs. RHE at Pt-Ru/Ti mesh anode (figure 6.1) due to the high catalytic activity of Pt-Ru catalysts for methanol oxidation. It can be seen that the oxidation current rises rapidly from an anode potential of about 300 mV vs. RHE to a current density of 500 mA cm^{-2} at about 660 mV. On the other hand, oxygen evolution is not apparent until potential is excess of 900 mV and

occure only significantly after the anode potential reaches a value of 1350 mV vs. RHE in 0.5 M H_2SO_4 solution (figure 6.1). The current rises rapidly beyond 1400 mV.

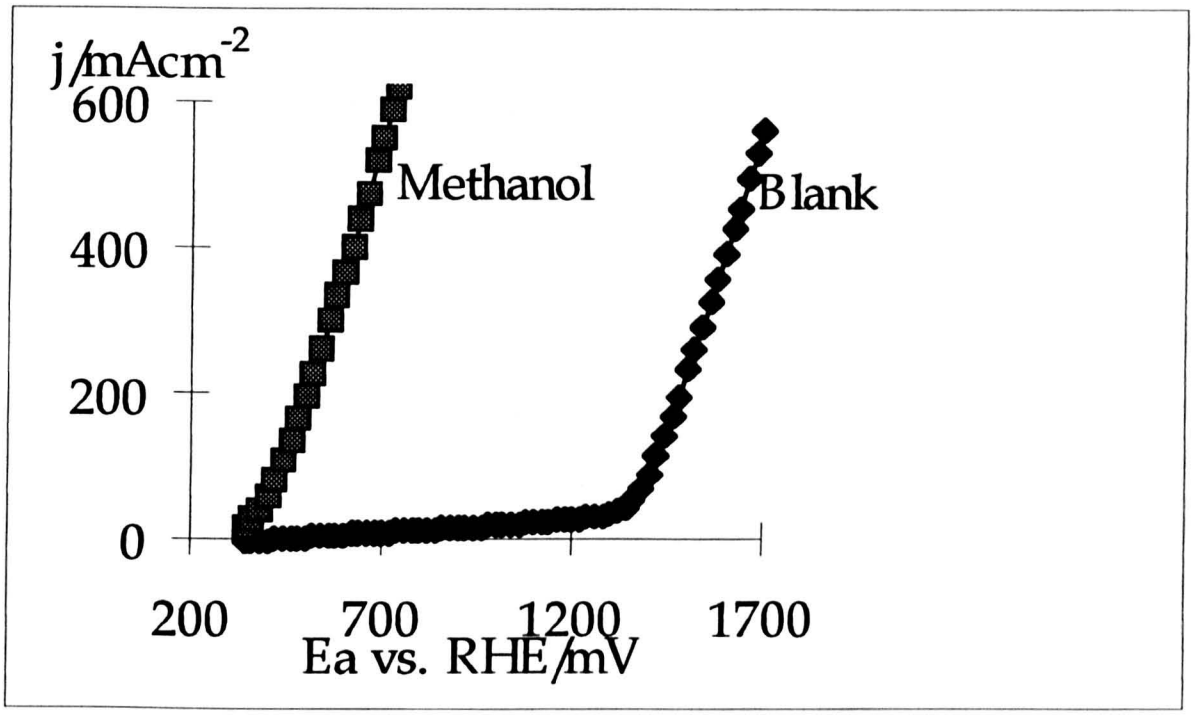

Figure 6.1. Anodic polarization curves for CH_3OH oxidation. Anode: Pt-Ru(2 mg Pt cm^{-2}+1 mg Ru cm^{-2})/Ti mesh; Anolyte: 1 M CH_3OH/0.5 M H_2SO_4 solution (Methanol) or 0.5 M H_2SO_4 solution (Blank); Cathode: Pt(2 mg Pt cm^{-2})/Ti mesh; Catholyte: 0.5 M H_2SO_4 solution; Scan rate: 5 mV/s; Temperature: 80°C; H-type glass cell.

The anodic current in the presence of methanol solution is mainly produced by methanol oxidation. This was confirmed by chromatography where the only detectable product was carbon dioxide which increases with prolonged electrolysis time. No intermediates from methanol oxidation were found. This suggests that methanol undergoes complete oxidation to carbon dioxide. The intermediates, if formed, are then oxidised at the anode with facilitation, leaving no soluble products to accumulate in the solution.

6.3.2. Effect of Catalysts

Catalyst Loading - The catalyst loading has a significant effect on methanol oxidation, especially at high temperature. Figure 6.2 shows data for three catalyst loading use 2:1 ratio of Pt:Ru. Below 300 mV vs. RHE or above 670 mV vs. RHE, the polarisation curves appear similar for all catalyst loading. At each catalyst loading, the polarisation curve rises abruptly at different anode potential, i.e., 400, 340 and 320 mV vs. RHE for the anode with 1, 2 and 4 mg Pt/cm^2 respectively. An increase in the catalyst loading from 1 to 2 mg Pt/cm^2 resulted in the polarisation reduction of about 60 mV at 100 mAcm^{-2} and 30 mV at 200 mAcm^{-2}. A further increase in the loading has no significant benefit regarding an increase in current density.

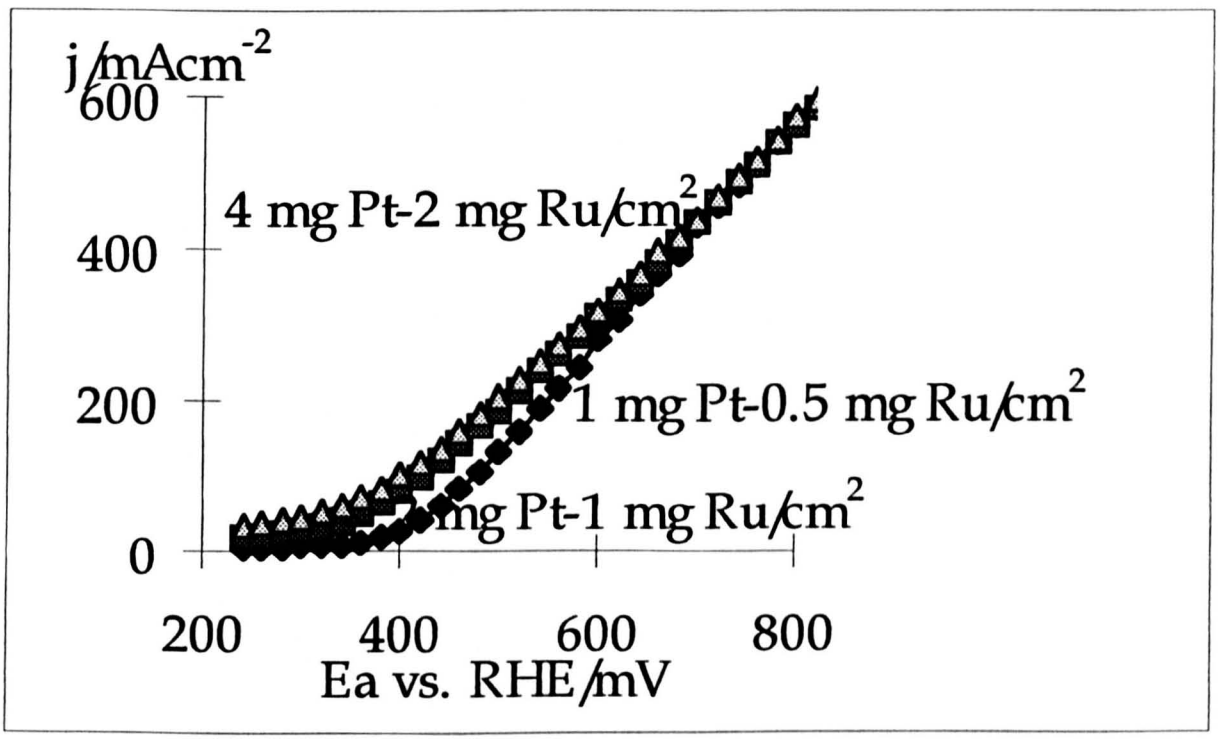

Figure 6.2. Comparison between anodic polarization curves for CH_3OH oxidation on Pt-Ru/Ti mesh anodes - Effect of catalyst loading. Anode catalyst loading (Pt:Ru ratio, from left to roght): 4:2, 2:1 and 1:0.5 mg cm^{-2}; Cathode: Pt(2 mg Pt cm^{-2})/Ti mesh; Anolyte: 1 M CH_3OH/0.5 M H_2SO_4 solution. Catholyte: 0.5 M H_2SO_4 solution; Scan rate: 5 mV/s; Temperature: 60°C; H-type glass cell.

The electrode efficiency did not increase in proportion to catalyst loading, as demonstrated by the small difference between the polarisation curves obtained

using 2 mg Pt or 4 mg Pt/cm². This suggests that there is poor catalyst utilisation above 2 mg Pt/cm². This can be seen from scanning electron micrographs (figure 6.3).

(a)

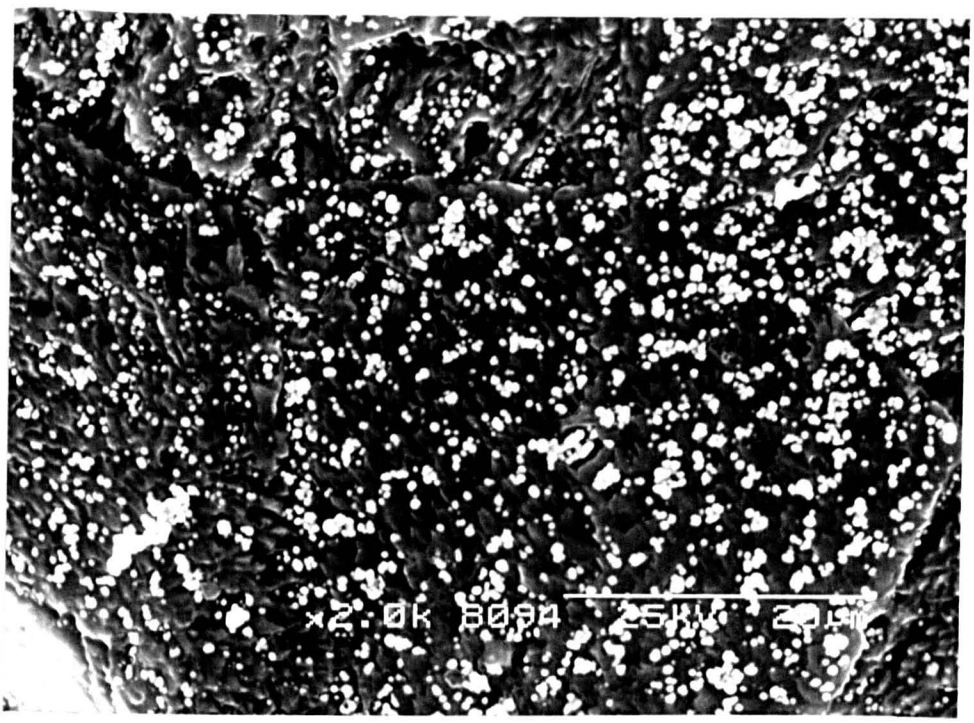

(b)

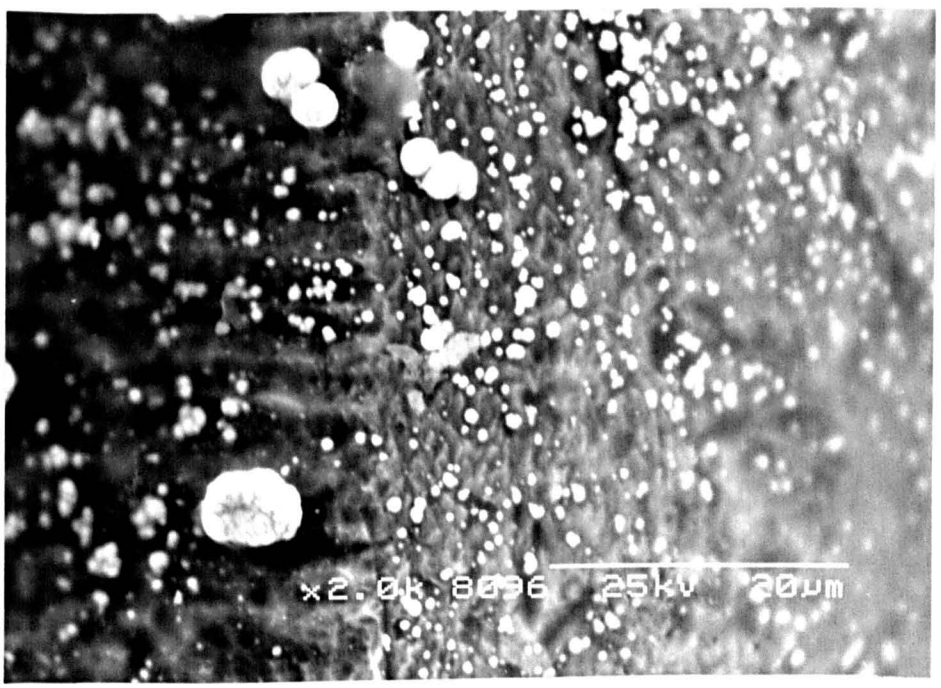

Figure 6.3. Scanning electron micrographs of the Pt-Ru/Ti mesh electrodes. (a) 2 mg Pt+1 mg Ru cm^{-2}; (b) 4 mg Pt+2 mg Ru cm^{-2} cm^{-2}.

The Pt and Ru particles on the titanium mesh surface, with a loading of 2 mg Pt+1 mg Ru cm^{-2}, are distributed homogeneously across the matrix (figure 6.3, a). The electrode shows significant phase segregation as illustrated in figure 6.3 (a). Discrete regions of substrate (dark) and Pt-Ru particles (white) are observed. The majority of the catalyst particles range from 250 to 500 nm in diameter and there are some bigger clusters (about 1.5 μm in diameter). On the other hand, the distribution of Pt and Ru particles on the electrode with a catalyst loading of 4 mg Pt+2 mg Ru cm^{-2} is not homogeneously (figure 6.3, b). Very big clusters (2.5-6.5 μm in diameter). These data confirm that a greater loading does not properly increase the active site due to poor deposits build up.

Figure 6.4 compares data obtained from the Pt-Ru/Ti mesh electrodes with those reported [15, 19]. At a loading of 2 mg Pt+1 mg Ru cm^{-2}, the Pt-Ru/Ti mesh shows similar performance as literature data [15]. At a loading of 1 mg Pt+0.5 mg Ru cm^{-2} the Pt-Ru/Ti mesh gave much better performance compared to the reported data [14]. For eample, at a potential of 0.5 V vs. RHE, current density is 78.2, 62, 60.8 and 17.2 mA cm^{-2} for Pt-Ru/Ti mesh 1, Pt-Ru/Ti mesh 2, Teflon-bonded Pt-Ru/C [15] and Teflon-bonded Pt/C [19] respectively. The optimum catalyst utilisation for the Ti mesh was achieved at a catalyst loading of 1 mg Pt+0.5 mg Ru cm^{-2} under the experimental conditions.

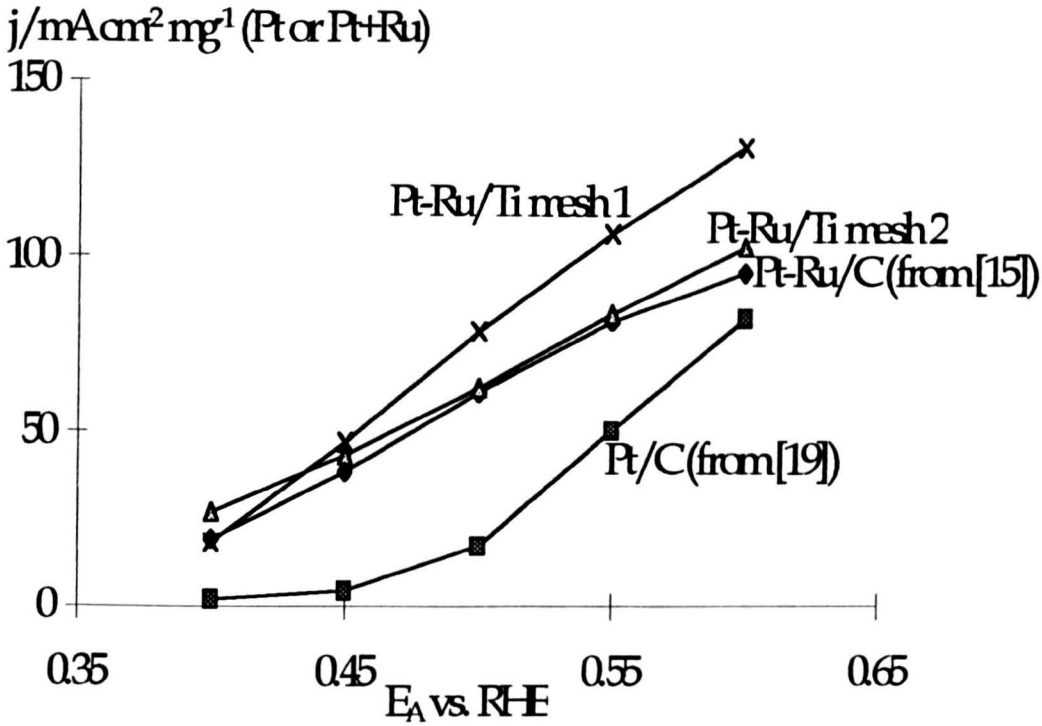

Figure 6.4. Anodic polarization curves showing the effect of catalyst loading on activity for CH_3OH oxidation.
Conditions for Pt-Ru/Ti meshes 1 and 2: Anode loading: 2 mg Pt+1 mg Ru cm^{-2} for Pt-Ru/Ti mesh 2 and 1 mg Pt+0.5 mg Ru cm^{-2} for Pt-Ru/Ti mesh 1; Anolyte: 1 M CH_3OH/0.5 M H_2SO_4 solution; Cathode: Pt(2 mg Pt cm^{-2})/Ti mesh; Catholyte: 0.5 M H_2SO_4 solution; Scan rate: 5 mV/s; Temperature: 60°C; H-type glass cell.
Conditions for Teflon-bonded Pt/C electrode (from [19]): Anolyte: 1 M CH_3OH/2.5 M H_2SO_4 solution; Cathode: Au plates; Catholyte: 2.5 M H_2SO_4 solution; Temperature: 60°C.
Conditions for Teflon-bonded Pt-Ru/C electrode (from [15]): Anolyte: 1 M CH_3OH/0.5 M H_2SO_4 solution; Temperature: 60°C.

Catalyst Type - The type of catalyst also has effect on the anode polarisation behaviour, as shown in figure 6.5 where three catalysts display different polarisation curves for methanol oxidation. A Ru catalysed anode showed relatively poor performance, potentials were some 150 mV greater than on Pt-Ru anodes at a fixed current density and a peak appeared at about 950 mV vs. RHE. The absence of the sharp decrease in current for the polarisation curve of Pt-Ru electrodes reflects the difference in catalytic activity between the pure Ru and the Pt-Ru coatings. The

poisoning of the catalyst during methanol oxidation was expected to be depressed at the Pt-Ru anode, and consequently it gave the best performance of the three catalysts for methanol oxidation. As anticipated, the effectiveness of the anode with Pt coating for methanol oxidation was inferior to that of the Pt-Ru catalyst, due presumably to the Pt catalyst poisoning, especially at low anode potentials, as shown in figure 6.5.

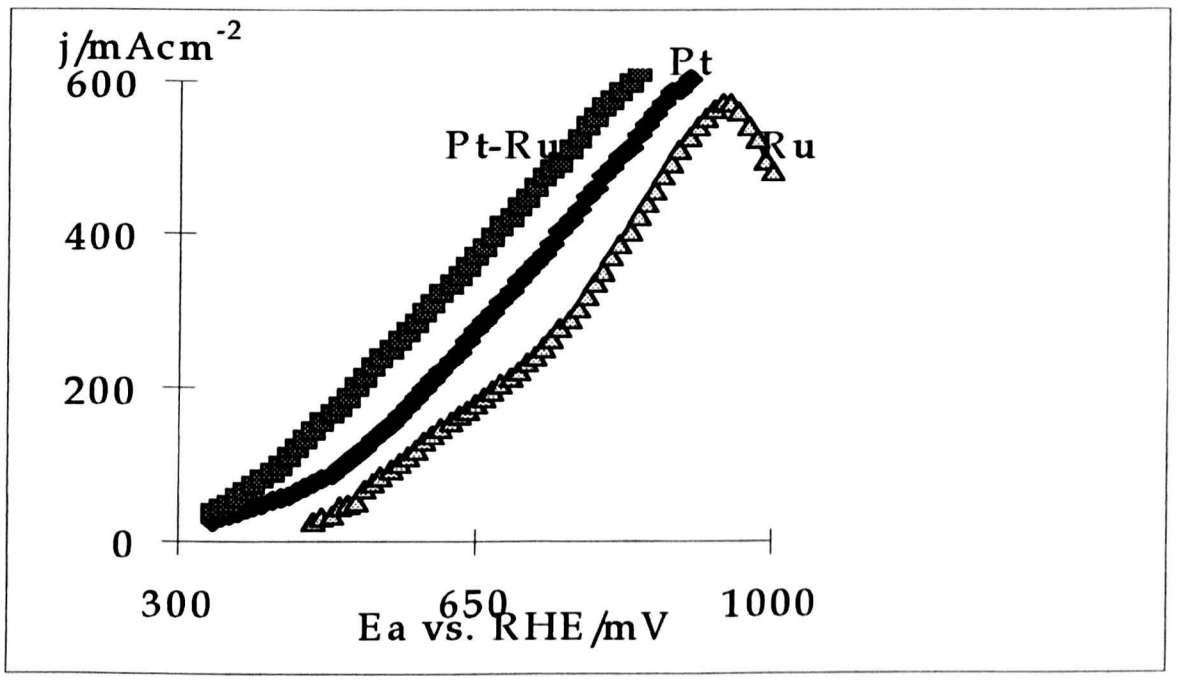

Figure 6.5. Comparison between anodic polarization curves for CH_3OH oxidation on different anodes. Anode catalyst loading: 2 mg Pt or Ru cm^{-2} for Pt or Ru/Ti mesh anode; 2 mg Pt+1 mg Ru cm^{-2} for Pt-Ru/Ti mesh anode; Cathode: Pt(2 mg Pt cm^{-2})/Ti mesh; Anolyte: 1 M CH_3OH/0.5 M H_2SO_4 solution. Catholyte: 0.5 M H_2SO_4 solution; Scan rate: 5 mV/s; Temperature: 60°C, H-type glass cell.

6.3.3. Effect of Temperature and Methanol Concentration

The investigation was extended to consider the effect of using linear sweep, chronopotentiometric, and chronoamprometric techniques. Figure 6.6 shows the polarisation curves on Pt-Ru/Ti mesh electrodes at different temperatures. An oxidation current peak appeared at 25°C since obvious mass transport limitations. At higher temperatures, the oxidation became more facile. From figure 6.6, it can be

seen that above 0.5 V vs. RHE the effect of increasing the temperature from 25 to 80°C results in an approximate doubling in current density at a fixed potential. The oxidation peak could not be seen at 60°C due to the signal output exceeded the equipment limit. Further raising the temperature to 80°C results in an increase in the oxidation current at a given anode potential. It is a general belief that suitable temperatures for methanol oxidation are around 60°C and above [15]. At high temperature, besides improving the oxidation kinetics, the effect of poisoning is less significant, compared to that observed at ambient temperature. The above results agree with these observations.

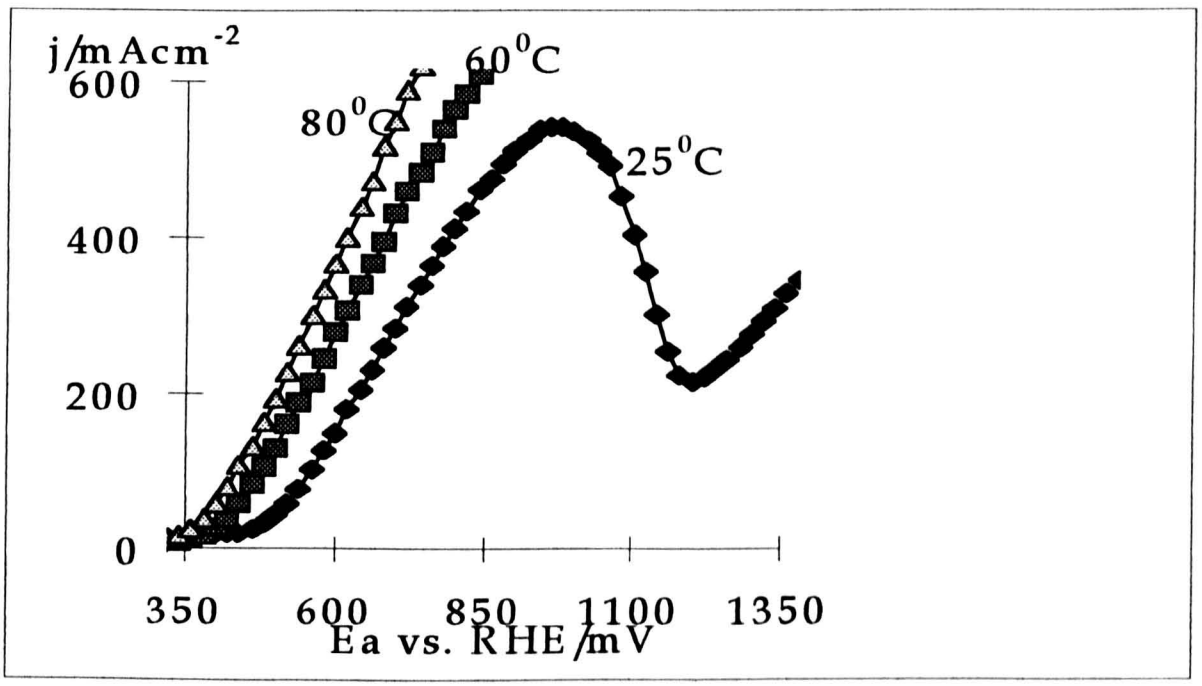

Figure 6.6. Anodic polarization curves of CH_3OH oxidation - Effect of temperatures. Anode: Pt-Ru(2 mg Pt cm^{-2} + 1 mg Ru cm^{-2})/Ti mesh; Anolyte: 1M CH_3OH/0.5 M H_2SO_4 solution; Cathode: Pt(2 mg Pt cm^{-2})/Ti mesh; Catholyte: 0.5 M H_2SO_4 solution. Scan rate: 5 mV/s; H-type glass cell.

Figure 6.7 shows the Tafel plots obtained on Pt-Ru/Ti mesh electrodes at different temperatures. As can be seen in figure 6.7, at each temperature, the overpotential changes slowly with increasing current in the low current density range (less than 5 $mAcm^{-2}$). The current density increases rapidly in the range between 5 and 150 mA

cm^{-2}. After this rapid increase, the current density rises very slowly. A significant reduction of polarisation is observed as the temperature is raised from 25 to 80°C. In the current density range of 10 to 200 mA cm^{-2}, the polarisation is reduced approximately 100 mV by this temperature increase. The Tafel slope obtained in an overpotential range of 0.3 to 0.4 V is about 125 mV/decade at the three temperatures. The exchange current density obtained by extrapolating to $(E_A-E_{A,e})=0$ at each temperature also has no obvious change which is about $1.0x10^{-5.2}$ mA cm^{-2}. The reported Tafel slopes and exchange current density, on Pt-Ru/C anode in 1 M CH_3OH+0.5 M H_2SO_4 solution, are 120 mV/decade and $1.0x10^{-5.2}$ mA cm^{-2} at both 25 and 45°C [15].

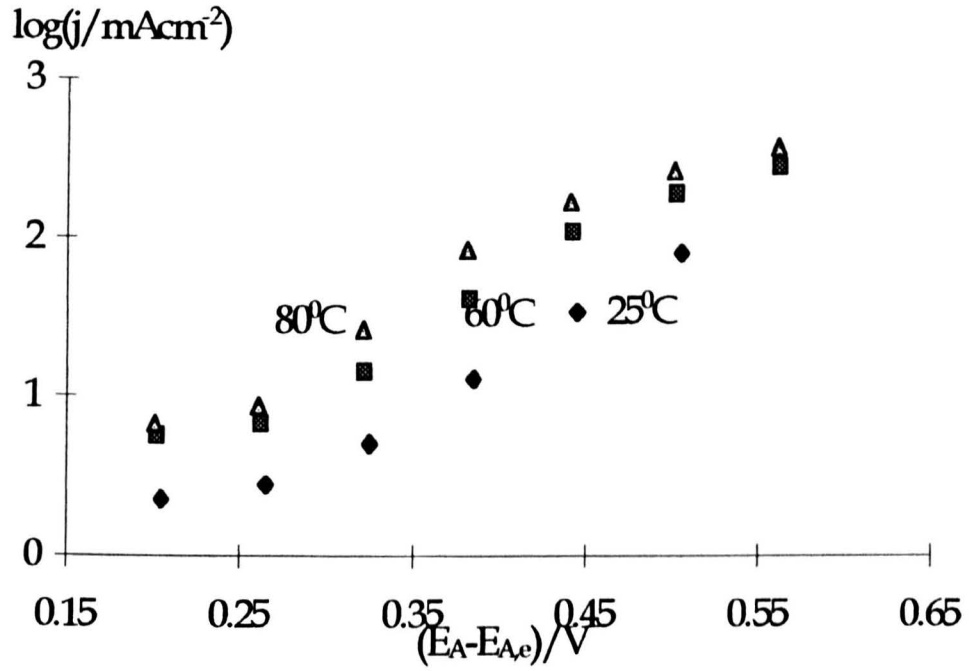

Figure 6.7. Tafel plots for methanol oxidation reaction on Pt-Ru/Ti mesh anode (2 mg Pt cm^{-2} + 1 mg Ru cm^{-2})/Ti mesh; Anolyte: 1M CH_3OH/0.5 M H_2SO_4) - Effect of temperature. Cathode: Pt(2 mg Pt cm^{-2})/Ti mesh; Anolyte: 1 M CH_3OH/0.5 M H_2SO_4 solution. Catholyte: 0.5 M H_2SO_4 solution; H-type glass cell.

Effect of Methanol Concentration - Figure 6.8 shows the effect of methanol concentration on the the polarisation curves on Pt-Ru/Ti mesh anode in different methanol concentrations. Current peaks were observed for 0.1 M and 0.5 M methanol solutions, suggesting that mass transport limitation may occur. At concentration of 1 M and above, the oxidation peak could not be seen due to the

signal output exceeded the equipment limit. At a constant current density, the potential decreases with increasing methanol concentration. For example, at 300 mA cm^{-2}, the anode potential is 800, 620, 580, and 520 mV for 0.5, 1, 4, and 8 M methanol solution, respectively. The maximum anodic current density at a given anode potential was achieved in 8 M methanol solution. However, such a high concentration should be avoided in practical fuel cells due to cross-over of methanol from anodic chamber to cathodic chamber.

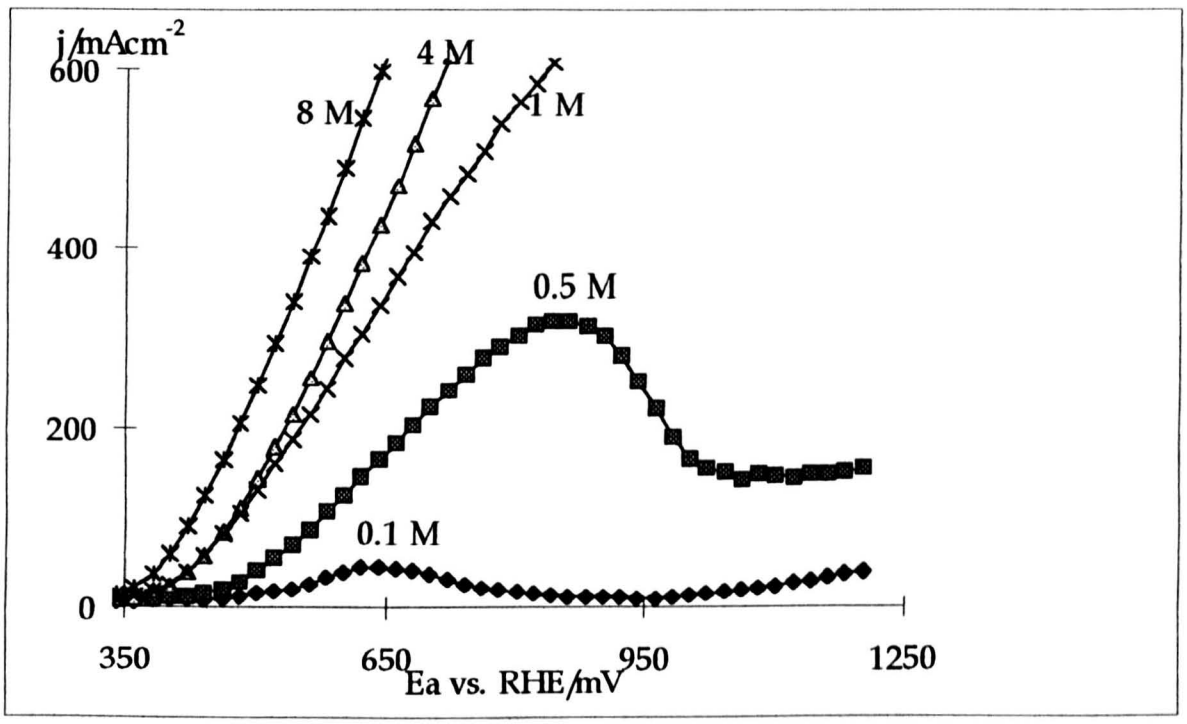

Figure 6.8. Comparison between anodic polarization curves for CH_3OH oxidation. - Effect of concentration. Anode: Pt-Ru (2 mg Pt cm^{-2}+1 mg Ru cm^{-2})/Ti mesh; Anolyte: CH_3OH+0.5 M H_2SO_4 solution; Cathode: Pt(2 mg Pt cm^{-2})/Ti mesh; Catholyte: 0.5 M H_2SO_4 solution; Scan rate: 5 mV/s; Temperature: 60°C; H-type glass cell.

The methanol oxidation kinetics are improved by increasing the concentration, as shown in figure 6.9. It is clear from figure 6.9 that, for all solutions investigated, the overpotential increases slowly with increasing current at low current density range (less than 5 $mAcm^{-2}$). It increases rapidly in the range between 5 and about 150

$mAcm^{-2}$. After this dramatic increase, the overpotential rises very slowly. Increasing the methanol concentration from 0.5 to 4 M resulted in a lowering the polarisation for the oxidation of methanol by about 80 mV in the current density range of 10 to 200 $mAcm^{-2}$.

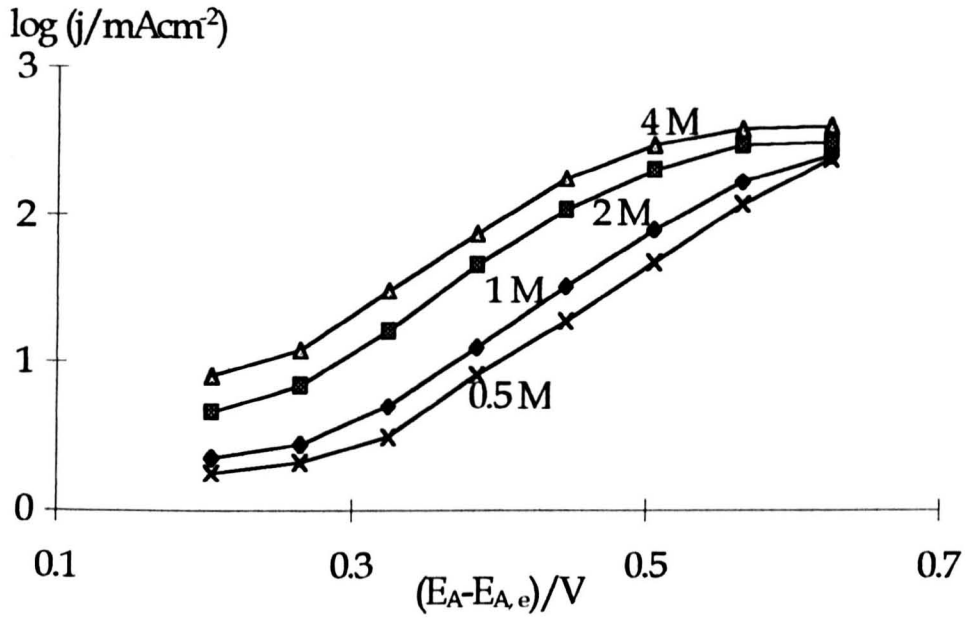

Figure 6.9. Tafel plots for methanol oxidation reaction on Pt-Ru/Ti mesh anode - Effect of concentration. Cathode: Pt(2 mg Pt cm^{-2})/Ti mesh; Anolyte: CH_3OH+0.5 M H_2SO_4 solution; Catholyte: H_2SO_4 solution; Temperature: 60°C; H-type glass cell.

The Tafel slope obtained in an overpotential range of 0.35 to 0.45 V from figure 6.9 is 120 mV/decade for all solutions. The exchange current densities are $10^{-4.56}$, $10^{-4.38}$, $10^{-3.95}$ and $10^{-3.70}$ A cm^{-2} for 0.5, 1, 2 and 4 M methanol solutions respectively. The Tafel slope agrees well with the reported results which is 120 mV/decade on Teflon bonded Pt-Ru/C anode in 1 M CH_3OH+0.5 M H_2SO_4 solution at 60°C [15] or on Pt electrode in 0.1 M CH_3OH+0.5 M H_2SO_4 solution at 75°C [14]. The exchange current densities obtained in this work show that the methanol oxidation kinetics are improved by increasing the methanol concentration. The reported exchange current densities are $10^{-5.2}$ mA cm^{-2} on Teflon bonded Pt-Ru/C anode in 1 M CH_3OH+0.5 M H_2SO_4 solution at 60°C [15] and $1.0x10^{-5.6}$ mA cm^{-2} on Pt electrode in 0.1 M CH_3OH+0.5 M H_2SO_4 solution at 75°C [14]. A complete understanding difference between the literature and this work's data needs further investigation.Figure 6.10

shows log j versus log $C_{Methanol}$ plots at three potentials obtained by using the steady state current densities for methanol oxidation on Pt-Ru/Ti mesh anode in 1 M CH_3OH+0.5 M H_2SO_4 solution at 60°C.

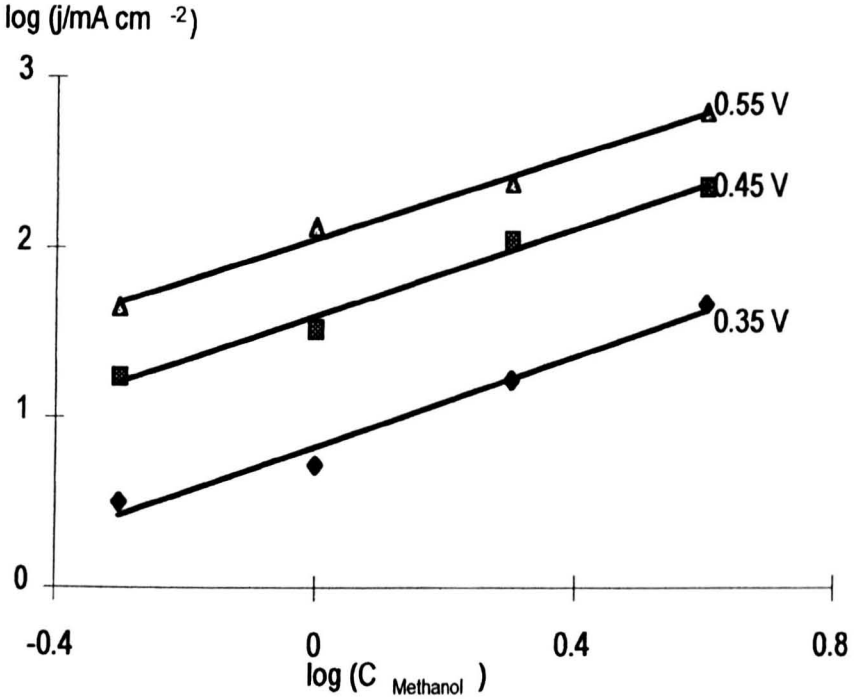

Figure 6.10. Tafel plots for methanol oxidation reaction on Pt-Ru/Ti mesh anode - Effect of concentration ($C_{Methanol}$ in mol dm^{-3}). Cathode: Pt(2 mg Pt cm^{-2})/Ti mesh; Anolyte: CH_3OH+0.5 M H_2SO_4 solution; Catholyte: H_2SO_4 solution; Temperature: 60°C; H-type glass cell.

The log j versus log $C_{Methanol}$ ($C_{Methanol}$ in mol dm^{-3}) plots are parallel at each potential and the slope gives an apparent reaction order of about 0.8 with respect to methanol concentration. For methanol oxidation on Pt electrode in the kinetic region, e.g., around 0.55 V vs. RHE for 0.1 M CH_3OH+0.5 M H_2SO_4 solution [13], the reported reaction order is usually 0.5 [9, 11]. Higher reaction orders, i.e., 0.7-1, were reported which is due to the beginning of the influence of the rate of methanol adsorption [13]. The data of this work agree with this observation.

6.3.4. Effect of Anode Substrate and Supporting Electrolyte

Effect of Anode Substrate - In developing anodes for methanol oxidation, the general approach has been to use electrocatalysts and supports that are capable of withstanding the high anodic potentials. In addition, the support must provide an

acceptable porous electrode structure. The approach chosen here is to utilise conductive Ti mesh to form a porous yet physically stable and self-supporting (no binders was needed) structure. Ti mesh electrodes are about 0.4 mm in thickness and had the very open structure and lower resistance than carbon electrodes. These properties should benifit to overcome some problems identified with the carbon cloth-type electrode, such as methanol diffusion and high electrode resistance. Figure 6.11 compares the polarisation curves obtained with three substrates for methanol oxidation in 1 M CH_3OH+0.5 M H_2SO_4 solution at 60°C. The details for preparing the gas diffusion electrodes are presented in Chapter 2.

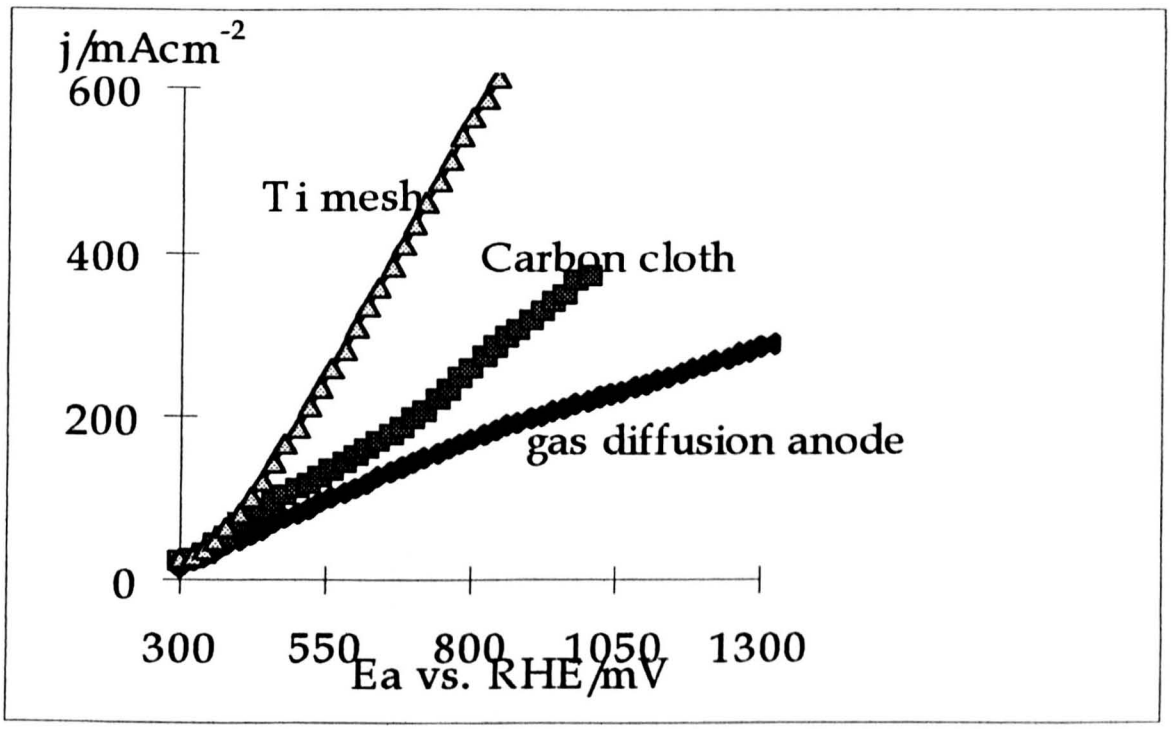

Figure 6.11. Comparison between anodic polarization curves for CH_3OH oxidation on Pt-Ru catalysed anodes with different substrates. Anode catalyst loading: 2 mg Pt+1 mg Ru cm^{-2}; Cathode: Pt(2 mg Pt cm^{-2})/Ti mesh; Anolyte: 1 M CH_3OH+0.5 M H_2SO_4 solution; Catholyte: 0.5 M H_2SO_4 solution; Scan rate: 5 mV/s; Temperature: 80°C; H-type glass cell.

The performances of the carbon cloth and titanium mesh electrodes electrodeposited with identical catalyst loading is very interesting. It can be seen that the introduction

of an "un-optimised" Ti mesh electrode has led to a significant improvements in electrochemical performance over the carbon cloth-type electrodes. For example, the carbon cloth-type electrode gave an electrode polarisation of 0.70 V vs. RHE at a current density of 200 $mAcm^{-2}$ compared with only 0.52 V vs. RHE for the catalysed Ti mesh electrode. The performance of Ti mesh electrode was particularly better at higher current densities. The gas diffusion electrode gave the poorest performance for methanol oxidation. For example, it gave an electrode polarisation of 0.90 V vs. RHE at a current density of 200 $mAcm^{-2}$. The polarisation increases dramatically with increasing current density. One of the factors responsible for the poor performance is the electrode resistance, which is higher than the Ti electrode.

Apart from high resistance compared to Ti mesh, the catalysed carbon cloth electrodes easily lost the catalysts. This has been confirmed by the scanning electron micrographs presented in figure 6.12.

(a)

(b)

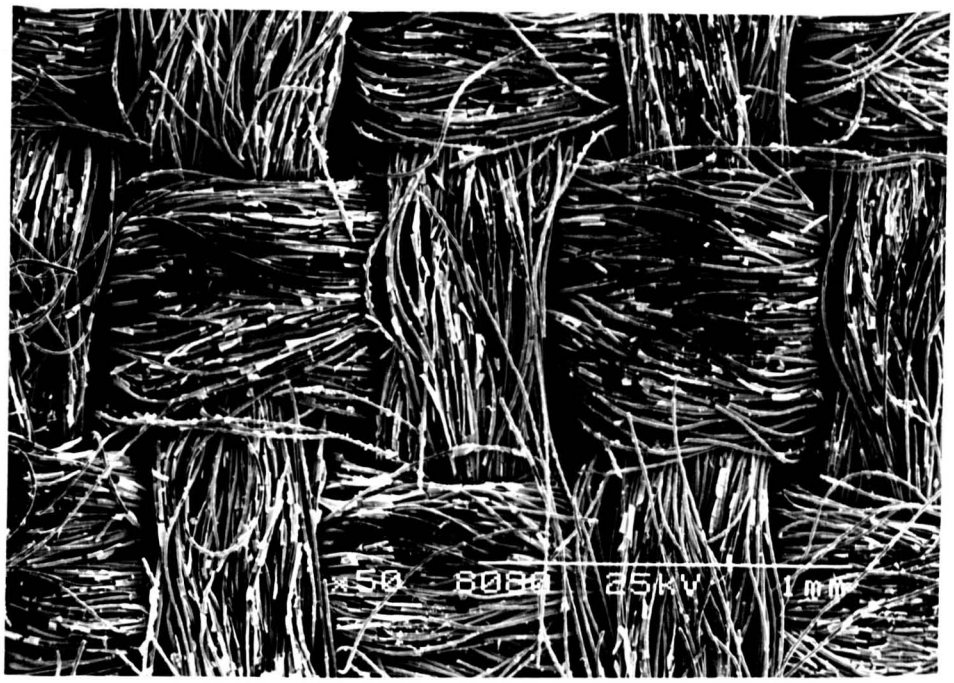

Figure 6.12. Scanning electron micrographs of the Pt (2 mg cm^{-2})-Ru (1 mg cm^{-2})/carbon cloth (a) before and (b) after using for methanol oxidation in 1 M CH_3OH+0.5 M H_2SO_4 solution at 80°C for about 10 hours.

As can be seen from the figure 6.12, the electrode surface was almost completely covered by platinum and ruthenium particles (figure 6.12, a). Most catalyst was removed from the carbon cloth surface after using in methanol oxidation (figure 6.12, b). This means that the adherence between the catalysts and carbon cloth is much poorer as compared to the catalysed titanium mesh electrodes.

Effect of Electrolyte Type - Three types of electrolyte were examined as candidates for methanol oxidation. Figure 6.13 shows the polarisation curves obtained on Pt-Ru/Ti mesh electrode with three supporting electrolytes for methanol oxidation in 1 M CH_3OH solution at 60°C. As can be seen, methanol oxidation occurs in completely different potential regimes in alkaline, neutral, and acidic media. The oxidation potential is up to over 1000 mV more negative in alkaline medium than in acidic medium for a constant current density, e.g., -0.34 or 0.56 V vs. RHE at 300 $mAcm^{-2}$ for the alkaline or acidic medium, respectively. It is interesting to note that in

neutral medium the current density is greater at low anode potentials, i.e., between 0.25 and 0.46 V vs. RHE. At higher potentials, in acidic medium, the current density increases more rapidly with the anode potential.

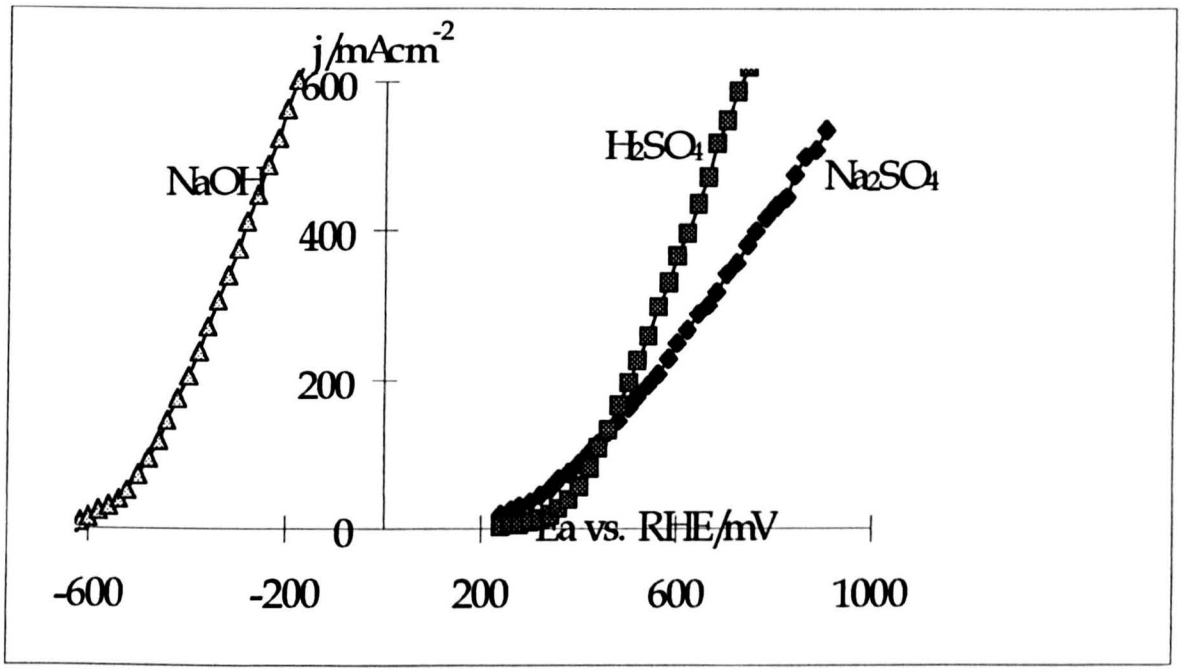

Figure 6.13. Comparison between anodic polarization curves for CH_3OH oxidation in different electrolytes. Anode: Pt-Ru/Ti mesh (2 mg Pt+1 mg Ru cm^{-2}); Cathode: Pt(2 mg Pt cm^{-2})/Ti mesh; Anolyte: 1 M CH_3OH in 1 M NaOH, H_2SO_4 or Na_2SO_4 solutions; Catholyte: 0.5 M H_2SO_4 solution; Scan rate: 5 mV/s; Temperature: 80°C; H-type glass cell.

Figure 6.14 shows the Tafel plots obtained on Pt-Ru/Ti mesh electrode with three supporting electrolytes for methanol oxidation in 1 M CH_3OH solution at 60°C. For all solutions investigated, the overpotential increases relatively slowly with increasing current density at low current density range (less than 5 mA cm^{-2}). Current density increases more rapidly in the range between 5 and 150 mA cm^{-2}, which the overpotential rises slowly. Changing the supporting electrolyte resulted in different behaviour, as shown in figure 6.14. The polarisation for the oxidation of methanol is lower for H_2SO_4 by about 50 to 80 mV than for NaOH and Na_2SO_4 in the current density range of 10 to 200 $mAcm^{-2}$ for different electrolytes.

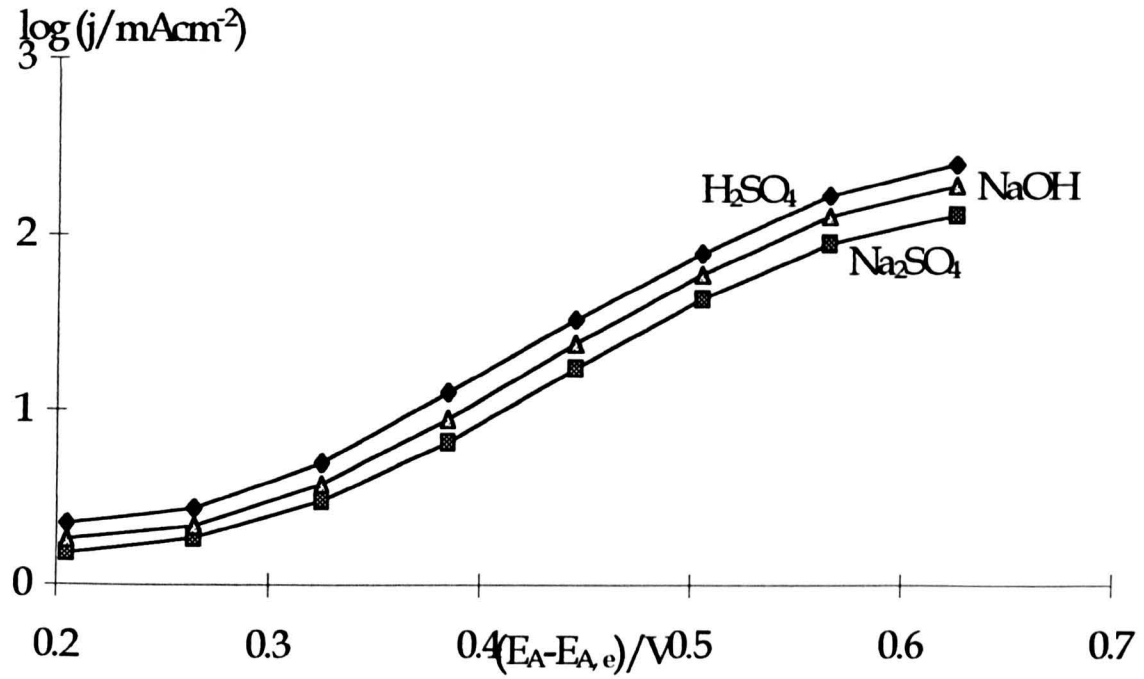

Figure 6.14. Tafel plots for methanol oxidation reaction on Pt-Ru/Ti mesh anode - Effect of supporting electrolyte. Cathode: Pt(2 mg Pt cm^{-2})/Ti mesh; Anolyte: 1 M CH_3OH in 0.5 M H_2SO_4, NaOH or Na_2SO_4 supporting electrolytes; Catholyte: 0.5 M electrolytes; Temperature: 60°C; H-type glass cell.

The Tafel slope obtained in an overpotential range of 0.35 to 0.5 V is 120 mV/decade for the three solutions. The exchange current density obtained by extrapolating to $(E_A-E_{A,e})=0$, where different $E_{A,e}$ for the three solutions are calculated according to the method described in Chapter 7. These data are recorded in Table 6.4.

Table 6.4. Tafel parameters for methanol oxidation in different electrolytes

Anolyte	Catholyte	Temp/°C	b/mVdecade^{-1}	-j_0/Acm^{-2}
1 M CH_3OH+0.5 M H_2SO_4	0.5 M H_2SO_4	60	125	$10^{-4.38}$
1 M CH_3OH+0.5 M Na_2SO_4	0.5 M Na_2SO_4	60	125	$10^{-6.37}$
1 M CH_3OH+0.5 M NaOH	0.5 M NaOH	60	125	$10^{-8.84}$

The reported Tafel slope is 120 mV/decade and exchange current densities are $10^{-5.2}$ and $10^{-10.1}$ A cm^{-2}on Teflon bonded Pt-Ru/C anode in 1 M CH_3OH+0.5 M H_2SO_4 solution at 60°C [15] and on Pt electrode in 0.3 M CH_3OH+1 M NaOH solution at 22°C [11] respectively.

Methanol oxidation mechanism changes with varying electrolyte, as described in Section 6.2.1. In alkaline medium, methanol oxidation should be linked with OH_{ad} layer formation [43]. It was observed that there are two forms of OH_{ad} radicals, i.e., reversible form and irreversible form. The reversible form of OH_{ad} produced on low potentials is more active for "poisoning species" oxidation, as well as for methanol oxidation than its irreversible form which participates in the total coverage with OH_{ad} species and becomes significant at more positive potentials. Carbonate residues are formed during methanol oxidation in alkaline media [3]. Formation of carbonate residues can be avoided in acidic media wherethe rate determining step is the oxidation of methanol adsorbate by an adsorbed hydroxy species or activated water group [10]. The different oxidation mechanisms lead different polarisation behaviours.

Effect of Electrolyte Concentration - Figure 6.15 shows polarisation characteristics obtained with varying supporting electrolyte compositions in the case of sulphuric acid electrolyte. The rate of the methanol oxidation at any potential increases with the acid concentration, as shown in figure 6.15. The anode potential decreases at a constant current density with increasing the electrolyte concentration, as shown in figure 7.8, although big difference can only be seen when the concentration increases from 0.1 M to 0.5 M. For example, at 500 $mAcm^{-2}$, the anode potential is 1.10, 0.80, 0.76, and 0.72 V vs. RHE for 0.1, 0.5, 1, and 2 M sulphuric acid solution, respectively.

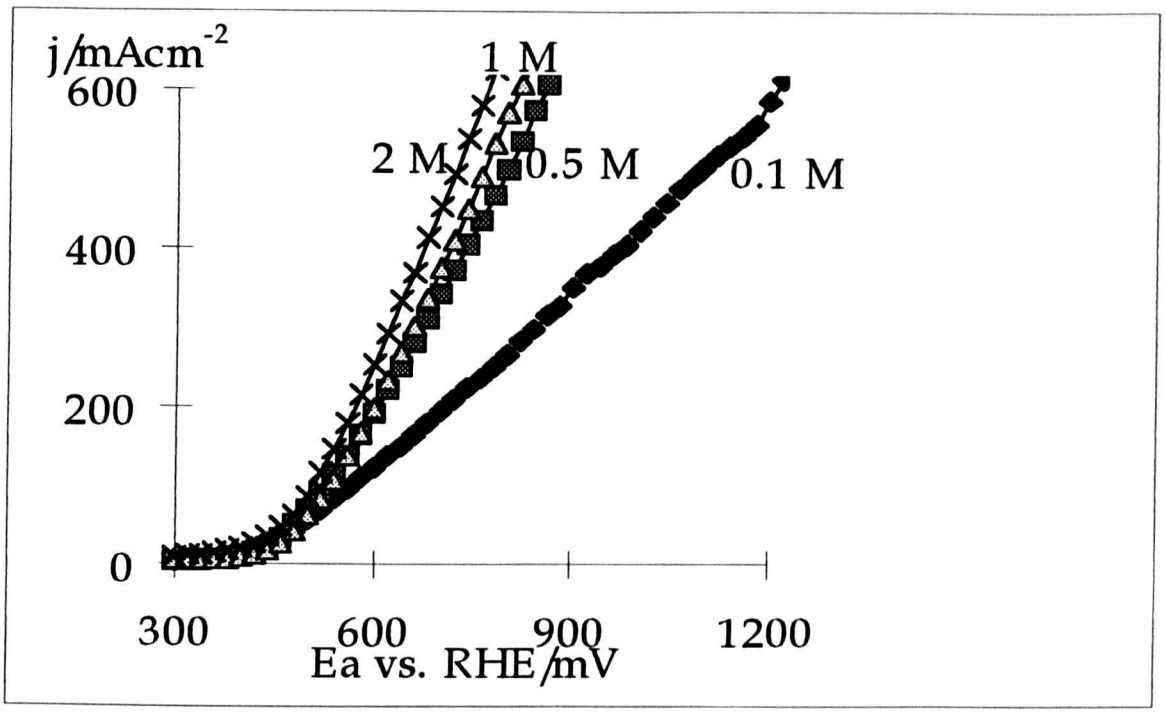

Figure 6.15. Anodic polarization curves for CH_3OH oxidation in different electrolyte concentrations. Anode: Pt-Ru/Ti mesh (2 mg Pt+1 mg Ru cm^{-2}); Cathode: Pt(2 mg Pt cm^{-2})/Ti mesh; Anolyte: 1 M CH_3OH+0.5 M H_2SO_4 solution; Catholyte: 0.5 M H_2SO_4 solution; Scan rate: 5 mV/s; Temperature: 60°C; H-type glass cell.

6.3.5. Effect of Nafion Coating

The DMFC is frequently operated with a solid polymer proton conducting membrane. Consequently a preliminary investigation was undertaken in which the catalysed Ti mesh was coated with Nafion. Figure 6.16 shows polarisation curves for methanol oxidation obtained on Nafion coating and no-Nafion coating Pt-Ru/Ti mesh electrodes in 1 M CH_3OH+0.5 M H_2SO_4 solution at 60°C. As can be seen, coating the electrodeposited electrodes with Nafion solution had minor effect on the performance of the electrode for methanol oxidation. The peak current density decreases from 198 to 185 $mAcm^{-2}$ with coating Nafion on the electrode. It is difficult to control quantity of Nafion to be coated for the Ti mesh electrodes and leads thick Nafion coating on the catalysed Ti mesh surfaces. The thick Nafion coating would present a mass transfer barrier for methanol. So the thick Nafion coating gave additional negative effect on methanol oxidation in acidic media.

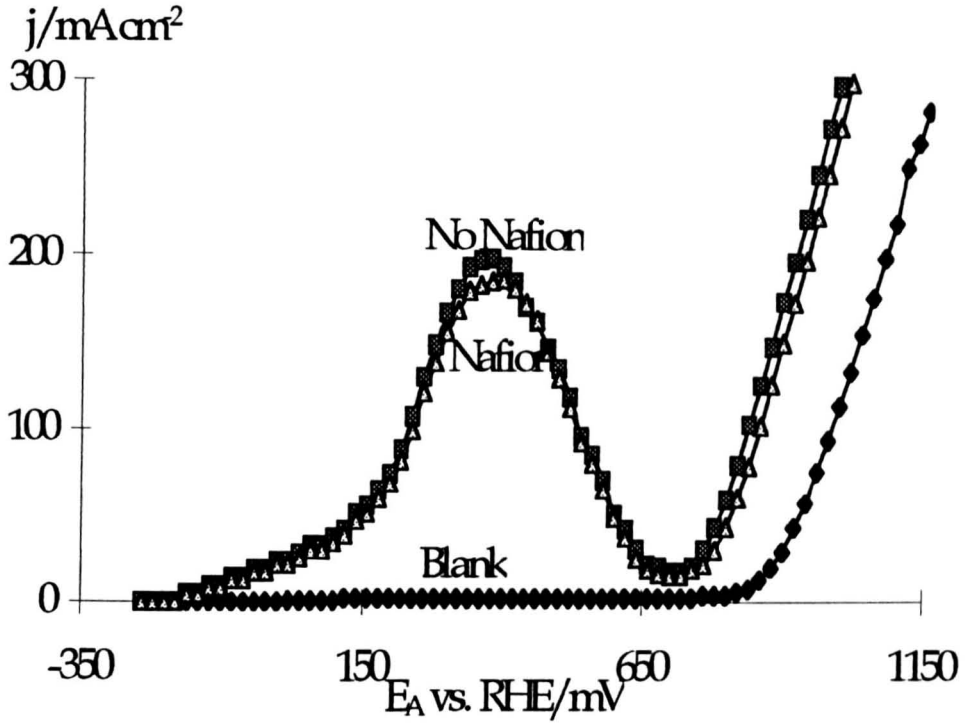

Figure 6.16. Linear sweep voltammograms of CH_3OH oxidation on electrodeposited Pt-Ru/Ti mesh without or coating with the Nafion solution. Anode: Pt-Ru/Ti mesh (2 mg Pt+1 mg Ru cm^{-2}); Cathode: Pt(2 mg Pt cm^{-2})/Ti mesh; Anolyte: 1 M CH_3OH +0.5 M H_2SO_4 solutions (only 0.5 M NaOH solution for the Blank curve); Catholyte: 0.5 M H_2SO_4 solution; Scan rate: 5 mV/s; Temperature: 60°C; H-type glass cell.

In alkaline solution, coating the electrodeposited electrodes with Nafion solution had effect on the performance of the electrode for methanol oxidation up to -300 mV vs. RHE, as shown in figure 6.17. The peak current density decreases from 220 to 140 $mAcm^{-2}$ with coating Nafion on the electrode. In this case, the thick Nafion coating would present a mass transfer barrier for for both methanol and OH^- ions transports. Since methanol oxidation relies on OH^- transport in alkaline media, so the thick Nafion coating gave additional negative effect on methanol oxidation in alkaline media. More work needs to be done to improve performane of methanol oxidation on Nafion coated electrodes.

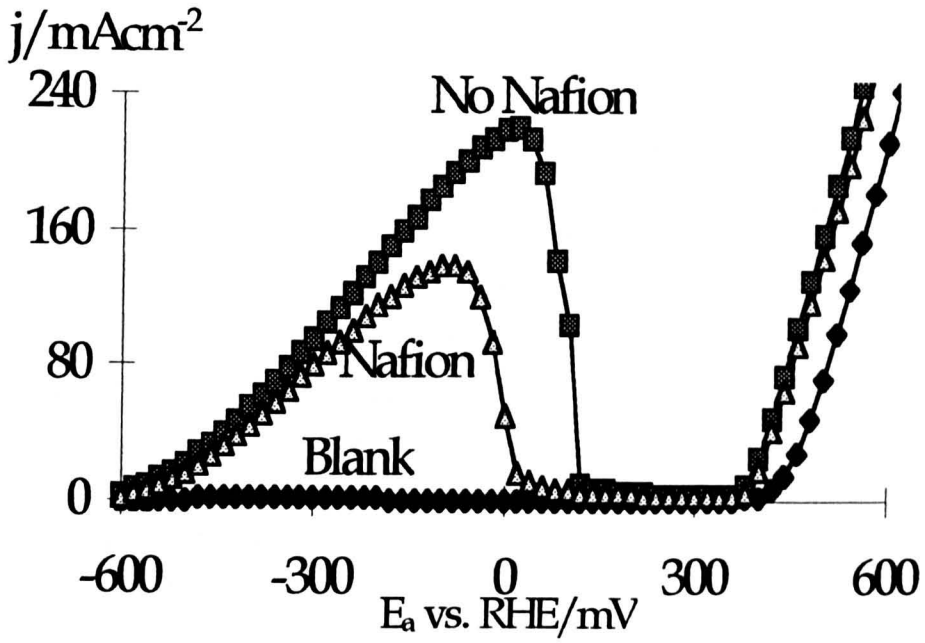

Figure 6.17. Linear sweep voltammograms of CH_3OH oxidation on electrodeposited Pt-Ru/Ti mesh without or coating with the Nafion solution. Anode: Pt-Ru/Ti mesh (2 mg Pt+1 mg Ru cm^{-2}); Cathode: Pt(2 mg Pt cm^{-2})/Ti mesh; Anolyte: 1 M CH_3OH +0.5 M NaOH solutions (only 0.5 M NaOH solution for the Blank curve); Catholyte: 0.5 M NaOH solution; Scan rate: 5 mV/s; Temperature: 60°C; H-type glass cell.

6.4. Methanol Oxidation In The Rotary Cell

The oxidation of methanol was investigated in an acceleration field using the rotary cell described in Chapter 2. This section describes the effect of centrifugal fields on the process.

6.4.1. Effect of Relative Acceleration Rate

Figure 6.18 shows the effect of cell rotation rate on anodic polarisation curves of methanol oxidation in the rotary cell. As expected, methanol oxidation behaviour was greatly affected by the centrifugal force, with a significant enhancement in performance as rotating speed increases.

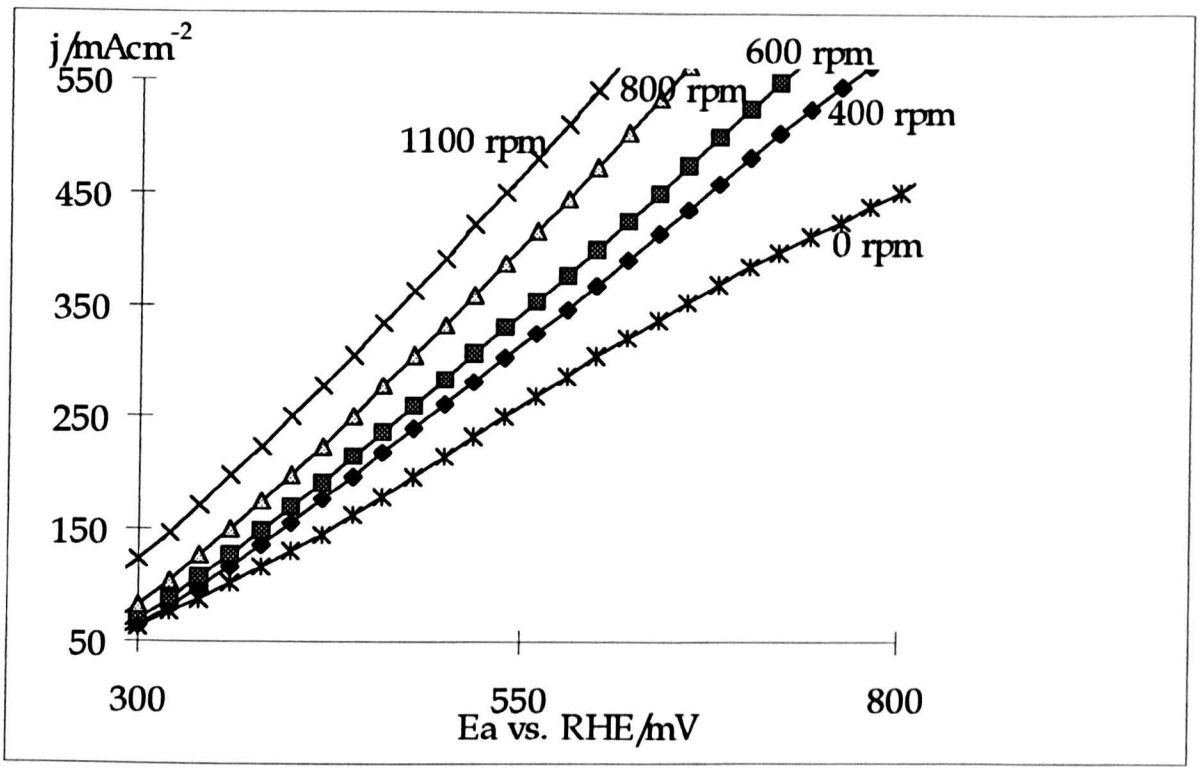

Figure 6.18. Anodic polarization curves for CH_3OH oxidation in the rotary cell. Anode: Pt-Ru/Ti mesh (2 mg Pt+1 mg Ru cm^{-2}); Cathode: Pt(2 mg Pt cm^{-2})/Ti mesh; Anolyte: 1 M CH_3OH+0.5 M H_2SO_4 solution; Catholyte: 0.5 M H_2SO_4 solution; Scan rate: 5 mV/s; Temperature: 80°C; The rotary cell.

The striking feature of the effect of rotating speed is the large variation of the anode potential, at a constant current density, with the relative acceleration rate, as shown in figure 6.19. The anode potential decreases with increasing applied G at all current densities, although the trend varies with the specific current densities. For example, at 300 $mAcm^{-2}$, the anode potential falls from 860 to 410 mV vs. RHE when the field increases from 1 G to 190 G; the values are 1100 to 570 mV vs. RHE at 500 $mAcm^{-2}$.

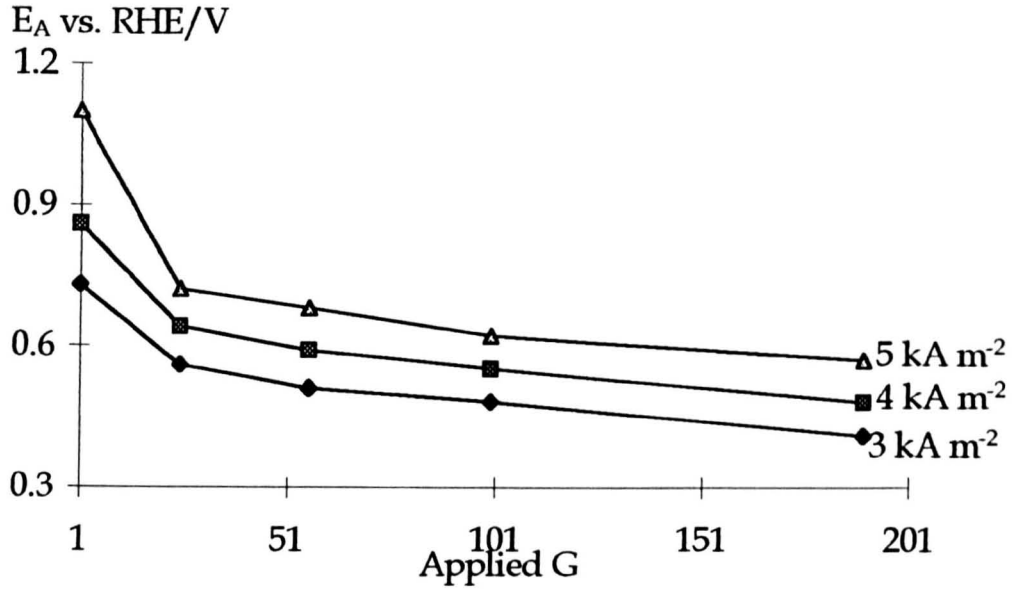

Figure 6.19. Anode potential against relative acceleration rate plots for CH_3OH oxidation in the rotary cell. Anode: Pt-Ru/Ti mesh (2 mg Pt+1 mg Ru cm^{-2}); Cathode: Pt(2 mg Pt cm^{-2})/Ti mesh; Anolyte: 1 M CH_3OH+0.5 M H_2SO_4 solution; Catholyte: 0.5 M H_2SO_4 solution; Scan rate: 5 mV/s; Temperature: 80^{0}C; The rotary cell.

Figure 6.20 shows anode potential reduction versus relative acceleration rate for methanol oxidation in the rotary cell. The anode potential reduction increases with increasing applied G. The higher the current density, the more marked the change. It is easily understood to consider that mass transport limitation of methanol would be very crucial and much more gas bubbles would be evolved at high current densities in the static cell. This introduces bubble polarisation and limits the current density and therefore leads to poor performance. On the other hand, this provides the opportunity to intensify the process in a powerful centrifugal field. Thus, much better improvement in the cell performance was observed in centrifugal fields. As the functions of centrifugal fields is not affected by current density applied, the higher the current density, the better the cell performance in centrifugal fields.

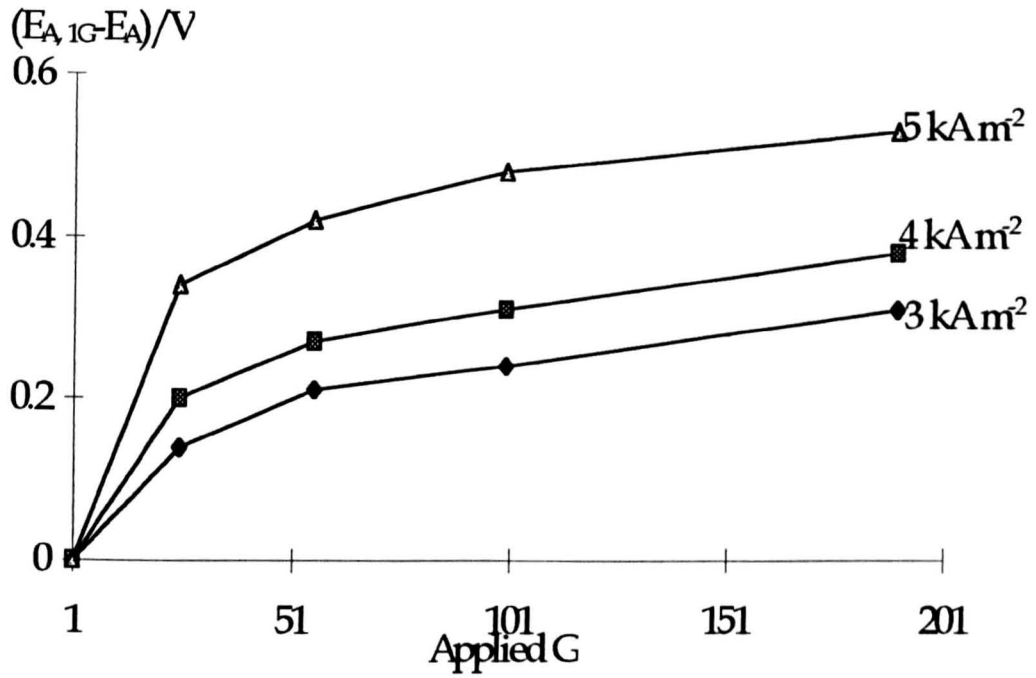

Figure 6.20. Anode potential reduction against applied G plots for CH_3OH oxidation in the rotary cell. Anode: Pt-Ru/Ti mesh (2 mg Pt+1 mg Ru cm^{-2}); Cathode: Pt(2 mg Pt cm^{-2})/Ti mesh; Anolyte: 1 M CH_3OH+0.5 M H_2SO_4 solution; Catholyte: 0.5 M H_2SO_4 solution; Scan rate: 5 mV/s; Temperature: 80°C; The rotary cell.

The Tafel data were also measured for the rotary cell which are given in figure 6.21.

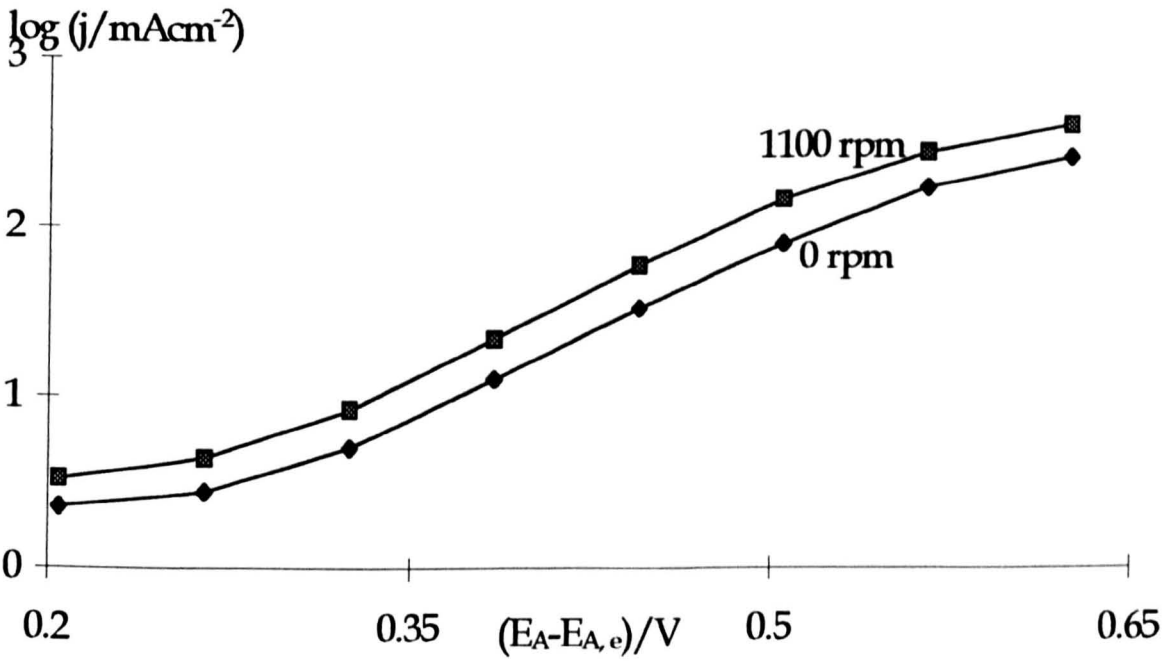

Figure 6.21. Tafel plots for methnol oxidation reaction on Pt-Ru/Ti electrode - Effect of acceleration rate. Anode: Pt-Ru/Ti mesh (2 mg Pt+1 mg Ru cm^{-2}); Cathode: Pt(2 mg Pt cm^{-2})/Ti mesh; Anolyte: 1 M CH_3OH+0.5 M H_2SO_4 solution; Catholyte: 0.5 M H_2SO_4 solution; Scan rate: 5 mV/s; Temperature: 80°C; The rotary cell.

The Tafel curves obtained at different rotating speeds is difficult to distinguish. Thus, only the data at 1100 rpm is presented in the figure. The Tafel slope obtained in an overpotential range of 0.35 to 0.5 V is 125 mV/decade for both the static and rotary cells. The exchange current density obtained by extrapolating to $(E_A-E_{A,e})=0$ are $10^{-4.38}$ and $10^{-4.58}$ A cm^{-2} for the static and the rotary cell respectively. The data obtained at 1 G agree with the reported results quoted in Section 6.3.3 [14, 15]. This demonstrates that methanol oxidation kinetics is improved little when increasing relative acceleration rate. In centrifugal fields, gas escapes relatively easily from the electrode surfaces. Therefore, the product of methanol oxidation, carbon dioxide, would be disengaged from the anode surface very effectively and leads to greater exposed electrode area. The centrifugal force may also affect the surface concentrations of the electroactive species. These are possible reasons of the observed increment of exchange current density in the rotary cell compared to the static cell. Further research is needed to complete understanding this effect.

6.4.2. Effect of Methanol Concentration

Figure 6.22 gives an example of the polarisation curves for methanol oxidation in the rotary cell with varying methanol concentrations. As shown in figure 6.22, even at a high acceleration field of 190 G, the peak due to mass transport limitation appeared in 0.5 M methanol solution. The mass transport limitations for the higher concentration solutions were not observed due to the signal output exceeded the equipment limit. The general effect of increasing methanol concentration is similar to that observed in the static cell, i.e., the polarisation curves shift to lower potentials. Although the effect of methanol concentration in centrifugal fields is qualitatively similar to that obtained in static cells, the cell polarisation behaviour is intensified in centrifugal fields. This can be seen by comparing the change in rate with methanol concentration for the rotary and static cell at a potential of 0.5 V vs. RHE, as presented in figure 6.23.

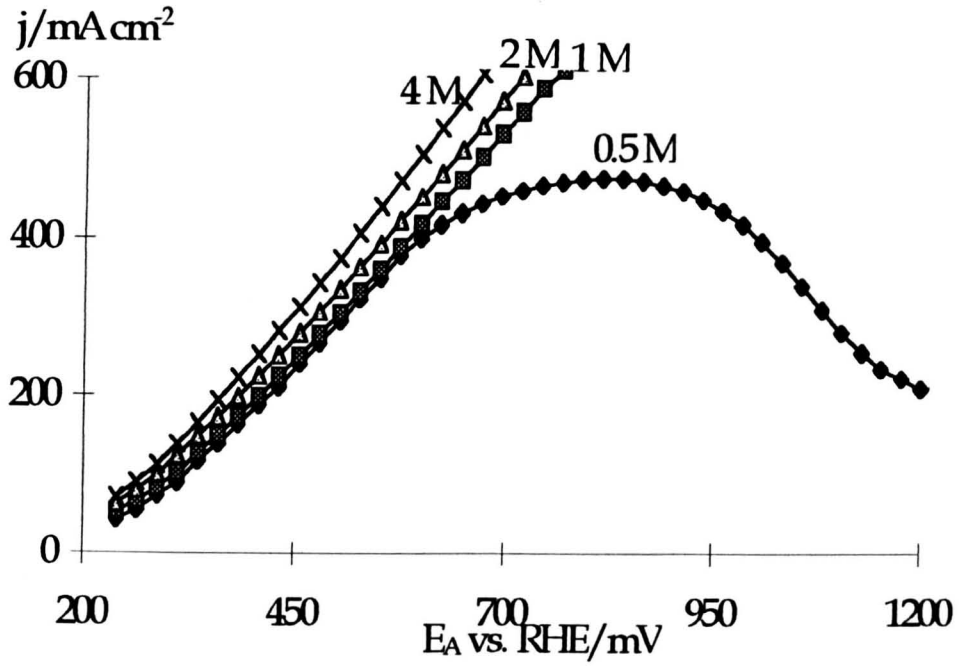

Figure 6.22. Comparison between anodic polarization curves for CH_3OH oxidation in different concentrations at 1100 rpm. Anode: Pt-Ru/Ti mesh (2 mg Pt+1 mg Ru cm^{-2}); Cathode: Pt(2 mg Pt cm^{-2})/Ti mesh; Anolyte: CH_3OH+0.5 M H_2SO_4 solution; Catholyte: 0.5 M H_2SO_4 solution; Scan rate: 5 mV/s; Temperature: 80°C; The rotary cell.

Figure 6.23 shows that the current density at 1100 rpm is always greater than that at 0 rpm and that the increase of the former with increasing the concentration also proceeds at a faster rate. At 1100 rpm, the average increase in rate of current density is about 1.58 kAm^{-2}/M from 0.1 M to 2 M which is larger than 1.00 kAm^{-2}/M obtained in the stationary cell. This enhancement comes from the improvement in mass transfer environment and the gas disengagement from the anode surface. Both factors promote more efficient methanol oxidation.

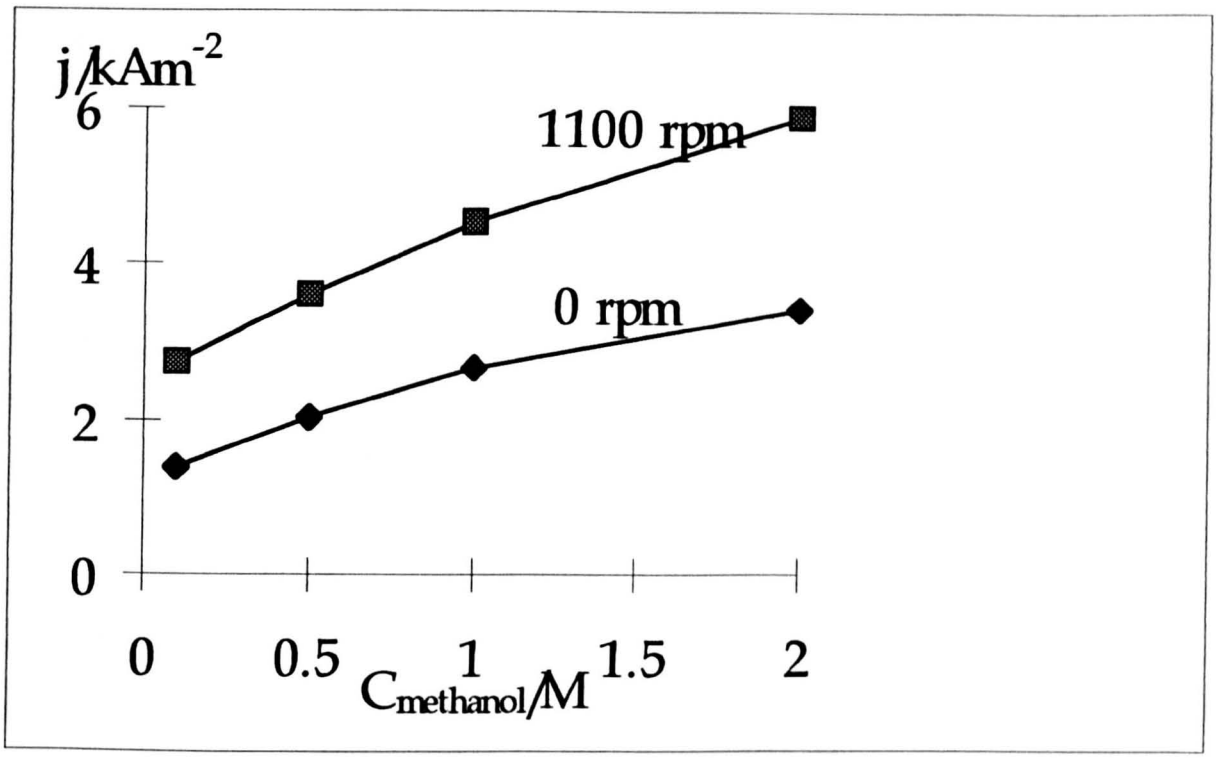

Figure 6.23. Enhancement of the concentration effect for CH_3OH oxidation in the rotary cell - Current density (at 0.5 V vs. RHE) versus methanol concentration curves. Anode: Pt-Ru/Ti mesh (2 mg Pt+1 mg Ru cm^{-2}); Cathode: Pt(2 mg Pt cm^{-2})/Ti mesh; Anolyte: CH_3OH+0.5 M H_2SO_4 solution; Catholyte: 0.5 M H_2SO_4 solution; Scan rate: 5 mV/s; Temperature: 80°C; The rotary cell.

6.4.3. Effect of Temperature

The effect of temperatureon the polarisation behaviour in centrifugal fields is in qualitative agreement with that obtained in the static cell. Figure 6.24 shows the typical results for methanol oxidation at varying temperatures in the rotary cell with Pt-Ru/Ti mesh electrodes and 1 M CH_3OH+0.5 M H_2SO_4 solution. It can be seen that the rate of methanol oxidation increases with temperature at a constant anode potential. Methanol oxidation was more efficient at 80°C, at the high anode potentials and the low anode potential, compared to other temperatures. However, what is quite different is that, in comparison to the results in the static cell, the effect of temperature had a greater influence on current density in centrifugal fields, as shown in figure 6.25.

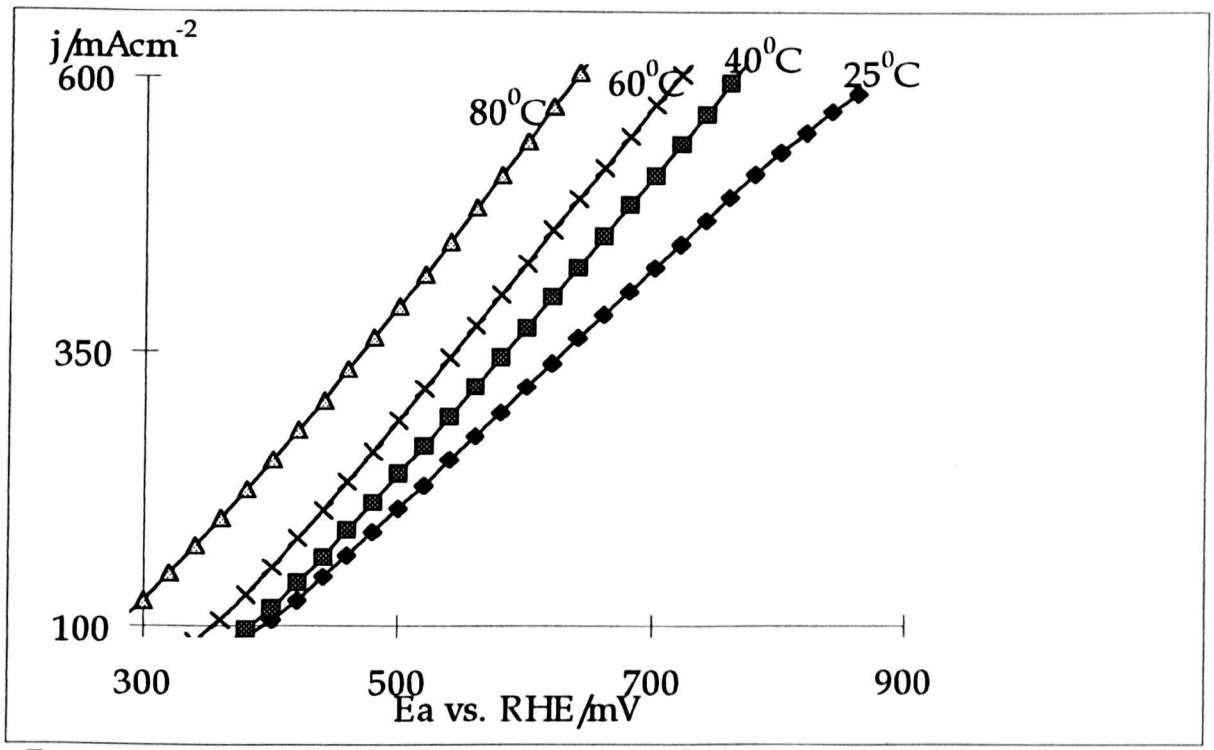

Figure 6.24. Anodic polarization curves of CH_3OH oxidation at different temperatures at 1100 rpm. Anode: Pt-Ru/Ti mesh (2 mg Pt+1 mg Ru cm^{-2}); Cathode: Pt(2 mg Pt cm^{-2})/Ti mesh; Anolyte: 1 M CH_3OH+0.5 M H_2SO_4 solution; Catholyte: 0.5 M H_2SO_4 solution; Scan rate: 5 mV/s; The rotary cell.

From figure 6.25, the average increase rate of anode current density is 57.5 $Am^{-2}/^0C$ at 1100 rpm, and in the static cell, the value is only 36.3 $Am^{-2}/^0C$. This means that higher temperature is better for high efficiency performance as well as high intensification of the processes in a rotary cell. It needs further research to explain the intensification of temperature effect in the rotary cell.

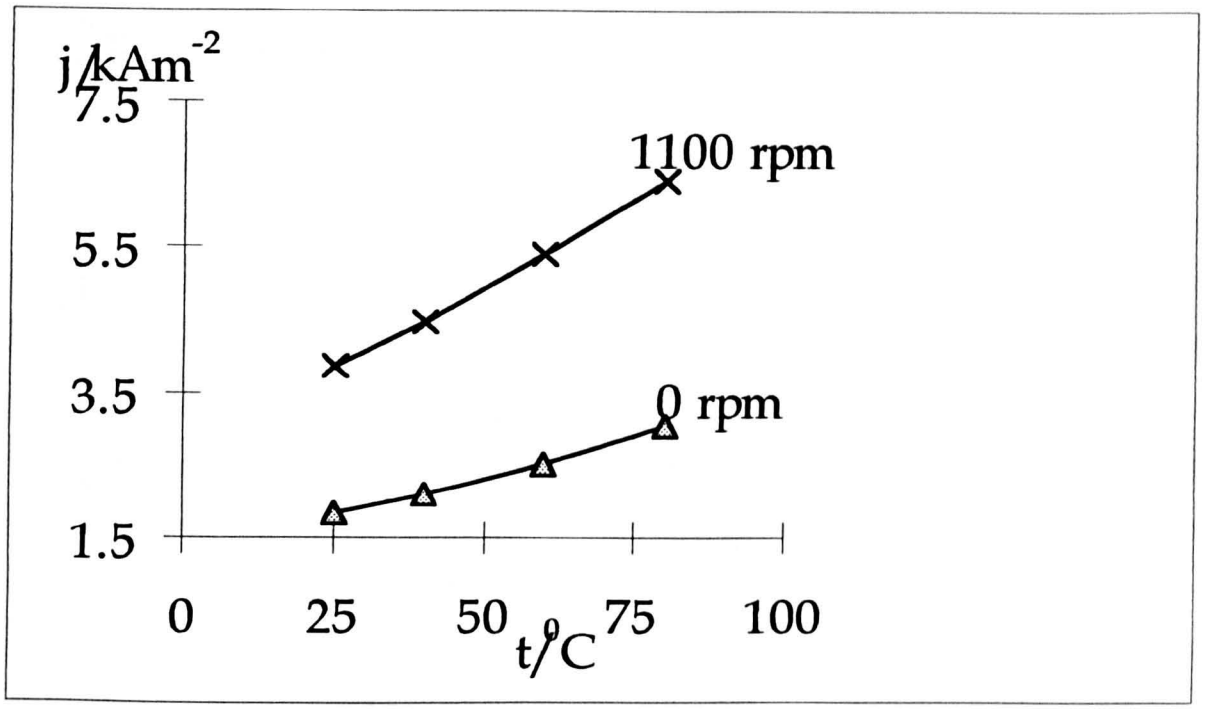

Figure 6.25. Enhancement of the temperature effect for CH_3OH oxidation in the rotary cell. - Current density (at 0.5 V vs. RHE) versus temperature curves. Anode: Pt-Ru/Ti mesh (2 mg Pt+1 mg Ru cm^{-2}); Cathode: Pt(2 mg Pt cm^{-2})/Ti mesh; Anolyte: 1 M CH_3OH+0.5 M H_2SO_4 solution; Catholyte: 0.5 M H_2SO_4 solution; Scan rate: 5 mV/s; The rotary cell.

6.5. Direct Methanol Fuel Cells

The functions of centrifugal fields in promoting mass transport and in disengaging gas bubbles from the electrode surface should benefit operation of DMFC where there are problems related the mass transport of methanol and the removal of CO_2 from the anode surface. This section describes the work has been undertaken.

6.5.1. Evaluation of the Ti Mesh Anode in DMFC

The Pt-Ru/Ti mesh anode was evaluated in a flow DMFC with a Teflon bonded carbon cloth gas diffusion cathode, which was prepared according to the method described in Chapter 2, in 2 M methanol solution at 90°C. Figure 6.26 presents a typical result.

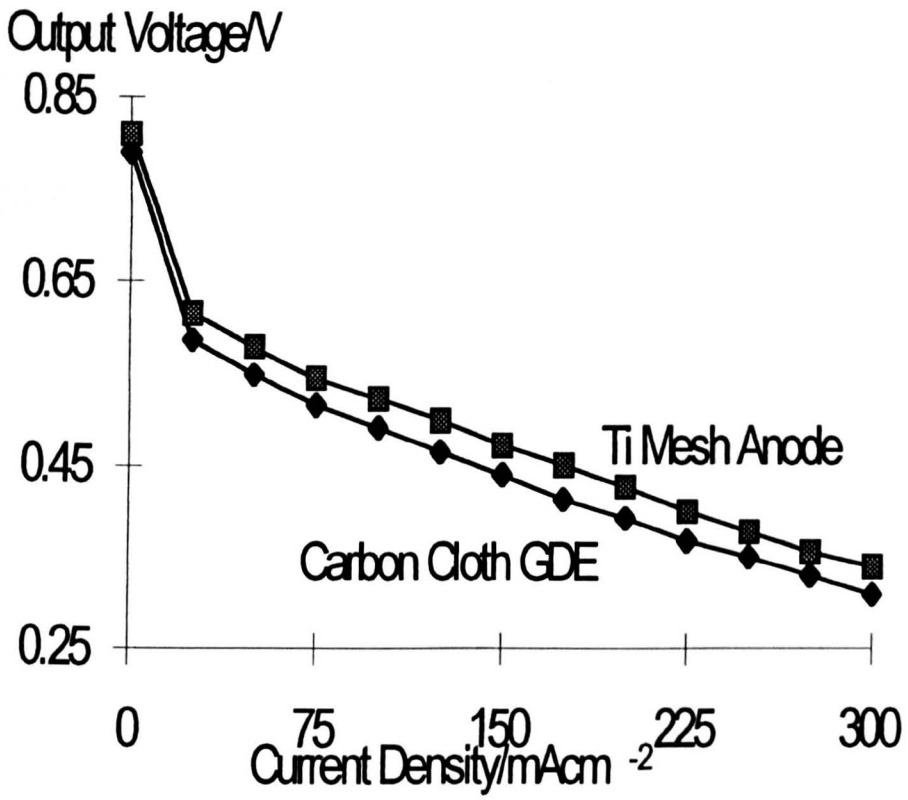

Figure 6.26. Effect of changing anode type on direct methanol fuel cell performance. Anode: Pt-Ru/Ti mesh or carbon cloth (2 mg Pt-1 mg Ru cm^{-2}); Cathode: Pt/carbon cloth GDE (1 mg Pt cm^{-2}); Anolyte: 2 M methanol solution; Anolyte flow rate: 1.2 ml/min; Air pressure (cathodic chamber): 1.5 bar; Temperature: 90°C; Nafion 117 membrane.

Figure 6.27 shows the cell power density versus current density curves for the flow DMFC with the Pt-Ru/Ti mesh anode and the Teflon bonded carbon cloth gas diffusion cathode. The flow fuel cell with the Ti mesh anode delivered higher power density (maximum power density is 102 mW cm^{-2}) compared the cell with the carbon cloth gas diffusion anode (maximum power density is 93 mW cm^{-2}), at potentials near 0.3 V at 90°C, as can be seen in figure 6.27. The reported maximum cell power density data, which is 125 mW cm^{-2} using O_2 at 90°C [15] or 110 mW cm^{-2} using air at 90°C [43]. Although the data obtained in this work are not optimal compared the reported results, it is clearly shown that an improvement in the output cell voltage about 30 mV can be achieved at all current densities by using the catalysed titanium mesh anode rather than the carbon supported gas diffusion anode. The improvement is not as good as expected based on the fact that the catalysed titanium mesh anodes give much better performance than the carbon gas

diffusion anode for methanol oxidation. This is partly due to the poor oxygen electrode performance often limits to reach a high efficiency of fuel cells [15, 37, 40, 41].

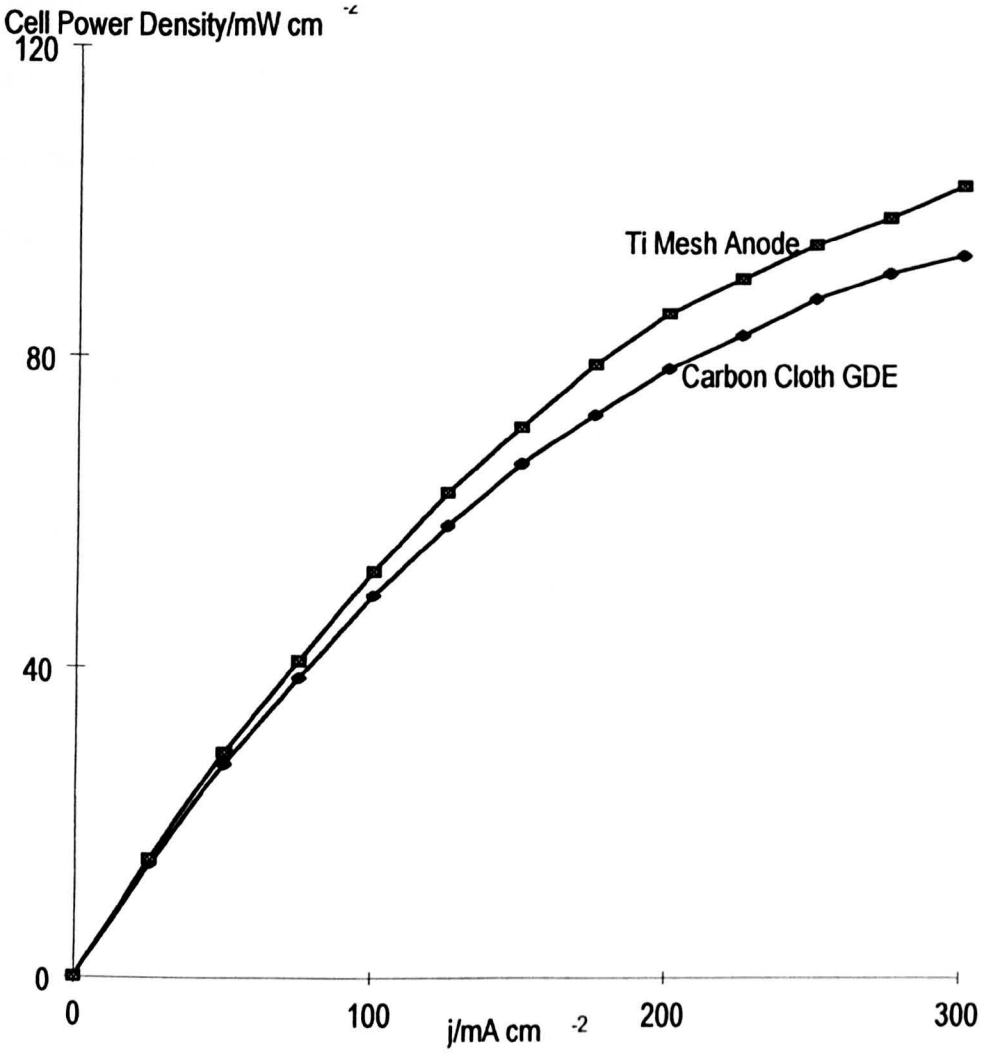

Figure 6.27. Cell power density versus current density plots of the direct methanol fuel cell. Anode: Pt-Ru/Ti mesh or carbon cloth (2 mg Pt-1 mg Ru cm^{-2}); Cathode: Pt/carbon cloth GDE (1 mg Pt cm^{-2}); Anolyte: 2 M methanol solution; Anolyte flow rate: 1.2 ml/min; Air pressure (cathodic chamber): 1.5 bar; Temperature: 90°C; Nafion 117 membrane.

6.5.2. The Performance of the Rotary DMFC

DMFC Using Gas Diffusion Cathode - This type of fuel cell directly consumes oxygen at the gas diffusion cathode and there is no need to use liquid catholyte. Thus, reactants can be contacted through the gas channels directly to the electrode rather than going through a gas-bubbling process. In this manner, the solubility

limitation of a gasous reactant in a liquid electrolyte no longer exists, and mass transport rate of gaseous reactants may be greatly increased. These advantages were proved in conventional fuel cells but, unfortunately, is not the case in the centrifugal fields. The typical results of the rotary fuel cell using Pt-Ru/Ti mesh anode and carbon cloth gas diffusion cathode in 2 M CH_3OH+1 M H_2SO_4 anolyte at 25°C are shown in figures 6.28.

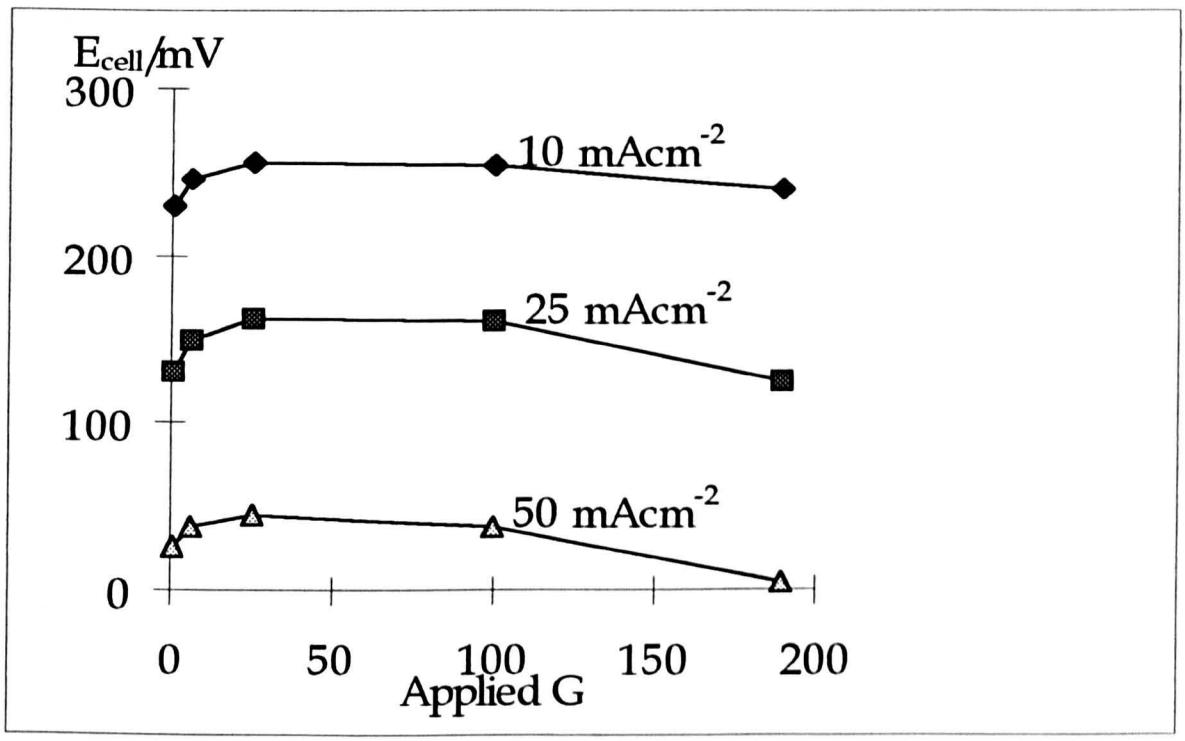

Figure 6.28. Output fuel cell voltage against applied relative acceleration rate plots for the rotary fuel cell. Anode: Pt-Ru/carbon cloth (2 mg Pt-1 mg Ru cm^{-2}); Cathode: Pt/carbon cloth (1 mg Pt cm^{-2}); Anolyte: 2 M CH_3OH+1 M H_2SO_4; Air pressure (cathodic chamber): 1.5 bar; Temperature: 25°C; The rotary fuel cell.

As shown in figure 6.28, a small increase in output cell voltage at all current densities were observed when the applied relative acceleration rate increases from 1 G to 25 G; the cell voltage was nearly constant between 25 G and 100 G; Above 100 G, the reverse effect was observed with lower cell voltage achieved. Also, the higher the output current density, the larger the decrease in cell voltages. The results were

very disappointing, the maximum power output is only 2.55, 4.05, and 2.25 $mWcm^{-2}$ at 10, 25, and 50 $mAcm^{-2}$, respectively. At 50 mA cm^{-2} and 190 G, almost no power was delivered.

Figure 6.29 shows the rotary cell output voltage against current density curves obtained from the rotary fuel cell using Pt-Ru/Ti mesh anode and carbon cloth gas diffusion cathode in 2 M CH_3OH+1 M H_2SO_4 anolyte at 25°C. As shown in figure 6.29, output cell voltage at 1100 rpm is about 10 mV higher than that of at 0 rpm at lower current densities up to 15 mA cm^{-2}. Above this current density, the reverse effect was observed with lower cell voltage achieved, at a fixed current density, at 1100 rpm than at 0 rpm.

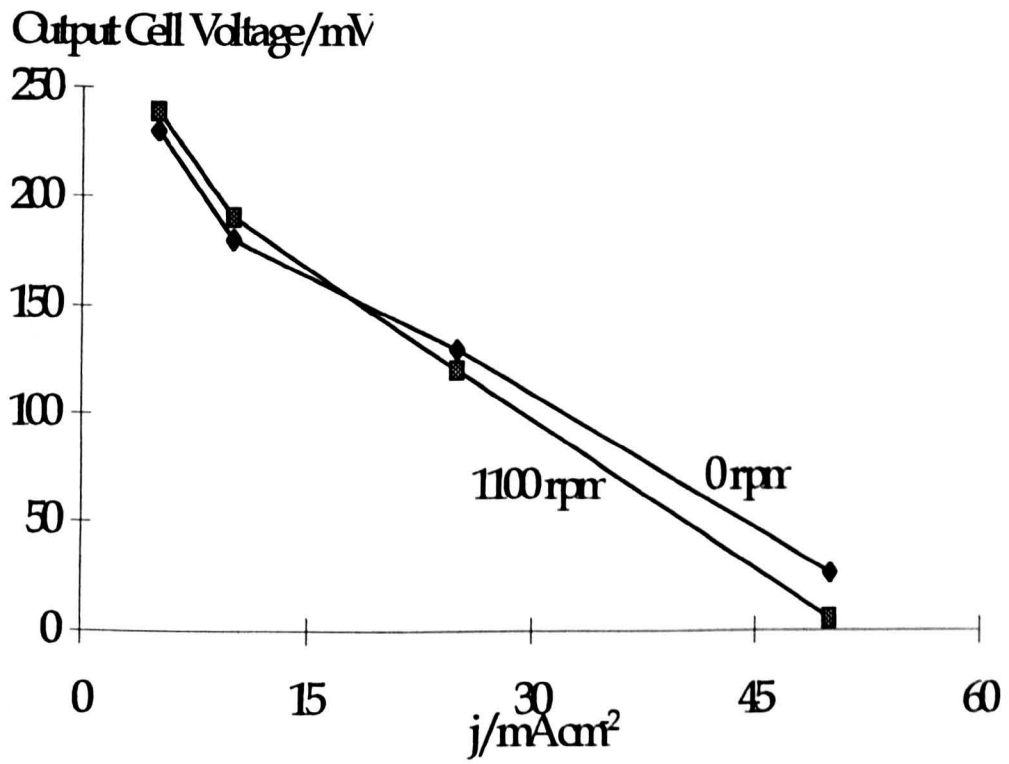

Figure 6.29. The rotary fuel cell polarisation curves. Anode: Pt-Ru/carbon cloth (2 mg Pt-1 mg Ru cm^{-2}); Cathode: Pt/carbon cloth (1 mg Pt cm^{-2}); Anolyte: 2 M CH_3OH+1 M H_2SO_4; Air pressure (cathodic chamber): 1.5 bar; Temperature: 25°C; The rotary fuel cell.

In theory, DMFC should be operated at higher temperature, i.e., above 60°C [13, 15, 42, 43]. Thus the rotary fuel cell operation at higher temperature was tried but no positive result was obtained due to the anolyte leaking to the cathodic chamber. Also, nearly no power was delivered when a Pt/Ti mesh cathode, operated as a gas diffusion electrode, was used in the rotary cell.

One of the reasons for the poor efficiency of the rotary fuel cell can be attributed to poor oxygen reduction in the rotary fuel cell where the high centrifugal force can do nothing to enforce the gas bubbles adhere on the cathode surface. The requirement of enough oxygen supply for efficient fuel cell operation would be very difficult to satisfy in centrifugal fields. In addition, as mentioned in Chapter 3, the setup used in the above work was not optium. More investigation is needed to know whether the gas diffusion electrode had adequate access to the oxygen in the rotary fuel. Moreover, it was observed that the anolyte leaked into the cathode chamber in the centrifugal fields. Several detrimental consequences were resulted from these intensified problems, such as the overwetting or flooding for the gas diffusion cathode. This blocks gas penetratration, impedes the transport of gaseous reactants to the reaction sites and therefore giving rise to a significant concentration polarisation. These factors add the more negative effects on the fuel cell performance. To completly understand the above observations needs further research.

DMFC With Air Bubbling Cathode - In this type fuel cell, oxygen or air is bubbling through the cathode immersed in liquid catholyte. The rotary fuel cell operated in this mode was tried more than ten runs but gave nearly zero power output.

In general, air electrode performance is controlled by a combination of electrode kinetics, mass transport, and ohmic conduction. Centrifugal fields can not overcome the obstacles from slow oxygen reduction kinetics as described previously. When the cathode was immersed in the catholyte and an oxygen was supplied as bubbles, very high gas transport limitation and very low oxygen solubility were introduced. The diffusion of gas reactants in liquid is much more difficult than in gas phase. Also, Centrifugal fields can not overcome the low oxygen solubility limitation, neither does efficiently enforce the reactant gas adhere on the cathode surface. As mentioned above, the setup used in the above work was not optium. Also, it is not clear at the moment whether the porous electrode had adequate access to the oxygen bubbles in the rotary fuel cell and whether the electrolyte circulated properly over the electrode, which needs more investigation. In addition, gas bubble imposes two effects on the air bubbling cathode: (i) The dispersion effect. Gas bubble enriched solution increases the bulk electrolyte resistivity and the solution ohmic drop due to nonconductive gas bubbles dispersing in the solution. The lower the gas voidage, the higher the resistance. This effect will remain even in centrifugal fields. If the air cathode is operated at high current densities, hydrogen evolution will be unavoidable. The thin layer of electrolyte close to the electrode surface will be more crowded with bubbles than the bulk electrolyte. The contribution of this "bubble curtain" to the total cell resistance is significant [44-46]. (ii) The shield effect. This effect reduces current at a fixed potential due to gas bubbles covering the electrode surface [45]. Centrifugal fields can reduce this effect significantly, but can not overcome other negative effects for operation of the rotary fuel cells.

Overall, the gas diffusion cathode appears to be the only feasible choice for efficient DMFC operation.

6.6. Conclusions

The above results support the following conclusions:

• With a Pt-Ru/Ti mesh anode, a very high performance was demonstrated for methanol electro-oxidation, which is very active, more so than for any of the other electrodes investigated, e.g., a polarisation as low as 0.52 V vs. RHE at a current density of 200 $mAcm^{-2}$, which is lower than those obtained at the catalysed carbon cloth anode (0.70 V vs. RHE) and the catalysed Teflon-bonded gas diffusion anode (0.90 V vs. RHE). It has been demonstrated that the novel method and the substrate allows reproducible fabrication of anodes with a suitable balance between micropores for gas access, micropores for liquid access, and conductive paths for electron access. The initial problems of high ohmic losses and low ionic conductivities appear to have been overcome to a large extent.

• Centrifugal fields make it possible to intensify the liquid reaction process to a great extent through maximising mass transport rate of methanol and minimising ohmic resistance by removing gas bubble as fast as they are formed. Like other gas evolving processes, methanol oxidation process is significantly intensified in centrifugal fields. The outstanding performance was demonstrated by subjecting the methanol anolytes to centrifugal force to promote both the mass transfer of methanol and the separation of gas bubbles from the anodes. The high acceleration field causes a significant reduction in the anode potential at a fixed current density. Anode potential reductions up to 500 mV at 3 kAm^{-2}, an anode current density

increment up to 2.5 kAm^{-2} at 0.5 V vs RHE were reached in an acceleration field of 190 G at 80°C in acidified methanol solutions, compared with a static cell.

• Electrolyte concentration and temperature also affect the anode performance. An increase in the electrolyte concentration can lead to a reduction in the cell resistance. In addition, an increase in working temperature also shows beneficial effects on the operational characteristics of the cells. Both the influences of concentration and of temperature are intensified in centrifugal fields.

• The performance of the rotary direct methanol fuel cell with the Ti mesh anode and the carbon cloth gas diffusion cathode was unsatisfactory, resulting in very low power output. This clearly represents serious obstacles to the development of fuel cells with this particular approach. The very low power output of this type of rotary fuel cell suggests the lack of an efficient gas supply to the cathode. Centrifugal fields seem no big benefit in solving the problems.

6.7. References for Chapter 6

[1] J. O'M. Bockris, B. E. Conway, E. Yeager, and R. R. White (Editors), "Comprehensive Treatise of Electrochemistry", Volume 3, Plenum Press, New York, 1981.

[2] B. D. McNicol, J. Electroanal. Chem., 118, 71, 1981.

[3] T. Frelink, W. Visscher, and J. A. R. van Veen, J. Electroanal. Chem., 382, 65, 1995.

[4] A. Hamnett, ETSU Draft Report, Feb. 1995.

[5] J. O'M. Bockris and S. Srinivasan, Fuel Cells: Their Electrochemistry, McGraw Hill, London, Chapter 10, 1969.

[6] P. A. Christensen and A. Hamnett, "Techniques and Mechanisms in Electrochemistry", Blackie/Chapman-Hall, 1994.

[7] V. S. Bagotzky and Y. B. Vassilyev, Electrochim. Acta, 12, 1323, 1967.

[8] V. S. Bagotzky, Y. B. Vassilyev and O. A. Khazova, J. Electroanal. Chem., 81, 229, 1977.

[9] H. A. Gasteiger, N. Markovic, P. N. Ross, and E. J. Cairns, J. Electrochem. Soc., 141, 1795, 1994.

[10 E. J. Cairns and D. C. Bartosik, J. Electrochem. Soc., 111, 1205, 1964.

[11] A. V. Tripkovic, K. D. Popovic, J. D. Momcilovic, and D. M. Drazic, Elechtrochim. Acta, 44, 1135, 1998.

[12] R. Parsons and T. VanderNoot, J. Electroanal. Chem., 257, 9, 1988.

[13] N. A. Mayorova, O. A. Khazova and V. S. Bagotzky, J. Solid State Electrochem., 1998 (2), 262.

[14] G. Meli, J. M. Leger, C. Lamy, and R. Durand, J. Appl. Electrochem., 23, 197, 1993.

[15] S. Surampudi, S. R. Narayanan, E. Vamos, H. Frank, G. Halpert, A. LaConti, J. Kosek, G. K. S. Prakash, and G. A. Olah, J. Power Sources, 47, 377, 1994.

[16] R. Parsons and T. VanderNoot, J. Electroanal. Chem., 257, 9, 1988.

[17] P. A. Christensen, A. Hamnett, J. Munk, and G. L. Troughton, J. Electroanal. Chem., 370, 251, 1994.

[18] J. Munk, P. A. Christensen, A. Hamnett, and E. Skou, J. Electroanal. Chem., 401, 215, 1996.

[19] J. B. Goodenough, A. Hamnett, B. J. Kennedy, R. Manoharan, and S. A. Weeks, Electrochim. Acta, 35, 199, 1990.

[20] B. B. Cattaneo, S. Wasmus, B. L. Mishima, and W. Vielstich, J. Appl. Electrochem., 23, 625, 1993.

[21] H. Nakajima and H. Kita, Electrochim. Acta, 33, 521, 1988.

[22] M. Hepel, Proc. -Electrochem. Soc., 96-8, 456, 1996.

[23] J. B. Goodenough, A. Hamnett, B. J. Kennedy, R. Manoharan, and S. A. Weeks, J. Electroanal. Chem., 240, 133, 1988.

[24] B. Beden, J. M. Leger, and C. Lamy, in "Modern Aspects of Electrochemistry", Vol. 22 (Edited by J'O. M. Bockris, B. E. Conway, and R. E. White), Plenum Press, New York, Chapter 2, p. 97, 1992.

[25] R. R. Adzic, in "Advances in Electrochemistry and Electrochemical Engineering", Vol. 13, (Edited by H. Gerisher and C. W. Tobias), Wiley & Sons, New York, p. 159, 1984.

[26] H. Binder, A. Kohling, and G. Sandstede in " Hydrogen Fuel Cell Technology", (Edited by B. S. Baker), Academic Press, New York, p. 91, 1965.

[27] B. D. McNicol and R. T. Short, J. Electroanal. Chem., 81, 249, 1977.

[28] M. Watanabe, M. Uchida, and S. Motoo, J. Electroanal. Chem., 229, 395, 1987.

[29] K. J. Cathro, J. Electrochem.Soc., 116, 1608, 1969.

[30] S. Motoo and M. Watanabe, J. Electroanal. Chem., 69, 429, 1976.

[31] J. A. Shropshire, J. Electrochem.Soc., 112, 465, 1965.

[32] B. A. Lopez De Mishima, H. T. Mishima, and G. Castro, Electrochim. Acta, 40, 2491, 1995.

[33] P. K. Shen and A. C. C. Tseung, J. Electrochem.Soc., 141, 3082, 1994.

[34] M. K. Ravikumar and A. K. Shukla, J. Electrochem. Soc., 143, 2601, 1996.

[35] A. K. Shukla, Personal communication, 1997.

[36] K.Scott, W. M. Taama, and P. Argyropoulos, submitted to J. Electrochem. Soc. 1998.

[37] N. A.-Vante, H. Tributsch, and O. S.-Feria, Electrochim. Acta, 40, 567, 1995.

[38] C.-C. Chang, T.-C. Wen, and H.-J. Tien, Electrochim. Acta, 42, 557, 1997.

[39] E. Yeager, Electrochim. Acta, 29, 1527, 1984.

[40] C. Pu, W. Huang, K. L. Ley, and E. S. Smotkin, J. Electrochem. Soc., 142, L119, 1995.

[41] M. W. Verbrugge, J. Electrochem. Soc., 136, 417, 1989.

[42] A. K. Shukla, P. A. Christensen, A. Hamnett, and M. P. Hogart, J. Power Sources, 55, 87, 1995.

[43] K. Scott, W. Taama and J. Cruickshank, J. Appl. Electrochem., 70, 40, 1998.

[44] H. Vogt, in "Comprehensive Treatise of Electrochemistry", Volume 6 (Edited by E. Yeager, J. O'M. Bockris, B. E. Conway, and S. Sarangapani), p 445, Plenum Press, New York, 1983.

[45] F. Goodridge and K. Scott, "Electrochemical Process Engineering", Chapter 5, Plenum Press, New York, 1995.

[45] G. Kreysa and M. Kuhn, J. Appl. Electrochem., 15, 517, 1985.

Chapter 7. Performance Modelling Of The Rotary Cell

7.1. Introduction

A thoroughly rigorous theoretical prediction of electrochemical processes in centrifugal fields is difficult and no generally accepted model is available. However, it is possible to produce a realistic model accounting for the centrifugal effect on electrochemical processes, in the case of gas evolving processes under reasonable assumptions. This chapter focuses on modelling electrochemical behaviour of the gas evolving electrodes in centrifugal fields using an approach that is analogous to that used to describe the behaviour of gas evolving electrodes in a gravitational field.

7.2. Literature Review

There is no report on modelling electrochemical behaviour of rotary cells with gas evolving electrodes, although some theoretical correlations are available for predicting mass transfer coefficients, as a function of rotational speed, in rotating packed beds, centrifugal reactors, centrifugal absorbers, centrifugal extractors, etc. [1-6]. This review concentrates on the modelling of electrochemical characteristics of the cells with gas evolving electrodes. The topic has been extensively studied in the last 30 years due to its role in promoting mass transport and in determining energy consumption in many industrial electrochemical processes.

7.2.1. Ohmic Drop in Bubble-Filled Electrolyte

A model was proposed to describe the relationship between current distribution and gas fraction for a stagnant electrolyte in a parallel plate cell [7]. The model assumes a uniform distribution of gas bubbles between the electrodes in the stationary electrolyte. Bubbles are assumed not to coalesce and to rise with a constant velocity

and obey Stoke's law. The local material balance on the gas evolution gives the rate of increase in local gas fraction f_{gx} with distance from the bottom of the cell x:

$$df_{gx}/dx = j_x R T/n F P u_g \delta_e \quad (7.1)$$

where j_x is the current density associated with the gas evolution, R the gas constant, T the temperature, n the number of electrons transferred in the gas evolution, F the Faraday constant, P the pressure, u_g the rise velocity of bubbles, and δ_e the distance between the electrodes. With the assumption that the mean potential drop in bubble-filled electrolyte, V_S is mainly due to the effective electrolyte resistance, the Bruggeman equation [see section 7.2.2] can be used to obtain V_S as:

$$V_S = j_x \delta_e (1-f_{gx})^{-1.5}/\sigma_s \quad (7.2)$$

where σ_s is electric conductivity of gas saturated solution.

Substituting the cell voltage equation (7.2) into (7.1) and integrating it, the gas fraction can be obtained (assuming a gas free solution at entry):

$$f_{gx} = 1-(1+V_S K x/2 L)^{-2} \quad (7.3)$$

where L is the cell length and constant $K = (R T \sigma L)/(n F P u_g \delta_e^2)$ and σ is electric conductivity of bubble-free electrolyte.

A combination of equations (7.2) and (7.3) gives the distribution of current density along the gas evolving electrode:

$$j_x = \sigma V_S/\delta_e (1+V_S K x/2 L)^3 \quad (7.4)$$

The average current density j_{av} is obtained from:

$$j_{av} = (_0\int^L j_x dx)/L \quad (7.5)$$

Combining equation (7.4) into equation (7.5) and integrating, yields:

$$V_S = 2[(1-j_{av} \delta_e K/L \sigma)^{-1/2}-1]/K \quad (7.6)$$

This model results in a general, qualitative understanding of the effects of gas evolution, which agrees well with experimental data at relatively low current densities when bubble coalescence does not occur. However, the analytical solutions apply to restricted conditions, such as the absence of polarisation effect and a simple geometry.

A similar model to that above considering the electrode polarisation was proposed [8], assuming a linear polarisation of the gas evolution reaction, using the Bruggeman equation, a relationship for the cell voltage was obtained

$$V_S = n\,F\,P\,u_g\,\delta_e^2\,[(\mu\,\sigma\,f_{gx}/\delta_e)+2(1-f_{gx})^{-0.5}-2]/R\,T\,H\,\sigma \qquad (7.7)$$

where μ is polarisation parameter of the cell and H the height of the electrolyte column in the cell. The model allows estimation of the resistance, voltage drop, and current distribution of bubble-filled electrolyte in industrial cells. However, due to the simple overpotential and neglect of electrolyte flow, substantial deviations from the experimental data were observed. This model was improved and a more sophisticated model accounting for the effects of bubble dispersion and shielding was proposed [9]. Based on the potential theory and the assumption that the dissolved gas obeys steady state diffusion within a concentration boundary layer, the coupled field equations were solved numerically using the boundary-element method. The model was successfully applied to the hydrogen evolution reaction in alkaline medium. Because of its complexity, there is no attempt to detail the model here.

A hydrodynamic model for the overall ohmic potential drop in a gas evolving cell with vertical electrodes was derived which considered the effect of the bubble curtain[10]. The model assumes that the interelectrode space can be divided into (a)

a fixed layer of the thickness δ_f, which ranges between 40 to 60 μm [10, 17], close to the gas evolving electrodes from where bubbles protrude into diffusion layers; and (b) a diffuse layer of the thickness (δ_e - 2 δ_f), if no a membrane or diaphragm was used, where the dispersion of gas bubbles in electrolyte is in movement. In this model, the effect of bubble curtain was quantitatively represented in the resistivity and gas fraction equations. Applying Ohm's law, the model yields a design equation for calculating the mean potential drop, V_S, of bubble-filled electrolyte:

$$V_S A \sigma / I \delta_e = 0.4(1-Y) \varepsilon[(1+\varepsilon)^{2.5} -1]+Y K \quad (7.8)$$

where A is electrode area, I is the total cell current, Y is the ratio of thickness of the fixed layer to the interelectrode distance, and ε the ratio of liquid flow rate to gas flow rate. Although not fully examined, the model agrees satisfactorily with experimental results, as shown in figure 7.1.

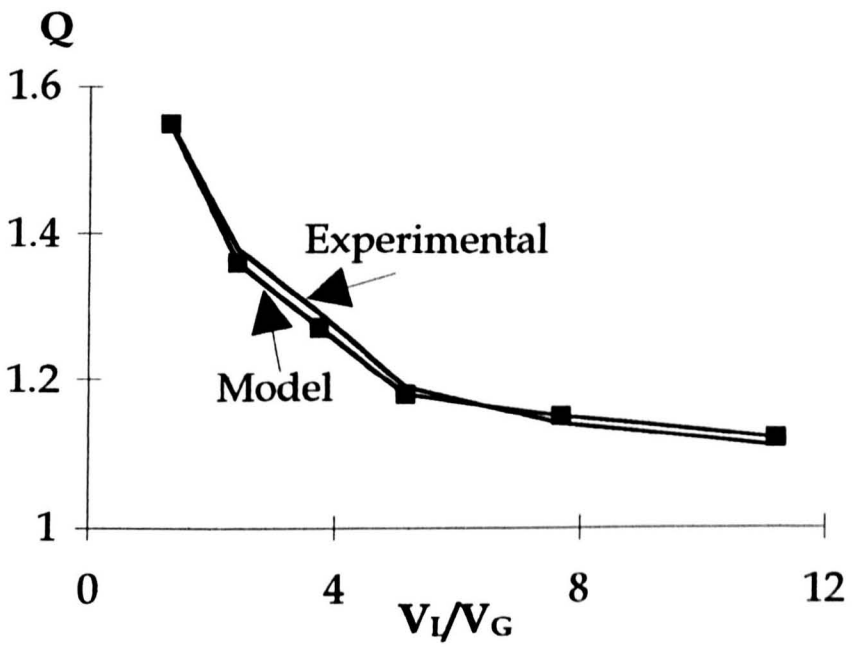

Figure 7.1. Mean relative resistivity ($Q = V_S A \sigma / I \delta_e$) against ratio of liquid to total gas flow rates plots - Comparison of experimental data with the hydrodynamic model. Data from figure 4 in [10].

7.2.2. Resistivity Models

The most significant effect of non-conducting gas bubbles evolved from gas evolving electrodes is the dramatic increase of cell resistivity, which constitutes a very active research field.

So far the most popular and reliable conductivity model is still the Bruggeman equation [11]. The model assumes that the conductivity of the medium surrounding a particle could be presented by the conductivity of the mixture as a whole, if the fractions of dispersed component in the mixture are high or the gas void fractions are low. Such a condition means that the bubbles do not influence each other. Based on the Maxwell equation:

$$\sigma_S/\sigma_L = 1 - 3(1 - \sigma_G/\sigma_L)/(2 + \sigma_G/\sigma_L) \tag{7.9}$$

a model was proposed for spheres:

$$1 - f_g = (\sigma_G-\sigma_S)/(\sigma_G-\sigma_L)\,(\sigma_L/\sigma_S)^{1/3} \tag{7.10}$$

where f_g is gas fraction, σ_G, σ_L, and σ_S are conductivity of a single sphere, an extended continuum, and an bubble-filled electrolyte, respectively.

When $\sigma_G/\sigma_L = 0$ and for nonconduting bubble spheres

$$\sigma_S/\sigma_L = (1 - f_g)^{3/2} \tag{7.11}$$

The Bruggeman equation is much better at predicting the effective resistivity than the Maxwell equation for larger volume fractions [7, 12]. Interestingly, although the Bruggeman equation was derived from the condition of low gas void fractions, it could be applied to gas bubbles attached to the electrode surface [13]. This means that the range of validity of the equation is much larger than the limited range for which it was derived.

Experiments in electrochemical gas evolving cells have distinguished two bubble regions: the fixed layer and the diffuse layer. The fixed layer is adjacent to the

electrode surface and crowded with bubbles in which the average solution flow velocity is relatively low. On the other hand, there are much fewer bubbles in the diffuse layer in which the average solution flow velocity is higher. From these observations, and the assumption that the gas void fraction in the fixed layer decreases linearly, applying the Bruggeman equation, the resistance of the fixed layer, R_f , is obtained [14]

$$R_f = R_{p\,0}\int^{a} [1 - f_{g,e} + (f_{g,e} - f_{g,b})\, x/a]^{-3/2}\, dx \qquad (7.12)$$

where R_p is the specific resistance of the solution, a is thickness of the fixed layer adjacent to the electrode surface, $f_{g,e}$ is gas void fraction at the electrode surface, $f_{g,b}$ is gas void fraction in the bulk electrolyte, x is distance from the electrode surface. The gas void fraction in the bulk electrolyte, $f_{g,b}$, was assumed constant over the entire width. Its value is approximated by dividing the volume of gas produced per unit time by the volume of electrolyte flowing through the cell per unit time. Therefore, the resistance of the diffuse layer, R_d, is expressed as

$$R_d = R_p (1 - f_{g,b})^{-3/2} (\delta_{ef} - a) \qquad (7.13)$$

where δ_{ef} is distance between the working electrode and the diaphragm. The relative resistance in the cell, R_r, was obtained by combining equations (7.12) and (7.13)

$$R_r/R_p = \{_0\int^{a} [1 - f_{g,e} + (f_{g,e} - f_{g,b})\, x/a]^{-3/2}\, dx + (1 - f_{g,b})^{-3/2} (\delta_{ef} - a)\}/\, \delta_{ef} \qquad (7.14)$$

The data predicted from the model is in qualitative agreement with the measured results for the hydrogen evolution, as shown in figure 7.2 which was obtained on the hydrogen evolving gold electrode in 1 M KOH solution at 30°C [14].

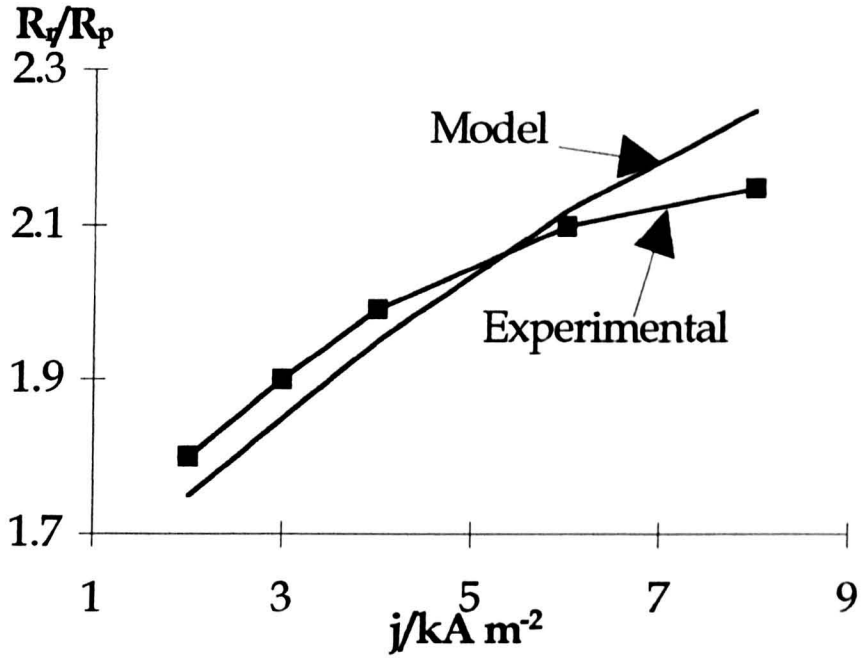

Figure 7.2. Calculated and measured relative resistivity as a function of current density at a flow rate of 0.05 m/s and at a hight of 35 cm from the bottom of the working electrode. Data from figure 14 in [14].

7.2.3. Mass Transfer Models

It is well known that gas bubbles evolved at gas evolving electrodes play a role in promoting mass transfer in electrolytes.

When a bubble reaches the departure diameter, it detaches from the elctrode and rises upward, transfering momentum to the surrounding liquid. As a result, a flow wake develops, causing a centripetal flow. Liquid from the outer edge of the concentration boundary layer or from outside is entrained to the electrode surface [15]. According to this observation, the penetration model [15, 16] assumes that the concentration of the liquid adjacent to the electrode is periodically replaced. During the waiting time, mass transfer is governed predominantly by non-steady state diffusion of the electroactive species. The mass transfer coefficient, the Sherwood number, is thus calculated for the condition of constant interfacial concentration by integrating the Cottrell equation and introducing the dimensionless parameters, i.e.,

$$Sh = (24/p)^{0.5} C^{-0.33} (Re\ Sc)^{0.5} (1-\theta)^{0.5} \quad (7.15)$$

where Sherwood number Sh = k α/D, k is the mass transfer coefficient, α is bubble departure diameter, and D the diffusion coefficient; Reynolds number Re = V_G α/A v, V_G/A is the volume flux of the evolved gas, v is kinematic viscosity; Schmidt number Sc = v/D; θ is the bubble fractional surface coverage; C is bubble shape factor and equals 8 and 4 for spherical and hemi-spherical bubbles, respectively. The penetration model can explain some experimental results.

The microconvection model [17] which is different from the penetration model, assumes that only liquid convective mass transfer, introduced by the growing bubbles, plays a decisive role. The model also assumes that the velocity distribution at the bubble-liquid interface is of plug flow type and develops steadily into a boundary layer flow as the distance from the bubble increases. The model gives a similar equation to the penetration model, except for extremely small fractional surface coverage:

$$Sh = 1.562\ (Re\ Sc)^{0.5} (1 + 0.29/Sc^{-0.17} + 0.0047\ Sc^{0.053})\ \theta^{0.25} (1 - \theta^{0.5})^{0.5} \quad (7.16a)$$

This equation was approximated as

$$Sh = 0.93\ Re^{0.5}\ Sc^{0.487} \quad (7.16b)$$

This mass transfer model agrees satisfactorily with experimental data, which is shown in figure 7.3. In figure 7.3, only experimental results at a fixed Sc value were available. H_2^a and O_2^a were obtained on the Pt electrodes in 0.03 M $K_4Fe(CN)_6$ + 1 M KOH solution at 298 K. H_2^b and O_2^b were obtained on the Pt electrodes in 0.1 M $K_3Fe(CN)_6$ + 2 M NaOH solution at 298 K. Model A was obtained from the flow pattern between plug and boundary layer flow. Model B was obtained only considering the plug flow [17].

As shown in figure 7.3, the scatter is considerable due to the simplicity of the models used and to the difficulties of the experiments and evaluation of the data.

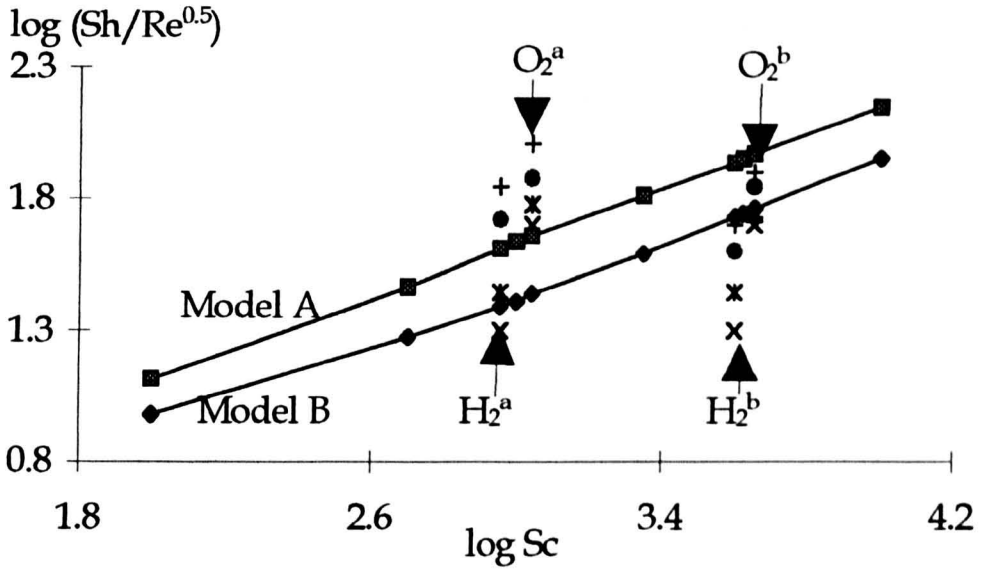

Figure 7.3. Comparison between the mass transfer models and experiments. Data from figure 3 in [17].

Another model, the hydrodynamic Model [15, 18-21] does not consider microeffects occurring in the vicinity of bubbles departing from the electrode, as does in the penetration model; and does not consider the microeffects of bubbles growing while adhering to the electrode, as in the microconvection model. The central assumption in the hydrodynamic model is that the ascending bubbles promote the electrolyte flow and this determines the mass transfer at the gas evolving electrode. Based on the mass transfer equation for natural convection at a plane wall, the model equation is:

$$k\,L/D = Q\,(Gr\,Sc)^{1/3} \qquad (7.17)$$

where k is mass transfer coefficient; Grashof number $Gr = g\,L^3\,(p_0-p)/p\,v^2$, g is gravitational constant (9.81 ms^{-2}), p_0 and p are density of bubble-free electrolyte and bubble-filled electrolyte, respectively, v is kinematic viscosity; L is electrode length;

and Q the constant.

The model was used successfully to correlate the experimental data in certain cases. For example, the experimental log δ/log v_g slope is about - 0.3, where δ is the thickness of the Nernst diffusion layer obtained from the penetration model and v_g is volumetric production rate of gas bubbles. This data was obtained on Pt electrodes for the hydrogen evolution in 1 M KOH solution and for the oxygen evolution in 1 M KOH solution at current density $j < 30$ mA cm^{-2} [19]. The penetration model explains these data very well [15, 19, 20]. But it does not include the mass transfer promoted by, for example, mechanical pumping. Based on the assumption of a fixed bubble layer, unaffected by current density and flow conditions, the hydrodynamic model was modified [10, 22-24] to widen the applicable range of the model.

The convection-penetration model [25] considers the effects of the both penetration and forced convection. It assumes that the adhered bubbles have no influence on the rate of mass transfer and only take into account the detaching bubbles. Followed the Cotrell equation, it gives the total mass transfer coefficient k for a gas evolving electrode under forced convection:

$$k = k_0 + D_i a A v_g / p k_0 V_b \qquad (7.18)$$

where k_0 is the mass transfer coefficient in the absence of gas bubble, D_i the diffusion coefficient of species i, a is the proportionality coefficient, A the average cross-section of the detached bubbles, v_g the volumetric production rate of gas bubbles, and V_b the average volume of departed bubbles.

7.3. Physical Model Of The Rotary Cell

7.3.1. Characteristics of Gas Evolving Electrode

The processes of interest here are those occurring at gas evolving electrodes and only via gas evolution. One of the peculiarities of such processes lies in the fact that the removal of the final product from the electrode surface may proceed not only through its diffusion into the bulk solution, but also by gas bubble formation at the electrode surface. This means that the electrochemical and chemical formation of a substance to be subsequently transformed to the gaseous phase. In particular, after a critically high current density of the gas evolving reaction, the supersaturation of the dissolved gas in the vicinity of the electrode increases rapidly. So the gas bubbles grow rapidly while the simultaneously adhering bubbles become numerous. Bubbles are positioned closer together and finally interact with each other and impede the liquid contact with the electrode. After the bubbles have detached from the electrode, they remain dispersed in the electrolyte for a certain time in the interelectrode space. Corresponding to these, two characteristics become clear [10, 23, 26-35]:

(1) A thin bubble layer or "bubble curtain" (thickness being the diameter of adhered bubbles, i.e., 40 to 60 μm [10, 14, 17]) is formed adjacent to the electrode surface. This layer, known as fixed layer, effectively screens the electrode, obstructs gas removal, and decreases the active electrode surface, and changes the environment around the electrode. This greatly increases the ohmic resistance and the overpotential at the electrode, and severely restricts the current flow.

(2) A gaseous phase non-uniformly dispersed in the interelectrode gap and the electrolyte, constituted a diffuse layer, which also contributes to increase the total cell resistance.

7.3.2. The Rotary Cell with Gas Evolving Electrodes

The rotary cell with gas evolving electrodes is sketched in figure 7.4. The electrode channels are magnified in figure 7.5. In figure 7.4, the axis is chosen so that x, y, and z are coordinate direction of parallel, perpendicular, and azimuthal to the electrode surfaces. The rotary cell consists of two parallel rectangular channels, with electrodes facing a membrane, which seperates anolyte and catholyte. In centrifugal fields, the mixture of gas and electrolyte rotates uniformly at the same speed as the cell body and flows outwards in radial direction; a rapid bulk radial flow of the gas bubbles is inwards to the axis. The fixed layers and diffuse layers are shown in the figure 7.5.

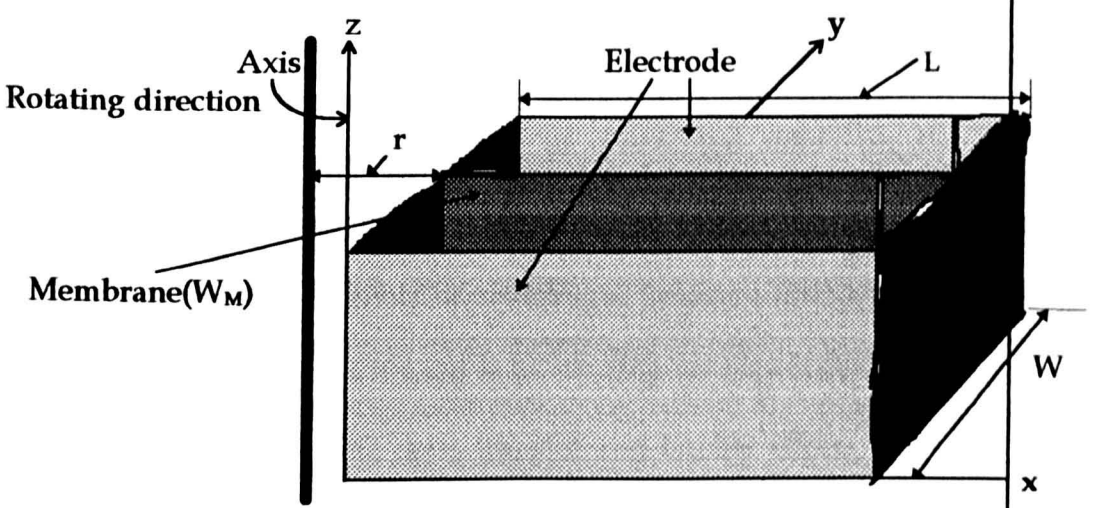

Figure 7.4. Schematic model of the rotary cell with gas evolving electrodes.

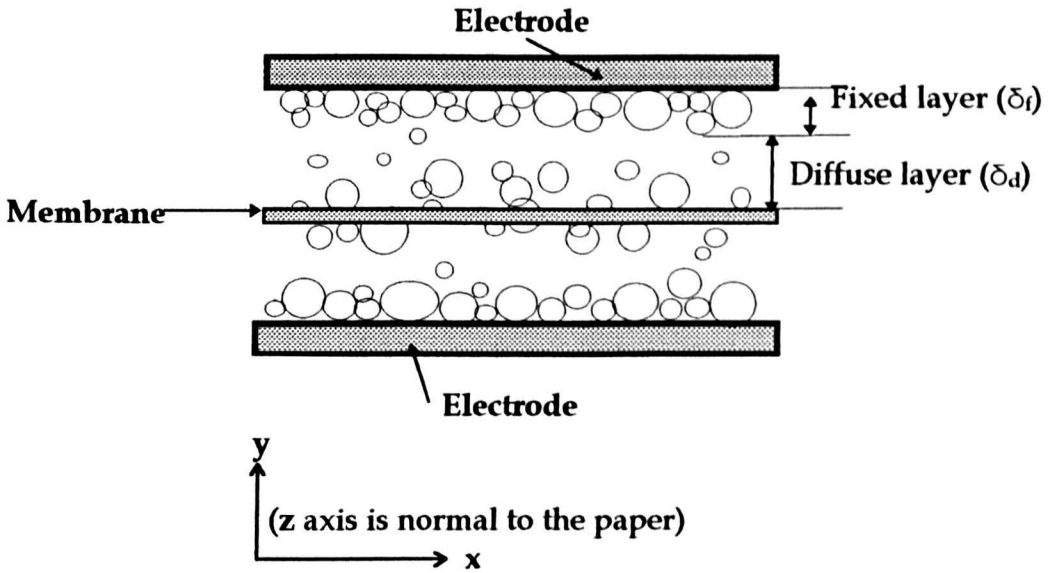

Figure 7.5. Section of the rotary cell with gas evolving electrodes. The bubbles at the electrode surfaces and membrane are closely packed while those in the rest of the solution are more dispersed.

Based on this physical model, a theoretical model will be detailed in the following sections, to examine the influence of centrifugal fields on the electrochemical behaviour of the rotary cell with gas evolving electrodes. The scope is restricted to voltage effects, i.e., the effect of centrifugal fields on ohmic drop and on electrode polarisation. The approach used is to develop an expression for the cell voltage of the rotary cell considering mass transfer and bubble effects, respectively, and then incorporate them into a centrifugal model. As in a gravitational field, the bubble-induced ohmic drop in a centrifugal field depends on many parameters, such as the centrifugal acceleration, bubble rise velocity, electrolyte flow rate, the cell geometry, etc.

7.4. The Rotary Cell Voltage

7.4.1. Cell Voltage Expression

The overall cell voltage, E_{Cell}, if defined as positive, can be presented as [28]:

$$E_{Cell} = E_A + |E_C| + \eta_A + |\eta_C| + V_A + V_C + V_M + V_{SA} + V_{SC} \qquad (7.19)$$

where E_A and $|E_C|$ are the anodic and the cathodic electrode equilibrium potentials respectively, η_A and $|\eta_C|$ are the anodic and the cathodic overpotentials respectively, and V_A, V_C, V_M, V_{SA}, and V_{SC} are the voltage drops caused by ohmic resistance on the anode, cathode, membrane, and in the anolyte and catholyte, respectively. In equation (7.19), the ohmic voltage drops in the anode and cathode electrical connections are ignored.

Generally, the calculation of the cell voltage is based on a simultaneous solution of the Laplace equations which is a rather difficult task, especially for the rotary cell configuration considered here. However, to aid the solution, the model can be simplified with a number of additional assumptions to lend clarity and simplicity to the mathematical treatment while not detracting significantly from the general validity of the model. Accordingly, each term in equation (7.19) is specified as follows.

7.4.2. Electrode Potentials and Ohmic Drops on Electrodes and Membrane

Electrode potentials, ohmic drops on electrodes and membrane can be expressed according to the Tafel equation as

$$E_A = E_{A,e} + a_A + b_A \log j_{av} \qquad (7.20)$$

$$E_C = E_{C,e} + a_C + b_C \log j_{av} \qquad (7.21)$$

where E_A and E_C are anode and cathode potential, respectively; $E_{A,e}$ and $E_{C,e}$ are anode and cathode equilibrium potential, respectively, j_{av} average current density flowing through the cell; a_A, b_A, a_C, b_C are Tafel constants for anode and cathode, respectively.

The ohmic drops on electrodes are expressed as

$$V_A = j_{av}\,\delta_A/\sigma_A \tag{7.22}$$

$$V_C = j_{av}\,\delta_C/\sigma_C \tag{7.23}$$

where σ_A and σ_C are conductivity of anode and cathode, respectively, δ_A and δ_C are the anode and cathode thickness, respectively.

The Nafion membrane behaves like an ohmic resistance under industrial conditions [36] and therefore, a linearised expression can also be applied to membrane

$$V_M = j_{av}\,\delta_M/\sigma_M \tag{7.24}$$

where δ_M and σ_M are thickness and specific conductivity of the membrane, respectively.

7.4.3. Ohmic Drop in Electrolytes

The calculation of the ohmic drop in bubble-filled electrolyte is based on models, such as a simple ohmic correlation [37]:

$$V_S = j\,H/\sigma_S \tag{7.25}$$

or more complex formulas, such as equation (7.7) [8] and equation (7.8) [10]. For convenience, both gas and liquid flows are treated as an ideal, incompressible, isobaric, and isothermal system and the electrolyte as a pure ionic conductor which can be described using Ohm's law. It was demonstrated that the flow was laminar for most gas evolving operations in gravitational field [8, 21]. In a high acceleration field, the liquid movement was also considered as laminar flow for convenience [2]. This means that the analogous approach as those in gravitational field can be used in centrifugal fields. More specifically, the bubbles are considered uniformly distributed in the horizontal cross-section of the cell and can be characterised by an average rise velocity, which is independent of height and current density. Constant solution conductivities can be assumed for the cells with gas evolving electrodes. Based on these assumptions and also from the physical model of the rotary cell, the main formula for the ohmic drop of the gas bubble-filled electrolyte, V_S, can be derived from

$$V_S = j_{av}\, S/\sigma_S \qquad (7.26)$$

Where $S = \delta_e - \delta_M$, δ_e is the distance between the anode and cathode, δ_M is the thickness of the membrane, j_{av} is the current density flowing through the electrolyte, σ_S is conductivity of the bubble-filled electrolyte.

7.4.4. Detailed Cell Voltage Expression

The equation (7.19) can now be expressed as:

$$E_{Cell} = E_{A,e} + |E_{C,e}| + a_A + |a_C| + (b_A + |b_C|)\log j_{av} + j_{av}(L/\sigma_A + L/\sigma_C + \delta_M/\sigma_M + S/\sigma_S) \qquad (7.27)$$

The quantities related to centrifugal acceleration rate, i.e., j_{av} and σ_S will be determined in the following sections.

7.5. Average Current Density

7.5.1. Main Equation

The very high acceleration in centrifugal fields efficiently promotes the mass transport of the reactants. The current density due to diffusion under the operating conditions of the rotary cell should therefore remain very high. The interface current density can be approximated as the limiting current density and calculated via

$$j_{av} = n\, F\, k_L (C_b - C_s) \qquad (7.28)$$

where k_L is the liquid phase mass transfer coefficient, C_b and C_s are the bulk and electrode surface concentration, respectively. To get a complete expression of equation (7.28), the concentration distribution and mass transfer coefficient should be determined. In order to do so, a solution velocity and its components are obtained first.

7.5.2. Solution Velocity

Under Boussinesq approximation and neglecting the changes in density and viscosity, the steady-state Navier-Stokes momentum equations for the rotary cell are [28, 37-40]:

$$\rho\,(u_x \partial u_x/\partial x + u_y \partial u_x/\partial y + u_z \partial u_x/\partial z) = \nu\,(\partial^2 u_x/\partial x^2 + \partial^2 u_x/\partial y^2 + \partial^2 u_x/\partial z^2) - \partial P/\partial x - \rho(x+r)\omega^2 \qquad (7.29)$$

$$\rho (u_x \partial u_y/\partial x + u_y \partial u_y/\partial y + u_z \partial u_y/\partial z) = \nu(\partial^2 u_y/\partial x^2 + \partial^2 u_y/\partial y^2 + \partial^2 u_y/\partial z^2) - \partial P/\partial y \quad (7.30)$$

$$\rho (u_x \partial u_z/\partial x + u_y \partial u_z/\partial y + u_z \partial u_z/\partial z) = \nu (\partial^2 u_z/\partial x^2 + \partial^2 u_z/\partial y^2 + \partial^2 u_z/\partial z^2) - \partial P/\partial z \quad (7.31)$$

The continuity equation is unaltered by the rotation [39]:

$$\partial u_x/\partial x + \partial u_y/\partial y + \partial u_z/\partial z = 0 \quad (7.32)$$

where u_x, u_y, and u_z are the liquid velocity component in x, y, and z direction (Refer to figure 7.2), respectively, ω is angular velocity, ρ is the density and ν viscosity of the bubble-filled electrolyte, respectively.

According to the Prandtl boundary-layer simplifications, the flow in the boundary layer may be considered as laminar and the z-components of the velocity is virtually constant. The thickness of the diffusion layer and of the hydrodynamic boundary layer is assumed very small compared to the dimensions of the distance between electrodes. The average velocity along the y-axis, $\partial u/\partial y$, is very much larger than those in the directions parallel to the electrode surface, $\partial u/\partial x$ and $\partial u/\partial z$. Therefore, we have $\partial^2 u/\partial x^2 << \partial^2 u/\partial y^2 >> \partial^2 u/\partial z^2$. It follows that $\partial^2 u_x/\partial x^2$, $\partial^2 u_x/\partial z^2$, $\partial^2 u_y/\partial x^2$, and $\partial^2 u_y/\partial z^2$ in the equations (7.29)-(7.32) can be neglected [28, 38-43]. Similar boundary assumptions, such as presence of considerable velocity gradients, laminar flow, etc., are applicable for the rotary cell. This is because the z-direction acceleration terms will not generate significant flow or cause pressure variations in that direction [2]. Moreover, the derivatives of pressure may be neglected in comparison with the centrifugal term. The equations of motion for the rotary cell, at steady-state, are therefore simplified as

$$u_x \partial u_x/\partial x + u_y \partial u_x/\partial y = (\nu/\rho)\partial^2 u_x/\partial y^2 (x+r)\rho^{-1}\omega^2 \quad (7.33)$$

$$\partial u_x/\partial x + \partial u_y/\partial y = 0 \quad (7.34)$$

The boundary conditions for the integration of equations (7.33) and (7.34) are

$$u_x = 0 \qquad \text{for } y = 0 \quad (7.35a)$$

$$u_x = u_0 \qquad \text{for } x = 0 \quad (7.35b)$$

$$u_x = u_0 \qquad \text{for } y = \delta \tag{7.35c}$$

where u_0 is average liquid velocity at $x = 0$ and may be assumed as $u_0 = u_s + r\,\omega$, u_s is bubble rising velocity in gravitational field, r is the distance between the axis and the rotary cell (see Figure 7.2), ω is angular velocity, δ is the thickness of the boundary layer.

As usual, a velocity profile including the centrifugal force term is assumed [2, 39]

$$u_y = u_x + (x + r)\,\omega \tag{7.36}$$

Substituting equations (7.34) and (7.36) into (7.33) gives an ordinary differential equation,

$$[u_x+(x+r)\,\omega]\partial u_x/\partial y - u_x\partial u_x/\partial y = (\nu/\rho)\partial^2 u_x/\partial y^2 - (x+r)d^{-1}\omega^2 \tag{7.37a}$$

$$\partial^2 u_x/\partial y^2 - (\rho/\nu)\,(x+r)\,\omega\,\partial u_x/\partial y - (x+r)\,\nu^{-1}\omega^2 = 0 \tag{7.37b}$$

The equation (7.37b) is a second-order differential equation which may be integrated immediately by conventional method [44-46]. Thus, the equation (7.37b) becomes

$$u'_x - (\rho/\nu)(x+r)\,\omega u_x - (x+r)\,\nu^{-1}\omega^2 y = A_1 \tag{7.38a}$$

$$u'_x - (\rho/\nu)(x+r)\,\omega u_x - (x+r)\,\nu^{-1}\omega^2 y = 0 \tag{7.38b}$$

where prime denotes d/dy and the constant of integration A_1 is obtained using the boundary condition (7.36). Analytical expressions for the solution of equation (9.37) are found

$$\begin{aligned} u_x &= \exp[\textstyle\int (\rho/\nu)(x+r)\,\omega dy]\{\,((x+r)\,\nu^{-1}\omega^2 y\exp[\textstyle\int -(\rho/\nu)\,(x+r)\,\omega dy]dy + A_2\} \\ &= \exp[(\rho/\nu)\,(x+r)\,\omega\,y]\{(x+r)\,\nu^{-1}\omega^2 \textstyle\int y\exp[-(\rho/\nu)\,(x+r)\,\omega\,y] + A_2\} \\ &= -\omega^2 y/\rho - \nu\omega^2/\rho^2(x+r) + A_2\exp[(\rho/\nu)\,(x+r)\,\omega y] \end{aligned} \tag{7.39a}$$

which can be approximated under an approximate Taylor expansion. The approximation is reasonable because the diffusion layer lies entirely within a practically linear part of the velocity profile [42, 47]. Thus

$$u_x \approx u_0 + (\delta - y)\omega^2/\rho \tag{7.39b}$$

A_2 is obtained using the boundary conditions (7.35):

$$A_2 = [u_0 + \omega^2\delta/\rho + \nu\omega^2/\rho^2(x+r)]\exp[-\rho\nu^{-1}(x+r)\omega\delta)] \tag{7.40}$$

A combination of equations (7.36) and (7.39), we have

$$u_y = u_0+(x+r)\omega +(\delta-y)\,\omega^2/\rho \tag{7.41}$$

Solution velocity can be expressed as

$$u_L = (u_x^2+u_y^2)^{1/2}$$

$$= \{[u_0+(\delta-y)\,\omega^2/\rho]^2+[u_0+(x+r)\,\omega+(\delta-y)\,\omega^2/\rho]^2\}^{1/2}$$

$$\approx (2u_0^2+2u_0\omega+x^2\omega^2)^{1/2} \tag{7.42}$$

Arithmetic mean velocities are

$$u_x(av) = (1/L\delta)\,{}_0\int^L\,{}_0\int^A u_x dxdy$$

$$= (1/L\delta)\,{}_0\int^L\,{}_0\int^A [u_0+\rho^{-1}(\delta-y)\omega^2]dxdy$$

$$= u_0+\delta\omega^2/2\rho \tag{7.43}$$

where $A = \delta$.

$$u_y(av) = (1/L\delta)\,{}_0\int^L\,{}_0\int^A u_y dxdy$$

$$= (1/L\delta)\,{}_0\int^L\,{}_0\int^A [u_0+(x+r)\omega+\rho^{-1}(\delta-y)\omega^2]dx\,dy$$

$$= u_0+(L/2+r)\omega+\delta\,\omega^2/2\rho \tag{7.44}$$

$$u_L(av) = (1/L\delta)\,{}_0\int^L\,{}_0\int^A [u_L dxdy$$

$$= (1/L\delta)\,{}_0\int^L\,{}_0\int^A (2u_0^2+2u_0\omega+x^2\omega^2)^{1/2}dxdy$$

$$= (1/L)\,((2u_0^2+2u_0\omega+x^2\omega^2)^{1/2}dx$$

$$= (2u_0^2+2u_0\omega+L^2\omega^2)^{1/2}+(2u_0^2+2u_0\omega)\omega^{-1}\{\ln[L\omega+(2u_0^2+2u_0\omega)^2]-(1/2)\ln(2u_0^2+2u_0\omega)\}$$

$$\sim (2u_0\omega+L^2\omega^2)^{1/2}+4u_0\ln(2u_0\omega)$$

$$\sim L\omega(1+u_0/L^2\omega)+4u_0\ln(2u_0\omega)$$

$$= u_0/L+L\omega+4u_0\ln(2u_0\omega) \tag{7.45}$$

7.5.3. Concentration Distribution

As is well known [28, 39, 43], gas evolution kinetics are typically very fast and the Schmidt number is very high. Therefore, mass transfer process takes place in the diffusion limited regime and is governed by the cell hydrodynamics of the flow. In the rotary cell, the flow hydrodynamics is under the influences of an imposed constant and uniform centrifugal field. The effects of gravity, surface tension and friction on the rotary cell are insignificant compared to the centrifugal force. The Coriolis acceleration, which is very small compared to the centrifugal acceleration in the developing region [2, 39]. As a consequence, only the case of an bubble-filled electrolyte flow induced by the centrifugal field should be considered. The resulting steady-state motion of the electrolyte can be described by the Navier-Stokes equations with the centrifugal force included [28, 38-40]:

$$u_x\partial C/\partial x+u_y\partial C/\partial y+u_z\partial C/\partial z = D(\partial^2 C/\partial x^2+\partial^2 C/\partial y^2+\partial^2 C/\partial z^2) \qquad (7.46)$$

where C is the local reactant concentration in the rotary cell, D is the diffusivity of the solute in the liquid, u_x, u_y, and u_z are liquid velocity component in x, y, and z direction (Refer to the figure 7.2), respectively.

Equation (7.46) can be solved using the method above for the velocity profile of solution.

It is reported that a bubble detached from the electrode surface after coalescence, leaves the surface at right angles to it in gravitational field. Mass transfer in the x direction is mainly due to convection rather than diffusion [19, 32, 39, 42]. In a centrifugal field, such a situation should be intensified, as indicated before [2]. So we have

$$\partial C/\partial y >> u_x\partial C/\partial x \text{ and } \partial C/\partial y >> \partial C/\partial z,\ \partial^2 C/\partial x^2 << \partial^2 C/\partial y^2 >> \partial^2 C/\partial z^2 \qquad (7.47)$$

Therefore, $\partial^2 C/\partial x^2$ and $\partial^2 C/\partial z^2$ in equation (7.46) can be neglected and the local convection diffusion component in the y direction becomes

$$u_x\partial C/\partial x+u_y\partial C/\partial y = D\partial^2 C/\partial y^2 \qquad (7.48)$$

The boundary conditions are for a constant concentration on the electrode surfaces and a uniform concentration in the bubble-filled electrolyte, i.e.

$$C = C_s \qquad \text{at } y=0 \text{ for } x>0 \tag{7.49a}$$

$$C = C_b \qquad \text{at } x=0 \text{ for } 0<y<\delta \tag{7.49b}$$

$$dC/dy = 0 \qquad \text{at } y=\delta \tag{7.49c}$$

where C_b and C_s are the bulk and electrode surface concentration of the solute, respectively. The condition (7.49c) is obtained based on an approximation due originally to literature [39]. From the material balance, we know

$$u_x(av)\, S\, [C_{av}-(C_{av}+dC_{av})] = N\, dx \tag{7.50}$$

where $S = \delta_e - \delta_M$, $u_x(av)$ is the average velocity in the x direction, C_{av}-and $(C_{av}+dC_{av})$ is the average reactant concentrations into and out of the cell element, respectively, and N is the mass flux per unit area of electrode which is constant. This means

$$dC_{av}/dx = dC_S/dx = dC/dx = b_0 \tag{7.51}$$

$$d^2C/dy^2-u_x(av)b_1D^{-1}+u_y(av)D^{-1}dC/dy = 0 \tag{7.52}$$

where b_0 is a constant to be determined, the velocity components are approximated as the average velocities.

Equation (7.53) may be integrated analytically to obtain

$$dC/dy = b_2\exp[u_y(av)y/D]-b_1 u_x(av)/u_y(av) \tag{7.53}$$

$$C-C_S = b_2Du_y(av)^{-1}\exp[u_y(av)y/D]-b_1u_x(av)y/u_y(av) \tag{7.54}$$

A combination of the boundary conditions (7.49), equations (7.53) and (7.54), yields

$$b_1 = b_2u_y(av)u_x(av)^{-1}\exp[u_y(av)\delta/D]$$

$$\approx -(C_b-C_s)u_y(av)/u_x(av)\delta \tag{7.55}$$

$$b_2 = (C_b-C_s)/[D/u_y(av)-\delta]\exp[u_y(av)\delta/D]$$

$$\approx -(C_b-C_s)D/u_y(av)\delta^2 \tag{7.56}$$

where the exponent in equations (7.55) and (7.56) have been approximated by the linear term of the Taylor expansion. This is reasonable because the diffusion layer lies within a practically linear part of the velocity profile [42]. Similar method was also used in a centrifugal field [2] where the concentration boundary layer was assumed much smaller than the viscous boundary layer, so that a linear velocity profile was assumed for the liquid in the concentration boundary layer.

7.5.4. Mass Transfer Coefficient

The average mass transfer coefficient, K_L is used in both centrifugal field and gravitational field, can be defined as [2, 39, 42]

$$K_L = -D(dC/dy)_{y=0}/(C_{av}-C_s) \tag{7.57}$$

From equation (7.54), we have

$$\begin{aligned}(dC/dy)_{y=0} &= b_2 - b_1 u_x(av)/u_y(av) \\ &\approx -(C_b-C_s)u_y(av)/u_x(av)\delta \end{aligned} \tag{7.58}$$

The bulk average concentration, C_{av}, is [2, 39, 42]

$$C_{av} = {}_0\int^A u_x C dy / {}_0\int^A u_x dy \tag{7.59a}$$

which on substituting for u_x and C using equations (7.39b), (7.54), (7.55) and (7.56) gives

$$\begin{aligned}C_{av} &= {}_0\int^A (u_0+\delta\omega^2/\rho - y\omega^2/\rho)[C_s-(C_b-C_s)D/u_y(av)\delta - (C_b-C_s)y/\delta]/((u_0+\delta\omega^2/\rho - y\omega^2/\rho)dy \\ &\approx C_s+(C_b-C_s)D/u_y(av)\delta - (C_b-C_s)/2+(C_b-C_s)\omega^2/3u_0\rho \\ &\approx C_s-0.5(C_b-C_s) \\ &= 0.5(C_s-C_b) \end{aligned} \tag{7.59b}$$

Thus, the average mass transfer coefficient is

$$\begin{aligned}K_L &= -D(dC/dy)_{y=0}/(C_{av}-C_s) \\ &= 2Du_y(av)/\delta\, u_x(av) \\ &\approx B_1 + B_1 (L/2 + r)\,\omega \end{aligned} \tag{9.60a}$$

where $B_1 = 2D/\delta$. Using the definition

Relative acceleration rate G = Centrifugal acceleration/gravitational acceleration

$$= (L/2 + r)\,\omega^2/g \qquad (7.61)$$

where g is gravitational acceleration and equals 9.81 m/s^2. Equation (7.60a) can be written as

$$K_L = B_1 + B_1 (L/2 + r)\,\omega$$

$$= B_1 + B_1 [(L/2 + r)\, g\, G]^{1/2} \qquad (9.60b)$$

The mass transfer coefficients calculated from the equation (7.60b) are presented in section 7.7.2.

7.5.5. Average Current Density

Using equations (7.54) and (7.56), we have

$$C_b - C_s \approx -b_2\delta^2 u_y(av)/D$$

$$\approx \delta^2 u_y(av) C_b/D$$

$$\approx \delta^2[u_0+(L/2+r)\omega]C_b/D \qquad (7.62)$$

Thus, average current density in a centrifugal field is obtained from equation (7.29)

$$j_{av,\,cf} = nF[B_1+B_1(L/2+r)\omega]\{\,\delta^2[u_0+(L/2+r)\omega]C_b/D\}$$

$$\approx (nF\delta^2C_b/D)[B_1u_0+B_1(L/2+r)(1+u_0)\omega+B_1(L/2+r)^2\omega^2\}$$

$$= j_0+B_2\,G^{1/2} + B_3\,G \qquad (7.63)$$

where j_0 is

$$j_0 = (nF\delta^2C_b/D)B_1u_0$$

$$= 2nF\delta u_bC_b$$

$$= 2\delta RTLj_{av,gf}C_b/(P-P^0)S \qquad (7.64)$$

$$B_2 = [(nF\delta^2C_b/D)B_1(L/2+r)(1+u_0)+2nF\delta rC_b]\,[g/(L/2 + r)]^{1/2}$$

$$= 2nF\delta C_b[(L/2+r)(1+u_0)+r]\,[g/(L/2 + r)]^{1/2} \qquad (7.65)$$

$$B_3 = [(nF\delta^2C_b/D)B_1(L/2+r)^2C_b/D]\,[g/(L/2 + r)]$$

$$= 2\,n\,F\,g\,\delta\,C_b\,(L/2+r)^2 \qquad (7.66)$$

7.6. Conductivity Of Bubble-Filled Electrolyte

7.6.1. Conductivity of the Diffuse Layer

Adopting a conventional method for the treatment of bubble effects [28], the diffuse layer of the bubble-filled electrolytes can be assigned an effective conductivity s_d which is typically correlated as a function of gas fraction in diffuse layer, f_{gd}. The theoretical and experimental investigations demonstrated that the Bruggemann equation is the most reliable correlation and can be applicable to systems with an approximately uniform gas fraction distribution. [7, 26, 28]. Based on this, we have

$$\begin{aligned} f_{gd} &= v_{G,d}/(v_{G,d}+v_{L,d}) \\ &= u_{G,d}/(u_{G,d}+u_{L,d}) \end{aligned} \qquad (7.67)$$

$$\begin{aligned} \sigma_d &= \sigma(1-f_{gd})^{3/2} \\ &= \sigma[1-u_{G,d}/(u_{G,d}+u_{L,d})]^{3/2} \\ &= \sigma(1+u_{G,d}/u_{L,d})^{-3/2} \end{aligned} \qquad (7.68a)$$

where $v_{G,d}$ and $v_{L,d}$ are gas and liquid volume flow rate in the diffuse layer, respectively, $u_{G,d}$ and $u_{L,d}$ are the gas and liquid velocity in the diffuse layer, respectively. Since $u_{G,d}/u_{L,d}<1$, the Binomial Theorem is applied to equation (7.67a) [38] to give a linear approximation to σ_d as

$$\sigma_d \approx \sigma(1-3u_{G,d}/2u_{L,d}) \qquad (7.68b)$$

Such an approximation introduces an error less than 2% in our case.

The volume flow rate of dispersed gas through the cell equals the total gas flow generated from the electrodes, calculated according to Faraday's law, provide that the current and gas bubbles distribute almost uniformly in the cell [8, 28, 37, 38, 49, 50]:

$$v_{G,d,gf} = C_1 H L j_{av} \qquad (7.69)$$

$$C_1 = RT(\phi_A/n_A+\phi_C/n_C)/F(P-P^0) \qquad (7.70)$$

where j_{av} is the average current density through the cell, ϕ_A and ϕ_C are current efficiency of the gas evolving reaction at anode and cathode, respectively, n_A and n_C are charge number of the anode and cathode electrode, respectively, P^0 is vapour pressure of the solvent (water in our cases), P is atmosphere pressure, T is cell temperature, and R gas constant.

Thus, an average gas velocity in a rotary cell can be calculated via

$$u_{G,d}(av) = u_{G,d,gf}(av) + u_{G,d,cf}(av)$$

$$= C_1 j_{av} + u_0 + \delta_d \omega^2/2\rho \qquad (7.71)$$

where d_d is thickness of the diffuse layer, $u_{G,d,gf}(av)$ and $u_{G,d,cf}(av)$ are average gas velocity in gravitational and centrifugal field, which are taken from the literature [38] or using $u_x(av)$ considering outlet direction of the gas bubbles in the rotary cell.

Using $u_L(av)$, i.e., equation (7.47), we have

$$\sigma_d = \sigma(1-3u_{G,d,cf}/2u_{L,d,cf})$$

$$= \sigma\{1-3(C_1 j_{av} + u_0 + \delta_d \omega^2/2\rho)/2[u_0/L+L\omega+4u_0\ln(2u_0\omega)]\} \qquad (7.72)$$

Ignoring the squared term in the binomial expansion introducing an error of only 0.1% in this case.

7.6.2. Conductivity of Fixed Layer

Using the similar method as for the diffuse layer, electrolyte conductivity of the fixed layer can be obtained. Now

$$f_{g\,f} = v_{G,f,cf}/(v_{G,f,cf}+v_{L,f,cf})$$

$$= u_{G,f,cf}/(u_{G,f,cf}+u_{L,f,cf}) \qquad (7.73)$$

$$\sigma_f = \sigma(1-f_f)^{3/2}$$

$$= \sigma[1-u_{G,f,cf}/(u_{G,f,cf}+u_{L,f,cf})]^{3/2}$$

$$= \sigma(1+u_{G,f,cf}/u_{L,f,cf})^{-3/2}$$

$$\approx \sigma(1-3u_{G,f,cf}/2u_{L,f,cf}) \qquad (7.74)$$

where $v_{G,d,cf}$ and $v_{L,f,cf}$ are gas and liquid volume flow rate in a centrifugal field, respectively, $u_{G,f,cf}$ and $u_{L,f,cf}$ are the gas and liquid velocity in a centrifugal field, respectively.

An average gas velocity of the fixed layer in a centrifugal field can be calculated via

$$u_{G,f} = u_{G,f,gf} + u_{G,f,gf}$$

$$= C_1 j_{av} + u_0 + \delta_f \omega^2/2\rho \qquad (7.75)$$

where δ_f is thickness of the fixed layer, $u_{G,d,gf}$ and $u_{G,d,gf}$ are gas velocity of the fixed layer in gravitational and centrifugal field, which are taken from the literature [38] or using $u_{x,f}$ (av). Combining $u_{G,d}$ with u_L(av), we have

$$\sigma_f = \sigma(1-3u_{G,f,cf}/2u_{L,f,cf})$$

$$= \sigma\{1-3(C_1 j_{av} + u_0 + \delta_f \omega^2/2\rho)/2[u_0/L+L\omega+4u_0\ln(2u_0\omega)]\} \qquad (7.76)$$

7.6.3. Ohmic Drop in Bubble Filled Electrolyte

A combination of equations (7.27), (7.72), and (7.76), yields:

$$V_S = j_{av}[(S-2\delta_f)/\sigma_d + 2\delta_f/\sigma_f]$$

$$= (j_{av}/\sigma)(S-2\delta_f)\{1-3(C_1 j_{av} + u_0 + \delta_d \omega^2/2\rho)/2[u_0/L+L\omega+4u_0\ln(2u_0\omega)]\}^{-1} +$$

$$+(2j_{av}\delta_f/\sigma)\{1-3(C_1 j_{av} + u_0 + \delta_f \omega^2/2\rho)/2[u_0/L+L\omega+4u_0\ln(2u_0\omega)]\}^{-1} \qquad (7.77a)$$

Under the experimental conditions used in this work, $C_1 j_{av}$ ($\approx 10^{-4}$) << u_0 ($\approx 5 \times 10^{-2}$ to 6.5) and $\delta_f \omega^2/2\rho$ ($\approx 10^{-4}$) << u_0, equation (7.76a) can be approximated as

$$V_S \approx [j_{av}(S-2\delta_f)/\sigma]\{1-3(u_0 + \delta_d \omega^2/2\rho)/2[u_0/L+L\omega+4u_0\ln(2u_0\omega)]\}^{-1} +$$

$$+(2j_{av}\delta_f/\sigma)\{1-3(u_0 + \delta_f \omega^2/2\rho)/2[u_0/L+L\omega+4u_0\ln(2u_0\omega)]\}^{-1} \qquad (7.77b)$$

Assuming $\delta_f \approx \delta_d$, (7.76b) can be approximated as

$$V_S = [j_{av}(S-2\delta_f)/\sigma + 2j_{av}\delta_f/\sigma]/\{1-3(u_0 + \delta_f \omega^2/2\rho)/2[u_0/L+L\omega+4u_0\ln(2u_0\omega)]\}$$

$$= 2 j_{av} S/\sigma B_4 \qquad (7.77c)$$

where

$$B_4 = [1-3(u_0 + \delta_f \omega^2/2\rho)]/2\,[u_0/L+L\omega+4\,u_0 \ln(2\,u_0\,\omega)] \qquad (7.77)$$

7.7. Centrifugal Model For The Rotary Cell

A model for the rotary cell is proposed and analysed in this section. The data used in the model analysis and their estimation are also illustrated.

7.7.1. Cell Voltage and its Reduction

Cell Voltage Behaviour - Returning to equation (7.27) and combining the relevant terms, the voltage for the rotary cell, $E_{cell,cf}$, can be expressed as:

$$E_{cell,cf} = E_A + E_C + j_{av,cf}(L/\sigma_A + L/\sigma_C + \delta_M/\sigma_M + S/\sigma B_4)$$

$$= E_{A,e} + E_{C,e} + a_A + |a_C| + (b_A + |b_C|) \log j_{av,cf} +$$

$$+ j_{av,cf}[L/\sigma_A + L/\sigma_C + \delta_M/\sigma_M + 2S/\sigma B_4] \qquad (7.79)$$

Equation (7.79) shows the effect of centrifugal acceleration fields on the electrolytic cell with gas evolving electrodes. Decreased voltage as a result of applying centrifugal fields means that the resistance of the cell is reduced and the mass transfer rate is enhanced. Figures 7.4 to 7.6 show the model and the experimental polarisation profiles, including the anode, the cathode and the cell voltage, for Cl_2 - H_2, O_2 - H_2 and CH_3OH - H_2 systems, at a current density of 3 kA m^{-2}. The model figures were obtained from the equation (7.79), provided that there is no change of the Tafel parameters in a centrifugal field and the gas evolution efficiencies in centrifugal fields are assumed as 100%. The cell geometric parameters are those used in the experimental programme. L/σ_A and L/σ_C are neglected since $L/\sigma_A \approx L/\sigma_C \approx 10^{-8}$ m^2/mho $<< \delta_M/\sigma_M \approx 10^{-5}$ m^2/mho. According to equation (7.63), $j_{av,cf}$ is $[B_2 (G - 1)^{1/2} + B_3 (G - 1)]$ higher than $j_{av,gf}$ at a fixed potential. Therefore, corresponding to calculate the anode and cathode potentials and the cell voltage for the static cell at a current density of 3 kA m^{-2}, a current density of $[3000 - B_2 (G - 1)^{1/2}$

- B_3 (G - 1)] is used as $j_{av, cf}$ to calculate the anode and cathode potentials and the cell voltage for the rotary cell.

Figures 7.4 to 7.6 show that the model behaviours agree well with the experiments. As expected, discrepancies can be seen in a quantitative sense.

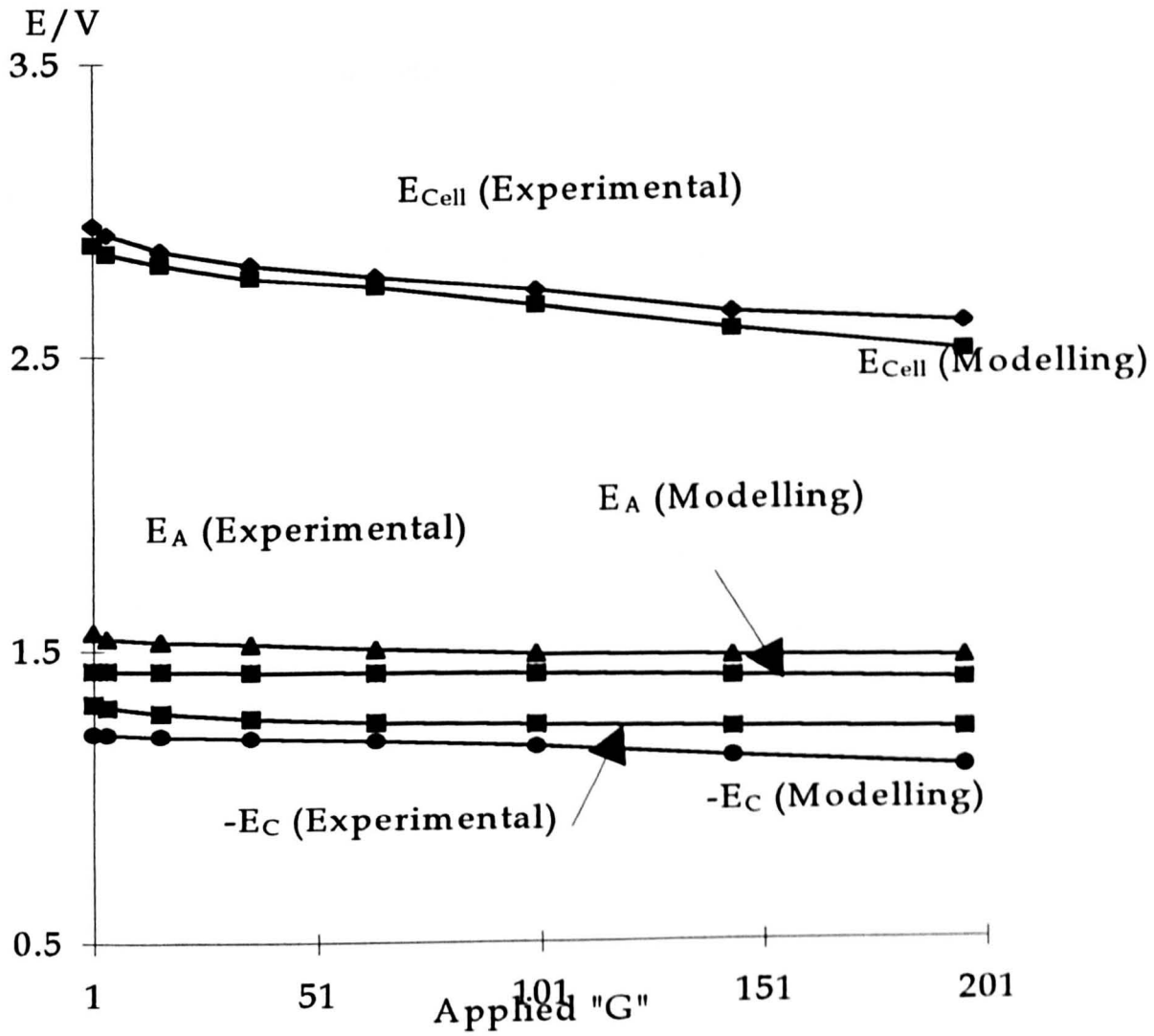

Figure 7.4. Simulated and measured electrode potentials and cell voltage versus relative acceleration rate curves at a current density of 3 kA m^{-2} for chlorine and hydrogen evolutions in the rotary cell.
Experimental conditions - Anode: RuO_2/Ti mesh (2 mg Ru cm^{-2}); Cathode: Pt/Ti mesh (2 mg Pt cm^{-2}); Anolyte: 0.5 M HCl + saturated NaCl solution; Catholyte: 0.5 M NaOH solution; Distance between the anode and cathode: 4 mm; Temperature: 80°C.
Parameters used in Calculation: See section 7.7.4.

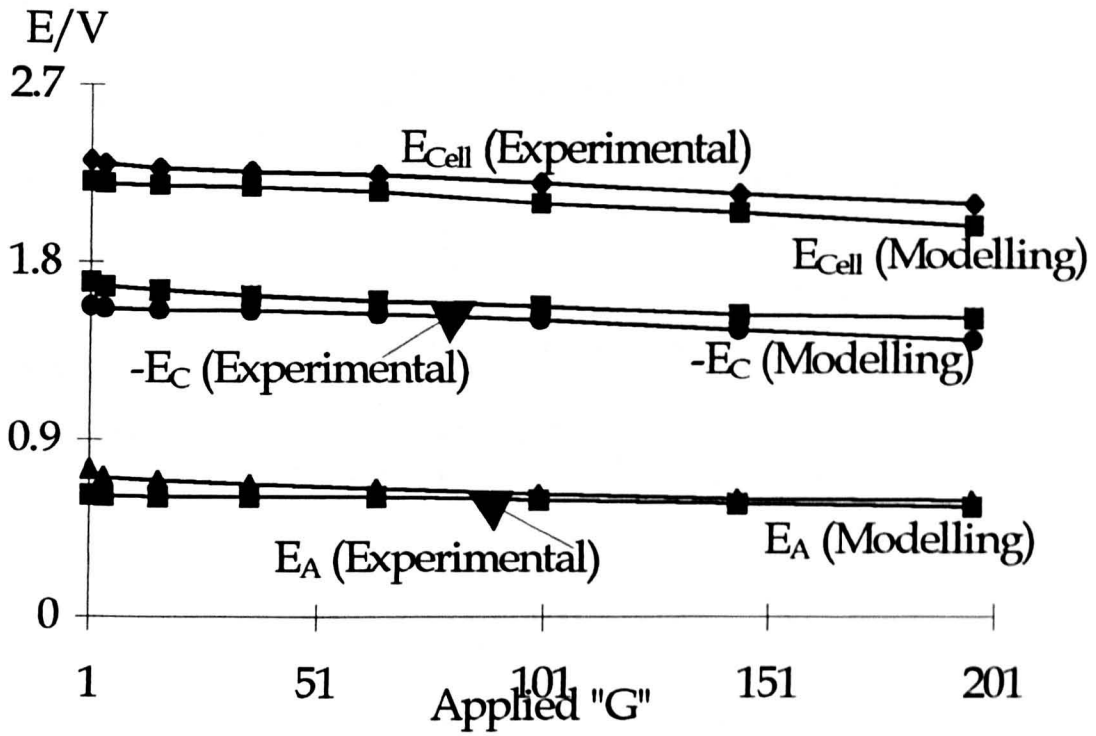

Figure 7.5. Simulated and measured electrode potentials and cell voltage versus relative acceleration rate curves at a current density of 3 kA m^{-2} for oxygen and hydrogen evolutions in the rotary cell.
Experimental conditions - Anode and cathode: Ni foam; Electrolytes: 4.5 M KOH solutions, Distance between the anode and cathode: 4 mm; Temperature: 80°C.
Parameters used in Calculation: See section 7.7.4.

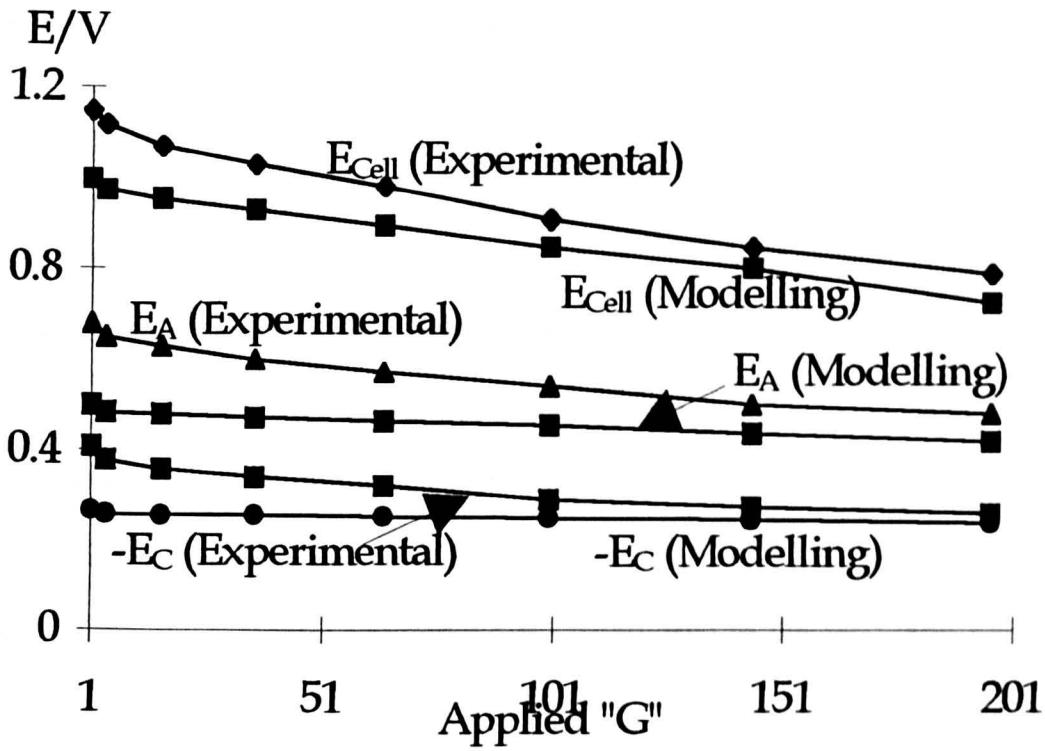

Figure 7.6. Simulated and measured electrode potentials and cell voltage versus relative acceleration rate curves at a current density of 3 kA m^{-2} for methanol oxidation and hydrogen evolution in the rotary cell.
Experimental conditions - Anode: Pt-Ru/Ti mesh (2 mg Pt cm^{-2} and 1 mg Ru cm^{-2}); Cathode: Pt/Ti mesh (2 mg Pt cm^{-2}); Anolyte: 1 M methanol in 0.5 M H_2SO_4 solution; Catholyte: 0.5 M H_2SO_4 solution; Distance between the anode and cathode: 4 mm; Temperature: 80°C.
Parameters used in Calculation: See section 7.7.4.

Cell Voltage Reduction - From the viewpoint of electrochemical engineering, cell voltage reduction is one of the most important quantity. The cell voltage reduction can be obtained from Equation (7.79), i.e., the cell voltage reduction of the rotary cell at a constant current density, e.g., 3000 A m^{-2}, is

$$E_{cell,\,gf} - E_{cell,\,cf} = (b_A + |b_C|) \log [3000 - B_2 (G - 1)^{1/2} - B_3 (G - 1)] + \\ + [3000 - B_2 (G - 1)^{1/2} - B_3 (G - 1)] (2 S/\sigma B_4) \quad (7.80)$$

Figures 7.7 to 7.9 show the cell voltage and electrode potential reductions against relative acceleration rate plots obtained from the model prediction and the

experimental results for Cl_2 - H_2, O_2 - H_2 and CH_3OH - H_2 systems, at a current density of 3 kA m^{-2}.

As expected, the cell voltage and electrode potential reductions increases with the increasing relative acceleration rate. The enhancement in mass transfer and decrease in ohmic resistance, as detailed later, both improve the overall rotary cell performance. The figure exhibits difference in quantitative sense between the model prediction and experimental results, although reasonable agreement is achieved, which confirmes the validity of the approach taken by this model. Differences in model and experimental predictions are partly due to the the assumptions and the estimation of parameters used in the model.

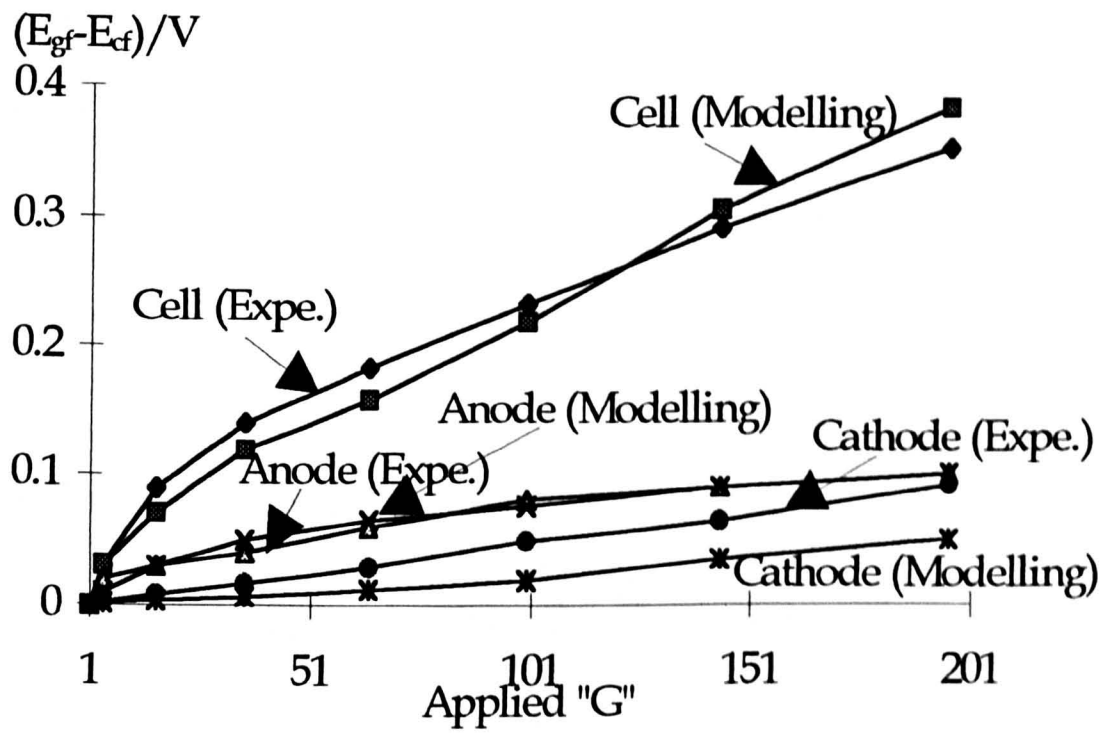

Figure 7.7. Simulated and measured electrode potential and cell voltage reductions as a function of the relative acceleration rate for chlorine and hydrogen evolutions in the rotary cell at a current density of 3 kA m^{-2}.
Experimental conditions and Parameters - are same as those in figure 7.4.

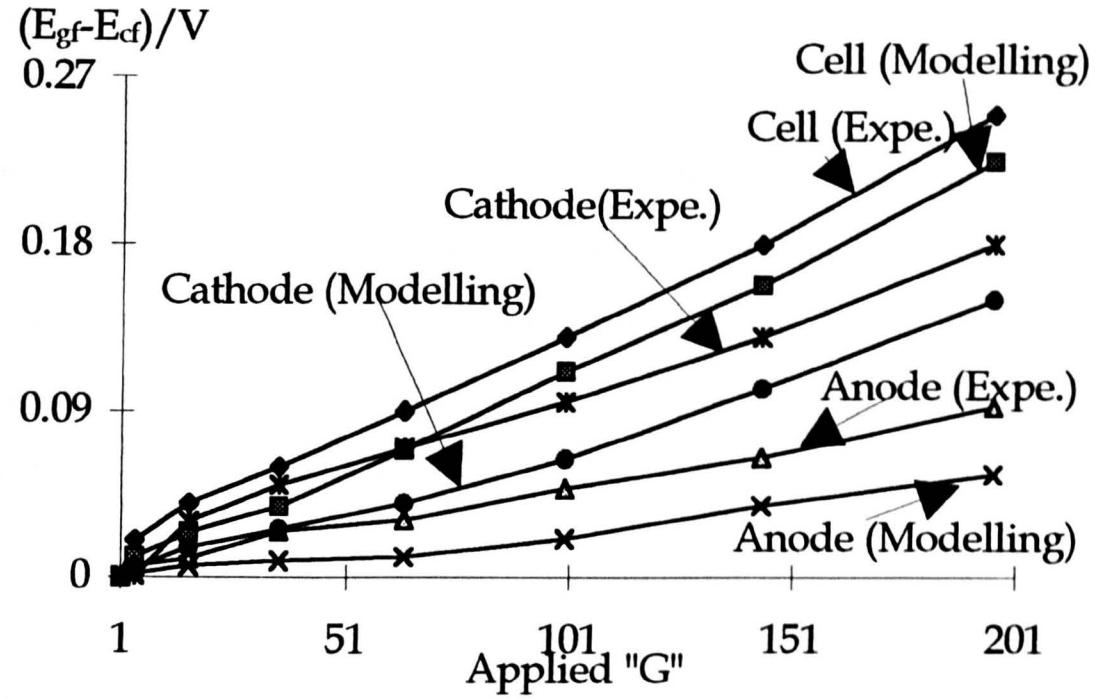

Figure 7.8. Simulated and measured electrode potential and cell voltage reductions as a function of the relative acceleration rate for oxygen and hydrogen evolutions in the rotary cell at a current density of 3 kA m^{-2}.
Experimental conditions and Parameters - are same as those in figure 7.5.

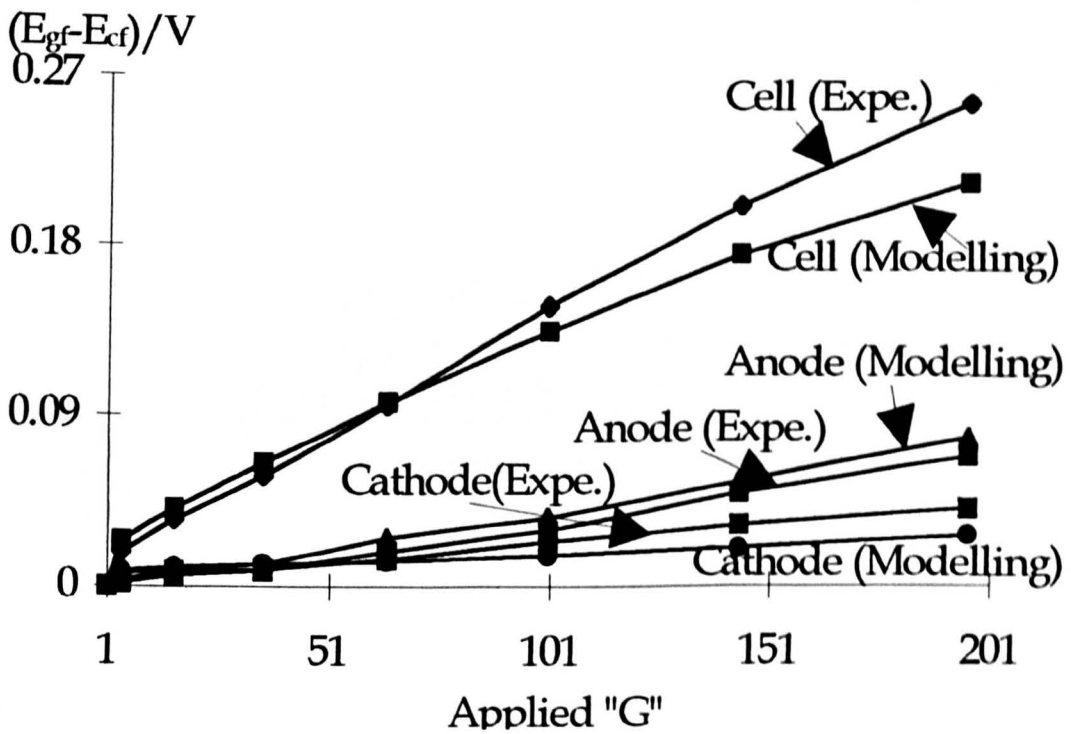

Figure 7.9. Simulated and measured electrode potential and cell voltage reductions as a function of the relative acceleration rate for methanol oxidation and hydrogen evolution in the rotary cell at a current density of 3 kA m^{-2}.
Experimental conditions and Parameters - are same as those in figure 7.6.

7.7.2. Mass Transfer Enhancement

Mass transfer enhancement can be estimated from equation (7.60), in which the average mass transfer coefficient is proportional to the angular velocity. Experiments were carried out using a limiting current technique to compare with the model prediction. The experimental details were described in Chapter 2. Figure 7.10 shows typical results, i.e., current density versus cell voltage curves, for ferricyanide reduction. The reduction rate was controlled by convective diffusion of the reactant to the electrode surface at cell voltages in the range about 0 to 0.7 V. Over this range of cell voltages, a distinct limiting current plateau was observed at all rotating speeds. The values of limiting current density vary with increasing the rotating speeds as shown in figure 7.10.

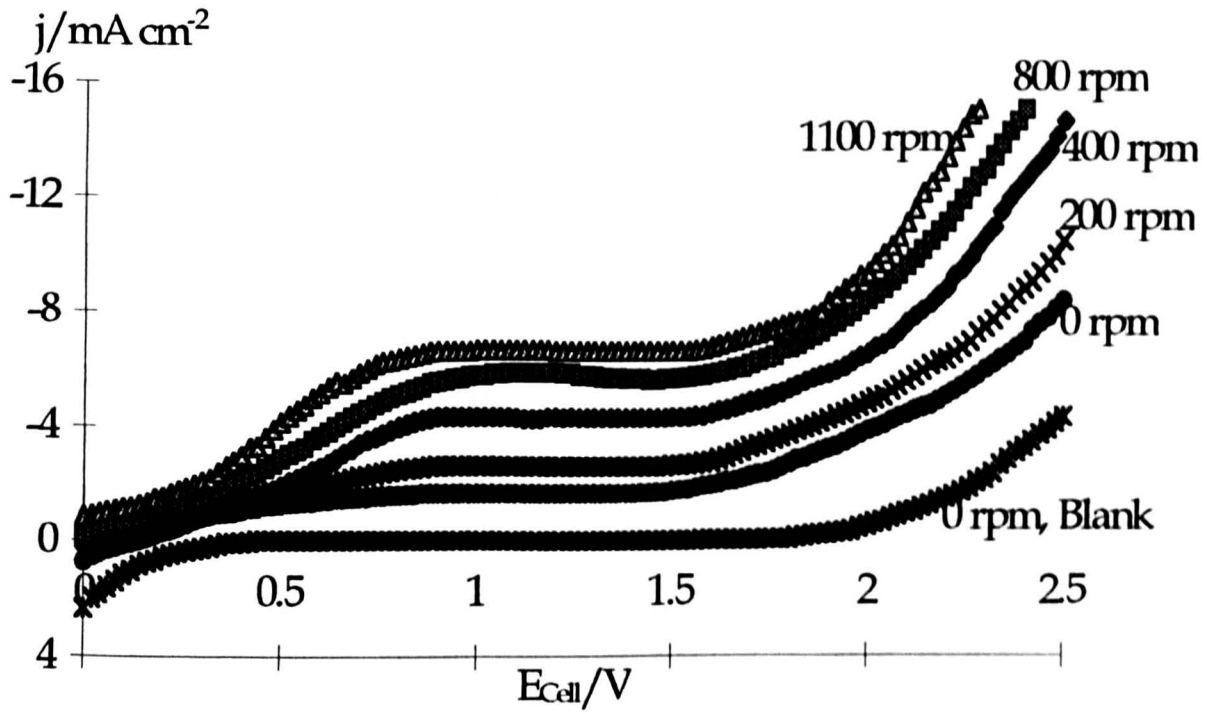

Figure 7.10. Current density versus cell voltage curves for the reduction of ferricyanide ions in the rotary cell. Cathode: Pt/Ti expanded metal; Anode: Ni foam; Catholyte: 0.01 M $K_4Fe(CN)_6$ + 0.1 M $K_3Fe(CN)_6$ + 0.5 M KOH solution; Catholyte for the blank run: 0.5 M KOH solution; Anolyte: 0.5 M KOH solution; Temperature: 26.5°C.

Experimental mass transfer coefficients were calculated from equation (2.8), which was shown in Chapter 2, using the limiting current densities, obtained from the data shown in figure 7.10 at a cell voltage of 1.2 V and at all rotating speeds. Modelling mass transfer coefficients were estimated from equation (7.60), i.e.,

$$K_L = B_1 + [B_1 gG/3p(L+2r)]/[u_b+\delta/3+rg^{1/2}G^{1/2}/(L/2+r)^{1/2}-gG/3\,p(L+2r)] \qquad (7.60b)$$

Note that K_L, obtained from (7.60) at G = 1, is the mass transfer coefficient in the static cell.

Both the modelling and the experimental data are illustrated in figure 7.11.

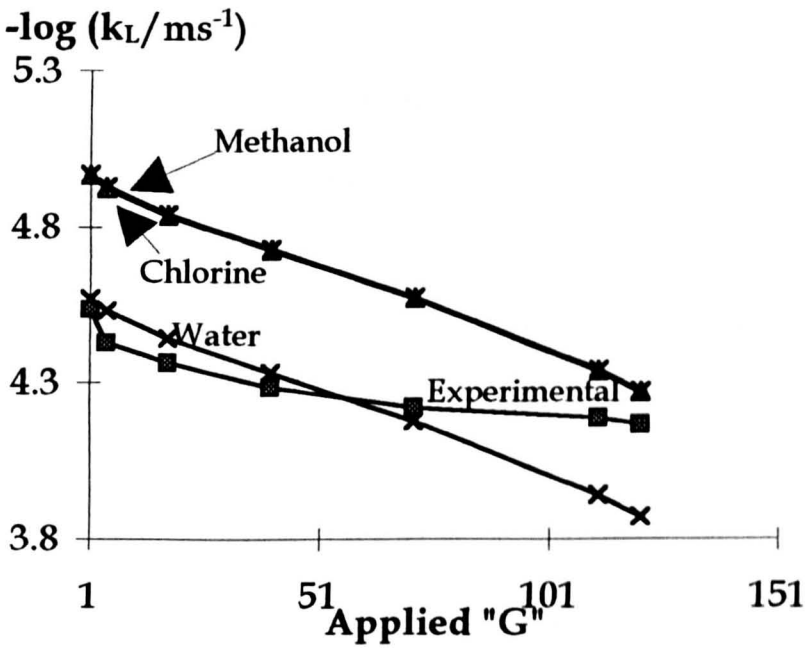

Figure 7.11. Simulated (Curves "methanol, chlorine and water") and measured (Curve "experimental) variations of the mass transfer coefficient with square root of relative acceleration rate at ambient temperature.
Model Parameters: See section 7. 7.4.
Experimental Conditions: Anode and Cathode: Pt/Ti mesh (2 mg Pt cm^{-2}); Catholyte: 0.01 M $K_3Fe(CN)_6$+0.05 M $K_4Fe(CN)_6$+1 M KOH solution; Anolyte: 1 M KOH solution; Temperature: 26.5°C.

As shown in figure 7.11, the mass transfer coefficient increases with increasing relative acceleration rate for all processes modelled. The chloeine and methanol systems gave nearly same curves, as shown in figure 7.11. The values range from

1.08×10^{-5} m/s to 1.34×10^{-4} m/s, which are qualitatively agreed with those obtained from the experiments, i.e., from 1.69×10^{-5} m/s to 6.84×10^{-5} m/s. The data from the model prediction for the three systems appear difference due to variation in the diffusion coefficients. These data are within range of those obtained in centrifugal fields from both theoretical modeling and experimental measurements [2, 48]. For example, the theoretical mass transfer coefficients are about 2.3×10^{-4}, 4.0×10^{-4} and 1.51×10^{-3} m/s at a rotating speed of 900, 3000 and 30000 rpm respectively, in rotating packed beds at a distance of 2 cm [2]. The experimental mass transfer coefficients are in a range of 5×10^{-4} to 4×10^{-3} m/s, in the centrifugal reactor, when the rotating speed increases from 160 rpm to 320 rpm [48]. Some difference can be seen due to the assumptions used and the parametric data used. However, it clearly shows that mass transfer enhancement is achieved in the centrifugal fields. Bear in mind that the average mass transfer coefficients in the static cells for hydrogen and oxygen evolutions under comparable conditions are 4.5×10^{-5} and 3.8×10^{-5} m/s respectively [25]. The reported data in static cells usually range between 3.25×10^{-6} and 2.56×10^{-4} m/s [38, 42]. These data demonstrate that gas evolving reactions occurring in the rotary cell are less likely to experience liquid phase mass transfer limitation, i.e., under comparable conditions, it can be reasonably expected that the mass transfer of the bubble-filled electrolyte is greatly enhanced in centrifugal fields. This contributes to the increase current density at a constant cell voltage or to reduce ohmic potential drops of the rotary cell at a fixed current density.

7.7.3. Gas Disengagement Acceleration

The effect of centrifugal fields on gas disengagement is shown by the relative conductivity data of bubble-filled electrolyte. The relative conductivity, defined as $Q=\sigma_{cf}/\sigma_{gf}$, can be calculated from equations (7.72) and (7.76):

$$\sigma_{cf} = \sigma_{cf,d} + \sigma_{cf,\delta}$$

$$= \sigma \{2 - (3/2) [2 C_1 j_{av} + 2 u_0 + r g G (\delta_d + \delta_f)/2 p (L/2 + r)]/[u_0/L +$$

$$+ L r g^{1/2} G^{1/2}/(L/2 + r)^{1/2} + 2 u_0 \ln (2 u_0 r g^{1/2} G^{1/2}) - u_0 \ln (L/2 + r)]\} \qquad (7.81a)$$

Since $C_1 j_{av} << u_0$ and $\delta r g G/2 p (L/2 + r) << u_0$, Equation (7.81a) can be approximated as

$$\sigma_{cf} \approx \sigma\{2 - 3/[1/L + L g^{1/2} G^{1/2}/u_0 (L/2 + r)^{1/2} +$$

$$+ 2 \ln (2 u_0 r g^{1/2} G^{1/2}) - \ln (L/2 + r)]\} \qquad (7.81b)$$

Use $u_0 = u_b + r g^{1/2} G^{1/2}/(L/2 + r)^{1/2} = u_b + 1.28 G^{1/2}$, we have

$$\sigma_{cf} = 2 \sigma - 3 \sigma/\{1/L + L g^{1/2} G^{1/2}/(u_b + 1.28 G^{1/2}) (L/2 + r)^{1/2} +$$

$$+ 2 \ln [2 (u_b + 1.28 G^{1/2}) r g^{1/2} G^{1/2}] - \ln (L/2 + r)\}$$

$$= 2 \sigma - 3 \sigma/\{12.813 + 1.28 G^{1/2}/(u_b + 1.28 G^{1/2}) +$$

$$+ 2 \ln [0.0626 (u_b + 1.28 G^{1/2}) G^{1/2}]\} \qquad (7.81c)$$

At G = 1, we have

$$\sigma_{gf} = 2 \sigma - 3 \sigma/[12.813 + 1.28/(u_b + 1.28) + 2 \ln (0.0626 u_b + 0.0801)] \qquad (7.82)$$

Therefore,

$$Q = \sigma_{cf}/\sigma_{gf}$$

$$= \{2 - 3/[12.813 + 1.28 G^{1/2}/(u_b + 1.28 G^{1/2}) +$$

$$+ 2 \ln (0.0626 u_b G^{1/2} + 0.0804 G)]\}/\{2 - 3/[12.813 +$$

$$+ 1.28/(u_b + 1.28) + 2 \ln (0.0626 u_b + 0.0804)]\} \qquad (7.83)$$

This relationship is illustrated in figure 7.12 where u_b was taken from [58] as 0.015, 0.0114, and 0.0419 m/s for H_2, O_2 and Cl_2 respectively.

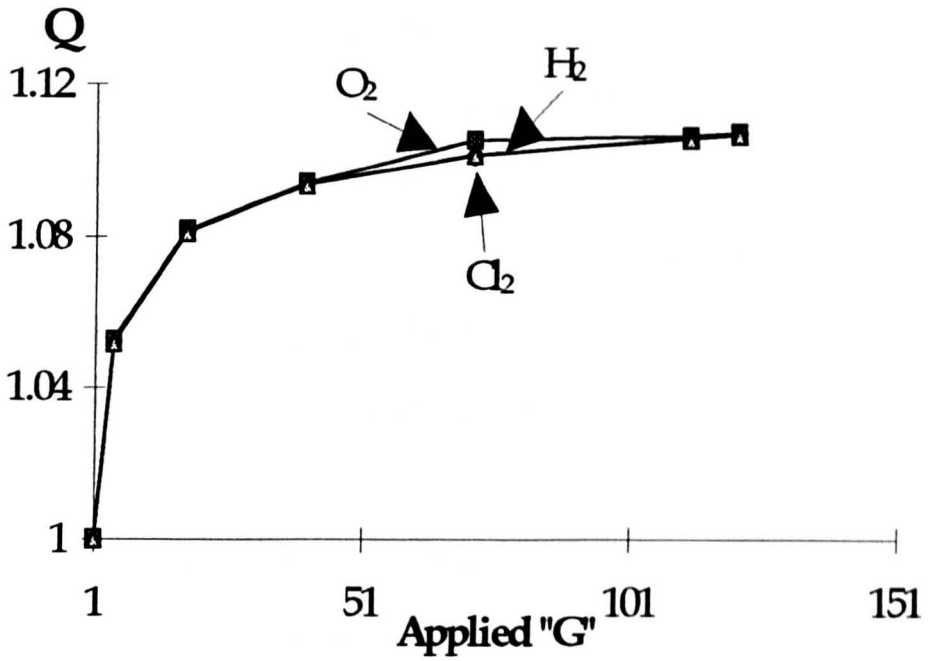

Figure 7.12. Simulated relationship between relative conductivity and relative acceleration rate. Model Parameters: see section 7.7.4.

As presented in figure 7.12, the relative conductivity increases with increase of angular velocity and is nearly regardless of the bubble species. The conductivity increases significantly with only a small increase in acceleration field. The increase in relative conductivity is in the range between 1.0075 and 1.02 times. Further increase in acceleration rate leads to only slightly higher conductivities. This trend results from the effect of the centrifugal field on the electrode surface coverage of bubbles, i.e., the bubble fraction, which is calculated from definition of gas fraction:

$$f_g = v_G/(v_G+v_L)$$

$$= u_G/(u_G+u_L) \qquad (7.84a)$$

where v_G and v_L are gas and liquid volume flow rate respectively, u_G and u_L are gas and liquid velocity, which are using $u_y(av)$, equation (7.44), and $u_L(av)$, equation (7.45) respectively, considering outlet direction of the gas bubbles in the rotary cell. Thus

$$f_g = u_G/(u_G+u_L)$$

$$= [u_0 + (L/2 + r)^{1/2}\, g^{1/2}\, G^{1/2} + \delta\, g\, G\, /2\, p\, (L/2 + r)]/\{u_0/L +$$

$$+ L\, g^{1/2}\, G^{1/2}/(L/2 + r)^{1/2} + 4\, u_0 \ln [2\, u_0 g^{1/2}\, G^{1/2}\, /(L/2 + r)^{1/2})] +$$

$$+ [u_0 + (L/2 + r)^{1/2}\, g^{1/2}\, G^{1/2} + \delta\, g\, G\, /2\, p\, (L/2 + r)]\}$$

$$= (u_0 + 0.767\, G^{1/2})/[11\, u_0 + 2.047\, G^{1/2} + 4\, u_0 \ln (25.58\, u_0\, G^{1/2})] \qquad (7.84b)$$

where $\delta\, g\, G\, /2\, p\, (L/2 + r)$ was neglected since it is much less than u_0. Substituting u_0 into equation (7.83b) yields

$$f_g = (u_b + 0.895\, G^{1/2})/[11\, u_b + 3.327\, G^{1/2} +$$

$$+ 4\, (u_b + 0.128\, G^{1/2})\, \ln (25.58\, u_b\, G^{1/2} + 3.277\, G)] \qquad (7.84c)$$

This result is shown in figure 7.13 where u_b was taken from [58] as 0.015, 0.0114, and 0.0419 m/s for H_2, O_2 and Cl_2 respectively.

The gas fraction calculated from equation (7.84c) in gravitational field is 25.15% and 21.52% for O_2 and H_2 respectively. In a water electrolyser which produces hydrogen and oxygen by the electrolysis about 35% KOH solution at 80°C and operated at a current density of 500 A m^{-2}, the hydrogen fraction is 35% and oxygen fraction is 20% [39]. These differences are not surprising since the numberical values used to calculate the gas fraction are taken rather arbitrarily. Although the difference can be seen between the model prediction values and the reported data, the model gives a qualitative figure for the effect of centrifugal field on gas fraction.

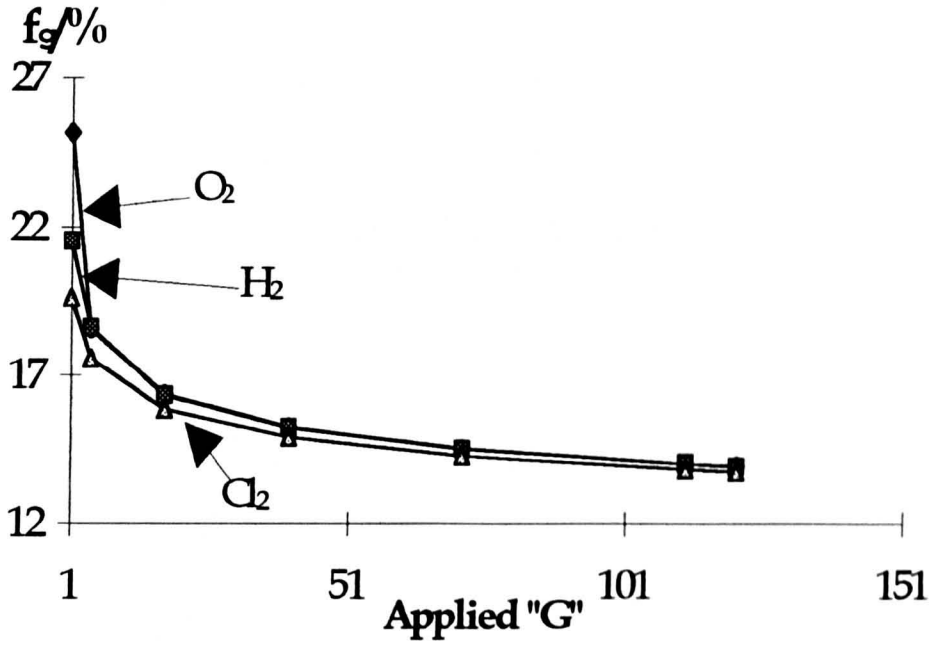

Figure 7.13. Simulated relationship between gas fraction and relative acceleration rate. Model Parameters: see section 7.7.4.

As can be seen in figure 7.13, the very high centrifugal force significantly enhances the gas disengagement from the electrode surfaces. The centrifugal force can remove gas bubbles from the electrode surfaces efficiently and create much more active sites for gas evolution. For example, the gas fraction of the oxygen decreases from 25.15% at 1 G to 15.25% at 40 G. Further increase in acceleration rate leads to only slightly lower gas fraction, e.g., from 15.25% at 40 G to 13.94% at 121 G.

7.7.4. Data for Model Calculation

A list of the model parameters for a quantitative comparison between the modelling values and the experimental data is given in Tables 7.1 to 7.5. The estimation method is shown later.

Table 7.1. Literature Data

Parameter	Value	Literature
Density -		
$\rho_{1\ M\ Methanol}(25^0C)x10^{-3}/kgm^{-3}$	0.99	[44, 45]
$\rho_{sat.\ NaCl}(80^0C)x10^{-3}/kgm^{-3}$	1.36	[45]
$\rho_{4.5\ M\ KOH}(80^0C)x10^{-3}/kgm^{-3}$	1.255	[45]
Solvent Vapour Pressure -		
$P^0_{1\ M\ Methanol}(80^0C)x10^{-4}$/Pascal	2.606	[44]
$P^0_{sat.\ NaCl}(80^0C)x10^{-4}$/Pascal	2.345	[45]
$P^0_{4.5\ M\ KOH}(80^0C)\ x10^{-4}$/Pascal	2.126	[45]
Viscosity -		
$\mu_{1\ M\ Methanol}(25^0C)x10^4/kgm^{-1}s^{-1}$	9.55	[44, 46, 47]
$\mu_{4.5\ M\ KOH}(90^0C)x10^4/kgm^{-1}s^{-1}$	9.19	[51, 52]
Diffusion Coefficient -		
D_{Cl^-}(25°C, infinite dilution in water)$x10^9/m^2s^{-1}$	2.032	[43]
D_{OH^-}(25°C, infinite dilution in water)$x10^9/m^2s^{-1}$	2.67	[39, 43]
$D_{1\ M\ Methanol}(15^0C)x10^9/m^2s^{-1}$	1.28	[44, 53]
Conductivity -		
σ_{Cl^-}(25°C, infinite dilution in water)$x10^{-3}/Sm^2\ eq^{-1}$	7.634	[43, 45]
σ_{Na^+}(25°C, infinite dilution in water)$x10^{-3}/Sm^2\ eq^{-1}$	5.011	[43, 45]
σ_{OH^-}(25°C, infinite dilution in water)$x10^{-3}/Sm^2\ eq^{-1}$	19.76	[43, 45]
σ_{K^+}(25°C, infinite dilution in water)$x10^{-3}/Sm^2\ eq^{-1}$	7.352	[43, 45]
σ_{H^+}(25°C, infinite dilution in water)$x10^{-3}/Sm^2\ eq^{-1}$	34.98	[43, 45]
$\sigma_{SO4\ 2-}$(25°C, infinite dilution in water)$x10^{-3}/Sm^2\ eq^{-1}$	8.0	[43, 45]
$\sigma_{Nafion\ 117\ in\ 0.1\ M\ HCl}(25^0C)/Sm^{-1}$	1.35	[54, 55, 68]
$\sigma_{DSA}(80^0C)x10^{-7}/Sm^{-1}$	1.0	[45]
$\sigma_{Pt}(80^0C)x10^{-7}/Sm^{-1}$	0.714	[45]
$\sigma_{Ni}(80^0C)x10^{-7}/Sm^{-1}$	1.05	[45]
Standard Electrode Potential -		
$E_{A,\ OH^-/O2}\ (25^0C)/V$	0.401	[39, 44-45]
$E_{A,\ Cl^-/Cl2}\ (25^0C)/V$	1.358	[39, 44-45]
$E_{C,\ H^+/H2}\ (25^0C)/V$	0	[39, 44-45]
$E_{C,\ OH^-/H2}\ (25^0C)/V$	0.828	[39, 44-45]
Tafel Constant -		
$a(H_2$, 4.5 M KOH, Ni, 80°C)/V	-0.154	[39, 44, 56-58]
$b(H_2$, 4.5 M KOH, Ni, 80°C)/V	0.154	[39, 44, 56-58]
$a(O_2$, 4.5 M KOH, Ni, 80°C)/V	0.141	[39, 44, 56-58]
$b(O_2$, 4.5 M KOH, Ni, 80°C)/V	0.051	[39, 44, 56-58]
$a(H_2$, 0.5 M NaOH, Pt/Ti, 80°C)/V	-0.10	[39, 44, 59]
$b(H_2$, 0.5 M NaOH, Pt/Ti, 80°C)/V	0.14	[39, 44, 59]
$a(Cl_2$, Sat. NaCl, DSA, 80°C)/V	0.044	[39, 44, 60-62]
$b(Cl_2$, Sat. NaCl, DSA, 80°C)/V	0.045	[39, 44, 61-63]

a(H_2, 0.5 M H_2SO_4, Pt/Ti, 80°C)/V	0.08	[39, 44]
b(H_2, 0.5 M H_2SO_4, Pt/Ti, 80°C)/V	-0.036	[39, 44]
a(CO_2, 1 M CH_3OH+0.5 M H_2SO_4, Pt-Ru/Ti, 80°C)/V	- 0.026	[64]
b(CO_2, 1 M CH_3OH+0.5 M H_2SO_4, Pt-Ru/Ti, 80°C)/V	0.126	[64]

Standard Thermodynamic Data at 25°C [69]

(Heat of Formation, ΔH^0_f, free Energy of Formation, ΔG^0_f and molar Heat Capacity, $C_f{}^0$)

Substance	ΔH^0_f/kJ mol^{-1}	ΔG^0_f/ kJ mol^{-1}	$C_f{}^0$/J mol^{-1} K^{-1}
Cl^- (aq.)	-167	- 131	- 136
Cl_2	0	0	34
OH^- (aq.)	-230	- 157	-149
H_2O (l)	- 285	- 237	75
H^+ (aq.)	0	- 0	0
H_2	0	0	29
O_2	0	0	30.8
CH_3OH	- 238.7	- 166.3	81.6
CO_2	- 393.5	- 394.4	37.1

Other Parameters -

Diffusion layer thickness, $\delta x10^4$/m	2.0	[70]
Nafion membrane thickness, $\delta_M x10^4$/m	1.78	[54]

Viscosity Estimation - Viscosity for the electrolytes and species, μ, is estimated using [43, 58]:

$$\mu \approx (1+mC)\mu^0 \tag{7.85}$$

where m is a constant, μ^0 is the viscosity of pure water under the same conditions, and C is concentration of electrolytes in a unit of mol/dm^3. For example, viscosity of 1 M H^+ at 25°C can be calculated, using values of m and μ^0 in [43, 58], via

$$\mu_{1\ M\ H^+} = (1 + 0.069x1)\ x8.903x10^{-4}$$

$$= 9.517x10^{-4}\ kg/m\ s$$

The estimated viscosities are recorded in table 7.2.

Table 7.2. Estimated Viscosities

Viscosity	Value	Original Data Source(s)
$\mu_{1\ M\ Methanol}(25^0C)x10^4/kgm^{-1}s^{-1}$	9.55	[44-47, 52]
$\mu_{4.5\ M\ KOH}(25^0C)x10^4/kgm^{-1}s^{-1}$	9.19	[43, 47, 52]
$\mu_{Sat.\ NaCl}(25^0C)x10^4/kgm^{-1}s^{-1}$	17.36	[43, 47, 52]
$\mu_{1\ M\ H^+}(25^0C)x10^4/kgm^{-1}s^{-1}$	9.517	[43, 47, 52, 58]

Estimation of Diffusion Coefficients - The diffusion coefficients of electrochemical active species and bubble-free electrolyte are obtained from [43, 65]:

$$D_i = A_i T/\mu \tag{7.86}$$

$$D = [D_+D_-(z_+ - z_-)]/(z_+D_+ - z_-D_-) \quad (7.87)$$

where A_i is a constant, z_+ and z_- are charge number of cations and anions respectively, D, D_+, D_-, and D_i are diffusion coefficient of electrolyte, cation, anion, and species i respectively.

The diffusion coefficients at high temperatures are obtained using approximate temperature dependence, i.e., the values of diffusion coefficients increase by 3 percent per kelvin [43]. For example, diffusion coefficient of 1 M methanol solution at 25^0C can be calculated via

$$D_{methanol}\ (25^0C) = D_{methanol}\ (18^0C)\ (1 + 3\%)$$

$$= 1.68 \times 10^{-9} \times 1.03$$

$$= 1.73 \times 10^{-9}\ m^2/s$$

The estimated diffusion coefficients are listed in table 7.3.

Table 7.3. Estimated Diffusion Coefficients

Diffusion Coefficients	Value	Original Data Source(s)
$D_{Cl^-}(25^0C$, saturated)$\times 10^9/m^2s^{-1}$	1.02	[43, 49, 62]
$D_{OH^-}(25^0C$, 4.5 M)$\times 10^9/m^2s^{-1}$	4.52	[39, 43, 66, 67]
$D_{Methanol}(25^0C$, 1 M methanol)$\times 10^9/m^2s^{-1}$	1.73	[43-46, 53]

Estimation of Conductivities - The following formula is used to calculate conductivities of the electrolyte [43]:

$$\sigma = (\lambda_+ + \lambda_-)z_+q_+C \quad (7.88)$$

where λ_+ and λ_- is ionic equivalent conductances of cations and anions in S m^2/equiv, respectively. Again, approximate temperature dependence, i.e., the values of ionic conductivities increase by 3 percent per kelvin [43], is adopted to get the high temperature conductivities. For example, conductivity of a saturated NaCL solution at 25^0C can be calculated using equation (7.88)

$$\sigma_{Sat.\ NaCl}\ (25^0C) = (\lambda_{Na^+} + \lambda_{Cl^-})\ z_+\ q_+\ C$$

$$= (5.011 \times 10^{-3} + 7.634 \times 10^{-3}) \times 1 \times 1 \times 6.2 \times 10^3$$

$$= 78.40\ S/m.$$

$$\sigma_{Sat.\ NaCl}\ (80^0C) = \sigma_{Sat.\ NaCl}\ (25^0C) \times (1 + 3\%)$$

$$= 78.40 \times 1.03$$

$$= 80.75\ S/m.$$

The estimated conductivities are listed in table 7.4.

Table 7.4. Estimated Conductivities

Conductivity	Value	Original Data Source(s)
$\sigma_{Sat.\ NaCl}\ (80^0C)\ /S\ m^{-1}$	80.75	[43-45]
$\sigma_{4.5\ M\ KOH}\ (80^0C)\ /S\ m^{-1}$	130	[39, 43, 44, 51]
$\sigma_{0.5\ M\ KOH}\ (80^0C)\ /S\ m^{-1}$	26	[39, 43, 44, 51]
$\sigma_{0.5\ M\ H2SO4}\ (80^0C)\ /S\ m^{-1}$	39.8	[39, 43, 44]
$\sigma_{1\ M\ Methanol+0.5\ M\ H2SO4}\ (80^0C)\ /S\ m^{-1}$	60.1	[37, 38, 43, 44]

Estimation of Equilibrium Electrode Potential and Cell Voltage

The equilibrium anode and cathode potentials at 25^0C were calculated employing the Nernst equation and the standard potentials in table 7.1. For an anode reaction

$$M = M^{n+} + ne^- \qquad (7.89)$$

The equilibrium anode potential has the form

$$E_{A,e} = E^0_{A,e} - (RT/nF) \ln (C_M/C_{M\,n+}) \qquad (7.90)$$

where $E^0_{A,e}$ is standard anode potential and the activities of the species M and M^{n+} were approximated as C_M and $C_{M\,n+}$. The corresponding anode potential is

$$E_A = E^0_{A,e} - (RT/nF) \ln (C_M/C_{M\,n+}) + a_A + b_A \log j_{av} \qquad (7.91)$$

For the reaction

$$N^{n+} + ne^- = N \qquad (7.92)$$

The cathode potential at 25^0C is

$$E_C = E^0_{C,e} + (RT/nF) \ln (C_M/C_{M\,n+}) + a_C + b_C \log j_{av} \qquad (7.93)$$

At higher temperatures, the equilibrium potentials can be obtained by integrating the Gibbs - Helmholtz equation, i.e.,

$$(\Delta G^0_2/T_2) - (\Delta G^0_1/T_1) = -\ {}_{T1}\int^{T2} (\Delta H^0/T^2)\, dT \qquad (7.94)$$

where ΔG^0_1 and ΔG^0_2 are the standard free energy change at temperatures T_1 and T_2 respectively, ΔH^0 is the standard heat of reaction at T which is given by

$$\Delta H^0 = (\Delta H^0_1 + \Delta C_p (T - T_1) \quad (7.95)$$

where ΔH^0_1 is the standard heat of reaction at T_1 and ΔC_p isthe sum of the mean heat capacities espressed by

$$\Delta C_p = \Sigma (v_i C_{p,i}) \quad (7.96)$$

where v_i is the number of moles of species I and $C_{p,i}$ is mean and molar heat capacity.

For the overall process

$$M + N^{n+} = M^{n+} + N \quad (7.97)$$

The cell voltage can be written as

$$E_{Cell} = E_A - E_C + j_{av}(L/\sigma_A + L/\sigma_C + \delta_M/\sigma_M + S/\sigma_S) \quad (7.98)$$

An example of calculating the anode and cathode potentials and the cell voltage for the chlorine cell is given below.

The electrode reactions are

Anodic: $$2\ NaCl = Cl_2 + 2\ Na^+ + 2\ e^- \quad (7.99)$$

Cathodic: $$2\ H_2O + 2e^- = H_2 + 2\ OH^- \quad (7.100)$$

Overall: $$2\ NaCl + 2\ H_2O = Cl_2 + 2\ NaOH + H_2 \quad (7.101)$$

The reactions were carried out in an anolyte of 6.2 M NaCl and a catholyte of 0.5 M NaOH at 80^0C, 3000 A m^{-2} and 1 atmosphere pressure.

At 25^0C, consider the anodic reaction (7.99), we have

$$\Delta G^0_{298} = \Delta G^0_{f,298}(Cl_2) - 2\ \Delta G^0_{f,298}(Cl^-) = 262000\ J/mol$$

$$\Delta H^0_{298} = \Delta H^0_{f,298}(Cl_2) - 2\ \Delta H^0_{f,298}(Cl^-) = 334000\ J/mol$$

$$\Delta C_p = C_p(Cl_2) - 2\ C_p(Cl^-) = 306\ J/mol\ K$$

Using equation (7.94) in this case yields

$$(\Delta G^0_{353}/353) - (\Delta G^0_{298}/298) = -\int_{298}^{353} [334000 + 306\,(T - 298)]/T^2)\, dT$$

Integrating and rearranging yields

$$\Delta G^0_{353} = 242800 + 64.4 \times 353 - 306 \times 353 \times \ln (353/298)$$

$$= 217067 \text{ J/mol}$$

So that

$$E^0_{A,e} = \Delta G^0_{353}/n\,F$$

$$= 217067/2 \times 96485$$

$$= 1.125 \text{ V}$$

Applying equation (7.89) the anode equilibrium potential at at 80^0C is

$$E_A = 1.125 - (8.314 \times 353/2 \times 96485) \ln 6.2 - 0.05 + 0.04 \times \log 3000$$

$$= 1.186 \text{ V}$$

Similarly, for the reaction (7.99), from equation (7.91) and table 7.1,

$$E^0_{C,e} = \Delta G^0_{353}/n\,F$$

$$= -[234800 - 251 \times 353 + 419 \times 353 \times \ln (353/298)]/\,2 \times 96485$$

$$= -171249/2 \times 96485$$

$$= -0.887 \text{ V}$$

Using equation (7.92) the cathode equilibrium potential at 80^0C is

$$E_C = -0.887 - (8.314 \times 353/2 \times 96485) \ln 0.5 - 0.10 + 0.14 \times \log 3000$$

$$= -0.510 \text{ V}$$

The cell voltage can be obtained from equation (7.98)

$$E_{Cell} = 1.18 - (-0.51) + 3000\,(1.78\text{x}10^{-4}/1.35 + 4\text{x}10^{-3}/80.75\text{x}0.8984 + 4\text{x}10^{-3}/26\text{x}0.8984)$$

$$= 2.09 \text{ V}$$

The estimated electrode potentials and cell voltages are listed in table 7.5.

Table 7.5. Estimated Electrode Potentials and Cell voltages

System	E_A/V	E_C/V	E_{Cell}/V	Original Data Source(s)
Cl_2-H_2[a]	1.125	- 0.510	2.09	[38, 43-47, 69]
O_2-H_2[b]	0.568	- 0.483	1.451	[38, 43-47, 69]
CO_2-H_2[c]	0.0434	- 0.143	0.637	[38, 43-47, 69]

a Cl_2 and H_2 evolutions on the RuO_2/ Ti mesh anode and the Pt/Ti mesh cathode in an anolyte of 6.2 M NaCl and a catholyte of 0.5 M NaOH at 80°C and 3000 A m^{-2}.

b O_2 and H_2 evolutions on the Ni foam anode and cathode in 4.5 M KOH solution at 80°C and 3000 A m^{-2}.

a Methonal oxidation and H_2 evolutions on the Pt-Ru/ Ti mesh anode and the Pt/Ti mesh cathode in an anolyte of 1 M CH_3OH +).5 M H_2SO_4 and a catholyte of 0.5 M NaOH at 80°C and 3000 A m^{-2}.

7.8. Conclusions

In this chapter, a centrifugal model for the rotary cell with gas evolving electrodes is proposed and tested. The model yields the relationship between cell voltage, and its reduction, and angular rotating velocity based on the principles of hydrodynamics, electrochemistry, and electrochemical engineering. It is tested against the experimental data over the range that the assumptions are considered valid. The model satisfactorily reproduces most of the experimental features.

Not surprisingly, the centrifugal model predicts that centrifugal force leads to a significant decrease in the cell voltage at a constant current density. This is attributed to the centrifugal fields in both promoting mass transfer and diverting gas bubbles away from the electrode surface.

Of course, the model is approximate due to assumptions used although gives at least a qualitative picture of the effect of centrifugal fields on electrochemical cells.

7.9. References for Chapter 7

[1] Y. Cohen and M. P. Dudukovic, Proceeding for AIChE meeting, Paper 22b, Chicago, November, 1985.

[2] S. Munjal, M. P. Dudukovic, and P. Ramachandran, Chem. Engi. Sci., 44, 2245, 1989.

[3] S. Munjal, M. P. Dudukovic, and P. Ramachandran, Chem. Eng. Sci., 44, 2257, 1989.

[4] C. Roizard, F. Mokrani, H. Le Gall, and N. Midoux, Chem. Eng. Sci., 48, 2599, 1993.

[5] Y. Maruoka and H. Brauer, Int. Chem. Eng., 29, 577, 1989.

[6] F. Otillinger and E. Blass, Chem. Eng. Tech., 11, 312, 1988.

[7] R. E. De La Rue and C. W. Tobias, J. Electrochem. Soc., 106, 827, 1959.

[8] C. W. Tobias, J. Electrochem. Soc., 106, 833, 1959.

[9] J. Dukovic and C. W. Tobias, J. Electrochem. Soc., 134, 331, 1987.

[10] H. Vogt, Electrochim. Acta, 26, 1311, 1981.

[11] D. A. G. Bruggeman, Ann. Phys., 24, 659, 1935.

[12] R. E. Meredith and C. W. Tobias, Adv. Electrochem. Electrochem. Eng., 2, 15, 1962.

[13] L. J. J. Janssen and E. Barendrecht, Electrochim. Acta, 28, 341, 1983.

[14] B. E. B.-Schlenter, L. J. J. Janssen, and S. J. D. van Stralen, and E. Barendrecht, J. Appl. Electrochem., 15, 537, 1985.

[15] N. Ibl, E. Adam, J. Venczel, and E. Schalch, Chem. Ing. Tech., 43, 202, 1971.

[16] N. Ibl, Chem. Ing. Tech., 35, 353, 1963.

[17] K. Stephan and H. Vogt, Electrochim. Acta, 24, 11, 1979.

[18] L. J. J. Jassen and J. G. Hoogland, Electrochim. Acta, 15, 1013, 1970.

[19] L. J. J. Jassen and J. G. Hoogland, Electrochim. Acta, 18, 543, 1973.

[20] L. J. J. Jassen, Electrochim. Acta, 23, 81, 1978.

[21] L. J. J. Jassen and E. Barendrecht, Electrochim. Acta, 24, 693, 1979.

[22] O. Lanzi and R. F. Savinell, J. Electrochem. Soc., 130, 799, 1983.

[23] H. Vogt, J. Appl. Electrochem. 13, 87, 1983.

[24] F. N. Ngoya, Electrochim. Acta, 28, 1865, 1983.

[25] L. J. J. Janssen and E. Barenderechet, J. Appl. Electrochem., 15, 549, 1985.

[26] L. J. J. Janssen, J. J. M. Geraets, E. Barendrecht, and S. J. D. van Stralen, Electrochim. Acta, 27, 1207, 1982.

[27] Z. Nagy, J. Appl. Electrochem., 6, 171, 1976.

[28] F. Goodridge and K. Scott, "Electrochemical Process Engineering", Plenum Press, New York, 1995.

[29] H. Vogt, Electrochim. Acta, 29, 167, 1984.

[30] H. Wendt and V. Plzak, Electrochim. Acta, 28, 27, 1983.

[31] A. T. Kuhn and M. Stevenson, Electrochim. Acta, 27, 329, 1345, 1982.

[32] L. J. J. Janssen and S. J. D. van Stralen, Electrochim. Acta, 26, 1011, 1981.

[33] P. J. Sides and C. W. Tobias, J. Electrochem. Soc., 127, 238, 1980.

[34] F. Hine and K. Murakami, J. Electrochem. Soc., 127, 292, 1980.

[35] O. de Nora, Chem. Ing. Tech, 42, 222, 1970.

[36] J. Jorne and J. F. Louvar, J. Electrochem. Soc., 127, 298, 1980.

[37] I. Rousar, V. Cezner, J. Nejepsova, M. M. Jacksic, M. Spasojevic, and B. Z. Nikolic, J. Appl. Electrochem., 7, 427, 1977.

[38] J. S. Newman, "Electrochemical Systems", Chapter 5, Second Edition, Prentice Hall, New Jersey,, 1991.

[39] D. J. Pickett, "Electrochemical Reactor Design", Second Edition, Elsevier Scientific Publishing Company, Amsterdam, The Netherlands, 1979.

[40] D. J. Tritton, "Physical Fluid Dynamics", Second Edition, Clarendon Press, Oxford, 1988.

[41] S. J. D. Van Stralen and W. M. Sluyter, J. Appl. Electrochem., 15, 527, 1985.

[42] N. Ibl and O. Dossenbach, in " Comprehensive Treatise of Electrochemistry", Volume 6, Chapters 2 and 3, (Edited by E. Yearger, J. O'M Bockris,, B. E. Conway, and S. Sarangapani), Plenum Press, New York, 1983.

[43] J. J. Tuma, "Enginering Mathematics Handbook", McGraw-Hill Book Company, New York, 1970.

[44] B. E. Conway, "Electrochemical Data", Elsevier Publishing Company, Amsterdam, 1952.

[45] D. R. Lide and H. P. R. Frederikse, "CRC Handbook of Chemistry and Physics", 76th Edition, CRC Press, New York, 1995.

[46] W. J. Hamer, "The Structure of Electrolyte Solutions", John Wiley & Sons, Inc., New York, 1959.

[47] R. A. Robinson and R. H. Stokes, "Electrolyte Solutions", Second Edition, Butter Worths, London, 1965.

[48] O. Chery, C. Roizard, G. Wild and N. Midoux, Trans. IChemE, 73, 325, 1995.

[49] H. Vogt, in " Comprehensive Treatise of Electrochemistry", Volume 6, Chapter 7, (Edited by E. Yearger, J. O'M Bockris,, B. E. Conway, and S. Sarangapani), Plenum Press, New York, 1983.

[50] I. Rousar, J. Electrochem. Soc., 116, 676, 1969.

[51] F. Hine, "Electrode Processes and Electrochemical Engineering", Plenum Press, New York, 1985.

[52] R. H. Stokes and R. Mills, "Viscosity of Electrolytes and Related Properties", Pergomon Press, London, 1965.

[53] R. E. Treybal, "Mass-Transfer Operations", Second Edition, McGraw-Hill Book Company, New York, 1968.

[54] J. Ahn and R. Holze, J. Appl. Electrochem., 22, 1167, 1992.

[55] P. Colomban, "Proton Conductors", Cambridge University Press, Cambridge, 1992.

[56] K. Kinoshita, "Electrochemical Oxygen Technology", John Wiley & Sons, Inc., New York, 1992.

[57] A. C. Forreira, E. R. Gonzalez, E. A. Ticianelli, L. A. Avaca, and B. Malvienko, J. Appl. Electrochem., 18, 894, 1988.

[58] H. E. G. Rommal and P. J. Moran, J. Electrochem. Soc., 132, 325, 1985.

[59] E. C. Potter, "Electrochemistry - Principles and Applications", Cleaver Hume, London, 1961.

[60] D. M. Novak, B. V. Tilak, and B. E. Conway, in "Modern Aspects of Electrochemistry", Volume 14 (Editors: J. O'M. Bockris, B. E. Conway, and R. E. White), Plenum Press, New York, 1982.

[61] V. Consonni and S. Trasatti, J. Electroanal. Chem., 228, 393, 1987.

[62] J. A. Harrison, in "Modern Chlor-Alkali Technology", C. Jackson (Editor), Ellis Horwood Limited, Chichester, 1983.

[63] J. A. Harrison, D. I. Caldwell, and R. E. White, Electrochim. Acta, 29, 203, 1984.

[64] V. S. Bagotzky and Y. B. Vassilyev, Electrochim. Acta, 12, 1323. 1967.

[65] R. S. Brodkey and H. C. Hershey, "Transport Phenomena", McGraw-Hill Book Company, New York, 1988.

[66] F. Fine, M. Yasuda, R. Nakamura, and T. Noda, J. Electrochem. Soc., 122, 1185, 1975.

[67] J. S.-Pierre and A. A. Wragg, Electrochim. Acta, 38, 1705, 1993.

[68] Product Bulletin, DuPont Company, USA.

[69] P. W. Atkins, "Physical Chemistry", fifth Edition, Oxford University Press, Oxford, 1994.

[70] A. J. Bard and L. R. Faulkner, "Electrochemical Methods: Fundamentals and Applications", John Wiley & Sons, New York, 1980.

Chapter 8. Conclusions

The primary aim of this project was to intensify the electrochemical processes with commercial significance. The chosen processes include gas consuming and evolution reactions. The effect of centrifugal fields on electrochemical processes is checked from cell voltage profiles and individual electrode behaviour.

As the starting point of the project, a number of electrodes based on carbon cloth or Ti mesh were prepared using chemical and electrochemical deposition techniques. Among them, the electrode based on Ti mesh was the most promising candidate for industrial applications. The electrode possesses numerous advantages over the carbon cloth electrodes including mechanical flexibility, fairly open structure for gas passage, reduced ohmic losses and increased activity. Compared to a conventional gas diffusion electrode, the Ti mesh electrode exhibits lower combined resistance and provides higher currents under comparable conditions. The networks of the mesh provide a highly conductive three-dimensional current collecting medium as well as a structural support to the catalyst within the electrode. This reduces electrode weight and makes the electrodes more efficient for the reactions.

A range of important electrochemical proceses were examined including: oxygen reduction, hydrogen oxidation, chlorine evolution, water electrolysis, methanol oxidation, and methanol fuel cell reactions. These processes were intensified in centrifugal fields with varying degrees. The intensifying degree of the gas evolving processes is much higher than that of the gas consuming processes.

Efficient catalysts accelerate the charge transfer rate and intensify the process. However, this is far from good enough. To take full advantage of the improvement in catalytic activity, high mass transport rate is necessary. This means that the

process should be intensified in a high acceleration field. Along this direction, the dual functions of centrifugal fields, i.e., promoting mass transport and disengaging gas bubbles from the electrode surface, were demonstrated for all processes examined. It was found that the two major functions play varying roles for different processes. Significant reductions in polarisation and mass transport resistance were observed for the gas evolution reactions, i.e., the chlorine evolution, the hydrogen evolution, the oxygen evolution, and the methanol oxidation. The dual centrifugal functions intensified these processes. The performance approached a maximum efficiency when the dual functions of centrifugal fields attained an optimum level. These can be mainly attributed to the high acceleration fields:

(i) Reduce the cell resistance drastically and supplement fresh electrolyte to the reaction sites efficiently through effectively disengaging gas bubbles from the electrode surface;

(ii) Overcome the mass transport limitations existed in these systems through generating powerful interphase buoyancy force;

(iii) Intensify the concentration and temperature effects.

The benefit of intensifying the gas consuming processes, i.e., oxygen reduction and hydrogen oxidation, has also been demonstrated although this is less pronounced. The centrifugal acceleration field promotes very high mass transfer rates for these reactions. However, the process kinetics, chemical properties (such as the adsorption of the reaction intermediates), and physical characteristics (such as solubility) limit the processes to a substantial extent. The centrifugal fields show little benefit in overcoming these obstacles. Also, the setup used in this work was not optimum. It not clear whether the porous electrode has adequate access to the oxygen or

hydrogen bubbles and whether the electrolyte was completely over the electrode. As a consequence, the intensification for these processes is relatively low.

For the rotary methanol fuel cell operation, the results are disappointing. In this case, although the anode process was intensified in centrifugal fields, very difficult choices for the cathode process were experienced. To intensify the processes in centrifugal fields, liquid catholyte should be chosen. This introduces a tremendous penalty of putting the fuel cell operation on a very low starting point due to very high gas transport limitation. The centrifugal function of disengaging gas bubble from the electrode surface limits to raise oxygen reduction efficiency. The similar cause also leads the poor performance for the fuel cell with the gas diffusion cathode (no liquid catholyte in the cathodic chamber).

In order to explain the experimental results, a centrifugal model for a cell with gas evolving electrodes was proposed and tested. In the model the cell voltage and cell voltage reduction are obtained from the hydrodynamic, electrochemical, and electrochemical engineering theories. The model yields the satisfactory mean cell voltage and cell voltage reduction predictions and is also able to reproduce most of the experimental features, although it is far from complete.

Recommendations for Further Work

· Optimise the rotary cell. This will improve the performance of the rotary cell in the gas consuming reactions.

· Mass Transfer Investigation: The systematic study of mass transfer characteristics of a rotary cell requires a flow cell which can provide variable and controllable parameters, such as concentration, temperature, flow rate, etc.

· It is necessary to solve the anolyte leaking problem for operation of a rotary methanol fuel cell at higher temperature, e.g., 60 - 90°C. Also, it is worthwhile to improve rotary methanol fuel cell performance by using catalysed Ti mesh anode, membranes with reduced methanol permeability and methanol insensitive cathode catalysts.

· There is a wide range of possibilities for further investigations for the use of rotary cells. For example, electrodeposition of noble metals.

· Performance modelling can be improved by solving the Laplace equations governing the rotary cell behaviour, including the entire potential and concentration fields using numerical methods, such as the boundary-element method, the boundary-integral-equation methods, etc.

Notation

The following is a list of symbols used throughout this thesis; the usual units used are shown in brackets.

A electrode area (m^2) or the average cross-section of the detached bubbles in Equation (7.18)

A_1 constant in Equation (7.38a)

A_2 constant in Equation (7.39a)

A_i constant in equation (7.85)

a thickness of the fixed layer adjacent to the electrode surface (m) or the proportionality coefficient in Equation (7.18)

a_A Tafel constant of anode (V)

a_C Tafel constant of cathode (V)

B_1 constant in equation (7.60), 2D/d

B_2 constant in equation (7.62)

B_3 constant in equation (7.62)

B_4 constant in equation (7.76b)

b_A, Tafel constant of anode (V)

b_C Tafel constant of cathode (V)

b_0 constant in Equation (7.51)

C local reactant concentration (mol dm^{-3} or k mol m^{-3}) in the rotary cell or bubble shape factor in Equation (7.15)

C_{av}- average reactant concentrations into cell (mol dm^{-3} or k mol m^{-3})

$C_{av}+dC_{av}$ average reactant concentrations out of cell (mol dm^{-3} or k mol m^{-3})

C_b bulk concentration (mol dm^{-3} or k mol m^{-3})

C_f^0 standard molar heat capacity (J mol^{-1} K^{-1})

C_s electrode surface concentration (mol dm^{-3} or k mol m^{-3})

C_1 constant as defined in Equation (7.69)

D diffusion coefficient (m^2/s)

D_i diffusion coefficient of species i (m^2/s)

D_+ diffusion coefficient of cation (m^2/s)

D_- diffusion coefficient of anion (m^2/s)

d differential symbol

E_A anode potential (V)

$E_{A,e}$ equilibrium anode potential (V)

$E^0_{A,e}$ standard anode potential (V)

E_C cathode potential (V)

$E_{C,e}$ equilibrium cathode potential

$E^0_{C,e}$ standard cathode potential (V)

E_{Cell} overall cell voltage (V)

$E_{cell,\ cf}$ voltage of the rotary cell (V)

$E_{cell,\ gf}$ voltage of the static cell (V)

F Faraday constant (96485 C/mol)

f_g gas fraction

$f_{g,b}$ gas fraction in the bulk electrolyte

f_{gd} gas fraction of diffuse layer

$f_{g,e}$ gas fraction at the electrode surface

f_{gx} local gas fraction in x direction

g gravitational constant (9.81 ms^{-2})

ΔG^0_f standard free energy of formation (kJ mol^{-1})

H height of the electrolyte column in the cell (m)

ΔH^0_f standard heat of formation (kJ mol^{-1})

I total cell current (A)

j_A anodic current density (A m^{-2})

$j_{A,0}$ exchange current densities for the anodic reaction (A m^{-2})

j_{av} average current density (A m^{-2})

$j_{av,gf}$ average current density in the gravitational field (A m^{-2})

$j_{av,cf}$ average current density in a centrifugal field (A m^{-2})

j_C cathodic current density (A m^{-2})

$j_{C,0}$ exchange current densities for the cathodic reaction (A m^{-2})

j_{lim} limiting current density (A m^{-2})

j_x local current density associated with the gas evolution in x direction (A m^{-2})

K constant in Equation (7.3), $(RTsL)/(nFPu_g d_e^2)$

k mass transfer coefficient (m/s)

k_L liquid phase mass transfer coefficient (m/s)

k_0 mass transfer coefficient in the absence of gas bubble (m/s)

L cell length (m) or electrode length (m)

m constant in equation (7.84)

n number of electrons transferred in the gas evolution reaction

n_A charge number of the anode reaction

n_C charge number of the cathode reaction

N mass flux per unit area of electrode (mol/m^2 s)

P atmosphere pressure (kg/m s^2)

P^0 vapour pressure of solvent (kg/m s^2)

Q relative conductivity, defined as $Q=s_{cf}/s_{gf}$, or constant in Equation (7.17)

r distance between the axis and the rotary cell (m)

R gas constant (8.314 J/K mol) or resistance (ohm)

R_d resistance of the diffuse layer

R_f resistance of the fixed layer

R_p specific resistance in Equations

R_r relative resistance in the cell in Equations

S net distance between the anode and cathode, $d_e - d_M$, (m)

T temperature (K)

u_b bubble rise velocity in gravitational field (m/s)

$u_G(av)$ average gas velocity (m/s)

$u_{G,d}$ gas velocity in the diffuse layer (m/s)

$u_{L,d}$ liquid velocity in the diffuse layer (m/s)

$u_{G,cf}$ (av) average gas velocity in centrifugal field (m/s)

$u_{G,gf}$ (av) average gas velocity in gravitational field (m/s)

u_0 average liquid velocity at $x = 0$, $u_0 = u_b + r\,\omega$, (m/s)

u_x liquid velocity component in x direction (m/s)

$u_x(av)$ average velocity in x direction (m/s)

u_y liquid velocity component in y direction (m/s)

u_z liquid velocity component in z direction (m/s)

V_A voltage drops caused by ohmic resistance on the anode (V)

V_C voltage drops caused by ohmic resistance on the cathode (V)

V_b average volume of departed bubbles (m^3)

v_g volumetric production rate of gas bubbles (m^3/s)

V_G volume of evolved gas (m^3)

$v_{G,d}$ gas volume flow rate in the diffuse layer (m^3/s)

$v_{L,d}$ liquid volume flow rate in the diffuse layer (m^3/s)

V_M voltage drops caused by ohmic resistance on the membrane (V)

V_S mean potential drop in bubble-filled electrolyte (V) [Equation (7.2)]

V_{SA} voltage drops caused by ohmic resistance in the anolyte (V)

V_{SC} voltage drops caused by ohmic resistance in the catholyte (V)

x coordinate direction parallel to electrode surface or distance from the bottom of the cell (m)

Y ratio of thickness of the fixed layer to the interelectrode distance in Equation (7.8)

y coordinate direction perpendicular to electrode surface (m)

z coordinate direction azimuthal to electrode surface (perpendicular xy plane) (m)

z_+ charge number of cations

z_- charge number of anions

Greek Letters

α bubble departure diameter (m)

α_A transfer coefficients for the anodic reaction

α_C transfer coefficients for the cathodic reaction

δ boundary layer thickness (m)

δ_A thickness of anode (m)

δ_C thickness of cathode (m)

δ_e distance between the electrodes (m)

δ_d thickness of the diffuse layer (m)

δ_f thickness of the fixed layer (m)

δ_{ef} distance between the working electrode and the diaphragm (m)

δ_M thickness of the membrane (m)

ε ratio of liquid flow rate to gas flow rate in Equation (7.8)

η overpotential

η_A anode overpotential

η_C cathode overpotential

θ bubble fractional surface coverage in Equation (7.15)

θ_{molar} molar energy consumption (J/mol)

λ_+ ionic equivalent conductances of cations (S m^2/equiv)

λ_- ionic equivalent conductances of anions (S m^2/equiv)

μ dynamic viscosity of solution (kg/m s) or polarisation parameter of the cell in Equation (7.7)

μ^0 viscosity of pure water (kg/m s)

ν kinematic viscosity of solution (m^2/s)

ρ density of bubble-filled electrolyte (kg m^{-3})

ρ^0 density of bubble-free electrolyte (kg m^{-3})

σ electric conductivity of bubble-free electrolyte (mho)

σ_A conductivity of anode (mho)

σ_C conductivity of cathode (mho)

σ_d effective conductivity of diffuse layer in bubble-filled electrolytes (mho)

σ_f effective conductivity of fixed layer in bubble-filled electrolytes (mho)

σ_G electric conductivity of a single sphere in Equations (7.9) - (7.11) (mho)

σ_L electric conductivity of an extended continuum in Equations (7.9-7.11) (mho)

σ_M specific conductivity of the membrane (mho)

σ_s electric conductivity of gas saturated solution (mho)

ϕ_A current efficiency of gas evolving reaction at anode

ϕ_C current efficiency of gas evolving reaction at cathode

ω angular velocity (rad/s)

Dimensionless Groups

Gr Grashof number, $g L^3 (\rho_0-\rho)/\rho\nu^2$

Re Reynolds number, $V_G a/A\nu$

Sc Schmidt number, ν/D

Sh the Sherwood number, $k a/D$